NASA Conference Publication 2123

NASA-CP-2123 19800019888

Flight Mechanics/Estimation
Theory Symposium

Arthur J. Fuchs, *Editor*
Goddard Space Flight Center

Proceedings of a symposium
held at Goddard Space Flight Center
Greenbelt, Maryland
October 17-18, 1979

NASA

NASA Conference Publication 2123

Flight Mechanics/Estimation Theory Symposium

Proceedings of a symposium
held at Goddard Space Flight Center
Greenbelt, Maryland
October 17-18, 1979

FOREWORD

The papers presented herein have been derived primarily from speakers' summaries of talks presented at the Flight Mechanics/Estimation Theory Symposium held October 17 and 18, 1979 at Goddard Space Flight Center. For the sake of completeness, abstracts are included of those talks for which summaries were unavailable at press time. Papers included in this document are presented as received from the authors with little or no editing.

CONTENTS

CONTENTS (continued)

SESSION III

SESSION I

A. J. Fuchs, Chairman

FORMULATION AND EVALUATION OF PARALLEL
ALGORITHMS FOR THE ORBIT DETERMINATION PROBLEM

Capt. Jeffrey S. Shaver,*
United States Air Force

.

ABSTRACT

Recent advances in parallel processor computer hardware architectures hold significant promise as a means of bringing large amounts of processing capability to bear on computationally intensive problems, such as the orbit propagation and orbit estimation problems. However, the utility of these new hardware architectures is heavily dependent on the structure of the computational problems. To realize the full advantages of the new parallel processors, the algorithmic structure of the application software must be complementary to the hardware architecture. This paper presents a parallel orbit propagation algorithm and a parallel orbit estimation algorithm, both of which are compatible with a single instruction stream/multiple data stream (SIMD) parallel processor architecture.

The orbit propagation algorithm computes, in parallel, Chebyshev series approximations to the right-hand members of the equations of motion over orbital arcs up to two revolutions. Analytical formulae are used to directly obtain Chebyshev series representing the integrals of the equations of motion. The algorithm uses a Picard iteration technique to obtain the converged solution. This algorithm has been applied to the Cowell Class II equations, the high-precision Variation of Parameters equations and the averaged Variation of Parameters equations. Numerical comparisons with high-precision Cowell integrations are presented for near-circular and elliptical test cases, including varied fitting parameters, arc lengths and force models. The effects of numerical error accumulation are demonstrated by comparison between a parallel integration of the two body problem and the analytic solution using the Lagrange coefficients.

A Parallel Variable Metric function minimization algorithm (gradient dependent) provides a compatible orbit estimation capability. The cost function minimized is the weighted squares of the observation residuals, and the solve-for parameters are the epoch state components. Analytical expressions have been developed in terms of the equinoctial elements for the state partial derivatives (needed for the gradient computation), which include the secular rates in the argument of perigee and the longitude of the ascending node due to the J_2 zonal harmonic. The software implementation of this algorithm is described. The performance of the Parallel Variable Metric algorithm is compared to the standard Differential Corrections algorithm in terms of accuracy and region of convergence. Speed-up ratios are calculated for both the orbit propagation and orbit estimation algorithms, indicating the potential performance improvement to be achieved if the algorithms were executed on a SIMD hardware architecture.

---

*Ph.D. Candidate, Massachusetts Institute of Technology

DIFFERENTIAL CORRECTION CAPABILITY
of the
GTDS USING TDRSS DATA

S. Y. Liu* and D. G. Soskey*
Computer Sciences Corporation

and

J. Jacintho
Goddard Space Flight Center

ABSTRACT

A differential correction (DC) capability was implemented in the Goddard Trajectory Determination System (GTDS) to process satellite tracking data acquired via the Tracking and Data Relay Satellite System (TDRSS). Configuration of the TDRSS will be reviewed, observation modeling will be presented, and major features of the capability will be discussed in this paper.

The following new types of TDRSS data can be processed by GTDS: 2-way relay range and Doppler measurements, hybrid relay range and Doppler measurements, one-way relay Doppler measurements, and differenced one-way relay Doppler measurements. These new types of data may be combined with conventional ground-based direct tracking data. By using Bayesian weighted-least-squares techniques, the new software allows the simultaneous determination of the trajectories of up to four different satellites--one user satellite and three relay satellites. In addition to satellite trajectories, the following parameters can be optionally solved for drag coefficient, reflectivity of a satellite for solar radiation pressure, transponder delay, station position, and biases. Signal travel time is corrected, and atmospheric refraction correction may be invoked optionally for the space-ground link. Finally, as an option, a statistical output report, which can be used for tracking system calibration and evaluation, will be generated.

1.0 INTRODUCTION

Conventionally, satellite tracking data are obtained by direct observation of a satellite from ground tracking facilities on the surface of the Earth. The field of view, however, is limited by the local horizon. Thus, in order to have continuous tracking, it is necessary to have many ground tracking sites well distributed over the surface of the Earth. The installation, maintenance, and operation of these ground tracking facilities is very costly. One plausible solution to this cost problem is to use geosynchronous satellites to track other satellites. This scheme not only could eliminate all but one ground tracking facility, but could also provide nearly 100 percent continuous coverage of a user satellite (Reference 1).

Indeed, satellite-to-satellite tracking (SST) has been proved to be feasible after a number of years of successful experiments using Application Technology Satellite-6 (ATS-6, a geosynchronous satellite situated at 220 degrees East longitude and 0.4 degrees North latitude at an altitude of 35,800 kilometers) as a relay satellite in tracking GEOS, NIMBUS-6 and ISEE-3.

In December 1976, the National Aeronautics and Space Administration (NASA) contracted with Western Union for 10-year leased services of the Tracking and Data Relay Satellite System (TDRSS) to maintain its orbiting satellites. The system is scheduled to become operational in the 1980s (Reference 1).

This paper presents a brief description of current capabilities of GTDS for support of the TDRSS.

2.0 TDRS TRACKING SYSTEM

2.1 System Configuration of TDRSS

The system will consist of three geosynchronous satellites and one common ground tracking facility. Two of the satellites are operational satellites and

the other is an orbiting spare satellite. The spare satellite may be converted for use as an operational satellite or may be scheduled for service in conjunction with the two operational satellites.

Satellite TDRS East will be at 41 degrees West longitude, TDRS West at 171 degrees West longitude, and TDRS spare at 106 degrees West longitude. These satellites will have circular orbits around the equator at an altitude of 36000 kilometers. The antenna coverage of the TDRSS is shown in Figure 1 (from Reference 1). Above an altitude of 1200 kilometers, the coverage is 100 percent for user satellites within the TDRS antenna pointing limits. For single-access antennas, the pointing limits are ±22.5 degrees east-west and ±31 degrees north-south. For multiple-access antennas, the field of view is a 26 degree cone (Reference 1). Below 1200 kilometers, there is a shadow zone located between 50 degrees East longitude and 125 degrees East longitude. The maximum amount of coverage lost due to the Earth occultation is 20 percent for a user satellite as low as 200 kilometers.

The common ground tracking facility will be at White Sands, New Mexico, located at 106.5 degrees West longitude and 32.5 degrees North latitude. The tracking facility includes three 18-meter, steerable antennas operated at K-Band frequency. Each of these antennas is able to track any of the TDRSs. The tracking equipment at the ground station is required to meet the following specifications (Reference 2):

- Systematic range light time error shall be less than ±20 nanoseconds (corresponding to ±6 meters).

- Maximum root-mean-square (rms) range light time noise shall be ±10 nanoseconds (or ±3 meters) for high data rate and ±20 nanoseconds (or ±6 meters) for low data rate.

- Maximum rms phase noise for Doppler measurement shall be ±0.1 radians for high data rate and ±0.2 radians for low data rate.

A sketch of the TDRSS ground tracking station at White Sands, reproduced from Reference 1, is shown in Figure 2.

Three TDRS antenna systems will be available for NASA use (Reference 1).

- TDRS to Tracking Station: a 2-meter antenna system operated at
  K-Band frequency (15 GHz)

- TDRS to Single Target: two 5-meter steerable single-access an-
  tenna systems operated at either K-Band or S-Band frequency
  (2 GHz); the steering range is ± 22.5 degrees in east/west direc-
  tion, and ± 31 degrees in north/south direction; the target can be
  a user spacecraft or a ground transponder

- TDRS to Multiple Targets: a 30-element electronically steerable
  multiple-access antenna system operated at S-Band frequency; the
  field of view of the multiple-access antenna system is a cone of
  26 degrees; a total of 20 targets can be tracked simultaneously

The TDRS spacecraft antenna configuration is shown in Figure 3, which is re-
produced from Reference 1.

2.2 Tracking Configuration of TDRSS

Basically, there are three categories of tracking configuration in TDRSS cur-
rently supported by GTDS:

- Hybrid tracking configuration
- Two-way tracking configuration
- One-way tracking configuration

For descriptive purposes, the path of the tracking signal will be defined as a
chain of nodes and legs. A NODE is either a station or a spacecraft which can
transmit and/or receive a tracking signal. A LEG is the signal path between
two nodes. The measurements related to these configurations are discussed
separately in the following subsections.

2.2.1 Hybrid Relay Range and Doppler Measurements

Using the definitions for nodes and legs, the signal path of a hybrid relay range
measurement is depicted schematically by Figure 4 (from Reference 1). The
tracking signal originates and is transmitted from an antenna at White Sands

station (node 1) and is propagated through the forward-link TDRS (node 2). The signal then arrives at a target (node 3), is relayed to the return-link TDRS (node 4), and is finally received at an antenna at the White Sands station (node 5). The target being tracked by the TDRSS either can be an orbiting user-satellite or a ground transponder.

For a hybrid relay Doppler measurement, the signal path is similar to that of a range measurement, except that there is an extra node and an extra leg. A coherent Doppler signal is transmitted from the receiving antenna (node 6) and is mixed at the return-link TDRS (node 4) to maintain the phase coherency with the Doppler signal transmitted from the transmitting antenna (node 1). The mixed Doppler signal is finally received at the receiving antenna (node 5). Node 6 and node 5 physically are the same antenna but at different positions in the inertial coordinate system due to Earth rotation.

2.2.2 Two-Way Relay Range and Doppler Measurement

For a two-way relay range or Doppler measurement, the tracking signal also originates from a transmitting antenna, is propagated via a TDRS to a target, is retransmitted by the target back to the same TDRS, and is received by the same ground antenna. Figure 4 shows the two-way tracking configuration in which nodes 1, 5, and 6 are physically associated with the same antenna, and nodes 2 and 4 are associated with the same TDRS.

2.2.3 One-Way Relay Doppler Measurements

For a one-way relay Doppler measurement, the wide-beam tracking signal originates from the target (node 3), proceeds to the return-link TDRS (node 4), mixes with the coherent Doppler signal transmitted from the ground receiving antenna (node 6), and is finally received by the ground receiving antenna (node 5). Note that there are no one-way range measurements.

9

2.2.4 Differenced One-Way Relay Doppler Measurements

A new type of measurement is feasible with the one-way tracking configuration.
With a wide-beam antenna system, the one-way tracking signal generated by
the user satellite may be received by all three TDRSs. By differencing two
streams of one-way Doppler measurements, the oscillator frequency bias can
be largely cancelled out. This is called differenced one-way relay Doppler
measurement. With a multiple-access antenna system on TDRS, up to five
user satellites can be tracked simultaneously with this type of measurement
(Reference 1).

2.3 Ground Transponder Tracking of TDRS

Theoretically, the target being tracked by TDRSS can either be in the sky (user
satellite) or on the ground (ground transponder) for all configurations. The
software design in GTDS does not impose any restrictions on a target in this
regard. In practice, however, a ground transponder usually employs a highly
directional antenna. Therefore, when a ground transponder is tracked with a
TDRS, only a two-way tracking configuration is anticipated. This mode of
tracking, using precisely surveyed ground locations of transponders, is pri-
marily used for determining TDRS trajectories for calibration of TDRSS.
With a multiple-access antenna system, the TDRS can track up to 10 ground
transponders almost simultaneously because it has the capability to electroni-
cally steer the antenna beam from one transponder to another essentially in-
stantaneously.

For hybrid and differenced one-way tracking configurations, the target must
transmit with a wide-beam antenna so that more than one TDRS can pick up the
signal to complete the configuration. Therefore, in practice the target is ex-
pected to be a user satellite instead of a ground transponder.

3.0 GTDS OBSERVATION MODELING

3.1 Modeling of Range Observation

The TDRSS range observation is obtained by measuring the time delay for a reference time marker (pseudorandom code phase) to travel from the White Sands ground tracking station, to the TDRS, to the target, and then back to the same TDRS or a different TDRS and to the ground station. The measuring process only gives the fraction part of a pseudorandom (PN) code period. The ambiguity, i.e., the whole number of PN periods, must be resolved by the orbit determination process. The actual range measurement is halved by a data preprocessor before it is input to GTDS for modeling.

In GTDS, the time tag associated with a measurement is treated as the receive time of the tracking signal at the receiving station. Therefore, the backward signal trace method is used in determining the time the signal is transmitted from each node and the position of the node at the moment the signal is transmitted. During the course of signal tracing, signal delay time for propagation at the speed of light is iteratively corrected for each leg. After the actual transmit time is determined at node 1, one half of the distances (legs) between nodes are summed as the computed range observation. This computed range observation is compared with the observed ambiguous range to resolve the range ambiguity. Transponder delay, atmospheric refraction on ground-to-space legs, measurement bias, timing bias, or station geodetics bias can be invoked optionally during modeling. The formulation of the relay range measurement and the associated partial derivatives are given in Figures 5, 6, and 7. A more complete description of the relay range measurement is contained in Reference 3.

3.2 Modeling of Doppler and Differenced Doppler Observations

Doppler measurements in TDRSS include hybrid, two-way, one-way, and differenced one-way. The raw data of the measurement consists of a nondestruct

Doppler count of a nominal bias frequency, 240 MHz, over a fixed time interval. The count is cumulative since the counter is not reset to zero between measurements.

A hybrid or a two-way Doppler measurement is performed by transmitting a signal at K-Band from the ground transmit station to a forward-link TDRS. The TDRS coherently translates the signal to the user spacecraft's tracking frequency in S- or K-Band and transmits it to the user spacecraft. The user coherently retransmits signal to the return-link TDRS at a ratio of either 240/221 for S-Band or 1600/1469 for K-Band. The TDRS then translates the signal to K-Band and transmits it to the ground receiving station (Reference 1).

The one-way Doppler measurement can be generated from either an autonomous spacecraft or a ground transponder. In the case of an autonomous spacecraft, the navigation might be performed over several days without commands from the ground. Any 10 of the 20 multiple-access service antennas of the TDRS may be simultaneously used for one-way Doppler measurements. Although the individual one-way Doppler measurements are dominated by oscillator frequency bias, a wide-beam antenna system on the autonomous spacecraft will allow the signal to be received by all three TDRSs with the same frequency bias being observed in each measurement. In differencing the measurements, this bias can be cancelled out. Thus, the tracking of a spacecraft can be as accurate as two-way measurements (Reference 1). The formulations of the relay Doppler and differenced Doppler measurements and their associated partial derivatives are given in Figures 5, 6, and 7. A more complete description of the Doppler measurements is contained in Reference 3.

4.0 DC CAPABILITIES

4.1 DC Solve for Parameters

Currently GTDS can solve for up to four satellite trajectories simultaneously, including one user satellite (target) and up to three TDRS relays in the TDRSS

observation processing mode of the Differential Correction (DC) Program. GTDS has the ability to solve for the following parameters simultaneously using any combination of the TDRSS measurement types in addition to the conventional ground-based direct tracking data of the TDRSs and the target:

- State vector of one user satellite
- State vectors of up to three TDRSs
- Drag on user satellite
- Reflectivity of the user satellite
- Reflectivity of the TDRSs being solved
- Measurement biases
- Time delay of ground transponder
- Time delay of satellite transponder
- Timing bias
- Geodetic location of tracking station and ground transponders
- Coefficients of geopotential harmonics

A Bayesian weighted-least-squares technique is employed by GTDS to process the observation data in the differential correction process. This is the same technique used in GTDS for all Differential Correction Program runs regardless of the type of tracking data being processed. The fundamentals of differential correction and the theory of estimation can be found in Reference 4.

4.2 Integration Techniques for Equations of Motion

The equations of motion for all satellites will be numerically integrated using the 12th order Cowell integrator in GTDS. The Cowell sums and accelerations will be stored on GTDS ORBIT Files from which position and velocity components will be reconstructed during the processing of TDRS observation data. The relay ORBIT Files can optionally be created prior to a DC Program run and stored for use by all GTDS program users, alleviating the need to generate the reference orbits for the TDRS relays during each DC Program run.

4.3 TDRSS Observation Selection Capabilities

GTDS provides the user with a flexible observation selection capability to process both TDRS observation data and conventional direct ground tracking data in the same DC Program. The following criteria can be used in combination for data selection:

- Satellite ID: Data can be selected and processed according to the satellite identifier for the user satellite and any, or all, of the TDRS relay satellites included in a DC Program run

- Tracking Mode: Data to be processed can be conventional direct tracking, TDRS relay tracking, or a combination of both

- TDRS measurement identifiers including the following:

    - return-link TDRS identifier number

    - forward-link TDRS identifier number

    - ground transponder identifier (if a ground transponder is tracked)

    - equipment mode (selection based on whether the relay-to-user link is operating in the S- or K-Band)

- Tracker Type: Select data according to tracking station type (i.e., GRARR, C-Band, TDRSS, etc.)

- GTDS Measurement Type: Select data according to unique GTDS measurement number assigned to each supported measurement type

- Observation Time Span: Start and end times

- Data Rate

The data selection capabilities are made possible by the construction of an observation data working file created within the GTDS. This working file includes, for each observation, a self-contained data record consisting of the following information:

- Observation receive-time tag

- Satellite identifier number

- Transmit and receive station index number

- Actual measurement of GTDS measurement type

- Doppler count interval (if applicable)

- Data sampling information

- Observation validity flags

- Observation correction flags

- TDRSS observation information including:

    - forward-link TDRS identifier number

    - return-link TDRS identifier number

    - ground transponder identifier number (if applicable)

    - user-to-relay frequency

    - single access or multiple access antenna identifier

5.0 DC PROGRAM FLOW

The basic DC Program flow was maintained in GTDS for processing TDRSS observation data. (For a complete description of the DC flow see Reference 5). A major design change was made in the handling of up to four simultaneous satellite ephemerides. The normal mode of observation processing in GTDS is to integrate the equations of motion of a single satellite during the point-by-point processing of observation data in each DC iteration. The TDRSS processing mode creates up to four GTDS ORBIT Files (Reference 5) prior to the DC program execution or prior to each DC iteration. The state vector and transition matrix for each satellite involved in an observation is retrieved from the appropriate ORBIT File during the point-by-point observation data processing. The DC program flow remains the same as the previous GTDS flow after the retrieval of the satellite state vector and the transition matrix. Figure 8 shows the overall DC flow for processing TDRSS data in GTDS.

Upon completion of the DC program, as an option, a Statistical Output Report (SOR) can be generated. This report contains observation-dependent information, including weighted observation residuals, observation edit status,

standard deviations, associated orbit plane angles, and other pertinent information used for tracking system evaluation, validation, and calibration. An SOR can be generated for the input vector (first DC iteration) and/or the final vector (last DC iteration).

6.0 FUTURE TDRSS CAPABILITIES IN GTDS

In the future, the DC program will be able to use either the Brouwer or Brouwer-Lyddane orbit generators in GTDS to create satellite ephemerides for the user (target) satellite, thus removing the present restriction of the use of the Cowell orbit generator for all satellites. A logical extension will be the use of any GTDS orbit theory for integrating the equations of motion for the user satellite.

Observation processing for the TDRS RF Beam angles, spatial beam direction, and spacecraft orientation angles is currently being implemented in GTDS. These angular measurements will be used to make observation corrections due to the center of mass to antenna offset.

The interactive graphics capability of GTDS is being enhanced to provide operational satellite missions support with TDRSS configuration tracking data.

The use of GTDS ORBIT Files in the DC Program to process TDRSS observations allows for the creation of the relay ORBIT Files prior to a DC program run. These files, which contain precision satellite ephemerides for all TDRS relays will be concatenated over a specific time span (e.g., one month) and stored for retrieval by all GTDS program users. This alleviates the need to create satellite ephemerides in each DC program run, and it allows GTDS to treat the TDRS relays as if they were ground-based tracking stations with precisely known positions while solving for the trajectory of the user satellite. The SOR will be modified to process the statistics for the RF Beam angle measurements and for the associated orientation angle information.

REFERENCES

1. Teles, J. and Ayres, C., "Advanced Spacecraft Tracking Techniques Using the Tracking and Data Relay Satellite System (TDRSS)," (paper presented to EES/EIAA Astrodynamics Conference, September 7-9, 1977)

2. National Aeronautics and Space Administration/Goddard Space Flight Center, S-805-1, Performance Specification for Services via the Tracking and Data Relay Satellite System (TDRSS), November 1976

3. Computer Sciences Corporation, CSC/SD-79/6148, Mathematical Specifications for Tracking and Data Relay Satellite System (TDRSS), S. Y. Liu, (to be published)

4. Goddard Space Flight Center, TMX-71106, Mathematical Theory of the Goddard Trajectory Determination System (GTDS), J. O. Cappellari, C. E. Velez, and A. J. Fuchs, April 1976

5. Computer Sciences Corporation, 3000-27900-02TM, Goddard Trajectory Determination System Design Manual, E. L. Zaveleta, et al., March 1975

FIGURES

Figures 1 through 8, which were cited in the preceding text, are presented on the following pages.
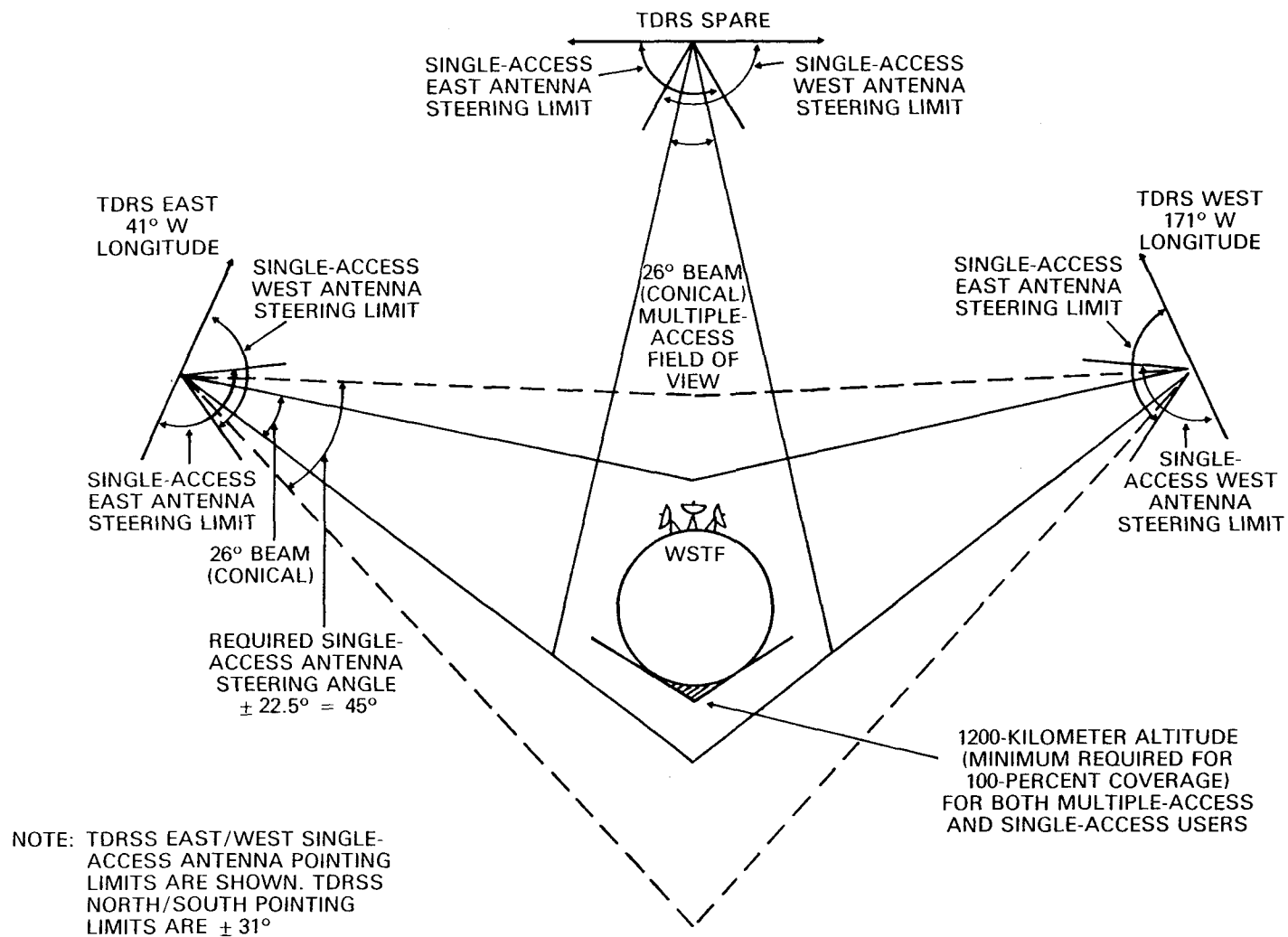
Figure 1. TDRSS Antenna Coverage

18-METER K-BAND
ANTENNAS
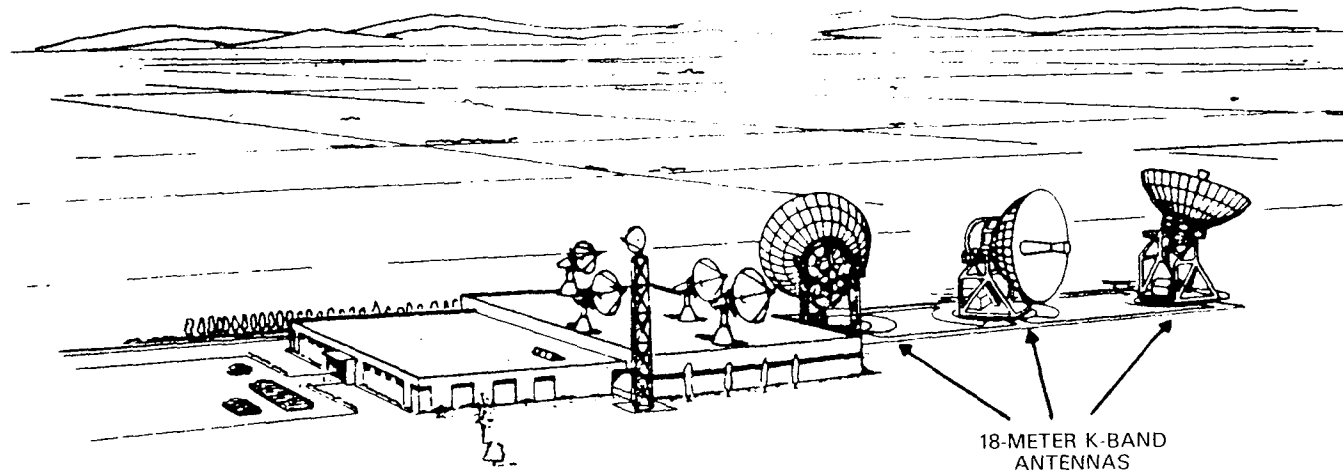
Figure 2.   TDRSS Ground Station, White Sands

MULTIPLE-ACCESS
S-BAND
PHASED ARRAY

K/S BAND
SINGLE ACCESS
ANTENNAS

SPACE-TO-GROUND
K-BAND ANTENNA
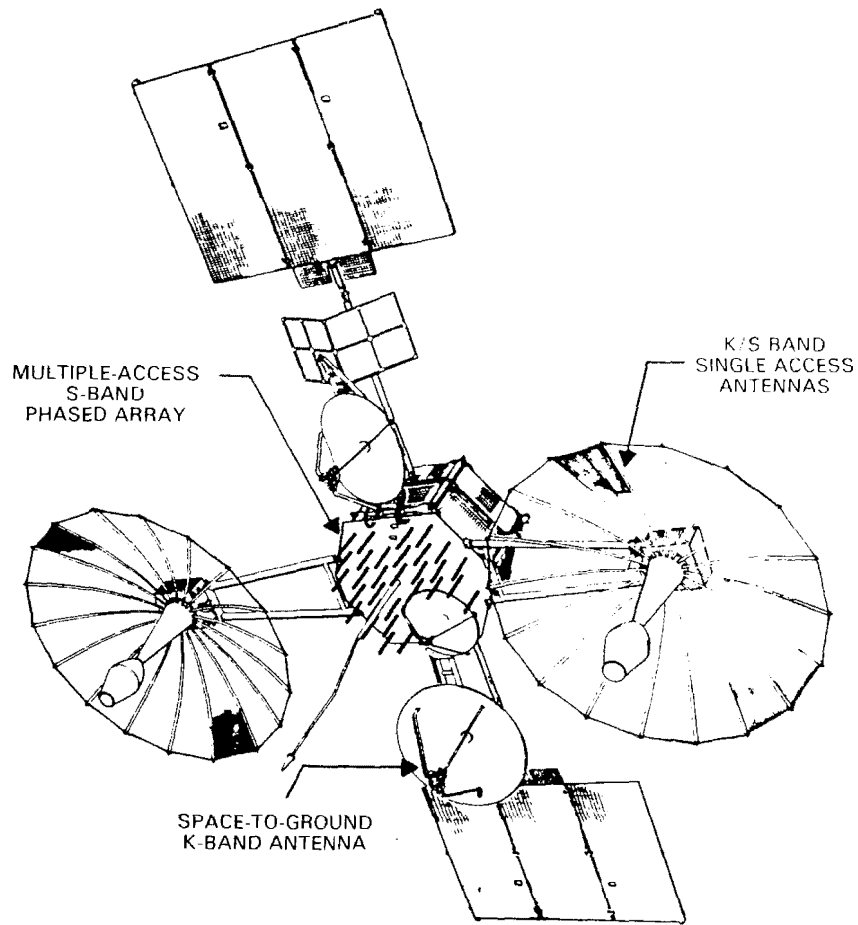
Figure 3. TDRS Spacecraft Configuration
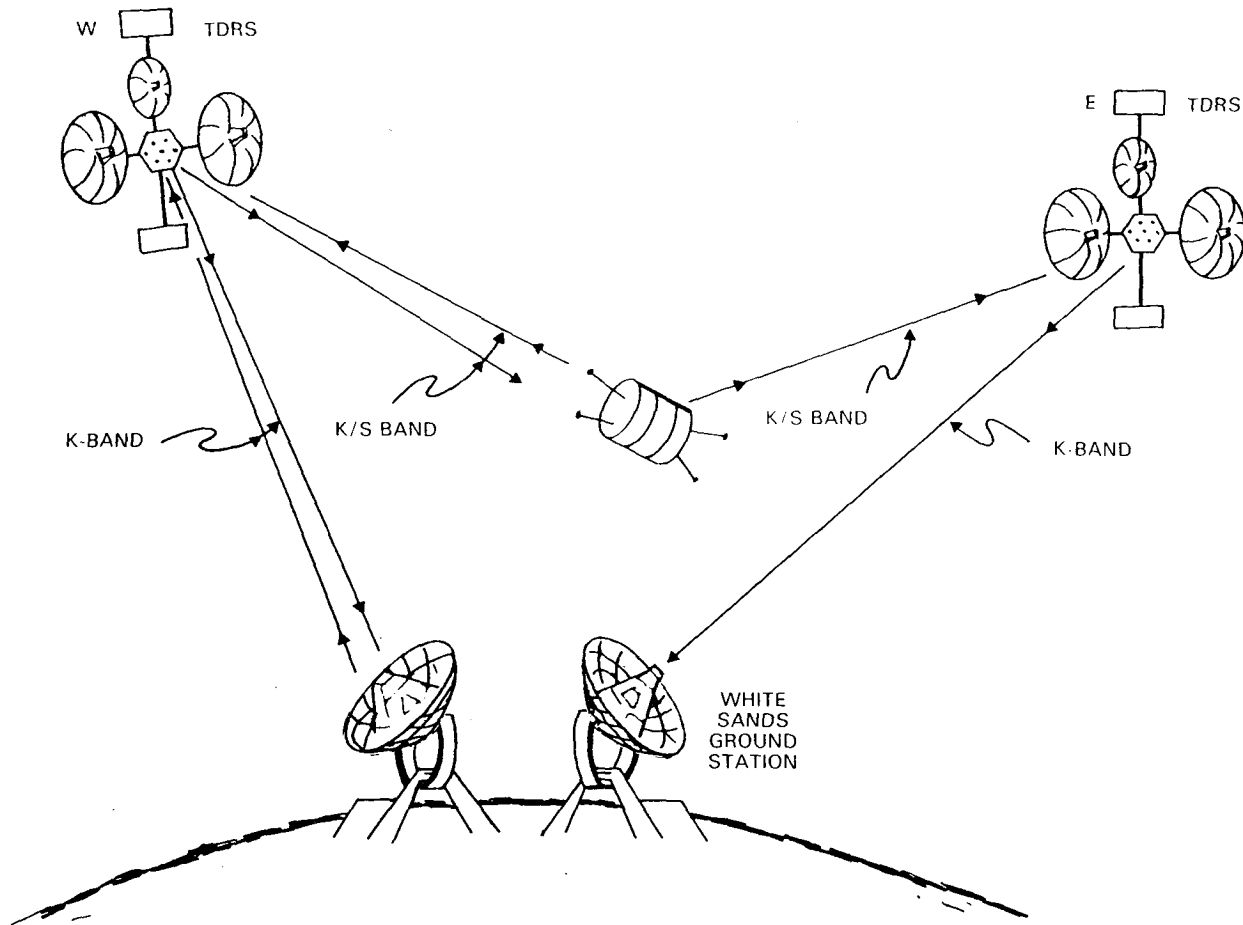
Figure 4. TDRSS Tracking Configuration

- **RELAY RANGE**

$$\rho(T) = \frac{1}{2} \left[\sum_{j=1}^{4} \rho_j + c \sum_{k=2}^{4} D_k \right]$$

- **RELAY DOPPLER**

$$\nu_d(T) = -\frac{1}{c\Delta T} \left[A \, \Delta\rho_l(T) + B \, \Delta\rho_s(T) \right]$$

WHERE $\Delta\rho(T) = \Sigma\rho_j \big|_T - \Sigma\rho_j \big|_{T-\Delta T}$

- **DIFFERENCED ONE-WAY RELAY DOPPLER**

$$\Delta\nu_d(T) = \nu_d(T) \big|_{\text{COMPARISON TDRS}} - \nu_d(T) \big|_{\text{REFERENCE TDRS}}$$

Figure 5. TDRSS Measurements Modeling

- **RELAY RANGE**

$$\frac{\partial \rho(T)}{\partial \dot{X}_j(t_o)} = \frac{\partial \rho(T)}{\partial \dot{X}_j(t_j)} \, \Phi(t_j, t_o)$$

- **RELAY DOPPLER**

$$\frac{\partial \nu_d(T)}{\partial \dot{X}_j(t_o)} = -\frac{1}{c\Delta T} \left[A \frac{\partial \Delta \rho_l(T)}{\partial \dot{X}_j(t_o)} + B \frac{\partial \Delta \rho_s(T)}{\partial \dot{X}_j(t_o)} \right]$$

- **DIFFERENCED ONE-WAY RELAY DOPPLER**

$$\frac{\partial \Delta \nu_d(T)}{\partial \dot{X}_j(t_o)} = \left. \frac{\partial \nu_d(T)}{\partial \dot{X}_j(t_o)} \right|_{\text{COMPARISON TDRS}} - \left. \frac{\partial \nu_d(T)}{\partial \dot{X}_j(t_o)} \right|_{\text{REFERENCE TDRS}}$$

Figure 6. Partial Derivatives of TDRSS Measurements
with Respect to Solve-For Parameters

ϱ (T) : **RANGE AT OBSERVATION RECEIVE TIME T**

D_K : **TRANSPONDER DELAY AT Kth NODE**

ν_d(T) : **DOPPLER FREQUENCY AT OBSERVATION**
RECEIVE TIME T

c : **SPEED OF LIGHT**

ΔT : **DOPPLER COUNT INTERVAL**

ϱ_l : **"LONG PATH" RANGE**

ϱ_s : **"SHORT PATH" RANGE**

A : **DOPPLER MULTIPLIER** } **HARDWARE RELATED**

B : **DOPPLER MULTIPLIER** } **CONSTANTS**

Φ (t_j, t_o) : **TRANSITION MATRIX FROM TIME t_o TO t_j**

Figure 7. Definition of Symbols
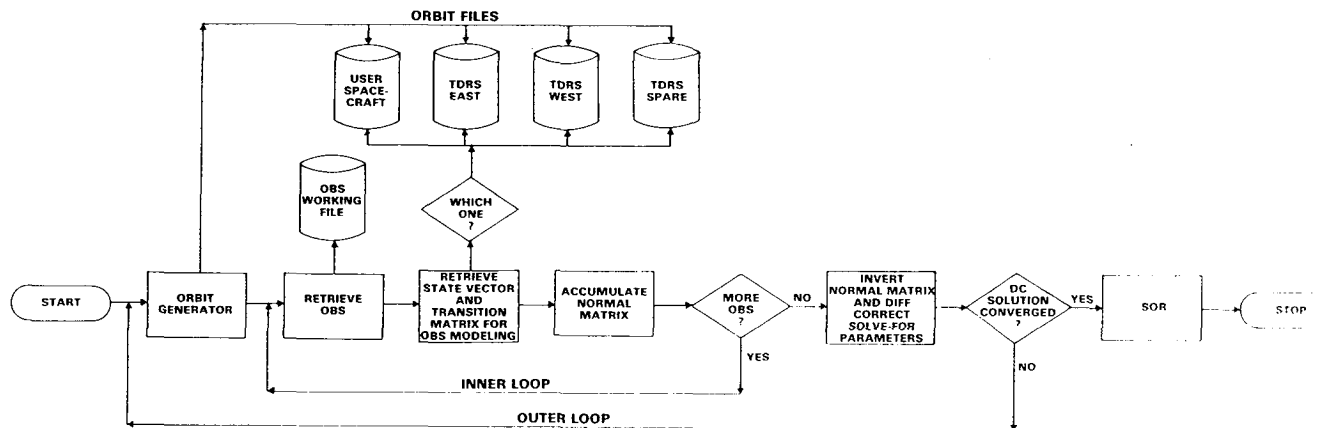
Figure 8. GTDS DC Flow for TDRSS Data

COVARIANCE ANALYSIS OF TDRS APPLICATIONS
REQUIRING TDRS STATE PREDICTIONS

James M. Leahy
Martin Marietta Aerospace

ABSTRACT

This paper presents an initial look at the results of error analysis of TDRS applications requiring TDRS state prediction. Such a need might arise for a TDRS user requiring near-real-time ephemeris processing in the absence of available TDRS tracking data. Analysis thus far has considered several near-earth users in performing a standard covariance analysis of weighted least squares orbit determination. Results include plots of TDRS and user state errors as well as comparisons of varying parameter estimation scenarios.

A STUDY OF THE EFFECTS OF STATE
TRANSITION MATRIX APPROXIMATIONS

Janet A. May
Goddard Space Flight Center

ABSTRACT

This paper investigates the effects of using an approximate state transition matrix in orbit estimation. The approximate state transition matrix results when higher order geopotential terms in the equations of motion are ignored in the formation of the variational equations. Two methods of orbit estimation were considered: the differential correction procedure (DC) and the extended Kalman filter (EKF). The system used for the study was the Research & Development version of the Goddard Trajectory Determination System (R&D GTDS). The effects of the approximation were analyzed on a number of orbits. These include orbits of various inclinations and semimajor axes. Other parameters studied include geopotential models and DC arc length.

Introduction

The state transition matrix plays an important role in orbit determination. It relates perturbations in the state at time t to perturbations in the state at epoch. Rice (4) suggests that divergence in orbit estimation methods might be linked to the use of an approximate state transition matrix. The objective of this project is to study the effects of approximating variational equations on orbit estimation methods.

We start with the equation of state:

$$\dot{X} = F(X(t);t) \tag{1}$$

which represents n-nonlinear simultaneous equations. An initial state vector $X(t_0)=X_0$ is associated with (1). The state transition matrix is described by the matrix differential equation

$$\dot{\phi} = F_x(X(t),t)\phi \tag{2}$$

where $\phi(t_0)=I$ and $F_x(X,t)$ is a matrix of partial derivations of $F(X,t)$ evaluated along a particular trajectory satisfying equation (1).

The force model, $F(X,t)$, used for this study includes perturbations involving only gravitational harmonics; other perturbations, such as drag, low thrust, etc., have been ignored. Specifically, the force function looks like

$$\dot{X} = f(X(t),t) + \sum_{i=2}^{N} \sum_{k=0}^{i} J_i^k g_i^k (X,t) \tag{3}$$

30

with $f(X,t)$ being the point mass gravitational force caused by the central body, $\sum_{i=1}^{N} \sum_{K=0}^{i} J_i^K g_i^K (X,t)$ the perturbation due to the nonsphericity of the central body. The transcendental functions $g_i^k(X,t)$ are extremely complex for $i \geq 3$. Based on this force model, equation (2) has the form

$$\dot{\phi} = \left[f_x(X,t) + \sum_{i=2}^{M} \sum_{K=0}^{i} J_i^K g_{ix}^K (X,t) \right] \phi , \quad M \leq N. \quad (4)$$

Due to the complexity of $g_i^k(X,t)$, the terms $g_{ix}^k(X,t)$ become very cumbersome.+ The question this study addresses can now be stated as: What is the effect on orbit determination methods when M is strictly less than N even though the resulting matrix $F_x(X,t)$ is still to be evaluated along a trajectory satisfying equation (3)? The main objective for setting M<N in (4) is a reduced cost in time and space in programming and evaluating these equations.

Relationship to Orbit Estimation

Orbit estimation is the process of solving for the values of a set of parameters from the observational model which will minimize the difference between a computed and an observed trajectory. The Research Version of the Goddard Trajectory Determination System (R&D GTDS) uses two methods of orbit estimation: A classical weighted least squares estimator (differential correction procedure) and a sequential estimator (Kalman filter).

The observational model is a nonlinear regression function of the state and time:

$$y(t) = G(X,t) + n \qquad (5)$$

+ Baker in Astrodynamics: Applications & Advanced Topics devotes Appendix E
   to "Partial Derivatives of Total Acceleration."

31

where n denotes random noise. The system is mx1, m being the number of observations. When least squares estimation is considered, the value of X which minimizes the weighted sum of the squares of the observational residuals is sought. The function to be minimized is called the loss function. It has the form:

$$Q(X) = [y - G(X,t)]^T W [y - G(X,t)].$$

(6)

The initial estimate of the state is X_0. Equation (6) will be minimized when $\frac{\partial Q}{\partial X} = 0$. Since $\frac{\partial Q}{\partial X}$ will be nonlinear, Q(X) is first linearized by expanding G(X,t) in a truncated Taylor's series about X_0. The linearized problem is now solved and the nonlinear problem is solved recursively via a Newton-Raphson iterative scheme to give the minimum difference between computed and observed trajectories. This briefly describes the differential correction process where a "batch" of m observations are processed simultaneously. The state transition matrix is utilized in the linearization of G(X,t).

The sequential estimator, or filter, handles the problem from a continuous process point of view. Rather than handling the data in batches as in differential correction, the filter processes new data immediately upon collection to yield an improved estimate of the state.

In this approach, observations from times t_0 and t_k are used to determine an estimate of the state residual from a reference trajectory $X(t_k)$ and a covariance matrix P_k. An observation from time t_{k+1} is added to this set. Values of the estimated state at t_{k+1}, $\hat{X}(t_{k+1})$, and the covariance matrix at t_{k+1}, P_{k+1}, are to be found. The filter used for this study is the Extended Kalman Filter (EKF) as programmed in R&D GTDS. The EKF corrects the reference trajectory to the most recent state estimate, which reduces the nonlinearities

32

of the original system and is desirable in real-time solution. In the EKF, the covariance matrix is propagated via the state transition matrix.

Study Results

This study has attempted to address the question of approximate state transition matrices by initially investigating a parameter, R, formulated by Rice (4). Mr. Rice defines a single parameter to monitor the state transition matrix. He presents a statistical argument to show that the quantity $R = \left\{ \sum_{i=1}^{3} \sum_{j=1}^{3} \phi_{ij}^{2} \right\}^{1/2}$, where ϕ_{ij} is an element of the transition matrix ϕ, can be interpreted as a measure of "error growth rate." Rice gives $P(t) = \phi P(0) \phi^{T}$ as a propagation formula for the covariance matrix, where

$$ P(0) = \left(\begin{array}{c|c} \sigma^{-2} I & O \\ \hline O & O \end{array} \right) $$

and states that the square root of the trace of $P(t)$ is commonly used as a statistical measure of position errors. Hence,

$$ (T_r)^{1/2} = \left(\sum_{i=1}^{3} P_{ii}(t) \right)^{1/2} = \sigma \left(T_r(\phi_1 \phi_1^T) \right)^{1/2} = \sigma R. $$

The signature of R suggested using the GTDS estimators with several parameters to be varied. These included arc length, geopotential modeling of state and variational equations, inclination and eccentricity. Being observed were the signature of R, the convergence/divergence of the estimator, and the rate of convergence.

As a starting point, three cases discussed in Mr. Rice's paper were compared. Case one used a force model based solely on the point mass force for both the state and state transition matrices, which will be denoted (J_0, J_0). Case two included the "J_2" harmonic term in both the equations of state and the variational equations, denoted (J_2, J_2), while case three included the J_2

harmonic term in the equations of state but only the point mass model in the variational equations, (J_2, J_0). The comparison of these three cases was based on a parameter of the state transition matrix and behavior (in terms of convergence/divergence) of the two estimators in R&D GTDS discussed above.

The first orbit considered was a circular (e=0.0), equatorial (i=0.0°) orbit with semi-major axis a=6550.524 km; this orbit will be referred to as SATORB1. The EPHEMERIS GENERATION (EPHEM) PROGRAM was used in the calculation of the quantity R. EPHEM is used to compute an ephemeris from a given set of initial conditions and, optionally, will compute the elements of the state transition matrix by numerically integrating the variational equations (Eq(4)). Using this option, the quantity R can be printed at any desired interval. The first results obtained printed the value of R every 5 minutes for the above-mentioned orbit with the modeling of cases 1, 2, and 3. Over 48 hours, little difference was observed between the corresponding values of

GRAPH 1

34
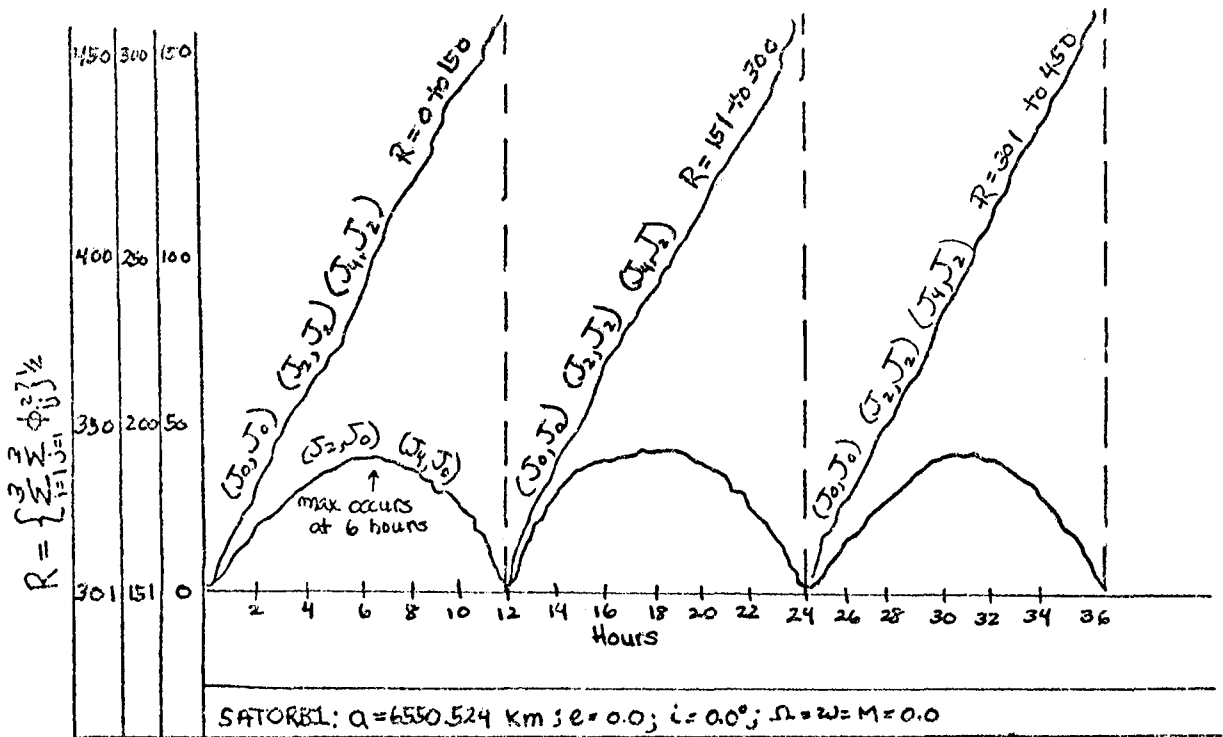
R in case 1 (J_0,J_0) and case 2 (J_2,J_2). However, the (J_2,J_0) case was vastly different. While in cases 1 and 2, R grew almost linearly with time, in case 3, R exhibited an approximately periodic behavior. Repeating the EPHEM runs with the same set of initial conditions but a different force model made the above comparisons even more striking. In this case, a 4x0 geopotential field was used in the equations of state. When generating the partial derivatives, 4x0, 2x0, and 0x0 force models were used. It is worth repeating at this time that the matrix of partial derivatives is always to be evaluated along a trajectory of the full equations of motion. Time histories of R for cases (J_4,J_4) and (J_4,J_2) were very similar to those of cases (J_2,J_2) and (J_0,J_0). Values of R for (J_4,J_0) followed the same oscillating behavior as (J_2,J_0). (See Graph 1.) These results suggest that when using a model for state with the format of eq(3), a simplified force model in the variational equations might be acceptable provided that the "J_2" geopotential term is explicitly included.

To test the effects of truncation on batch estimation, a 5-day simulated observation file was generated on tape via the GTDS DATASIM program. Range and range rate observations were made of SATORB1, where an ephemeris of SATORB1 was created with J_2 included in the state force model. The measurement standard deviations for range and range rate were 15 meters and 2 cm/sec, respectively. With a=6550.625 km, e=.00012, i=.002°, Ω =ω=M=0.0 as an initial estimate of the state, DC runs were made for cases (J_2,J_2) and (J_2,J_0) over 24 hours. In the (J_2,J_2) case, the DC procedure converged* to the correct solution in 4 iterations. The (J_2,J_0) case diverged.

These runs were repeated over a 6-hour and 12-hour arc. For the (J_2,J_0) case, 6 hours was the time at which the parameter R reached its maximum and

* The criteria for convergence of the DC are based on the iterative reduction of the RMS (square root of the mean square of the observation residuals;
$$RMS_i = \left\{ \tfrac{1}{m} (\Delta \bar{g}_i^T w \, \Delta \bar{g}_i) \right\}^{1/2}$$
where $\Delta \bar{g}_i = \bar{g} - \bar{g}(\hat{x})$ are the observation residuals, and m is the number of observations. When $RMS_{i+1} < RMS_i$, the solution is considered converging.

35

hence the time at which R started to decrease in value. In other words, for the initial 6 hours, R is monotonically increasing which more accurately reflects the "error growth rate" expected in the state transition matrix. The period of SATORB1 was about 90 minutes, so that a 6-hour arc covers about 4 orbits. When the DC program was used with (J_2, J_0) to correct over the 6-hour arc, it converged in 9 iterations; the 12-hour correction diverged. In other words, a short term (where 4xP, P being the period of the orbit, might be a guideline for short term) correction might be possible with a point-mass force model for the variational equations with a loss of speed in convergence.

It has been demonstrated that using an approximate state transition matrix can be a detriment to the differential correction process. A logical question at this point might be "how much, if any, of an approximation to the variational equations can be tolerated by the DC?" The behavior of the parameter R when (J_4, J_4), (J_4, J_2) and (J_4, J_0) ephemerides are compared hints that a truncation is permissible, provided J_2 is explicitly included in the variational equations. To test this hypothesis, simulated observations were made with SATORB1 elements using a 5x5 geopotential field in the equations of motion. Five DC runs were made with J_0, J_2, J_3^3, J_4^4, and J_5^5 models for the variational equations and the same initial estimate of the state as mentioned above. The DC programs converged in 4 iterations for cases (J_5^5, J_5^5), (J_5^5, J_4^4) and (J_5^5, J_3^3). Convergence was achieved in 5 iterations for the (J_5^5, J_2) case. (J_5^5, J_0) diverged. Table 1 lists RMS values for the last two iterations of these cases as an indication of how little is lost when a truncation from J_5^5 to J_2 for the variational equations is used.

Iteration #	(J_5^5, J_5^5)	(J_5^5, J_4^4)	(J_5^5, J_3^3)	(J_5^5, J_2^0)
3	1.1273019	1.0687897	1.7389176	2.1896022
4	.99626079	.99626079	.99631702	.99647488
5				.99626083

TABLE 1

36

The above runs were all made with a 24-hour arc. The (J_5^5, J_0) DC case did

converge in 9 iterations when used for the short (6 hour) term correction.

By looking at a typical term of the matrix of partial derivatives, it becomes

clear that the J_2 term dominates the term $\sum_{i=2}^{M} \sum_{k=0}^{i} J_i^k g_{i_x}^k (X,t)$. From Baker,

the following term is the term added to the 2-body partial derivative when

forming $\frac{\partial g'}{\partial x}$ for i=2,3 and K=0:

$$-\frac{X\mu}{r^3}\left[\frac{3}{2}\left(\frac{J_2}{r^2}\right)\left(1-5\left(\frac{z}{r}\right)^2\right)+\frac{5}{2}\left(\frac{J_3}{r^3}\right)\left(3-7\left(\frac{z}{r}\right)^2\right)\left(\frac{z}{r}\right)\right]$$

To begin with, the term J_2 is three orders of magnitude larger than J_i, $i \geqslant 3$.

Also, J_i is divided by r^i, rapidly decreasing the relative magnitude of each J_i

term for i increasing. In other words, the term J_2 will reflect the vast

majority of the perturbation due to the asphericity of the earth. Hence, it

is not at all surprising that the terms $\sum_{i=3}^{N} \sum_{k=0}^{i} J_i^k g_i^k$ can be truncated when forming

the partial derivatives without jeopardizing convergence in the DC.

Other orbits were used to test the relationship between inclination and

behavior of the DC in the (J_2, J_0) case. SATORB2 had initial elements a=6550.524 km,

e=.0, i=30°, Ω= ω=M=0. A DC program was run for a 24-hour arc with an initial

estimate of the state as a=6550.624 km, e=.00012, i=30.002° and Ω=ω =M=0.

Again, the (J_2, J_2) case converged in four iterations and (J_2, J_0) diverged.

Again, using SATORB2 elements with 5x5 geopotential field in the equations of

motion, a (J_5^5, J_2) DC run over 24 hours will converge in six iterations. These

results support the suggestion that an approximate state transition matrix might

be acceptable provided the J_2 potential term is included.

Several more inclinations were tried: i=60°, i=90°, i=98°, i=120°. At

this point, different results were achieved. The initial orbital elements

used are listed in Table 2. Simulated observations were made for each orbit.

	a	e	i	Ω	ω	M
SATORB3	6550.524	0	60°	0	0	0
SATORB4	6550.524	0	90°	0	0	0
SATORB5	6550.524	0	98°	0	0	0
SATORB6	6550.524	0	120°	0	0	0

TABLE 2

For the initial estimate of the state in each DC run, the same error was added to the orbital elements: 100 meters added to the semi-major axis, eccentricity was increased to .00012, $.002^\circ$ added to the inclination and no error added to Ω, ω and M. Rapid convergence occured for all (J_2, J_2) DC runs. With computed observations based on an ephemeris of SATORB3, the (J_2, J_0) DC run showed a definite trend toward convergence. After 12 iterations, the current state was given as a=6550.257, e~0(-6), i=60.00003°, $(\Omega+\omega+M)=720^\circ$. DC runs based on simulated observations of SATORB4, SATORB5, and SATORB6 were also converging in the (J_2, J_0) case, though at a slower rate than SATORB3. The results are summarized in Table 3.

Value of State

	No. of Iterations	a	e	i
SATORB4	20	6550.534	$.4578 \times 10^{-4}$	89.99754
SATORB5	27	6550.525	$.2398 \times 10^{-5}$	98.00005
SATORB6	24	6550.252	$.6327 \times 10^{-6}$	120.0

TABLE 3

Table 4 compares the RMS value for various iterations for SATORB3, 4, 5, and 6 (J_2,J_0). This serves as a monitor for the rates of convergence.

RMS Values (J_2,J_0)

Iteration #	SATORB3	SATORB4	SATORB5	SATORB6
1	2084.7695	2261.6206	1766.1576	2307.2376
6	74.458092	1175.0753	742.93831	103.57066
12	57.808147	521.06515	260.84572	112.82074

TABLE 4

As one might expect, since $\cos\frac{\pi}{3} = |\cos\frac{2\pi}{3}|$ and $\sin\frac{\pi}{3} = \sin\frac{2\pi}{3}$ the RMS values are most similar for $i=60^0$ and $i=120^0$, (SATORB3 and SATORB6). In these two cases, the first 12 iterations alternated between converging and diverging, with large decreases of RMS value in convergent iterations. (This accounts for $RMS_{12} > RMS_6$ in SATORB6.)

In order to examine the sensitivity to inclination, it is helpful to look at first order perturbations. In Methods of Orbit Determination, Escobal devotes a chapter to "Secular Perturbations," where the term secular describes variations "associated with a steady nonscillatory, continuous drift of an element from the adopted epoch value."[*] He represents the perturbing potential as $A \equiv \Phi - V$ where Φ is the potential due to an aspherical earth and V is the potential of a spherical earth. He segregates from A those terms which will contribute secular variations in the elements and arrives at

$$\hat{A} = K^2 n \left[\frac{3}{2} \frac{J_2}{a^2} \left(\frac{a}{r}\right)^3 \left\{\frac{1}{3} - \frac{1}{2}\sin^2 i\right\}\right] \qquad (7)$$

where $K^2 m = n^2 a^3$. Note that this is a first order expression in J_2 and for the sake of this analysis, the J_i, $i \geqslant 3$, terms have been neglected. Little is lost

[*] Escobal, P.R., 1965, p. 362.

39

by neglecting J_i, $i \gtrsim 3$ as the J_3 term is approximately 10 orders of magnitude smaller than the J_2 term and the relative magnitude of J_i and J_2 becomes even more drastic for $i > 3$. Expression (7) is then averaged over one revolution, resulting in:

$$\hat{A}^* = K^2 n \left[\frac{3}{2} \frac{J_2}{a^3} (1-e^2)^{-3/2} \{ \frac{1}{3} - \frac{1}{2} \sin^2 i \} \right]$$

(8)

Using this as the perturbing function due to J_2, it is easy to see that the secular effect of J_2 is eliminated in the equations of motion when $i = 54.7^{\circ}$ (since $1/3 - 1/2 \sin^2 54.7^{\circ} = 0$). In other words, at this specific inclination, the satellite, in a secular sense, perceives the earth as approximately (i.e., to first order J_2) spherical.

With the aid of the above model for the perturbing function, Escobal develops the following equations representing the gradual drift of the classical elements from their adopted epoch values. Note that only Ω, ω and M experience this drift and a, e and i are taken to be constant. (It might be worthwhile to state again that this is only a first order secular perturbation theory.)

Anomalistic mean motion:

$$\bar{n} = n_0 \left[1 + \frac{3}{2} \frac{J_2 (1-e^2)^{1/2}}{p^2} (1 - \frac{3}{2} \sin^2 i) \right]$$

Mean Anomaly:

$$M = M_0 + \bar{n} (t - t_0)$$

Longitude of the ascending Node:

$$\Omega = \Omega_0 - (\frac{3}{2} \frac{J_2}{p^2} \cos i) \bar{n} (t - t_0)$$

Argument of Perigee:

$$\omega = \omega_0 + (\frac{3}{2} \frac{J_2}{p^2} [2 - \frac{5}{2} \sin^2 i]) \bar{n} (t - t_0)$$

40

Between these critical inclinations of 54.7° and 125.3°, the rate of the
secular variations of the elements is smaller than outside of this region.
This accounts for convergence in the DC procedure with (J_2, J_0) modeling
for orbits with inclinations between 54° and 125°.

To conclude the differential correction section of this study, two more
orbits were considered. These orbits were elliptical with a greater
semi-major axis. Simulated observations were made of these orbits. The
initial states are given in Table 5.

	a	e	i	Ω	ω	M
SATORB7	7278.360	.1	0	0	0	0
SATORB8	9357.89143	.3	0	0	0	0

TABLE 5

A larger value for a will decrease the effect of J_2 which is readily seen in
equation (8). However, the effect of $\dot{J}_2$ is not absent from these two orbits
and the graph of the parameter R with (J_2, J_0) modeling suggests that the DC
procedure will have trouble converging over a 24 hour arc, which it indeed does.
But the period of SATORB7 and 8 is increased to 103 minutes and 150 minutes,
respectively. Because of its period, it is not surprising that SATORB8 converges
in 11 iterations over a 12-hour span with the (J_2, J_0) modeling. With SATORB7,
P=103 minutes so that 7 hours ($\sim 4xP$) should be a reasonable time arc in the
(J_2, J_0) DC. When a 6-hour arc is used, the (J_2, J_0) DC converges to SATORB7
elements in 11 iterations with rapidly decreasing RMS values. With a 12-hour
arc, convergence was still not achieved after 30 iterations.

The results obtained using the FILTER as an orbit estimator are more
difficult to examine than the results from the DC. As input to the FILTER
program, the user supplies an initial estimate of the state along with an

initial estimate of the covariance matrix.* The a priori covariance matrix contains the state standard deviation and correlations, hence points the filter in the right direction.

For this study, the observational residuals were used to monitor filter performance, with decreasing residuals within a pass and modestly larger residuals appearing after a data gap indicating convergence. The arc length used in the filter portion of this study was 18 hours.

When testing the effect of approximating the state transition matrix in the filter, only the SATORB1 orbit was used. With $i=0.0^\circ$ and $e=0.0$, this orbit is particularly susceptible to perturbations due to the earth's J_2 nonsphericity. As will be demonstrated below, the filter has an added dimension of sensitivity, that being the a priori covariance matrix. Because of this and time constraints, the use of the filter was restricted to this orbit.

The first offset imposed on the state was the same as that used for the DC: $\Delta a=100m, \Delta e=.00012, \Delta i=.002^\circ, \upsilon =\Omega=M=0.0$. With this offset, the cartesian elements at t_0 are $x=6549.8379$ km, $y=z=0.0$ km, $\dot{x}=0$ km/sec, $\dot{y}=7.801531422$ km/sec and $\dot{z}=-.0002723$ km/sec. At t_0, the true cartesian elements are $x=6550.524$ km, $y=z=0.0$ km, $\ddot{x}=\ddot{z}=0.0$ km/sec and $\dot{y}=7.8006548$ km/sec. Four different a priori covariance matrices were tried in the filter with this initial state estimate. All four covariance matrices were diagonal, implying there was no correlation among the errors in the state estimate. The first covariance matrix exactly reflected the errors in the state:

* The DC procedure has an a priori covariance matrix default value of infinite magnitude so that its inverse is the null matrix. In the DC procedure it is this inverse which is an additive term to the loss function (eq(6)); however, it has been omitted in eq(6) as it is the null matrix.

$\sigma_x = .68$ km, $\sigma_y = \sigma_z = .1 \times 10^{-4}$ km, $\sigma_{\dot{x}} = .1 \times 10^{-4}$ km/sec, $\sigma_{\dot{y}} = .87 \times 10^{-3}$ km/sec and $\sigma_{\dot{z}} = .27 \times 10^{-3}$ km/sec.

The results obtained for (J_2, J_2) and (J_2, J_0) were very similar, both cases converging. Table 6 below lists, for the last 6 passes, the largest residual in meters within a pass for both cases:

Pass Number

	19	20	21	22	23	24
(J_2, J_0) max $|0-C|$	23	20	29	21	19	31
(J_2, J_2) max $|0-C|$	31	43	22	27	21	30

TABLE 6

These results change greatly when a different a priori covariance matrix is used. With $\sigma_x = \sigma_y = .1$ km, $\sigma_z = .01$ km and $\sigma_{\dot{x}} = \sigma_{\dot{y}} = \sigma_{\dot{z}} = .1 \times 10^{-4}$ km/sec, the (J_2, J_0) case failed to converge. This covariance matrix fails to recognize the error in the $\dot{y}$ component, $\Delta\dot{y} = .00087$ km/sec, so that the actual error in $\dot{y}$ is 87 times larger than is reflected in the standard deviation associated with it: $\sigma_{\dot{y}} = .1 \times 10^{-4}$ km/sec. The largest residual in the last 6 passes is listed below. Note that the (J_2, J_2) case fares much better than (J_2, J_0) and is considered converging.

Pass Number

	19	20	21	22	23	24
(J_2, J_0) max $|0-C|$	997	1151	1184	1094	1250	982
(J_2, J_2) max $|0-C|$	35	72	21	58	45	81

TABLE 7

If the standard deviation of $\dot{y}$ is increased to $\sigma_{\dot{y}} = .00004$ so that $\Delta\dot{y}$ is approximately 20 times larger than is reflected in the standard deviation,

the (J_2,J_0) case responds a little better. However, it is not considered

converging. The residuals during the first 9 hours suggest the filter

has a handle on the correct state. The next 9 hours shows increasing

residuals as the filter drifts away from the possible steady state.

Lastly, the standard deviation of $\dot{y}$ was increased again to $\sigma\dot{y}$=.00015 or 5 times

smaller than the error on $\dot{y}$. Here the (J_2,J_0) case did as well as the

(J_2,J_2) case. Table 8 summarizes the results for $\sigma\dot{y}$=.0004 and

$\sigma\dot{y}$=.00015, with σ_x=σ_y=.1,σ_z=.01,$\sigma\dot{x}$=$\sigma\dot{z}$=.1 x 10^{-4}.

Pass Number

	19	20	21	22	23	24
$\sigma\dot{y}$ =.0004 km/sec (J_2,J_0) max $\lvert$0-C$\rvert$	190	226	230	220	242	227
(J_2,J_2) max $\lvert$0-C$\rvert$	28	39	22	28	12	41
$\sigma\dot{y}$ =.00015 km/sec (J_2,J_0) max $\lvert$0-C$\rvert$	32	23	31	33	29	47
(J_2,J_2) max $\lvert$0-C$\rvert$	28	37	23	28	14	38

TABLE 8

Although these results are far from conclusive, some inferences can

be drawn from them. It has been demonstrated that for this case the filter

responds well with an approximate state transition matrix provided the a

priori covariance matrix reflects the state errors within five standard deviations.

The test cases used for this study suggest that when the error is between 20

and 90 times larger than the standard deviation, the (J_2,J_0) case fails, yet

the (J_2, J_2) case is able to reach a steady state solution. This suggests that when the a priori covariance matrix is considered an accurate indication of the state error, truncated variational equations might not harm the performance of the filter. On the other hand, when the initial covariance matrix somewhat inaccurately reflects the state error, the full partial derivatives are needed to help steer the filter toward steady state. (The term "somewhat" is used here as a precaution; a totally inaccurate a priori covariance matrix can easily cause a (J_2, J_2) filter case to diverge.) This sensitivity to the initial covariance matrix makes it difficult to draw conclusions regarding the filter's performance as a function of the state transition matrix.

Conclusions

This paper has attempted to evaluate the effects of an approximate state transition matrix on the differential correction procedure and the filter procedure as used for orbit estimation. The DC results fall into four categories: the effects due to (1) extent of the approximation, (2) orbital inclination, (3) length of time arc, and (4) orbital eccentricity. Coinciding with these categories is the behavior of the parameter $R = \left\{ \sum_{i=1}^{3} \sum_{j=1}^{3} \phi_{ij}^2 \right\}^{1/2}$. R can be used to "predict" convergence/divergence in the DC and its behavior suggested these four categories as meaningful avenues to investigate. When using a force model for the state which includes the J_n^m harmonic term, it has been shown that it is a safe practice to approximate the variational equations provided that the J_2 term is included. When this approximation is made, the DC process will still converge as it would with the full variational equations with only a

negligible loss of speed. A total truncation of the harmonic terms in
the variational equations will, in general, cause divergence in the DC.
One exception to this is orbits with inclinations between 54.7^O and 125.3^O
In this range of inclination, the effect of the nonsphericity of the earth
is minimized. Here (J_2, J_0) DC cases will converge but so slowly that
the truncation might, in practice, be undesirable

The oscillatory signature of R when the most drastic truncation is
made suggests the possibility of short term differential corrections. The
maximum value of R tends to occur after four periods of the orbit. Hence an
arc length of four times the orbital period becomes a reasonable guideline
for short term corrections. In this arc length, convergence is achieved but
speed of convergence again becomes the trade-off for the truncation. As the
orbital period lengthens with greater semi-major axis, so does the time
arc over which the (J_2, J_0) case converges in the DC procedure.

With the filter as an estimator, less conclusive results are found.
The effect of a truncation in the variational equations on filter performance
was highly correlated to the initial covariance matrix. When the a priori
covariance matrix was a good indication (within 5 standard deviations) of
the actual error imposed on the state, little difference was seen in the convergent
behavior of the filter for the (J_2, J_2) and (J_2, J_0) cases. However, when the
accuracy of the a priori covariance matrix is relaxed, the (J_2, J_0) case showed
divergence in the cases tested. Furthermore, when the accuracy of the a priori
covariance matrix is completely lost, neither the (J_2, J_0) nor the (J_2, J_2) case
will converge.

The results obtained in the filter section of this paper leave another set of questions open. It was assumed that using the low altitude, circular equatorial orbit where the perturbations due to the nonsphericity of the earth are most pronounced would be a good orbit to test the effects of truncated variational equations in the filter. This appears to be a valid assumption in view of the analysis mentioned above based on equations (7) and (8). However, other sets of orbital elements could be tested in order to help determine the limits of accuracy needed in the a priori covariance matrix when using an approximate state transition matrix. Also, this study was restricted to variations in $\overline{\sigma_{\dot{u}}}$. Certainly many other variations could be tested, although this starts to drift away from the original intent of the study. Also, is there a level of state noise which might be used to help compensate for the use of an approximate state transition matrix?

In general, this study could be expanded to nonpotential accelerations such as drag and solar radiation pressure. What, then, would be the effect of including a nonpotential acceleration in the equations of motion but excluding it in the variational equations?

Lastly, the stability properties of the state transition matrix is a question of interest. Does the solution to the variational equations exhibit one type of stability for the (J_2,J_2) modeling which is different from (J_2,J_0) modeling?

Although many questions remain open, it is hoped that this study sheds some light on the appropriateness of state transition matrix approximations.

REFERENCES

1. Baker, R.M.L., M.L., <u>Astrodynamics Applications and Advanced Topics</u>, Academic Press, New York, 1967.

2. Escobal, P.R., <u>Methods of Orbit Determination</u>, Wiley, New York, 1965.

3. Kaula, W.M., <u>Theory of Satellite Geodesy</u>, Blaisdell Publishing Company, Toronto, 1966.

4. Rice, D.R., "An Investigation into the Effects of Using Simplified Force Models in the Computation of State Transition Matrices," presented at AIAA 5th Aerospace Sciences Meeting, New York, January, 1967.

A SEMIANALYTICAL THEORY FOR THE
PARTIAL DERIVATIVES FOR PERTURBED MOTION

W. McClain,* A. Green,[†] A. Bobick,** and P. Cefola[††]
Charles Stark Draper Laboratory

ABSTRACT

A semianalytical theory for the partial derivatives of perturbed motion is described. The theory is based upon the generalized method of averaging. The required functional capabilities include the solution of the variational equations for the averaged equations of motion and the evaluation of the short-periodic partials. The results are presented in the framework of both the analytical and numerical averaging methods. Additional two-body functions (the partial derivatives of the Poisson brackets with respect to elements and the second partial derivatives of position with respect to elements) are required and these have been derived with the aid of the computerized algebra system, MACSYMA. However, for the initial developmental effort, two-sided divided difference techniques have been used to construct the partial derivatives of the averaged equations of motion and the short-periodics with respect to the slowly varying elements. Partial derivatives with respect to the phase angle are constructed analytically. This implementation allowed duplication, in the partial derivatives, of the force models specified in the averaged equations of motion and the short-periodics with a relatively small software development effort. Numerical comparisons of the semianalytical partials with the Cowell partials are given.

*Staff Engineer
†CPT, ARMOR, U.S. Army
**MIT Dept. of Electrical Engineering and Computer Science
††Section Leader, Space Systems Analysis, Air Force Programs Department

TARGETING WITH FIXED PROPELLANT LOAD

Geza S. Gedeon
TRW Defense and Space Systems Group

ABSTRACT

The Inertial Upper Stage (IUS) for the Space Shuttle Operation employs solid rocket stages with fixed, propellant loadings. This means that, if for a given mission the satellite weight is less than the maximum, the IUS will deliver higher ΔV-s than required. Then, means must be found to waste the excess capability in order to achieve the desired orbit. One way would be to execute a nonoptimal transfer which would require higher than maximum ΔV-s. In the following, an algorithm is presented which defines take-off points on the parking orbit and the injection points on the target orbit* for which transfer orbits require a fixed ΔV_1 and a fixed ΔV_2 (defined by the satellite weight).

To have complete generality, it is assumed that both the parking and the target orbit are elliptical. This allows the use of the same algorithm for guidance, i.e., to compensate for ΔV errors. Namely the transfer orbit achieved by the erroneous ΔV_1 is regarded as a new parking orbit and the new transfer problem is solved by assuming a $\delta \Delta V_1$. The maximum value of $\delta \Delta V_1$ is the ΔV_1 variation and its minimum value is the one which still yields a solution by the algorithm. ΔV_2 errors are regarded orbit injection errors and compensated the usual way.

---

*For interplanetary missions the target-orbit is the IUS parking orbit from which the third stages inject the spacecraft into a departure hyperbola.

Figure 1 shows the performance of the two-stage IUS. Also shown are on the
figure the minimum ΔV_1 and ΔV_2 required to transfer a satellite from the
Shuttle orbit into a 2.9° inclined synchronous (circular) orbit. For a
satellite which weighs ≈ 5300 lb, the IUS would produce these ΔV-s, thus
a Hohmann transfer, from node to node, would be feasible. But for a
satellite weighing less than 5300 lb, the IUS delivers an extra performance
which has to be wasted some way. This can be done, e.g., by a non-optimum
transfer scheme shown on Figure 2. Instead of transferring from node to node,
transfer is made between non-nodal points D and A. If the points are
correctly chosen the equations shown under the figure are simultaneously
satisfied with the same h = angular momentum value. In those equations A and B
are simple constants which depend on the chosen geometry, γ_i are direction
cosines of the chord vector $\vec{c}$ in two coordinate systems, the first one is
shown, the other would be in the target plane with the X axis through A.
V_R and V_T are the radial and transverse velocity components of the parking
(p) and the target (t) orbit velocities. Finally, ΔV_1 and ΔV_2 are the ideal
rocket velocities delivered by the IUS to a satellite with the particular
weight.

Generally the two equations do not yield simultaneous solutions, one of the
points or both have to be moved to get a solution. There are many different
ways to use residues to move one of the points to the correct location, any
of these can be implemented on a digital computer.

The following figures show examples of transferring from a 150 n mi circular
Shuttle orbit a 2900 lb satellite into different final orbits. Figure 3a
shows the case of transferring from a 28.5° inclined Shuttle orbit into a
24 hour circular equatorial orbit. The angle of the first burn is measured
in the parking orbit from the node where the target orbit "ascends" (northward)
through the parking orbit plane. The second angle measured in the target
orbit from the node where the parking orbit "descends" through the target
orbit plane (same location). Values for a Hohman transfer would be 0 and 180.
For a satellite weighing only 2900 lb, solutions are represented by the two
curves on Figure 3a.

Figure 3b shows the corresponding angular momentum values, i.e., the simultaneous solutions of the two ΔV equations. The cross marks are serving to interrelate the corresponding branches of the curves. If two radii vectors and the angular momentum are known, then the transfer orbit is completely defined, transfer time, transfer angle, perigee, apogee altitudes, burn directions, etc., can be all calculated.

Figures 4a and b show transfer possibilities to a 12-hour critically inclined circular orbit from a 37.5° inclined Shuttle orbit. Both orbits have the same right ascension of the nodes, (most favorable case).

Figures 5a and b show "Type I"* transfers to a 12-hour critically inclined eccentric orbit from a 37.5° inclined Shuttle orbit. The perigee altitude of the final orbit is 150 n mi and its apogee altitude is 21390 n mi. The argument of the perigee is 270°.   The right ascension of the target orbit is five degrees behind that of the parking orbit which was found to be approximately the best geometry. Even so the range of solution is rather restricted. A much more broad range was found for "Type II" transfers shown on Figures 6a and b. It is interesting to note that if departure is made between -98° and -70° both Type I and II transfers are possible, i.e., the quartics produce four real roots.

---

* Like on interplanetary missions Type I trajectories have less than 180° transfer angles. Type II trajectories have more than 180° transfer angles.
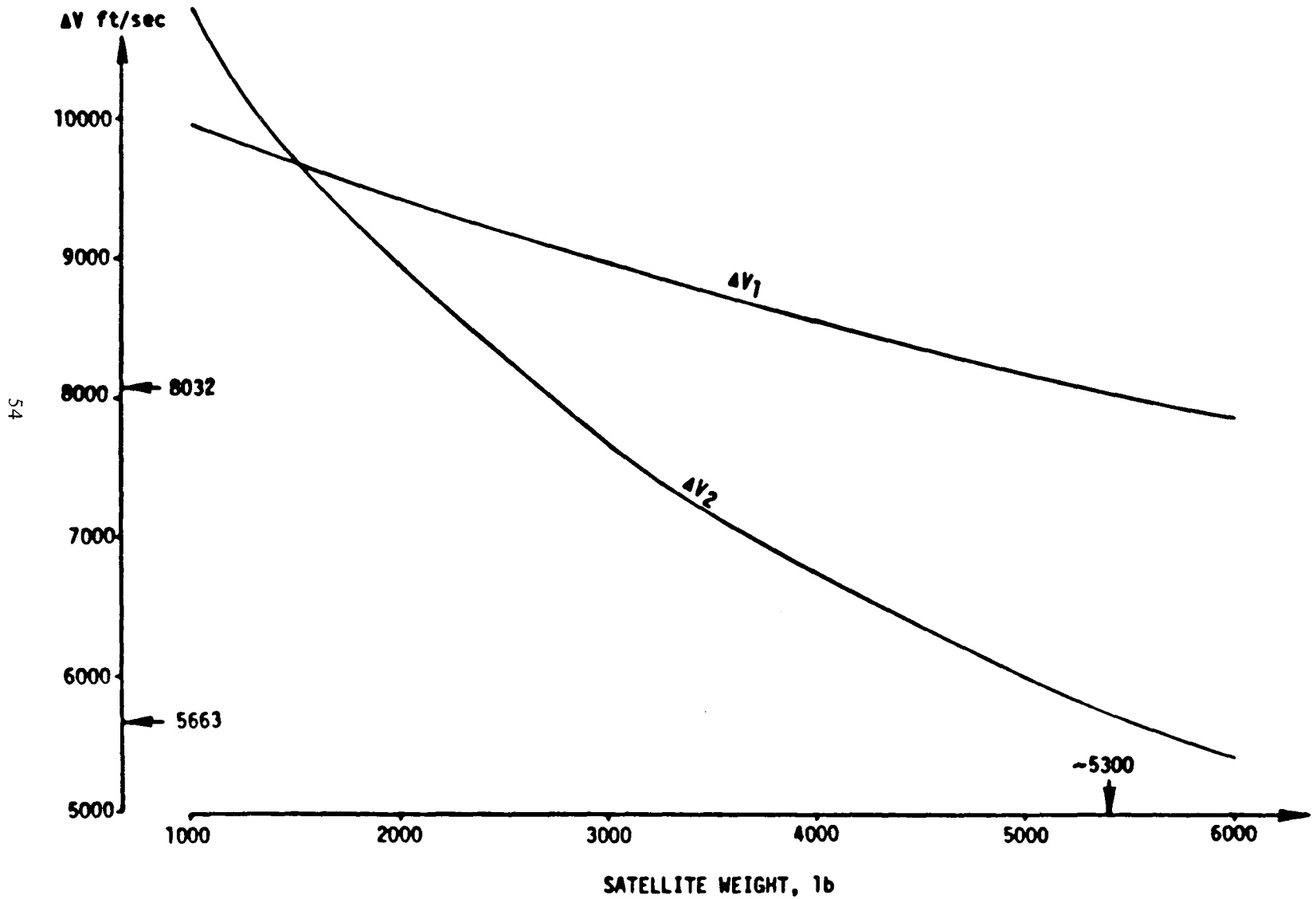
FIGURE 1. IUS PERFORMANCE
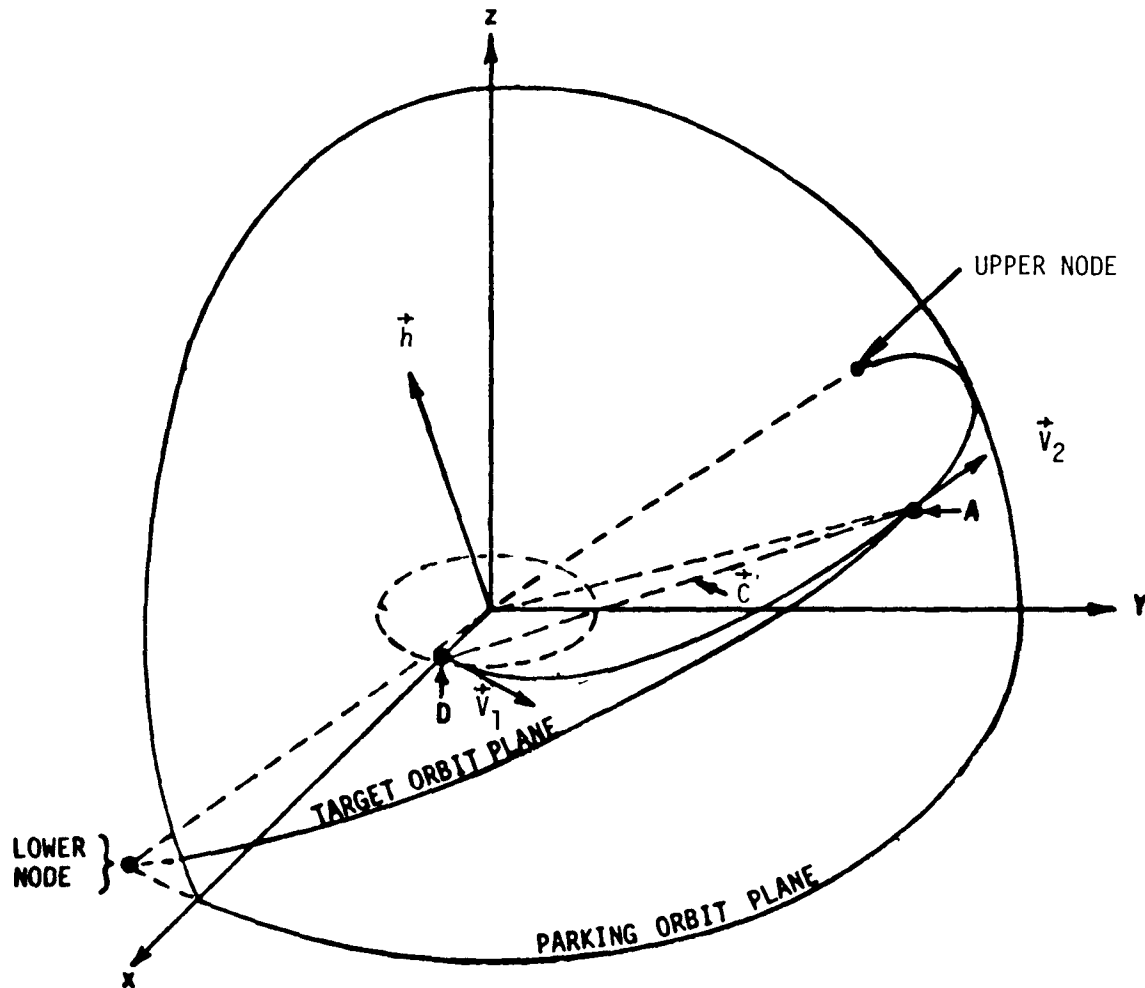
$$(\Delta V^2) = A^2 h^2 - 2A(\gamma_1 V_R + \gamma_2 V_T)h + (V_R^2 + V_T^2 + 2q\gamma_1 AB) - 2qBV_R/h + B^2/h^2$$

for ΔV_1: $q = +1$, $(V_R, V_T, \gamma_1)_p$ for ΔV_2: $q = -1$, $(V_R, V_T, \gamma_1)_t$

FIGURE 2. METHOD OF SOLUTION
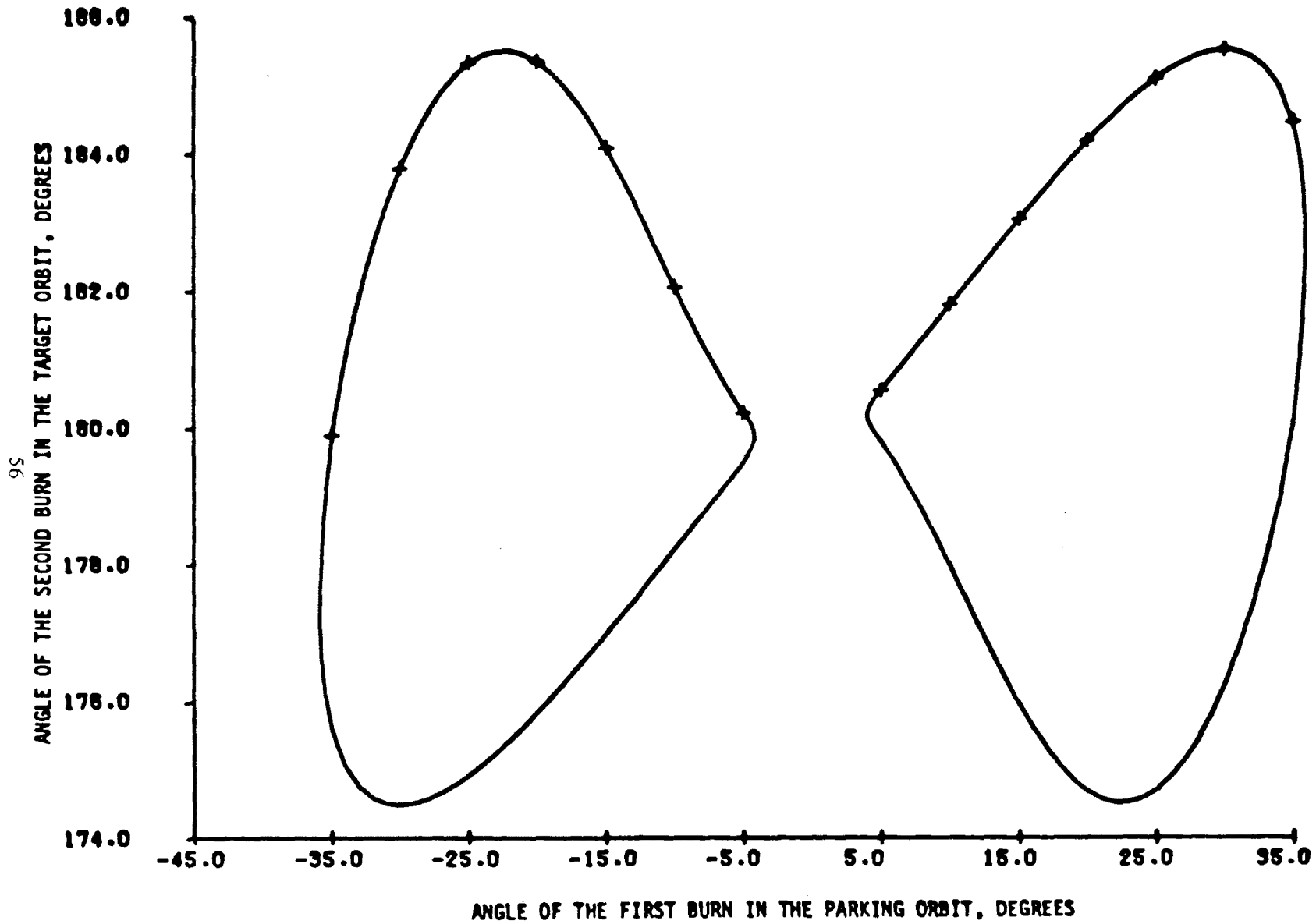
FIGURE 3a.   TRANSFER TO A 24 HOUR ORBIT.

i = 0, e = 0
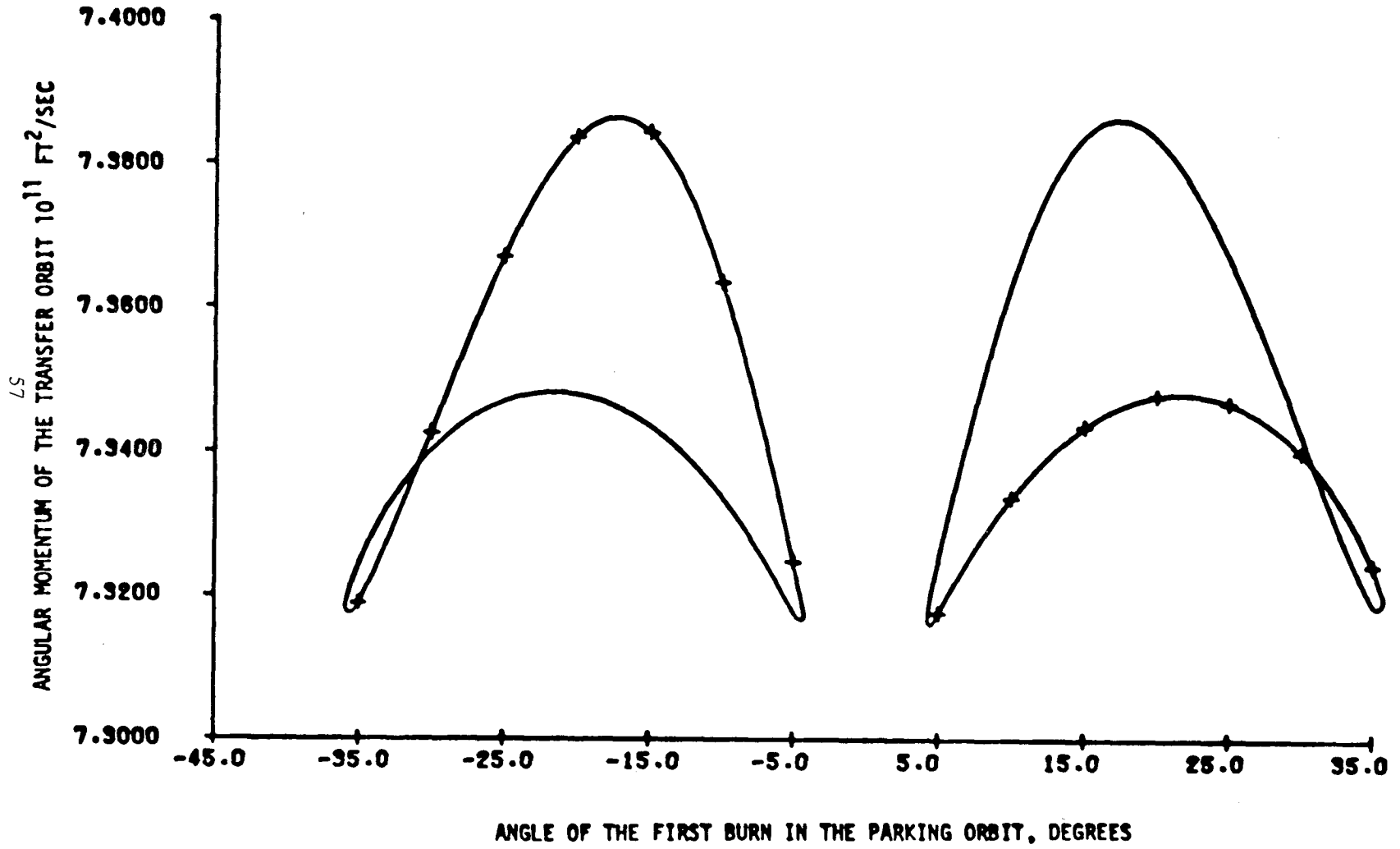
FIGURE 3b. ANGULAR MOMENTUM OF THE TRANSFER ORBIT

FIGURE 4a.   TRANSFER TO A 12 HOUR CIRCULAR ORBIT

i = 63°, e = 0

The y-axis is labeled "ANGLE OF THE SECOND BURN IN THE TARGET ORBIT, DEGREES" with values from 166.0 to 194.0.
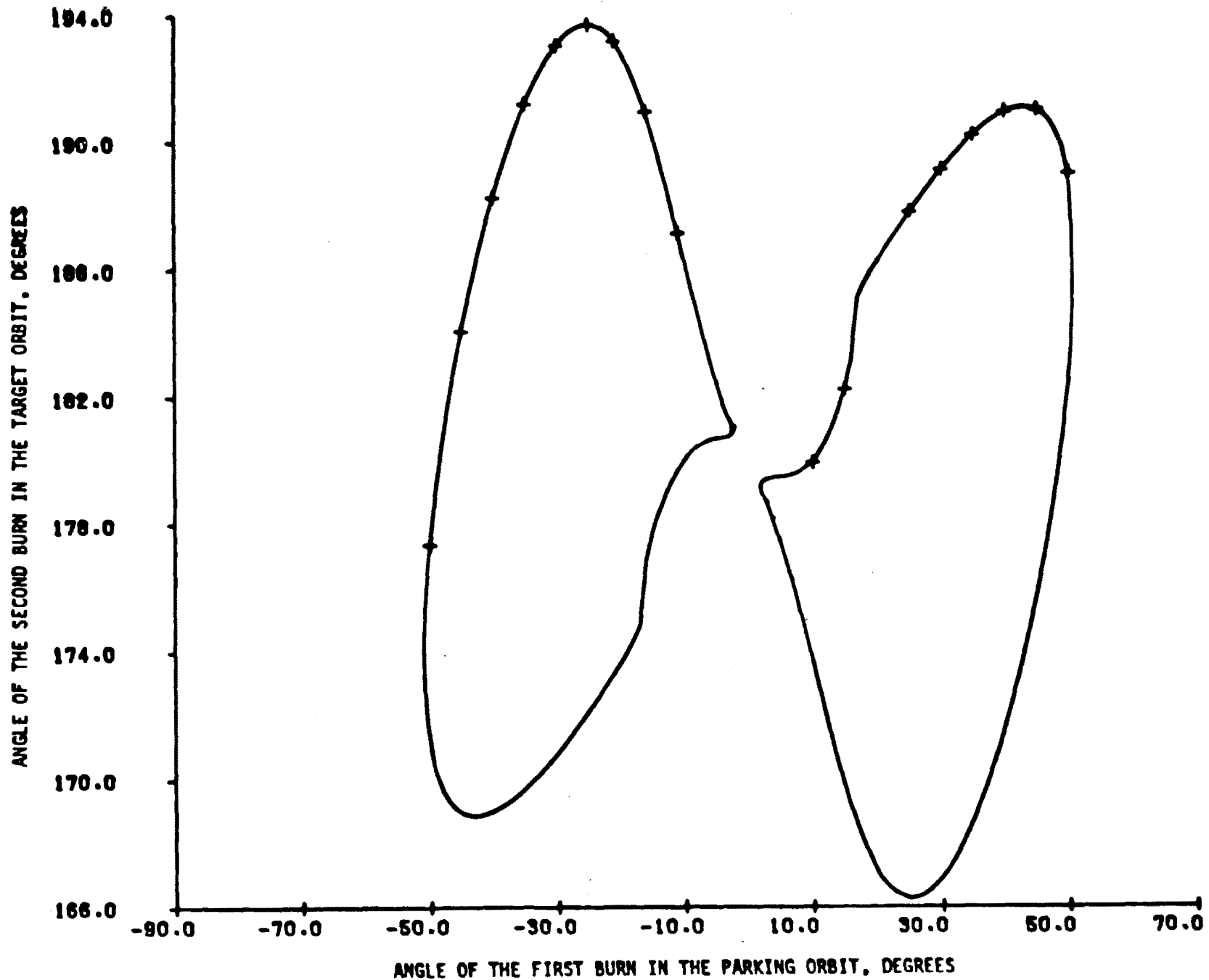
The x-axis is labeled "ANGLE OF THE FIRST BURN IN THE PARKING ORBIT, DEGREES" with values from -90.0 to 70.0.

58
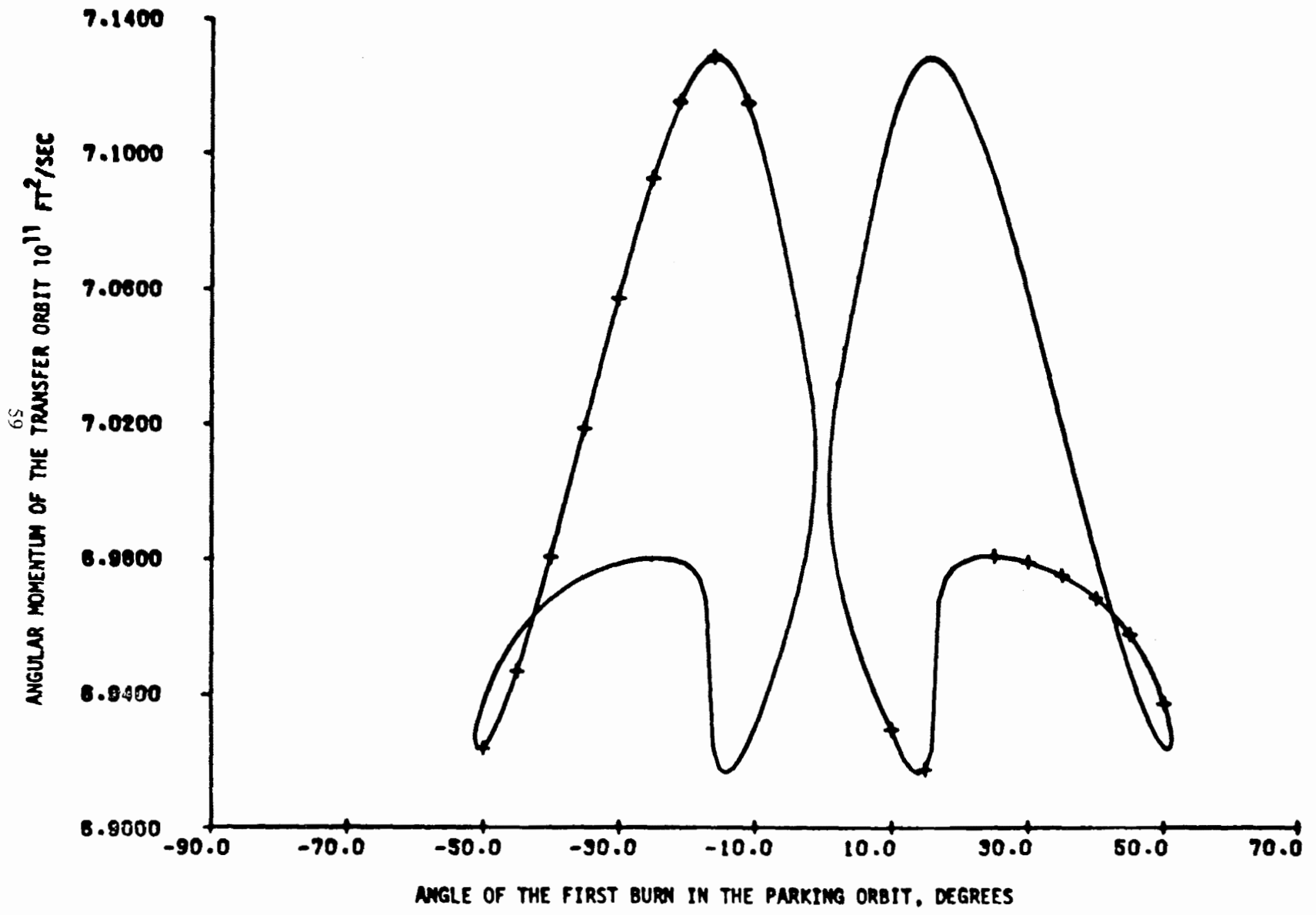
FIGURE 4b. ANGULAR MOMENTUM OF THE TRANSFER ORBIT
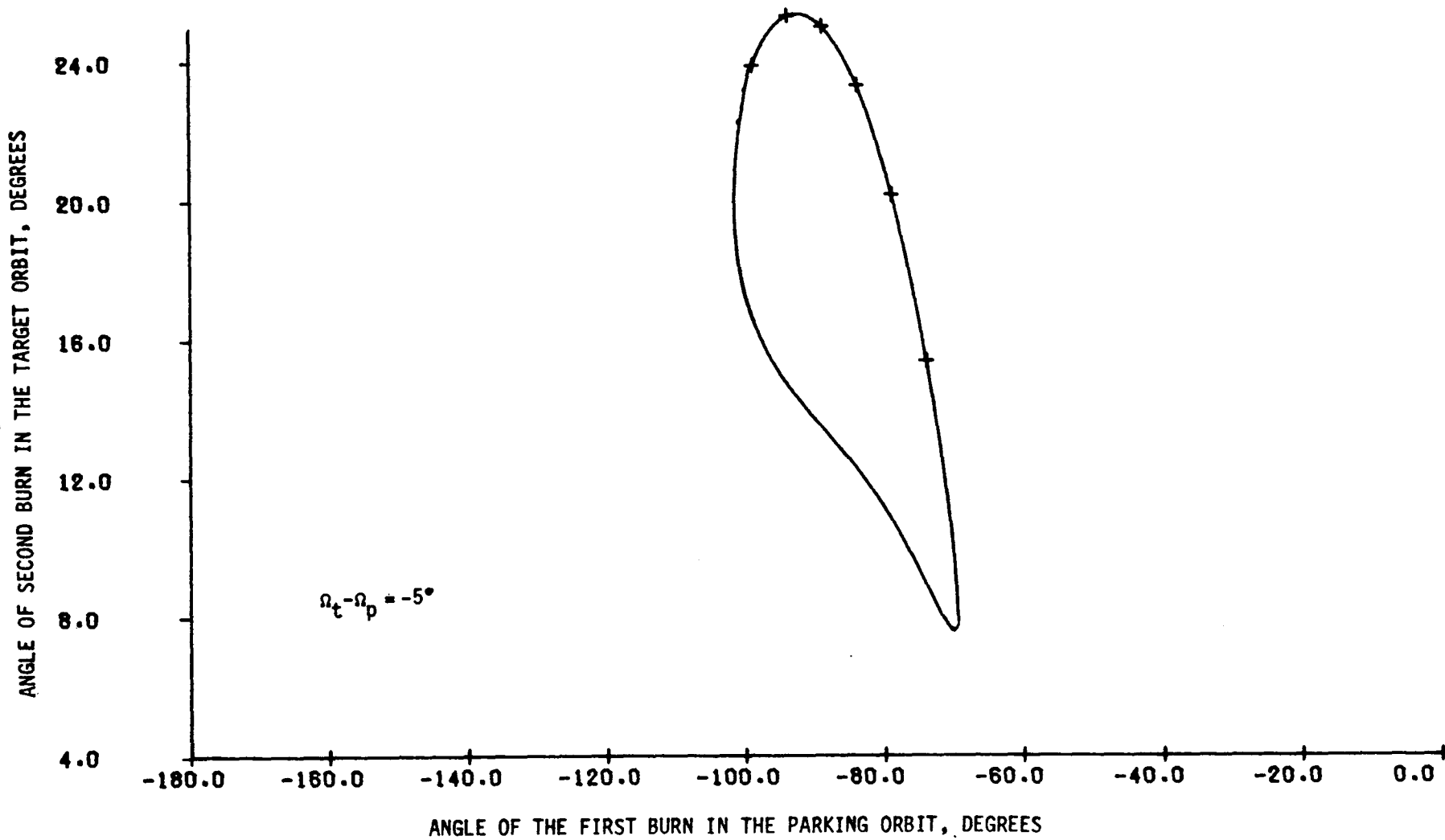
FIGURE 5a.   TYPE I TRANSFER TO A 12 HOUR ECCENTRIC ORBIT

$i = 63°$ $h_p = 150$ nmi $h_a = 21390$ mi
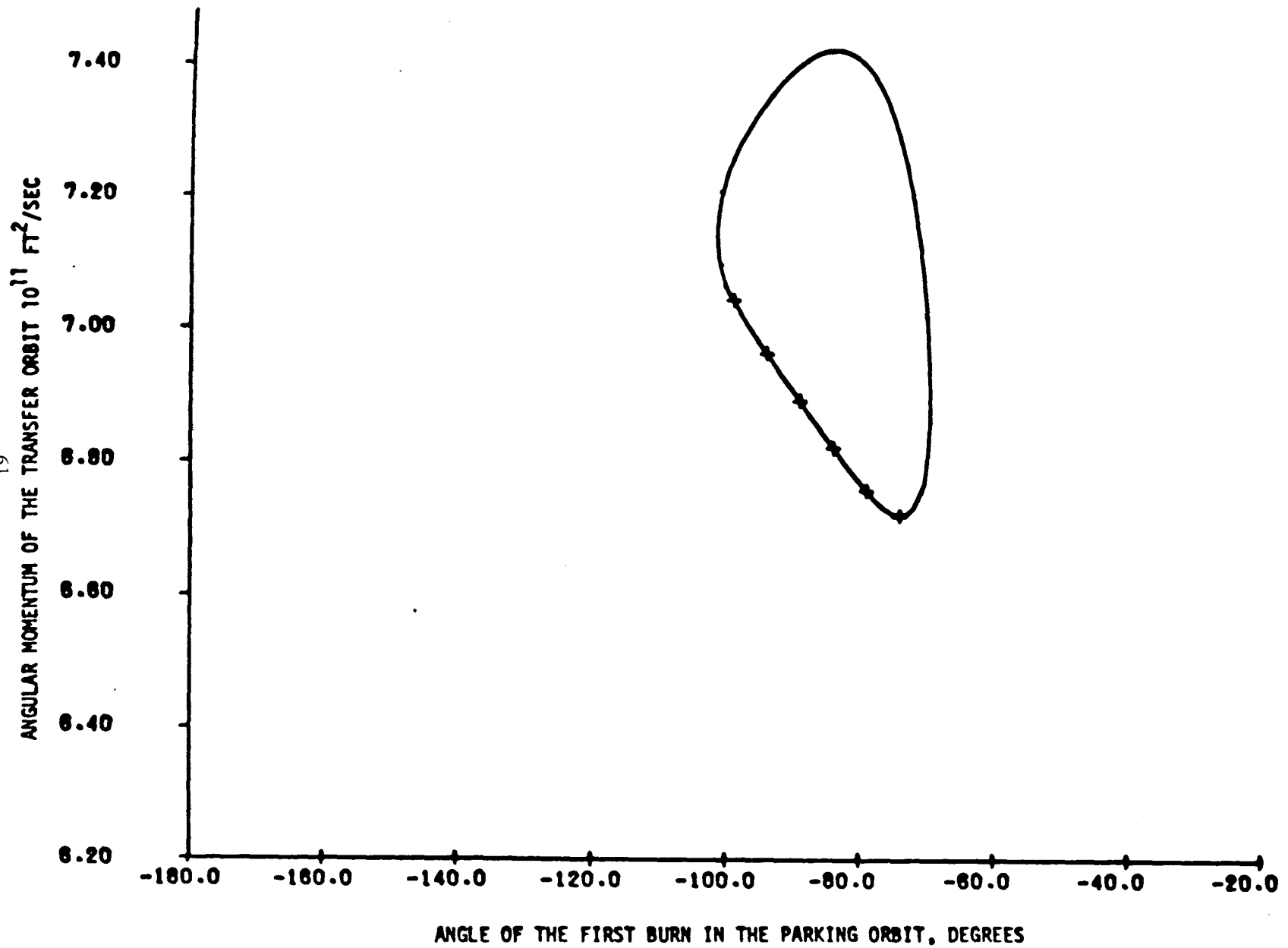
FIGURE 5b. ANGULAR MOMENTUM OF THE TRANSFER ORBIT
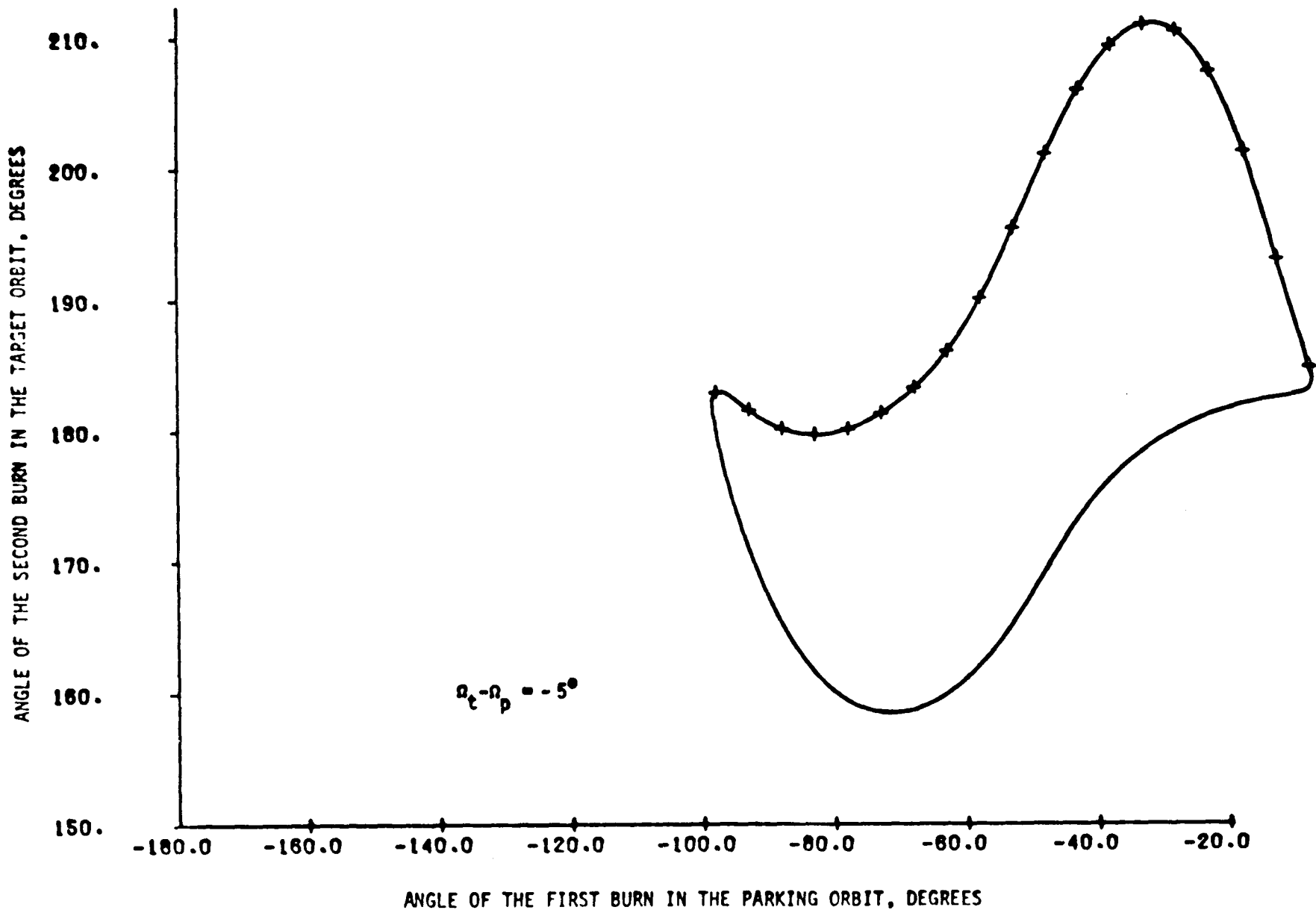
FIGURE 6a.   TYPE II TRANSFER TO A 12 HOUR ECCENTRIC ORBIT
$i = 63°$ $h_p = 150$ nmi $h_a = 21390$ nmi
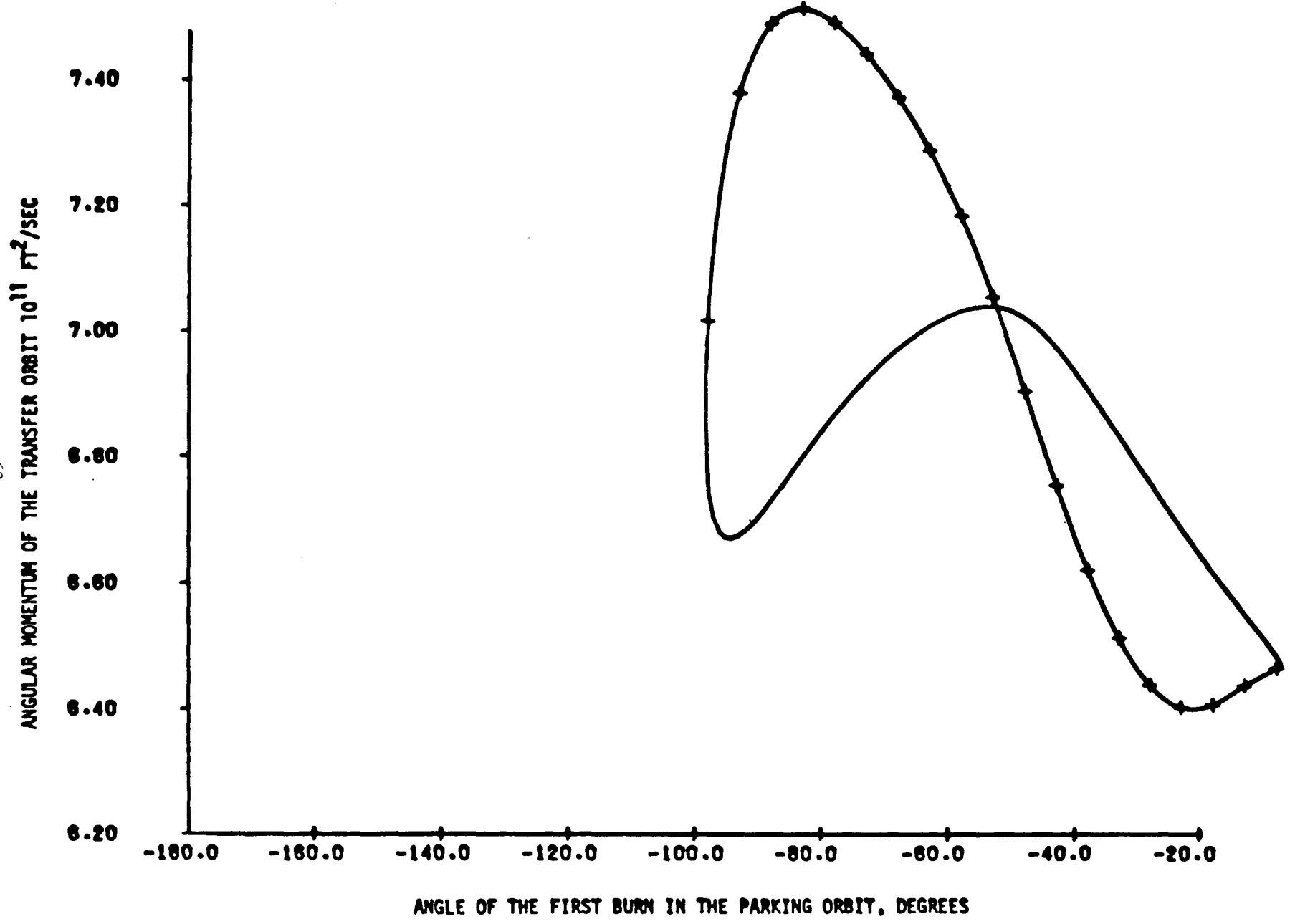
FIGURE 6b. ANGULAR MOMENTUM OF THE TRANSFER ORBIT

SESSION II

Dr. W. H. Wooden, Chairman

A SEMIANALYTICAL SATELLITE THEORY
FOR WEAK TIME–DEPENDENT PERTURBATIONS

P. Cefola,* W. McClain,[†] L. Early,[†] and A. Green**
Charles Stark Draper Laboratory

ABSTRACT

Previously, Semianalytical Satellite Theories based upon the Generalized Method of Averaging have been developed for

- perturbations with no explicit dependence on time, and

- perturbations with a strong explicit dependence on time

While the assumption of time independence (TI) is exact only for zonal harmonics and for static atmosphere density models, the assumption has also been applied successfully to develop the averaged equations of motion for lunar-solar perturbations of satellite orbits with periods up to two days (see AIAA preprints 78-1382 and 75-9). However, recent testing of the lunar-solar short periodics produced via the TI assumption for the GPS orbital flight regime (12 hr period) indicates that the relative accuracy of these short-periodics is significantly less than the accuracy of the zonal short-periodic variations.

This paper describes the modifications of the Semianalytical Satellite Theory required to include these 'weak' time – dependent perturbations. The new formulation results in additional terms in the short-periodic variations but does not change the averaged equations of motion. Thus the m-monthly terms are still included in the averaged equations of motion. This contrasts with the usual approach for the strongly time-dependent perturbations in which the m-monthly (or m-daily, if tesseral harmonics are being considered) terms would be eliminated from the averaged equations of motion and included in the short-periodics computation.

Numerical test results for the GPS case obtained with a numerical averaging implementation of the new theory demonstrate the accuracy improvement.

---

*Section Leader, Space Systems Analysis, Air Force Programs Department
†Staff Engineer
**CPT, ARMOR, U.S. Army

A SEMIANALYTICAL SATELLITE THEORY

FOR WEAK TIME-DEPENDENT PERTURBATIONS

Outline

- Review of Analytical Results for Time-Independent (TI) Case

- Numerical Results for Low Altitude Case w/TI Theory

- Numerical Results for High Altitude (GPS) Case w/TI Theory

- Analytical Development of Weak Time-Dependent (WTD) Theory

- Numerical Results for High Altitude Case w/WTD Theory
  (Zonals, Lunar-Solar, and Solar Pressure)

- Numerical Results for High Altitude Case w/WTD Theory
  (Zonals, Lunar-Solar, Solar Pressure, and 2x2 Tesserals)

68

SHORT PERIODICS

$a_i = \bar{a}_i + \epsilon n_{i,1}(\underline{\bar{a}},\bar{\lambda})$

$\int_0^{2\pi} \epsilon n_{i,1}(\underline{\bar{a}},\bar{\lambda})d\bar{\lambda} = 0$

$(i = 1,2,3,4,5,6)$

OSCULATING ELEMENT SPACE

$\dot{a}_i = \epsilon F_i(\underline{a},\lambda)$

$\dot{\lambda} = n + \epsilon F_6(\underline{a},\lambda)$

MEAN ELEMENT SPACE

$\dot{\bar{a}}_i = \epsilon A_{i,1}(\underline{\bar{a}})$

$\dot{\bar{\lambda}} = \bar{n} + \epsilon A_{6,1}(\underline{\bar{a}})$
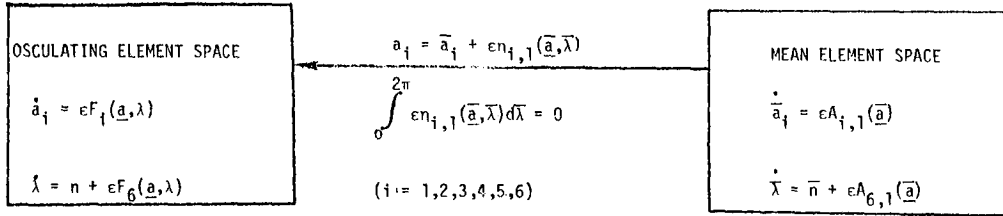
ASSUME

$$\dot{a}_i = X_{i0} + \epsilon \sum_{\sigma=1}^{\infty} [X_{i\sigma} \cos(\sigma\bar{\lambda}) + Z_{i\sigma} \sin(\sigma\bar{\lambda})]$$

BY USE OF THE GENERALIZED METHOD OF AVERAGING

$$X_{i0} = \bar{n}\delta_{i6} + \epsilon A_{i,1}(\underline{\bar{a}}) = \dot{\bar{a}}_i$$

$$A_{i,1}(\underline{\bar{a}}) = \frac{1}{2\pi} \int_0^{2\pi} \epsilon F_i(\underline{\bar{a}},\bar{\lambda})d\bar{\lambda}$$

$$\bar{n} \left[\frac{\partial n_{i,1}(\underline{\bar{a}},\bar{\lambda})}{\partial \bar{\lambda}} \right] = \sum_{\sigma=1}^{\infty} \left[X_{i\sigma} \cos(\sigma\bar{\lambda}) + Z_{i\sigma} \sin(\sigma\bar{\lambda}) \right]$$

DEFINE

$$C_{i\sigma} \equiv \frac{X_{i\sigma}}{\sigma\bar{n}} \qquad\qquad D_{i\sigma} = \frac{Z_{i\sigma}}{\sigma\bar{n}}$$

$$\epsilon n_{i,1}(\underline{\bar{a}},\bar{\lambda}) = \sum_{\sigma=1}^{\infty} \left[\epsilon C_{i\sigma} \sin(\sigma\bar{\lambda}) - \epsilon D_{i\sigma} \cos(\sigma\bar{\lambda}) \right]$$

$$\epsilon C_{i\sigma} = \frac{1}{\sigma\bar{n}\pi} \int_0^{2\pi} \epsilon F_i(\underline{\bar{a}},\bar{\lambda}) \cos(\sigma\bar{\lambda})d\bar{\lambda} + \left(\frac{3\epsilon D_{1\sigma}}{2\sigma\bar{a}_1} \right) \delta_{i6}$$

$$\epsilon D_{i\sigma} = \frac{1}{\sigma\bar{n}\pi} \int_0^{2\pi} \epsilon F_i(\underline{\bar{a}},\bar{\lambda}) \sin(\sigma\bar{\lambda})d\bar{\lambda} - \left(\frac{3\epsilon C_{1\sigma}}{2\sigma\bar{a}_1} \right) \delta_{i6}$$

$$i = 1,2,3,4,5,6$$

-- SHORT PERIODIC COEFFICIENTS ARE FUNCTIONS OF THE FIVE SLOWLY VARYING MEAN ELEMENTS AND THEREFORE SHOULD ALSO BE SLOWLY VARYING.

-- COUPLING OF THE FAST VARIABLE SHORT PERIODIC VARIATION WITH THE SEMIMAJOR AXIS SHORT PERIODIC VARIATION.

-- FOR CONSERVATIVE FORCES, ANALYTICAL EXPRESSIONS ARE POSSIBLE FOR $\epsilon C_{i\sigma}$ AND $\epsilon D_{i\sigma}$.

LOW ALTITUDE TEST CASE

● EPOCH CONDITIONS: 1974, Oct. 21, 10 hrs, 24 min.

OSCULATING ELEMENTS | MEAN ELEMENTS (PCE)

$a = 6644.586$ $\overline{a} = 6636.3797$

$e = .01$ $\overline{e} = .0106045$

$i = 67.98538419°$ $\overline{i} = 67.97090021°$

$\Omega = 91.99738418°$ $\overline{\Omega} = 91.9949106°$

$\omega = 200.6741688°$ $\overline{\omega} = 200.21097331°$

$M = 164.3173126°$ $\overline{M} = 164.77124281°$

● S/C

$C_D = 2.0$

Area $= 1.86m^2$

Mass $= 677.kg$

● ATMOSPHERE

Modified Harris-Priester

$w/\overline{F}_{10.7} = 150$

● FORCE MODELS

COWELL (30 second step)

$J_2,...,J_6$

and drag

SEMIANALYTICAL (1 day step)

First Order: $J_2,...,J_6$ and Drag

Second Order: $J_2^2 + J_2$-Drag Coupling
in the AOG
(IZSAK + Analytical Drag - J_2)

70

HIGH ALTITUDE TEST CASE

1. ASSUME A SET OF EPOCH MEAN ELEMENTS; THESE ARE 'CONSTANTS' FOR THE
   SEMI-ANALYTICAL THEORY

2. AT EPOCH, USE THE SHORT-PERIODIC GENERATOR TO PRODUCE OSCULATING
   ELEMENTS

3. CONVERT THE OSCULATING ELEMENTS TO POSITION AND VELOCITY; THESE
   ARE THE CONSTANTS FOR THE COWELL THEORY

4. PROPAGATE THE ORBIT USING BOTH THE SEMI-ANALYTICAL THEORY AND COWELL
   AND COMPARE THE RESULTING POSITION AND VELOCITY HISTORIES

TEST CASE #2 FORCE MODELS

COWELL	SEMI-ANALYTICAL
$J_2,\ldots,J_6$	$J_2,\ldots,J_6$ PLUS J_2^2
LUNAR-SOLAR	LUNAR-SOLAR (TI)
SOLAR RADIATION PRESSURE	SOLAR RADIATION PRESSURE (TI)

SEMI-ANALYTICAL THEORY

FOR WEAKLY TIME-DEPENDENT

PERTURBATIONS

- OSCULATING EQUATIONS

$$\frac{da_i}{dt} = \epsilon F_i(\vec{a}, \lambda, t)$$

$$\frac{d\lambda}{dt} = n + \epsilon F_6(\vec{a}, \lambda, t)$$

- ASSUMED FORMS

$$\frac{d\bar{a}_i}{dt} = \epsilon A_i(\vec{\bar{a}}, t) \qquad\qquad a_i = \vec{\bar{a}}_i + \epsilon n_i(\vec{\bar{a}}, \bar{\lambda}, t)$$

$$\frac{d\bar{\lambda}}{dt} = n(\bar{a}_1) + \epsilon A_6(\vec{\bar{a}}, t) \qquad\qquad \lambda = \bar{\lambda} + \epsilon n_6(\vec{\bar{a}}, \bar{\lambda}, t)$$

- MATCHING EXPRESSIONS FOR da_i/dt AND $d\lambda/dt$ GIVES

$$A_i + \bar{n} \frac{\partial n_i}{\partial \bar{\lambda}} + \frac{\partial n_i}{\partial t} = F_i(\vec{\bar{a}}, \bar{\lambda}, t), \qquad i = 1, \dots, 5$$

$$A_6 + \bar{n} \frac{\partial n_6}{\partial \bar{\lambda}} + \frac{\partial n_6}{\partial t} = F_6(\vec{\bar{a}}, \bar{\lambda}, t) - \frac{3\bar{n}}{2\bar{a}} n_1(\vec{\bar{a}}, \bar{\lambda}, t)$$

- ASSUME:

$$\frac{1}{2\pi} \int_0^{2\pi} \frac{\partial n_i}{\partial t} d\bar{\lambda} = 0, \qquad i = 1, \dots, 6$$

PHYSICALLY, THIS TAKES THE M-MONTHLIES OUT OF THE SHORT PERIODICS

- THEN

$$A_i = \frac{1}{2\pi} \int_0^{2\pi} F_i(\vec{\bar{a}}, \bar{\lambda}, t) d\bar{\lambda}, \qquad i = 1, \dots, 5$$

72

- DEFINE

$$F_i{}^S(\vec{a},\bar{\lambda},t) \equiv F_i(\vec{a},\bar{\lambda},t) - A_i$$

- ASSUME

$$F_i{}^S(\vec{a},\bar{\lambda},t) \equiv \sum_{\sigma=1}^{\infty} [X_{i\sigma}(\vec{a},t) \cos \sigma\bar{\lambda} + Z_{i\sigma}(\vec{a},t) \sin \sigma\bar{\lambda}]$$

$$n_i(\vec{a},\bar{\lambda},t) \equiv \sum_{\sigma=1}^{\infty} \frac{1}{\sigma\bar{n}} [M_{i\sigma}(\vec{a},t) \sin \sigma\bar{\lambda} - N_{i\sigma}(\vec{a},t) \cos \sigma\bar{\lambda}]$$

- SUBSTITUTING INTO THE MATCHING EXPRESSIONS GIVES PDE's

$$X_{i\sigma} = M_{i\sigma} - \frac{1}{\sigma\bar{n}} \frac{\partial N_{i\sigma}}{\partial t}$$

$$Z_{i\sigma} = N_{i\sigma} + \frac{1}{\sigma\bar{n}} + \frac{\partial M_{i\sigma}}{\partial t}$$

- ASSUME SOLUTION TO PDE

$$M_{i\sigma} \equiv X_{i\sigma} + \Delta^{(1)}$$

$$N_{i\sigma} \equiv Z_{i\sigma} + \Delta^{(2)}$$

- FIRST ORDER RESULT

$$n_i = \sum_{\sigma=1}^{N} \frac{1}{\sigma\bar{n}} \left\{ \left[C_{i,\sigma} + \frac{\partial D_{i,\sigma}}{\partial t} - \left(\frac{3\,\delta_{i,6}}{2\,\bar{a}_1\,\sigma} \right) \frac{\partial C_{1,\sigma}}{\partial t} \right] \sin \sigma\bar{\lambda} \right.$$

$$\left. - \left[D_{i,\sigma} - \frac{\partial C_{i,\sigma}}{\partial t} - \left(\frac{3\,\delta_{1,6}}{2\,\bar{a}_1\,\sigma} \right) \frac{\partial D_{1,\sigma}}{\partial t} \right] \cos \sigma\bar{\lambda} \right\}$$

- NOTE: $C_{i,\sigma}$ AND $D_{i,\sigma}$ ARE THE COEFFICIENTS COMPUTED WITH THE TI ASSUMPTION

TEST CASE #2

- FORCE MODEL

COWELL	SEMI-ANALYTICAL
$J_2,\ldots,J_6$	$J_2,\ldots,J_6$ PLUS J_2^2
LUNAR-SOLAR	LUNAR-SOLAR (WTD)
SOLAR RADIATION PRESSURE	SOLAR RADIATION PRESSURE (WTD)

- MEAN ELEMENTS

a = 26559.5 km Ω = 0.0°

e = .001 ω = 0.0°

i = 63.0° M = 0.0°

- OSCULATING ELEMENTS

a = 26561.56567 km Ω = 359.9999657°

e = .00104842 ω = 359.8560915°

i = 63.001124° M = .1436848842°

TEST CASE #2 RESULTS

TIME (DAYS)	Δx(m)	Δy(m)	Δz(m)	RSS(m)
2	-.01	.8	1.317	1.54
4	-.22	1.574	2.704	3.14
6	-.63	2.278	4.395	4.99
8	-1.31	2.866	6.274	7.02
10	-2.14	3.601	7.801	8.85
12	-3.70	4.702	9.342	11.09
14	-5.58	5.322	10.510	13.04

TEST CASE #3

● FORCE MODEL

COWELL	SEMI-ANALYTICAL
$J_2, \ldots, J_6$	$J_2, \ldots, J_6$ PLUS $J_2{}^2$
LUNAR-SOLAR	LUNAR-SOLAR (WTD)
SOLAR RADIATION PRESSURE	SOLAR RADIATION PRESSURE (WTD)
$(C,S)_{2,1} + (C,S)_{2,2}$	$(C,S)_{2,1} + (C,S)_{2,2}$

● MEAN ELEMENTS

$a = 26559.5$ km $\Omega = 0.0°$

$e = .001$ $\omega = 0.0°$

$i = 63.0°$ $M = 0.0°$

● OSCULATING ELEMENTS

$a = 26561.54781$ km $\Omega = 359.9999706°$

$e = .00104802$ $\omega = 359.8538535°$

$i = 63.001118°$ $M = .1459308175°$

75

Figure 1. Radial Difference after 23 hours from Epoch/Semianalytical
minus Cowell for the Low Altitude Circular Test Case

```
       ***** POSITION DIFFERENCE
       I.----------.----------.----------.----------.----------.----------.----------.----------.----------.----------.I
 1.000 .                                                                                                              .
       I                                                                                                              I
       I                                                                                                              I
       I                                                                                                              I
       I                                                                                                              I
 0.800 .                              **                                                                              .
       I                               *                                                                              I
       I                                                                                                              I
       I                               *                                                                              I
       I                              *  *                                                                            I
 0.600 .                             *                                                                                .
R      I                                                                                                              I
A      I                           *                                                                                  I
D      I                               *                                                                              I
I      I                                                                                                              I
A 0.400 .               **                                                                                            .
L      I               * *                                                                                            I
       I              *                                                                                               I
D      I             *  *        *    *                                                                               I
I      I           ***                                   **                                                          I
F 0.200 .         ***          *                          *                     *                                    .
F      I          **       *                             *                    * **                                   I
E      I       *                                        *                    *                                       I
R      I   ***        *        *                       *                    **                                       I
E      I *                 *                  ****                          **                                       I
N 0.0  . *            *                  *              *                  *                                          .
C      I                               *                                  *                                          I
E      I*                                                                  *                                         I
S      I              *  *                              *                                                            I
       I                                 *     *       *                                                             I
I-0.200 .*                                    *  *   *                                                               .
N      I              *                                 *     *                                                      I
       I                *  *                     ** *       *                                                        I
M      I                                          *                                                                 I
E-0.400 .               * *                   *             *                                                        .
T      I                *                                  *                                                        I
E      I                                    * *           *                                                         I
R      I                                      *          *                                                         I
S      I                                      *         **                                                         I
-0.600 .                                            *                                                               .
       I                                             *                                                              I
       I                                           **                                                              I
       I                                                                                                           I
-0.800 .                                                                                                            .
       I                                                                                                           I
       I                                                                                                           I
       I                                                                                                           I
-1.000 .                                                                                                            .
       I.----------.----------.----------.----------.----------.----------.----------.----------.----------.----------.I
       0.0     15.00     30.00     45.00     60.00     75.00     90.00    105.00    120.00    135.00    150.00
```

TIME FROM YYMMDD HHMMSS IN MIN
                741022   92100
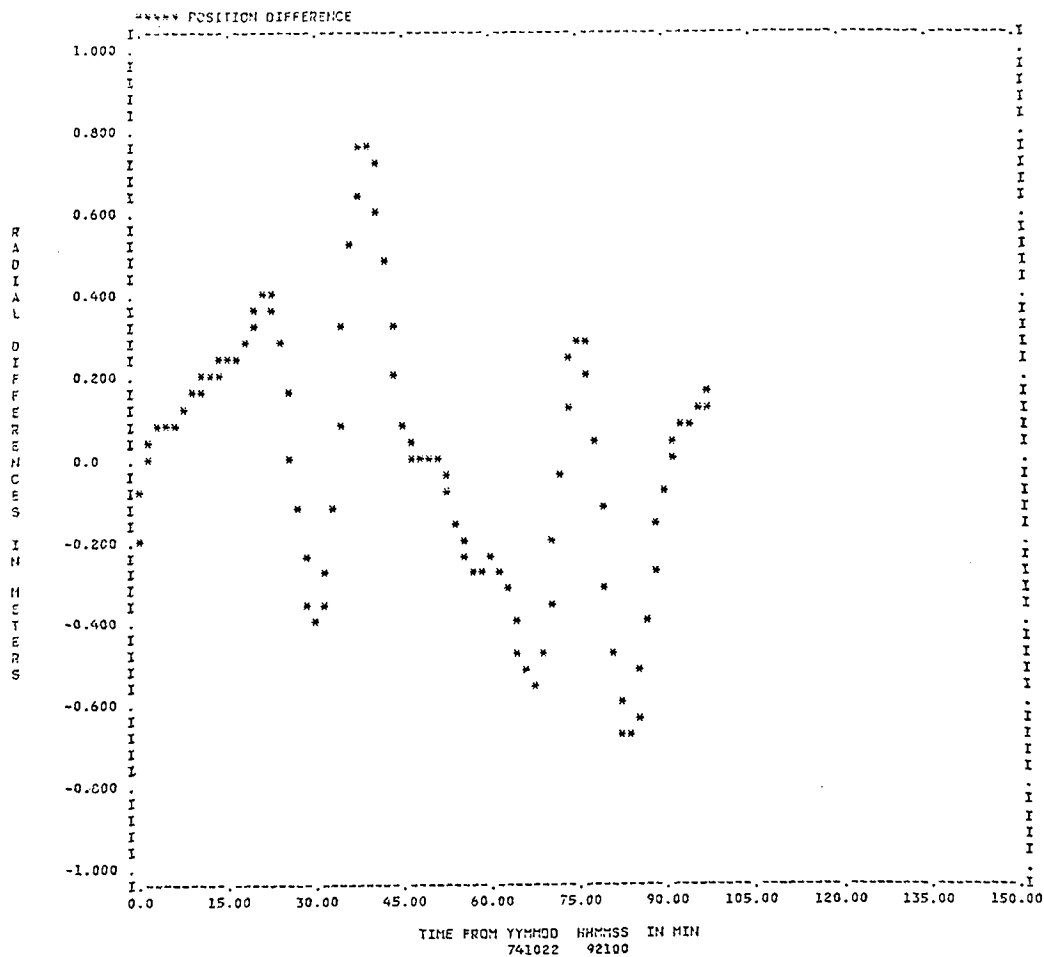
Perturbations
    Cowell: 6x0 gravitational field any drag: 30 sec numerical integration
             time step

    AOG: 1st order analytical expressions for the 6x0 gravitational field,
             Zeis' expressions for J_2^2 effects and option 7 for drag (48 pt
             quadrature order 1 day numerical integration time step

    SPG: 6x0 gravitational field$_2$(7/48) and drag (7/48) to first order,
             Zeis' expressions for J_2^2 effects.

    Initial Conditions: PCE

76

Figure 2. Cross Track Difference after 23 hours from Epoch /Semianalytical minus Cowell for the Low Altitude Circular Test Case
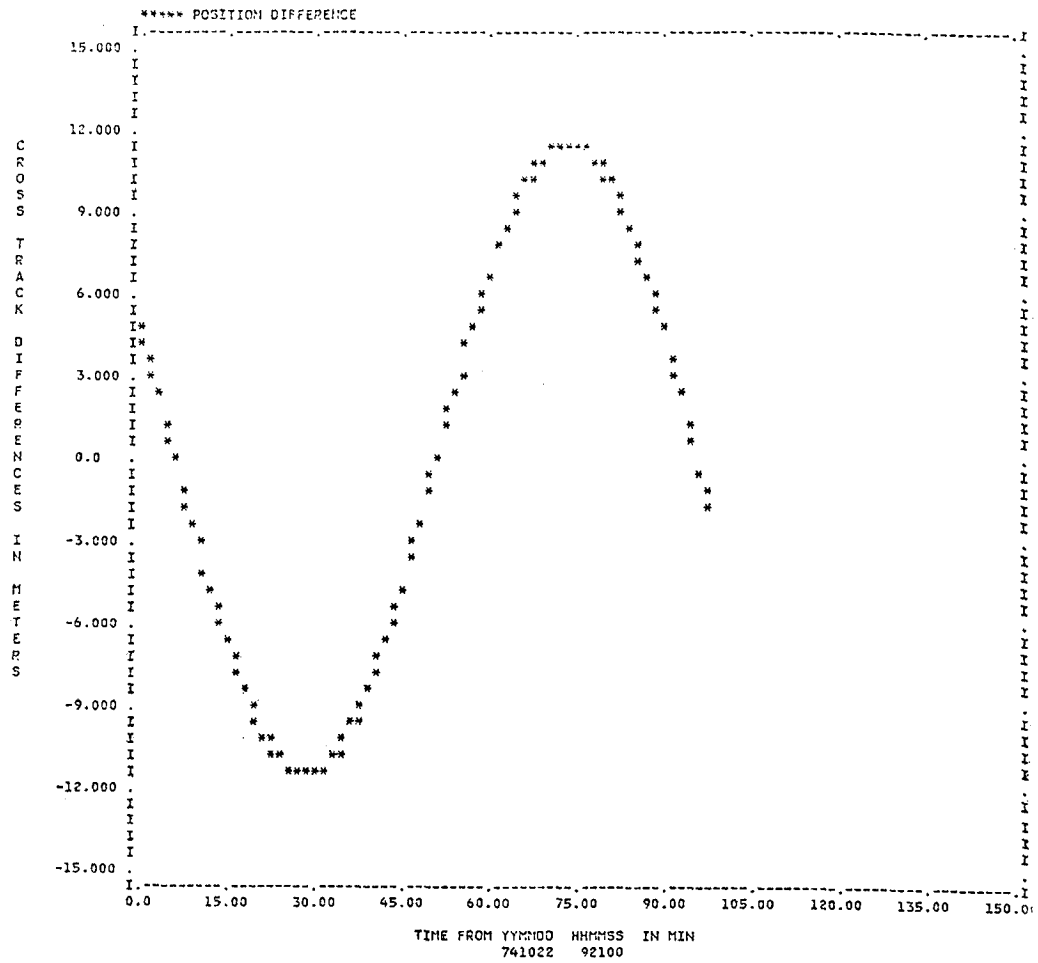
Same initial conditions and perturbations as in Figure 1.

Figure 3. Along Track Difference after 23 hours from Epoch/Seminalytical minus Cowell for the Low Altitude Circular Test Case
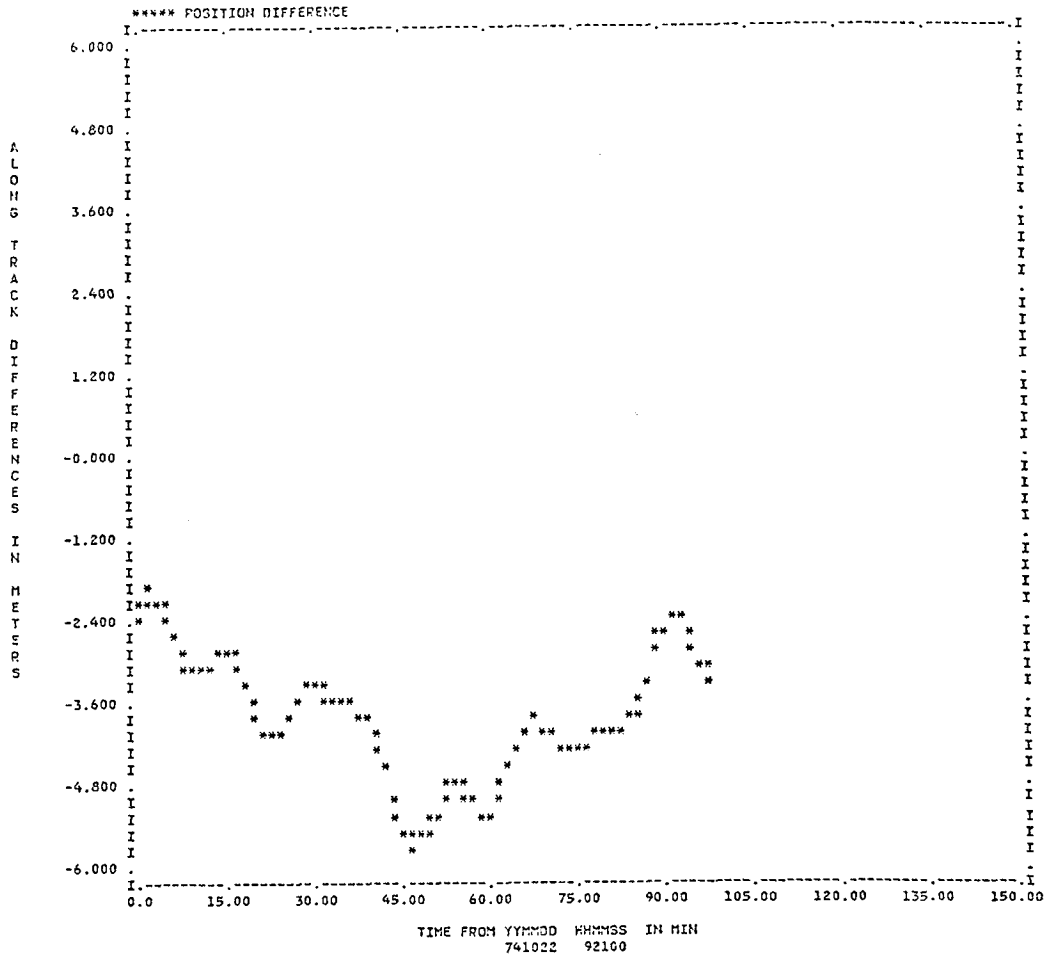
Same perturbations and initial conditions as in Figure 1.

Figure 4   Time History of the Zonal Semimajor Axis Short Periodic Coefficients* for the Low Altitude
            Circular Test Case

            * The $2\bar{\lambda}$ coefficients, $C_{1,2}$ and $D_{1,2}$

            Same initial conditions and perturbations as in drag option 6 of AAS-79-133
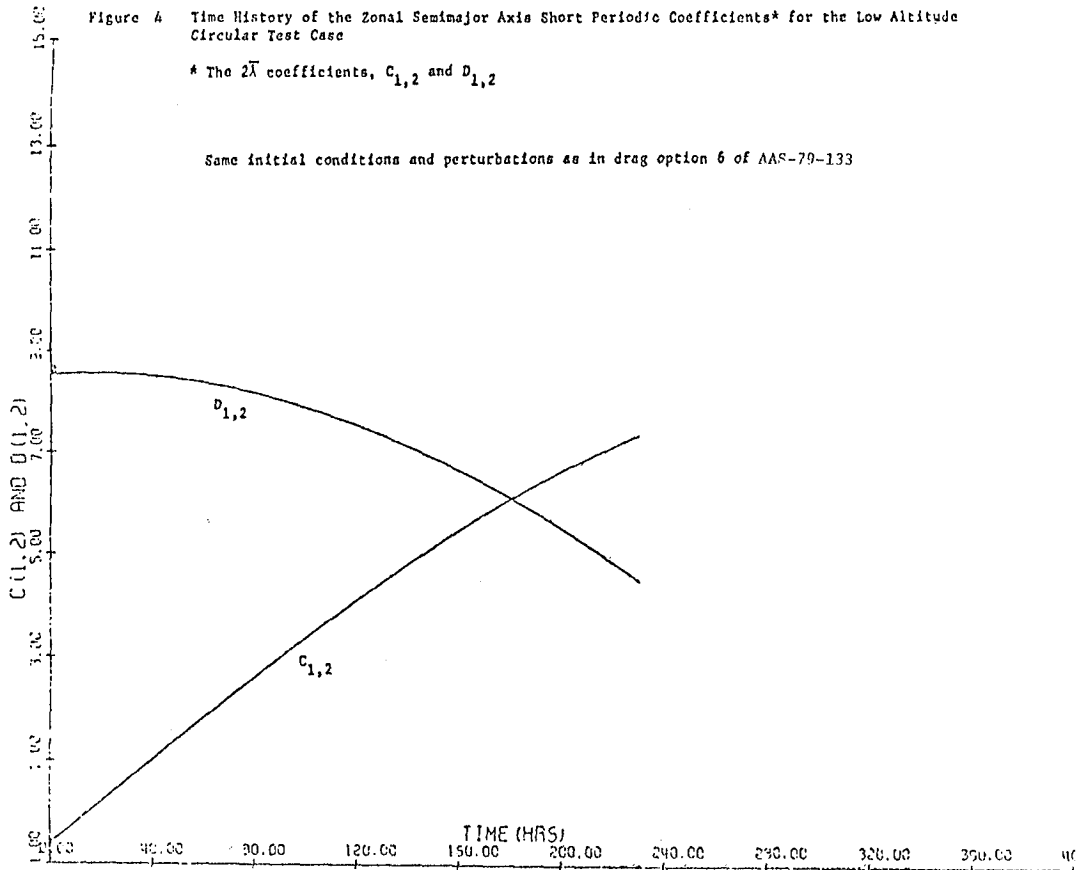
Figure 5   Time History of the Drag Semimajor Axis Short Periodic Coefficients* for the Low Altitude
            Circular Test Case

* The $1\overline{\lambda}$ coefficients, $C_{1,1}$ and $D_{1,1}$

Same initial conditions and perturbations
as in drag option 6 of AAS-79-133

$D_{1,1}$

$C_{1,1}$

TIME (HRS)

C (1,1) AND C(1,1) (X10^{-1})
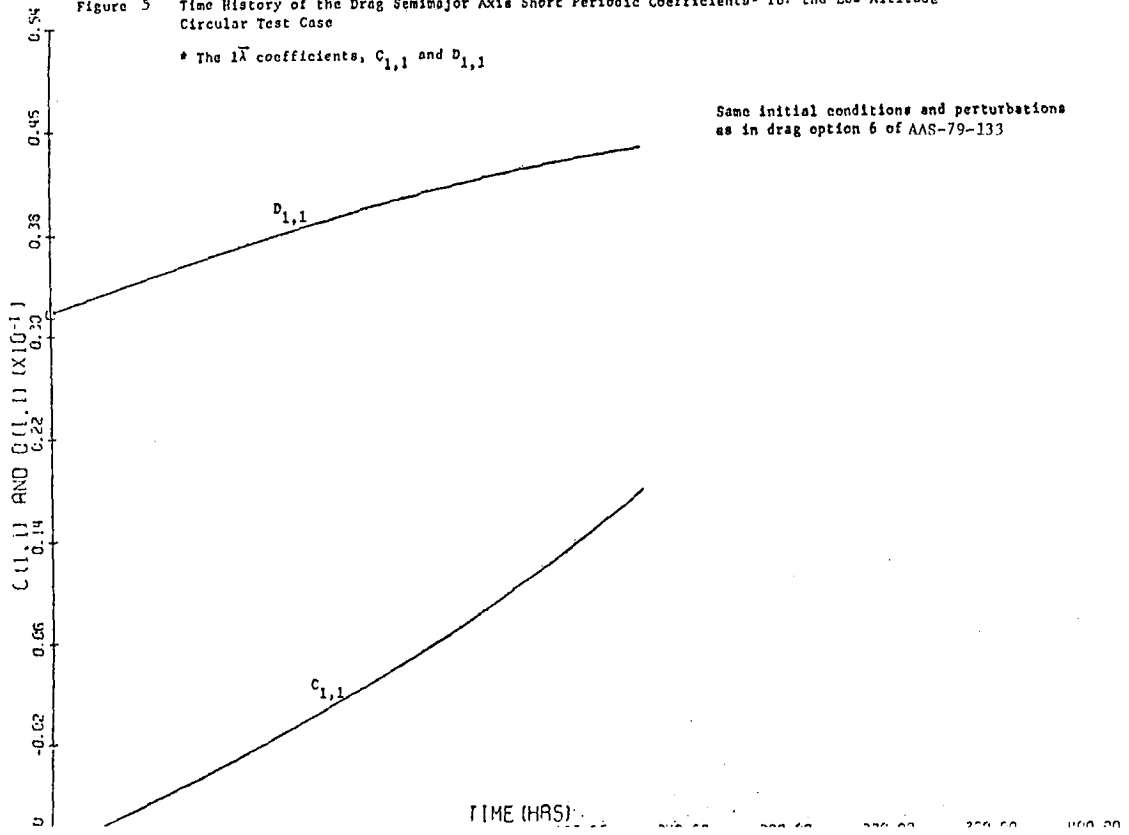
Figure 6. Radial Difference (TI Theory)
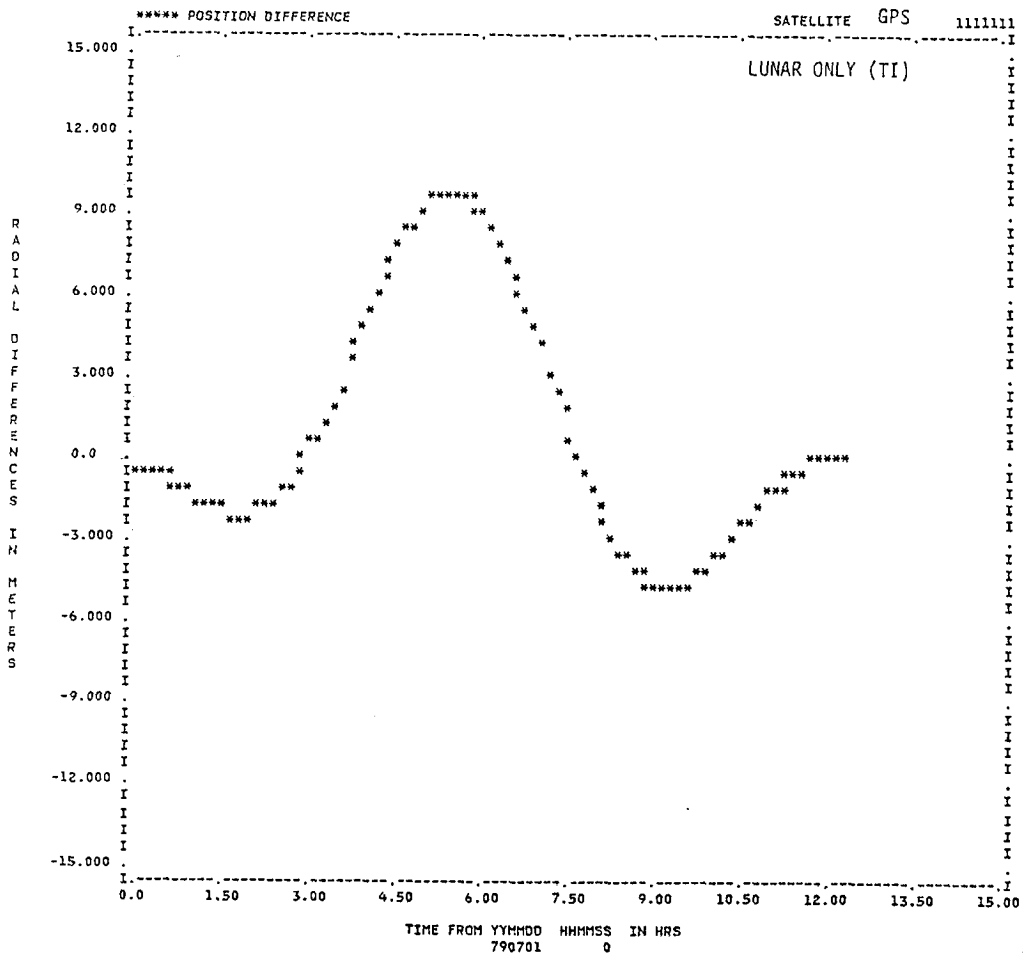
Figure 7. Cross Track Difference (TI Theory)
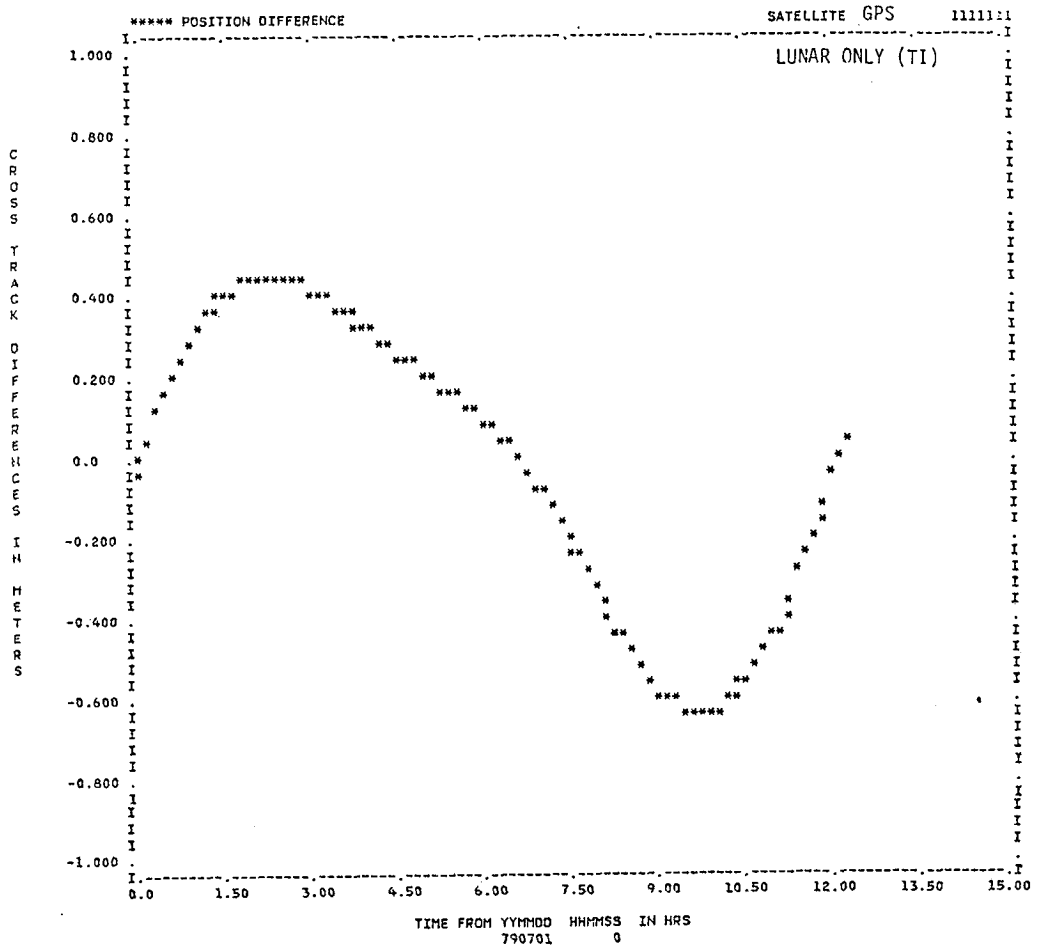
Figure 8. Along Track Difference (TI Theory)
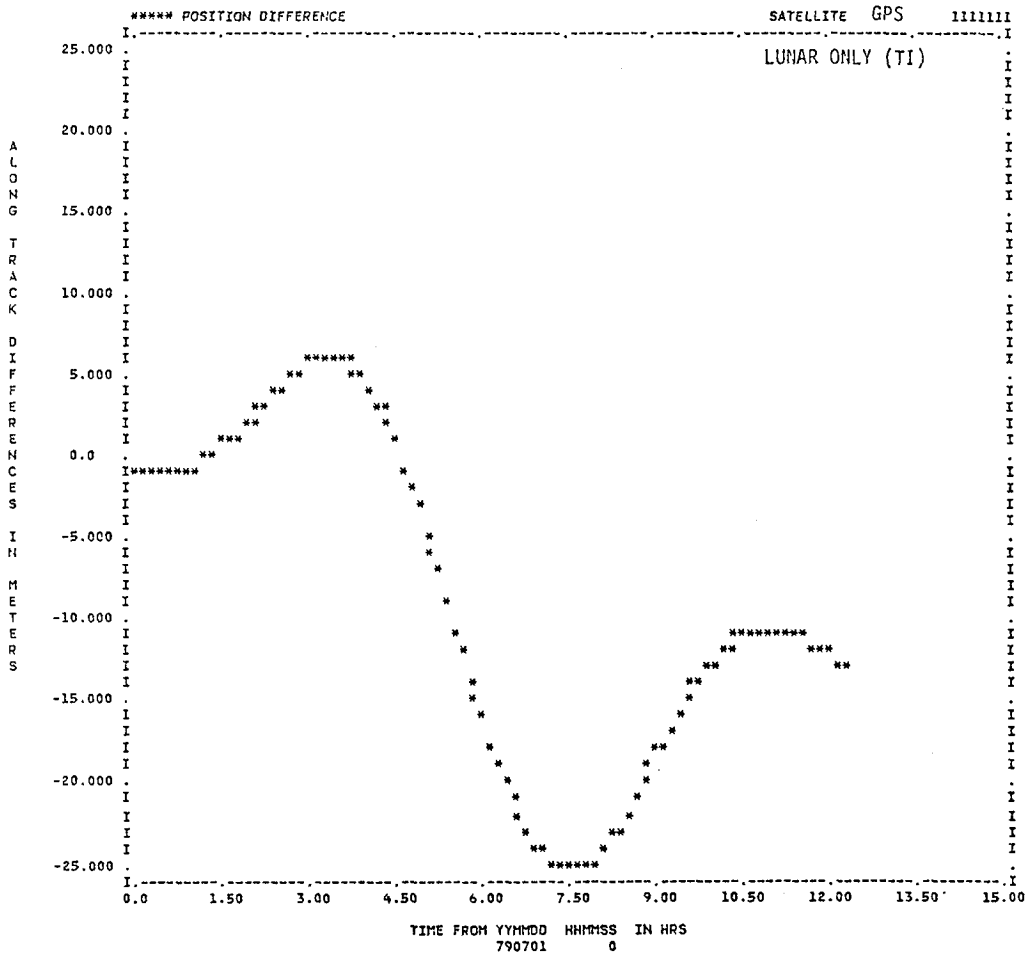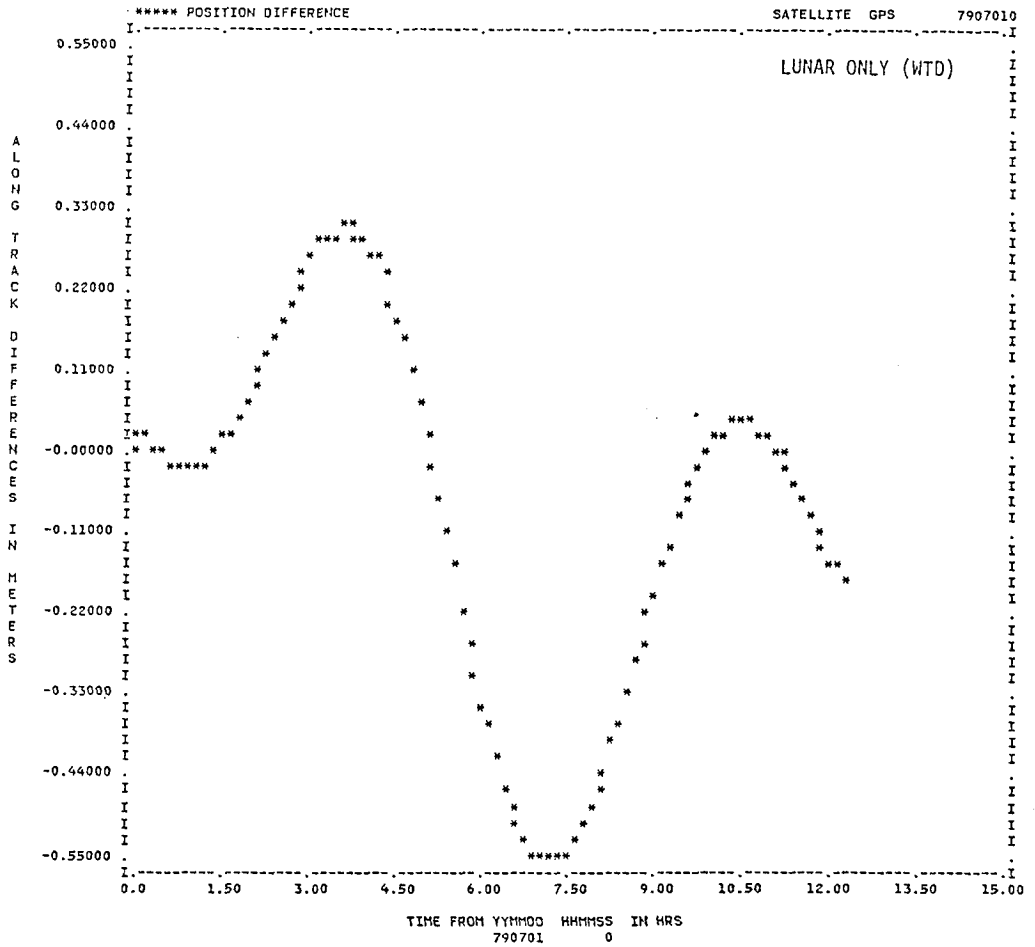
Figure 9. Along Track Difference (WTD Theory)

Figure 9. Along Track Difference (WTD Theory)

Figure 10. Along Track Difference (WTD Theory)
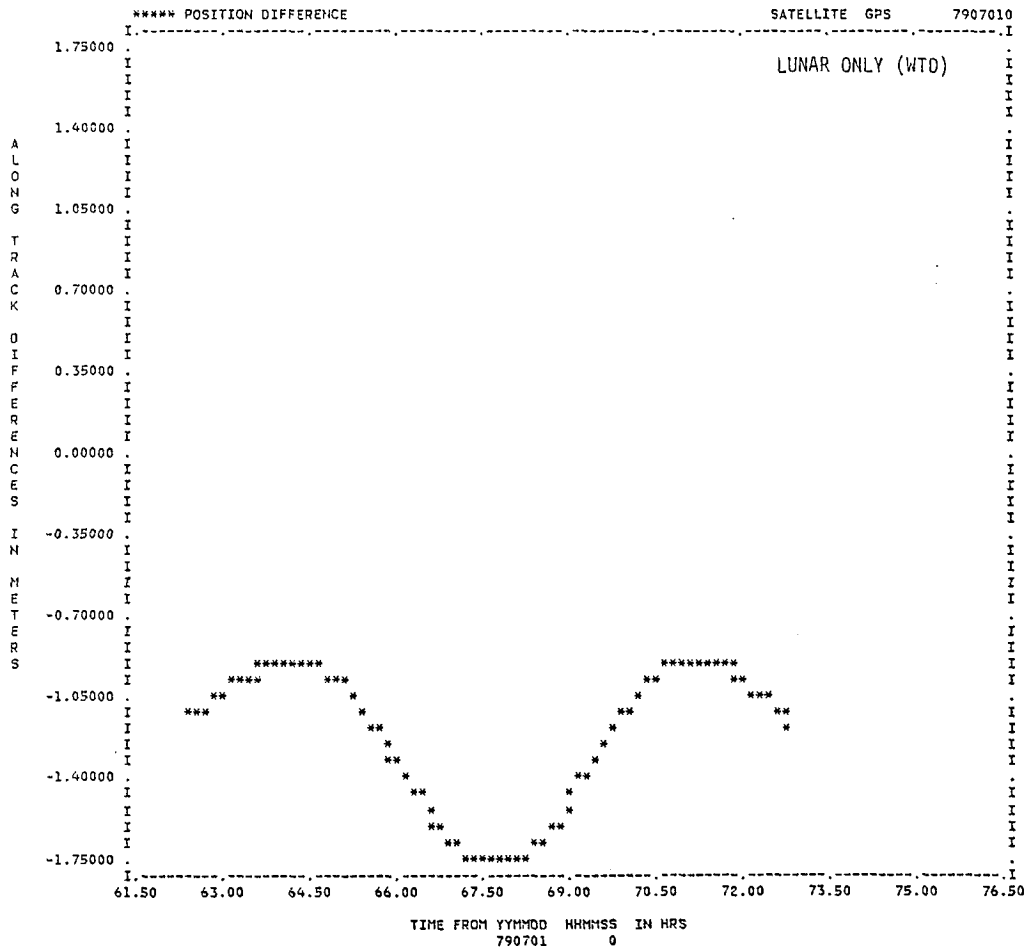
Figure 11. Radial Difference/Semianalytical minus Cowell for the GPS Test Case
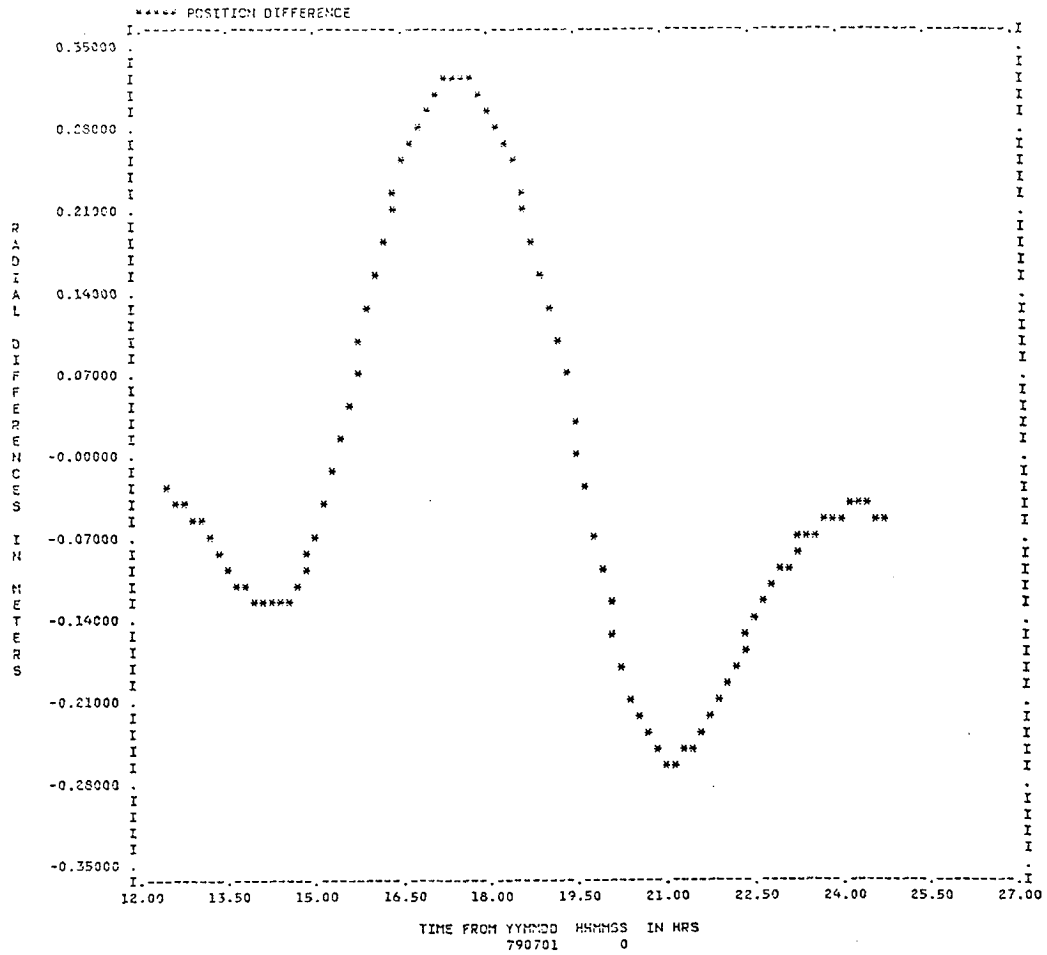
Perturbations

Cowell: 6x0 field, lunar-solar, solar radiation pressure: 300 sec
         integration time step

AOG: 1st order analytical expressions for 6x0 field and lunar-solar pt
         mass effects, Zeis's J_2^2 expressions, numerical solar radiation
         pressure effects (48 pt quadrature order): 1 day integration time
         step

SPG: 1st order weak time-dependent model for 6x0 field (7/48), Zeis's J_2^2
         expressions

Initial Conditions: $[EPC]^{-1}$

86

Figure 12. Cross Track Difference/Semianalytical minus Cowell for the GPS Test Case
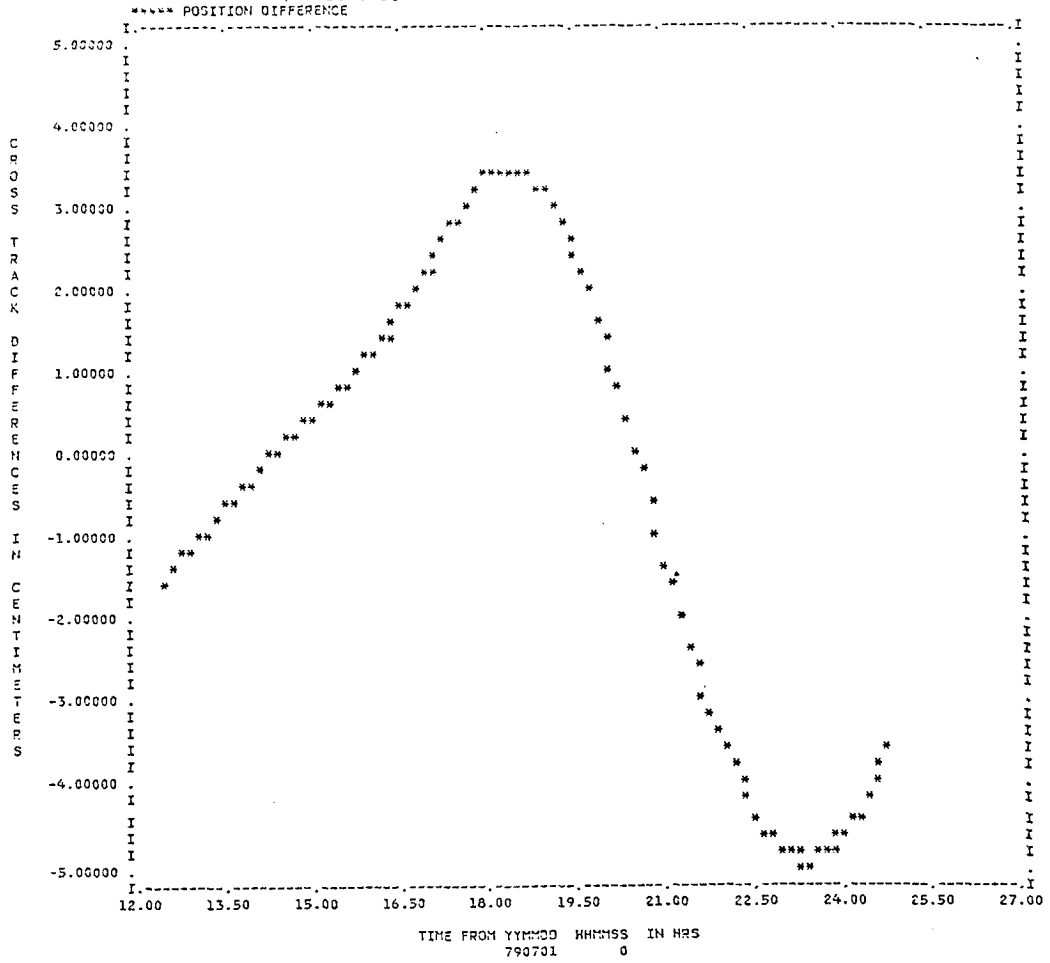
Same initial conditions and perturbations as in Figure 11.

Figure 13. Along Track Difference/Seminalytical minus Cowell for the GPS Test Case

Same initial conditions and perturbations as in Figure 11.

88

Figure 14. Radial Difference/Semianalytical·minus Cowell for
            GPS (Test Case #3)
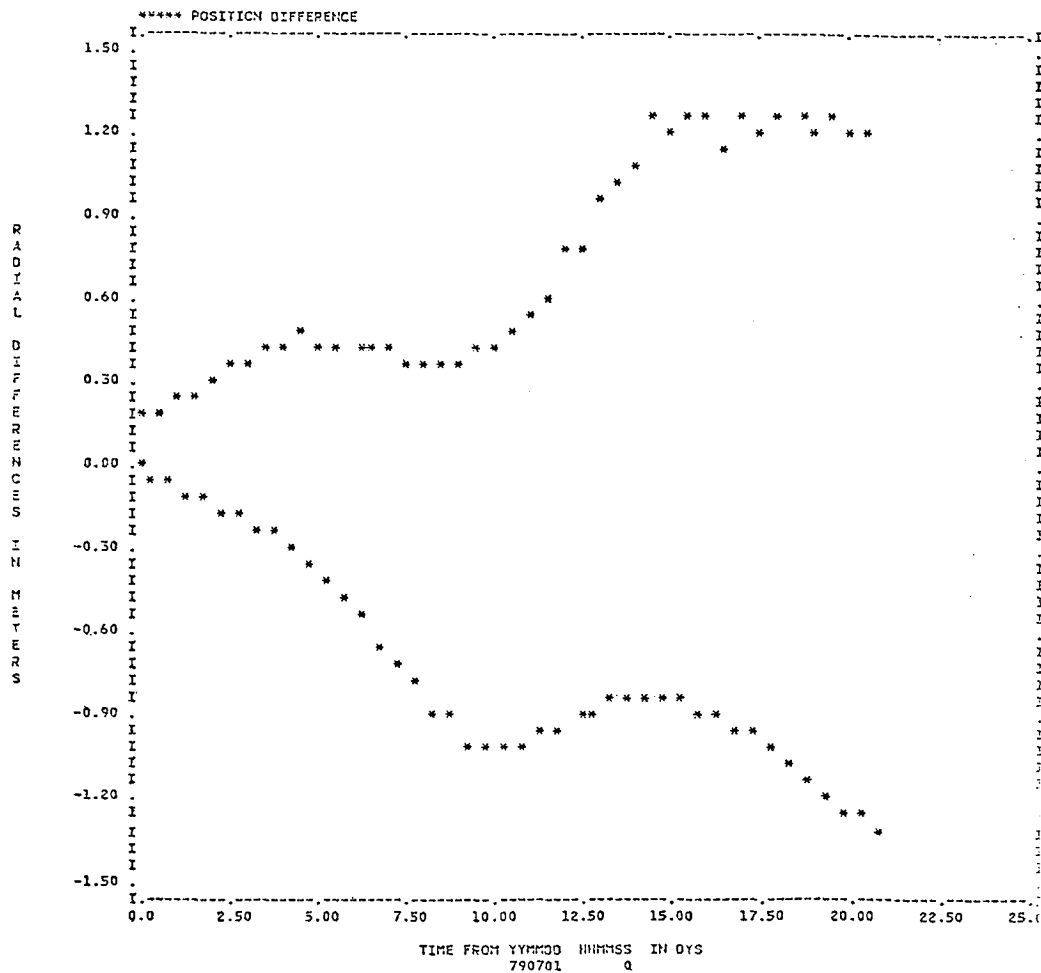
Figure 15. Cross Track Difference/Semianalytical minus Cowell for GPS (Test Case #3)
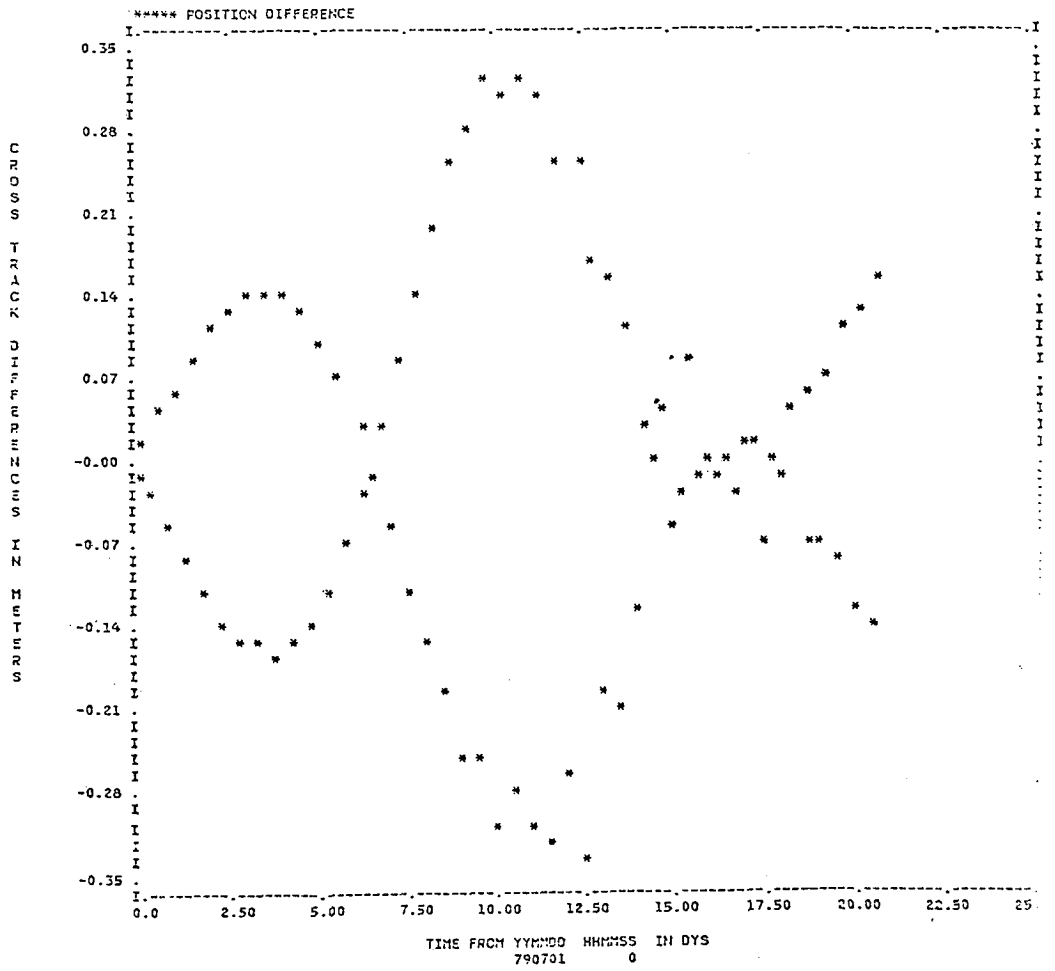
Figure 16. Along Track Difference/Semianalytical!minus Cowell for GPS (Test Case #3)
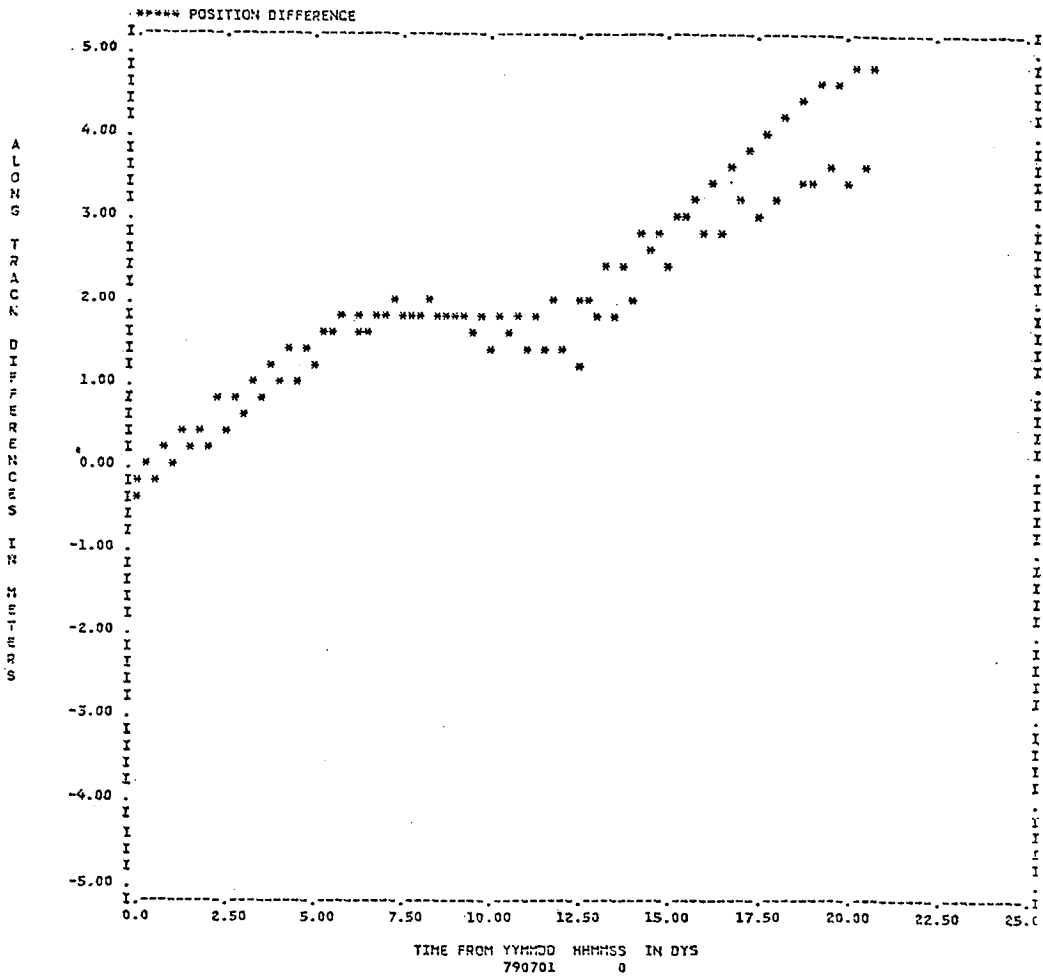
PHASE I NAVSTAR/GPS EPHEMERIS
AND SPACE VEHICLE CLOCK PERFORMANCE SUMMARY

Albert B. Bierman
The Aerospace Corporation

ABSTRACT

The Navstar/Global Positioning System (GPS) has been under evaluation for more than one year. This paper, one of several Major Field Test Objective reports, addresses the issue of Control Segment accuracy in predicting Space Vehicle (SV) clock and ephemeris states for broadcast to the user community. Both the highly precise ephemeris and clock prediction data blocks and the less precise (but longer period of utility) almanac data block are evaluated.

1. INTRODUCTION

The Navstar/Global Positioning System (GPS) is a satellite-based navigation system that provides extremely accurate three-dimensional position, velocity and time information to properly equipped users anywhere on or near the earth. It is a Joint Service Program, managed by the Air Force with deputies from the Navy, Army, Marines, Defense Mapping Agency, Coast Guard and NATO with technical support provided by The Aerospace Corporation.

Phase I - Concept Validation - has been undergoing test and evaluation in preparation for the second stage of the Defense Systems Acquisition Review Council (DSARC-2) in Spring 1979. An extensive flight test program has been conducted at the Yuma Proving Ground in Arizona and, to a lesser extent, off the coast of Southern California and at other sites in the continental United States.

While the ultimate objective is to demonstrate precision navigation for a wide range of military missions, it is equally important to verify the performance of all aspects of the GPS system. To accomplish these goals a series of papers has been prepared to support major field test objectives for DSARC-2.

1.1   OBJECTIVES

This paper addresses the accuracy of the ephemeris and space vehicle (SV) clock predictions which are vital to the user navigation function. The Phase I system specification (Ref.1) allocates 3.66 meters (1 sigma) for the ephemeris error

contribution to the User Equivalent Range Error during the twenty-four hour period after the satellite upload message has been prepared. Phase I satellites have rubidium frequency references as atomic standards. The GPS error budget allocates 2.74 meters (1 sigma) for the SV clock error during the two hour period after the satellite upload message has been generated. The Phase I clock error is predicated on a rubidium atomic standard with fractional frequency stability of 1 part in 10^{12} over a two hour period. Operational satellite clocks will be cesium beam tube or hydrogen maser standards. These clocks offer frequency stability of 1 part in 10^{13} or better over 24 hours. Thus the Phase III Operational GPS can be expected to provide better than 3 meters (1 sigma) accuracy over the twenty-four hour period after the navigation message has been prepared.

1.2   SCOPE

This assessment will evaluate (1) the ephemeris and SV clock error contributions to user ranging error (URE) during the two-hour periods following navigation data uploads; (2) the error contributions throughout the twenty-four hour period following navigation data uploads; and (3) SV almanac data accuracy for 2 weeks or more after upload. It is important to note that while item (2) addresses twenty-four hour accuracy, there is no prescribed Phase I clock error budget beyond two hours.

The adequacy of item (3) will be judged against the almanac URE (1 sigma) values (Ref. 2) presented in Table I.

Table I. Almanac Accuracy

Time	User Equivalent Range Error estimated by analysis (meters)
1 day	1000
1 week	2500
2 weeks	5000
3 weeks	10000
4 weeks	15000
5 weeks	20000

2. SYSTEM DESCRIPTION

GPS is comprised of three system components (1) the
Space Segment, (2) the User Segment, and (3) the Control
Segment.

2.1   SPACE SEGMENT

The Space Segment provides the spaceborne navigation
payload. Phase I uses four space vehicles in 10,900 nmi
(20,200 km) altitude circular orbits inclined 63 degrees with
respect to the equator. The satellites are distributed in two
inertial planes which provide an hour or more of usable four
Space Vehicle (SV) geometry for daily user testing at the Yuma
Proving Ground (YPG). Table 2 presents a summary of the
constellation configuration. The orbit periods are controlled
to cause the ground traces to repeat each day. Fig. 1
illustrates the repeating satellite geometries. Because of the
sidereal effect of the earth's motion about the sun, and orbit
torques by the oblate earth and by sun-moon effects, each day's
events occur approximately 4 minutes and 3.4 sec earlier than
the previous day's events. Satellite geometry at the YPG is
described by the azimuth-elevation time history in Figure 2.
The satellite positions at 1 January 1979/1700 GMT are shown on
Figs. 1 and 2. At that time, the opportunity for four
satellite navigation at YPG was nearing termination due to the
fade of Navstar 4.

The major elements comprising the navigation payload
are the pseudo random noise sub assembly (PRNSA), atomic
frequency standard, processor, and L-band antenna. The PRNSA
includes the baseband generator, which produces the P (precise)
and C/A (coarse/acquisition) ranging codes and encodes naviga-
tion data from the processor onto the pseudo random noise (PRN)

Table II. Navstar Phase I Orbits at First Ascending Node on 1 Jan. 1979

SATELLITE IDENTIFIER	NODAL PERIOD, min	INCLINATION, deg	LONGITUDE OF FIRST ASCENDING NODE, deg	RIGHT ASCENSION OF ASCENDING NODE[1], deg	TIME OF FIRST ASCENDING NODE, GMT	ECCENTRICITY	ARGUMENT OF PERIGEE, deg	DATE OF LAUNCH
NS-1	717.982	63.12	46.12	218.06	0448:18	0.0034	345.5	21 FEB 1978
NS-2	717.983	63.41	331.61	100.25	0155:30	0.0051	93.4	12 MAY 1978
NS-3	717.985	63.03	352.81	98.15	0022:18	0.0015	350.4	7 OCT 1978
NS-4[2]	717.988	63.13	95.71	217.67	0033:48	0.0008	77.4	10 DEC 1978

(1) Referenced to astronomical coordinates of 1950.0
(2) Data for 15 January 1979

LONGITUDE

————————	NS – 1	
—— —— ——	NS – 2	
— — — — —	NS – 3	
—— — —— —	NS – 4	
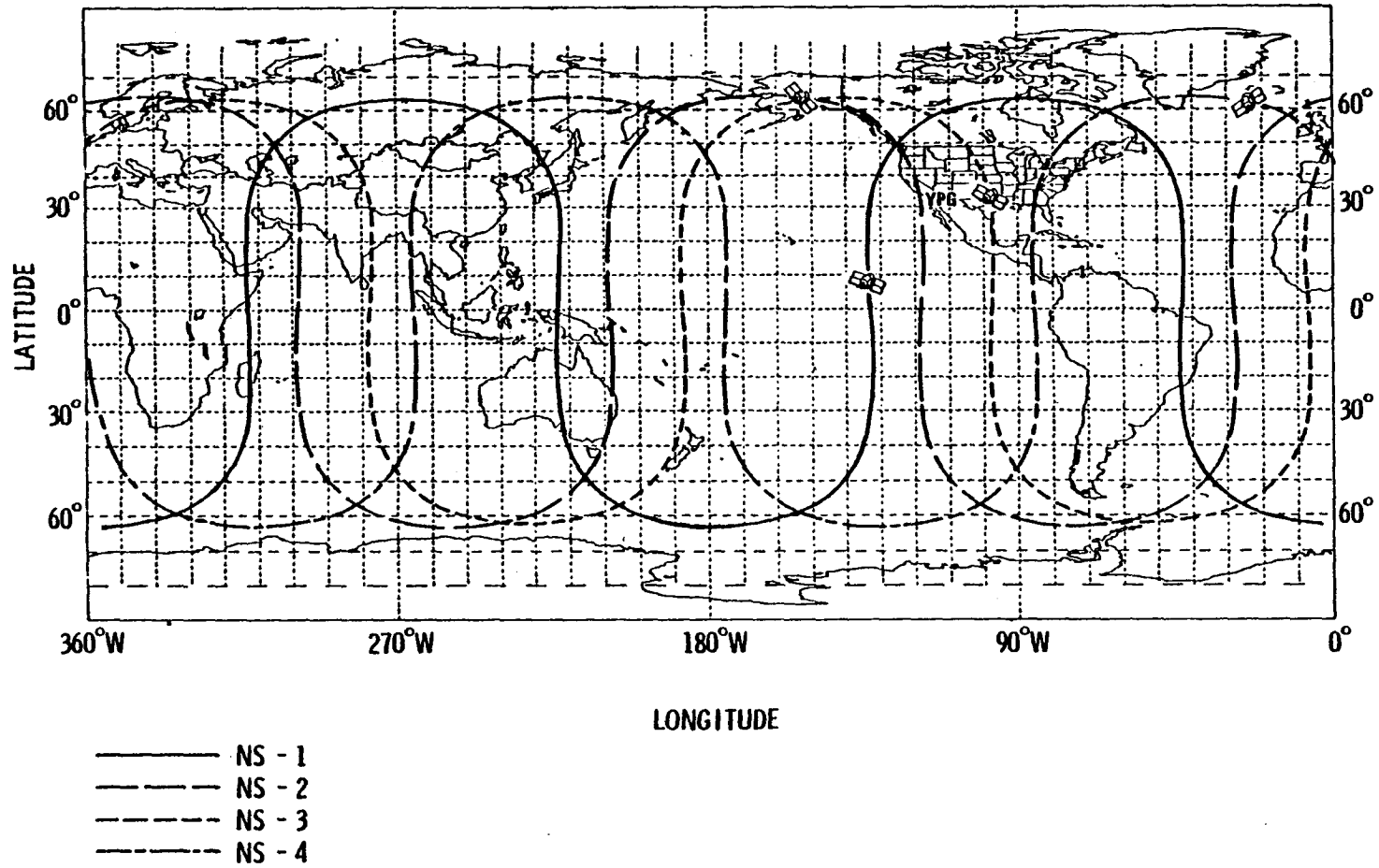
Figure 1. Ground Traces of the Phase I Constellation
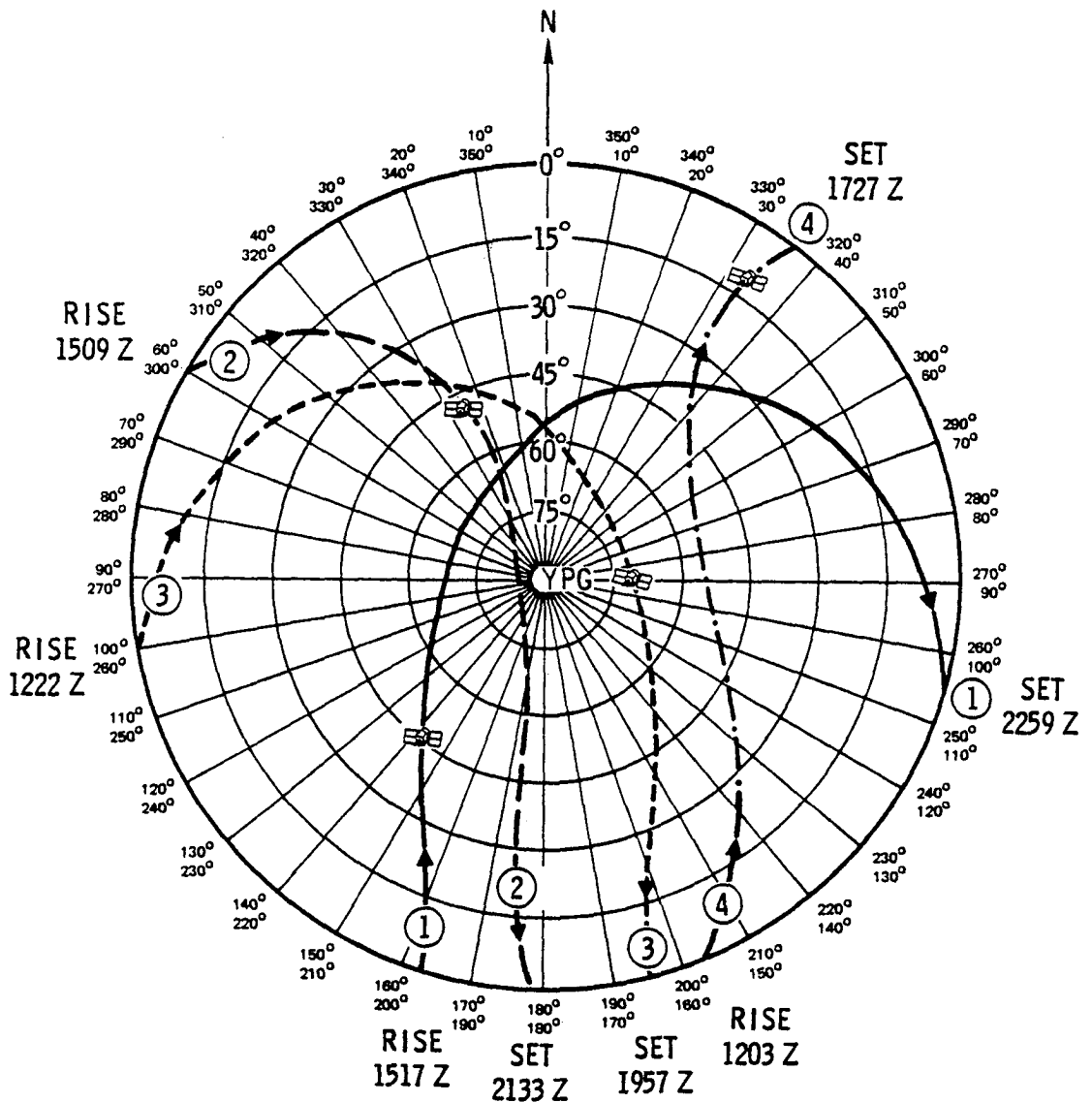
NOTE: 1. TIMES SHOWN ARE GREENWICH MEAN TIME
2. SATELLITE LOCATIONS INDICATE POSITIONS
AT 1700Z ON 1 JAN 1979
3. RISE = SATELLITE APPEARANCE ABOVE HORIZON
SET = SATELLITE DISAPPEARANCE BELOW HORIZON

Figure 2.   Satellite Geometries at the Yuma Proving Ground

ranging signal; the amplifier/modulator units that supply the L_1 (1575.42 MHz) and L_2 (1227.6 MHz) carrier frequencies modulated by the PRN ranging signals; and the high-power amplifiers that amplify the carrier signals for transmission.

2.2   USER SEGMENT

The User Segment consists, in part, of navigation avionics which measure pseudo range and delta (pseudo) range using the navigation signal from each satellite. Pseudo range is the true distance from the satellite transmitter to the user antenna phase center plus an offset due to the user's clock bias. Similarly, delta range is the incremental range change over a specified time interval plus an offset due to the user's frequency bias. Each signal carries ephemeris data and system timing information modulated at 50 bps. The low data rate information forms the navigation message, which permits the user receiver/processor to convert pseudo range and delta range measurements to user three-dimensional position and velocity.

Navigation message data consists of five subframes each containing 300 bits of data (Fig. 3). Subframe 1

Subframe 1	Subframe 2	Subframe 3	Subframe 4	Subframe 5
SV Clock Data	SV Ephemeris Data	SV Ephemeris Data	Special Messages	Almanac Data
Single Frequency Ionospheric Model Data				

Data Block I   Data Block II   Data Block III
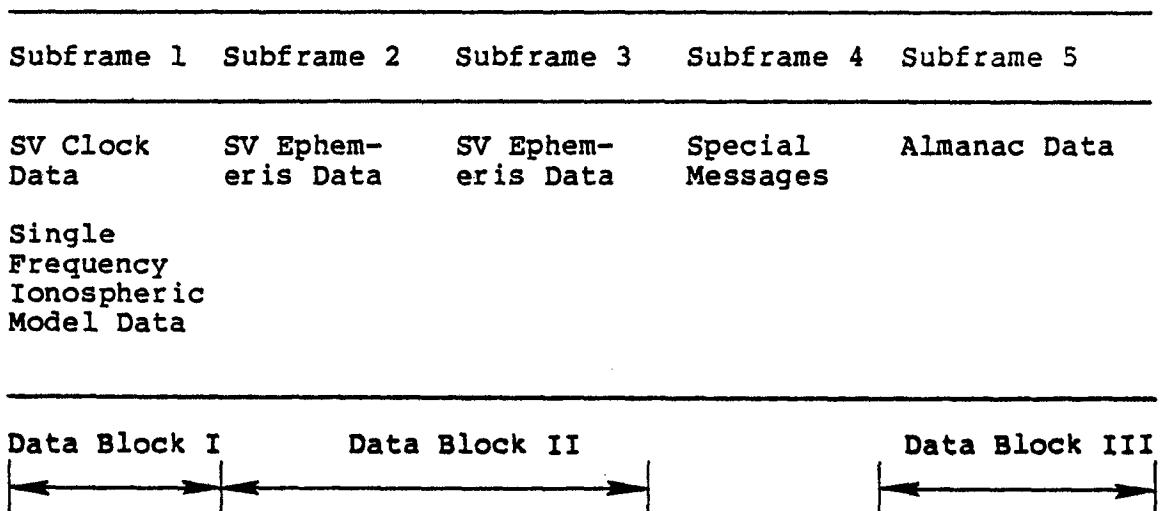
Figure 3.   Navigation Message Structure

contains data to establish system time and a set of
coefficients with which a single frequency user can model the
signal delay due to the ionosphere. The data in subframe 1 is
also referred to as data block I. Subframes 2 and 3 contain
data from which the satellite position and velocity can
accurately be determined. These two subframes are referred to
as data block II. Subframe 4 contains alpha numeric data
irrelevant to navigation. Subframe 5 provides data similar to
data block II but of reduced accuracy. Every thirty seconds
the almanac of a different satellite appears in data block III.

2.3   CONTROL SEGMENT

The Control Segment consists of a Master Control
Station (MCS), an Upload Station (ULS), and monitor stations
(MS) located in Hawaii, Guam, Alaska, and at Vandenberg AFB,
California. The monitor stations passively track all
satellites in view and accumulate pseudo ranging data, which is
transmitted to the MCS where it is processed to provide
estimates of the satellite ephemerides and clock offsets. At
least once a day these estimates are extrapolated forward in
time to provide predictions of the SV ephemeris and clock
states. These predictions are the basis of the new navigation
message that is transmitted by the upload station to the
satellites for subsequent downlink transmission encoded on the
carrier signals. The MCS, ULS, and the Vandenberg monitor
station are co-located.

As previously described, the satellite-station
geometries repeat, occurring somewhat less than 4 minutes
earlier each day. Fig. 4 presents the tracking contacts for 1
January 1979. Tracking opportunities for some SV-MS pairs
occur 23 hours per day with as many as 12 satellite-station
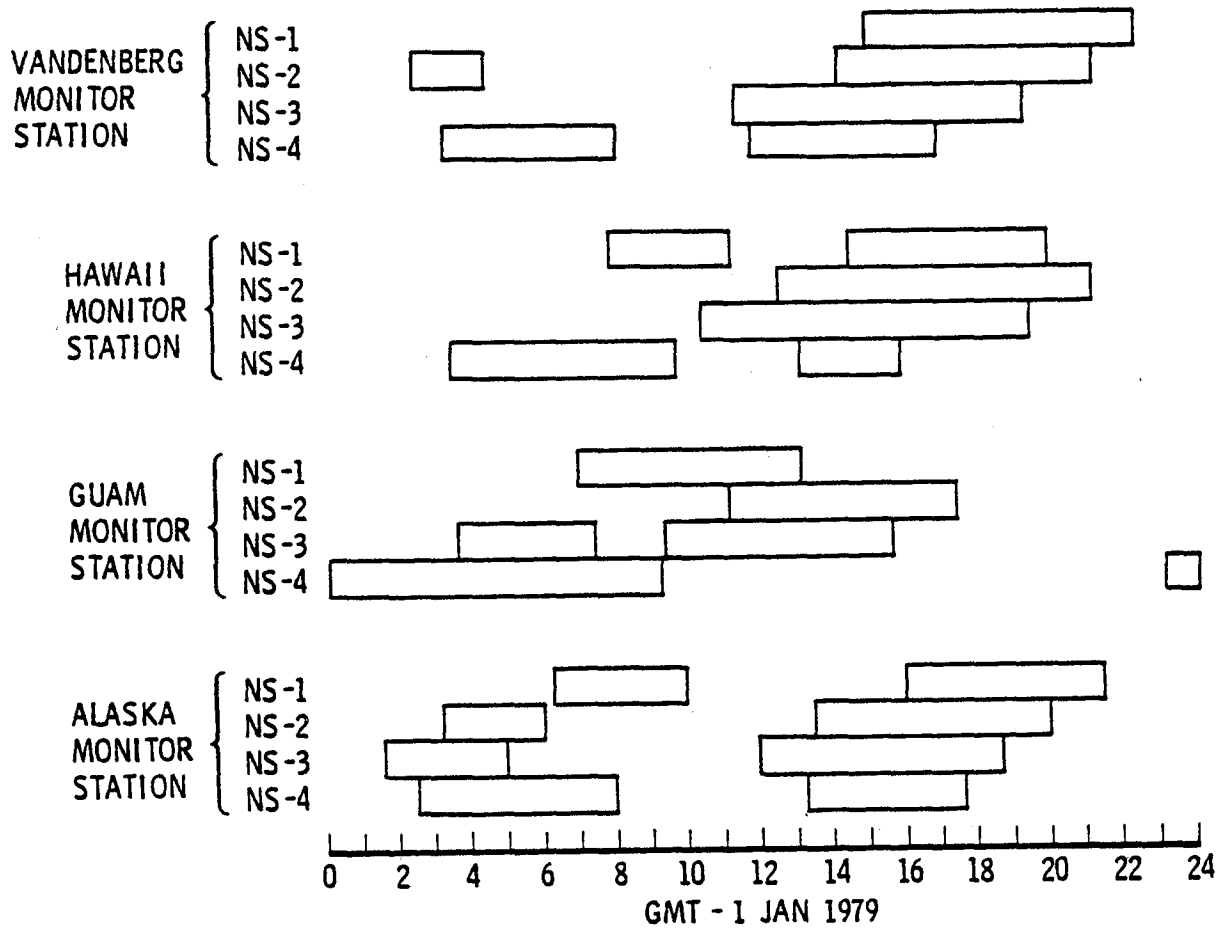
Figure 4. Monitor Station Tracking Schedules

103

contacts occurring simultaneously, e.g., 1600 GMT. Yuma
Proving Ground can be considered to have the same tracking
opportunities as Vandenberg monitor station because of their
proximity. Thus, the opportunity for four SV tracking at Yuma
occurs between 1515 and 1725 GMT on 1 January 1979 where the
earlier time is determined by the rise of Navstar 1 while the
later time is determined by the fade of Navstar 4. The
desirability of incorporating Vandenberg tracking data prior to
preparing the upload further reduces the available test window.

3. EVALUATION METHODS

Control Segment operations have been supporting Phase I satellites for nearly two years. Much of this time has been used to integrate the system, de-bug hardware and software, and to refine system parameters in order to optimize performance. Sufficient data have been accumulated during the last year to enable the Phase I Control Segment evaluation. Evaluation activities fall into two categories: (1) Master Control Station system performance evaluation and (2) independent validation activity.

3.1 Master Control Station System Performance Evaluation

Within the Master Control Station software is a program for system performance evaluation. This program performs various computational checks and comparisons to monitor Control Segment performance. These checks generally involve comparisons of parameters or functions generated some time in the past with corresponding parameters or functions at current ("real") time. In particular, two computations involving the navigation message have proved useful as a measure of Control Segment performance: (1) measurement residuals and (2) user range error (URE).

3.1.1 Measurement Residuals

Throughout a satellite pass, raw monitor station measurements (pseudo range and delta range) are edited; corrected for such physical phenomena as tropospheric and ionospheric delays, relativity, satellite lever arms, and light transit time delay; and smoothed to yield a current measure of the slant range between the satellite and the monitor station. Using the applicable data block I and II portions of the

navigation message which were last uploaded to the satellite, one can compute the corresponding (predicted) slant range to the satellite. The difference between the smoothed and predicted measurement represents the range error due to the navigation message errors. Fig. 5, is a simplified illustration of the measurement residual computations.

3.1.2   User Range Error

The navigation message is prepared and uploaded during the time when the Vandenberg monitor station is tracking. After upload, the satellite is tracked for at least another hour (SV4) and for as much as another five hours (SV2). The newest data represents the best (real time) information on the satellite clock and ephemeris. A predicted pseudo range measurement to a stationary site at Yuma Proving Ground, Arizona is computed from the applicable navigation message (see Fig. 6). A corresponding pseudo range measurement is computed using the current (real time) satellite clock and ephemeris estimates. The difference between these pseudo range computations represents the user range error (URE) attributable to the Control Segment (i.e., navigation message).

3.2   INDEPENDENT VALIDATION

In support of the Phase I activities, The Aerospace Corporation has performed independent evaluations of Control Segment performance (see, for example, Reference 3). Evaluation efforts involve post flight ephemeris and clock reconstruction using GPS-supplied data as well as S-band ranging data collected by the Air Force Satellite Control Facility (AFSCF). Also, extensive simulation activity where the truth is precisely known has been used to validate Control Segment performance.
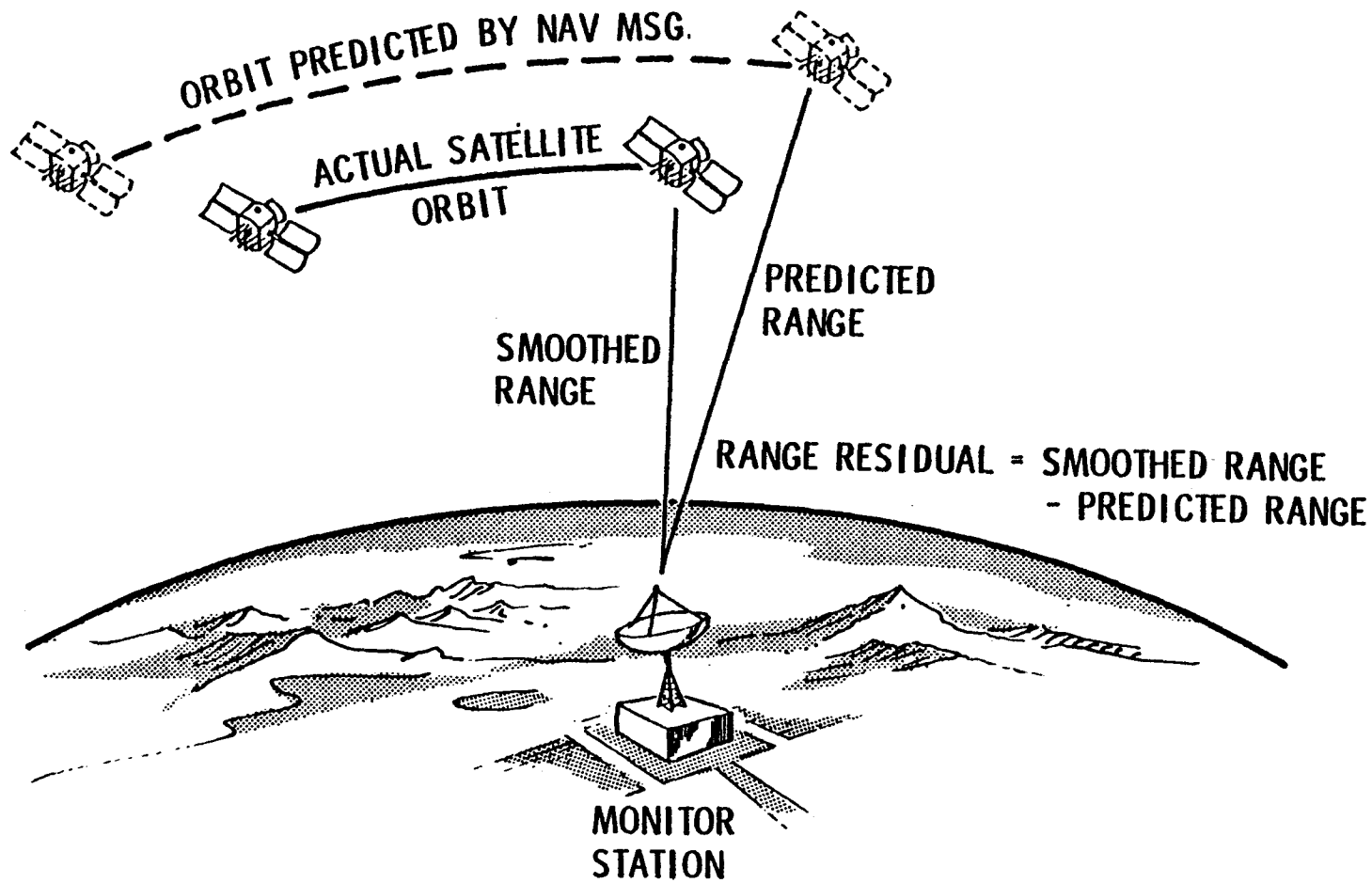
Figure 5. System Performance Evaluation Measurement Residual
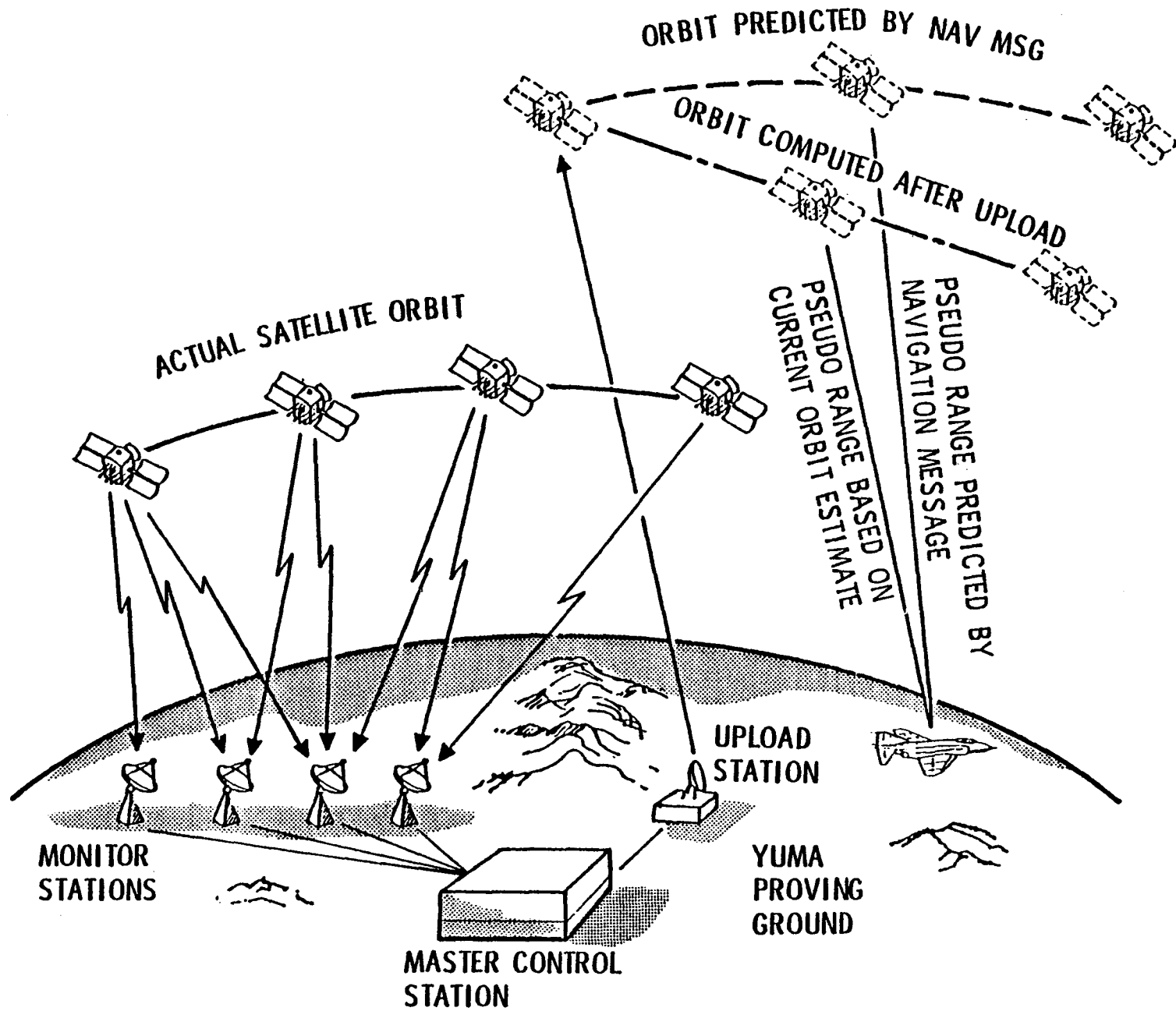
Figure 6. Master Control Station User Range Error Computation

3.2.1   Best Fit Ephemeris and Clock

Absolute satellite ephemeris and clock accuracies are difficult to establish. To accomplish post flight reconstruction, a special version of the TRACE program (Ref. 4) has been used to generate best fit ephemeris and clock (BFE/C) estimates. For evaluation purposes, BFE/C estimates are considered to be the closest representations of the "truth" currently available. Three types of data have been used for post flight reconstructions: MCS generated smoothed ranging data (SRTAP), Aerospace generated smoothed ranging data (named APOLY, after the software which generates it) and AFSCF radar ranging data.

3.2.1.1   SRTAP Data

The Master Control Station generates smoothed pseudo range and delta range measurements every fifteen minutes when monitor station tracking data exists. These data referred to as SRTAP data, are the input to the linearized Kalman filter which computes the real time satellite ephemeris corrections and clock states. In addition, this same data is forwarded to the Naval Surface Weapons Center/Dahlgren Laboratories where a reference trajectory for the MCS Kalman filter linearization is generated weekly.

3.2.1.2   APOLY Data

As an alternative to using MCS prepared smoothed data, The Aerospace Corporation has developed a program (named APOLY) which converts raw monitor station (6 second interval measurement) ranging data into smoothed data. Moreover, APOLY uses integrated delta range rather than polynomial generated

range differences to complement the pseudo range data. By
doing their own editing, correcting, and smoothing, Aerospace
Analysts have absolute control over which data are used and
obtain explicit measures of the quality of the data.

3.2.1.3 AFSCF Data

As part of AFSCF support, the GPS satellites are
tracked with S-band radars from Satellite Control Facility
(SCF) sites extending from the Indian Ocean to northeastern
United States. Six daily contacts of 10 minute minimum
duration (the Indian Ocean site often gathers as much as one
hour), while sparse vis-a-vis GPS tracking densities, provide
tracking coverage over more of the orbit than the four GPS
monitor station network. The GPS sites stretch only from Guam
to Vandenberg AFB.

3.2.1.4 Ephemeris Comparisons

Best Fit Ephemerides (BFE) for the period 16-30 August
1978 were generated: one based on SRTAP data, a second based on
APOLY data, and a third based on SCF data. The solution
trajectories of each fit were differenced with each other.
Agreement between the BFEs was quite good. Figure 7 is an
example of the differences between Navstar 2 BFEs using SCF and
SRTAP data. Estimated differences in terms of URE are
approximately three meters (one sigma). These results are more
notable when one considers that Navstar 2 experienced roll
momentum dumps on the twentieth and the twenty sixth day of
August.

The momentum dumping process was performed with a
coupled-pair of 0.1 lb reaction control jets. The location of
these jets caused a plume impingement onto the space vehicle,
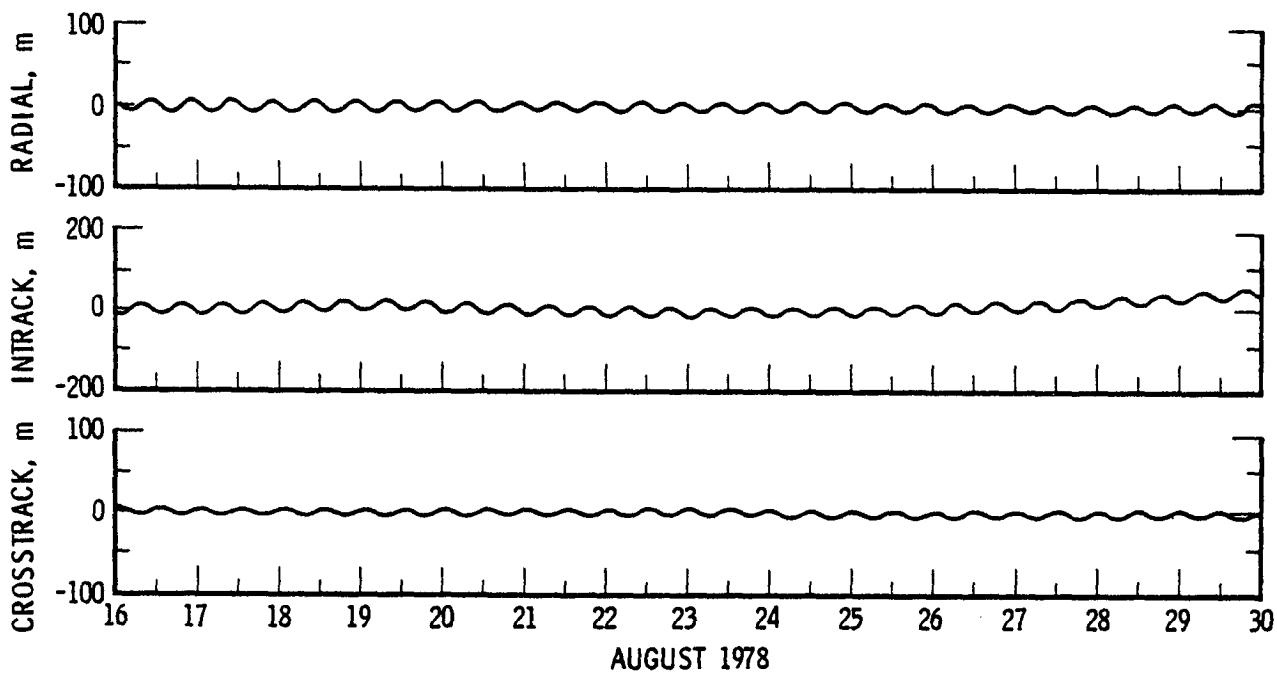
Figure 7.   Best Fit Ephemeris Differences for SCF and SRTAP
            Data: Navstar 2 Data for 16-30 Aug 1978

producing an intrack position error of about one hundred meters impulsive per day. A judicious choice of fit parameters to include in-track thrusts in the BFE solutions removed essentially all of the intrack error due to this source.

3.2.2   Ephemeris End Around Check

The ephemeris end around check (EEAC) involves a sophisticated simulation of GPS data inputs and outputs (see Ref. 5). Some aspects of the activity are still not completed. When they are, they will be documented. For now, two aspects of EEAC will be useful to this presentation: (1) best fit ephemeris and clock solutions, and (2) monitor station location solutions (geodetic survey). Monitor station survey will be discussed in Para. 4.3. The best fit activity is cited here to demonstrate the efficacy of the post flight reconstruction methodology since in this case the truth is precisely known.

One case (Case 3.X) involved the simulation of two Phase I satellites and four monitor stations. Reference 5 gives specific details of all the simulated effects. Briefly, one satellite was characterized by a cesium frequency standard and Navy's Navigation Technology Satellite II (NTS II) the solar pressure force model, while the second satellite had a rubidium frequency standard and a Navstar solar pressure force model. Force model errors were introduced into the solar pressure and geopotential force models. Other simulated errors included monitor station location coordinates, pole wander values, monitor station clock instabilities based upon ground cesiums, SV random and deterministic clock errors, tropospheric and ionospheric refraction corrections, and white noise on all measurement links.

This data was fit using the same methodology applied to real data. Figures 8 and 9 present the differences between the best fit solutions and the truth. All the error components display the twelve hour periodic structure typical of GPS orbits. Radial errors have amplitudes between one and two meters. Horizontal errors (the root sum square of intrack and crosstrack errors) are approximately fifteen meters for Navstar 1 and ten meters for NTS II. As a result of the altitude of the GPS orbits only between zero (at zenith) and twenty four percent (on the horizon) of the horizontal error maps into the user range error. Hence, the estimated contribution to the user ranging error is about three meters (one sigma).

3.3.   DATA COLLECTION

Although Control Segment data is collected daily, special data collection periods have been designated for the purpose of performance evaluation. Table III presents a summary of these special periods. The SEG tests (CS-SEG-1) were intended to verify Control Segment performance in support of one, two, and three satellites. Each test was nominally scheduled for four weeks of normal operations. As evidenced in Table III, none of the SEG tests had four consecutive weeks of normal operations. The CS-S-1 (S-1) test was a four satellite full system evaluation. Initially scheduled for 17 January to 13 February, 1979, it was rerun from 26 February to 25 March, 1979. This latter period was devoid of significant anomalies and is considered to be representative of normal operations.

During these test periods extensive data collections were performed and forwarded to General Dynamics/Electronics Division in San Diego, California and The Aerospace Corporation in El Segundo, California for analysis. It is primarily the results of these data analysis activities that are reported in the following section.
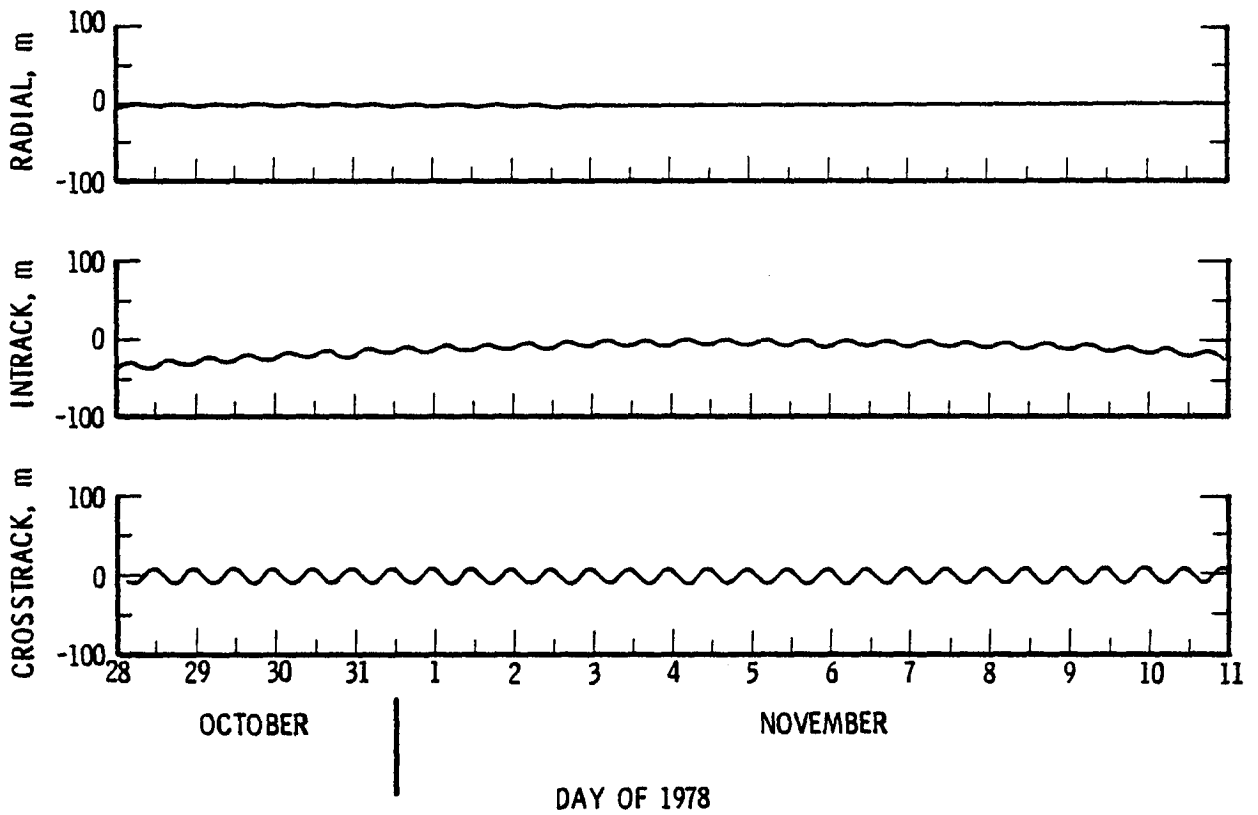
Figure 8   Best Fit Ephemeris Errors for Simulated NTS-II
            Satellite Data

114
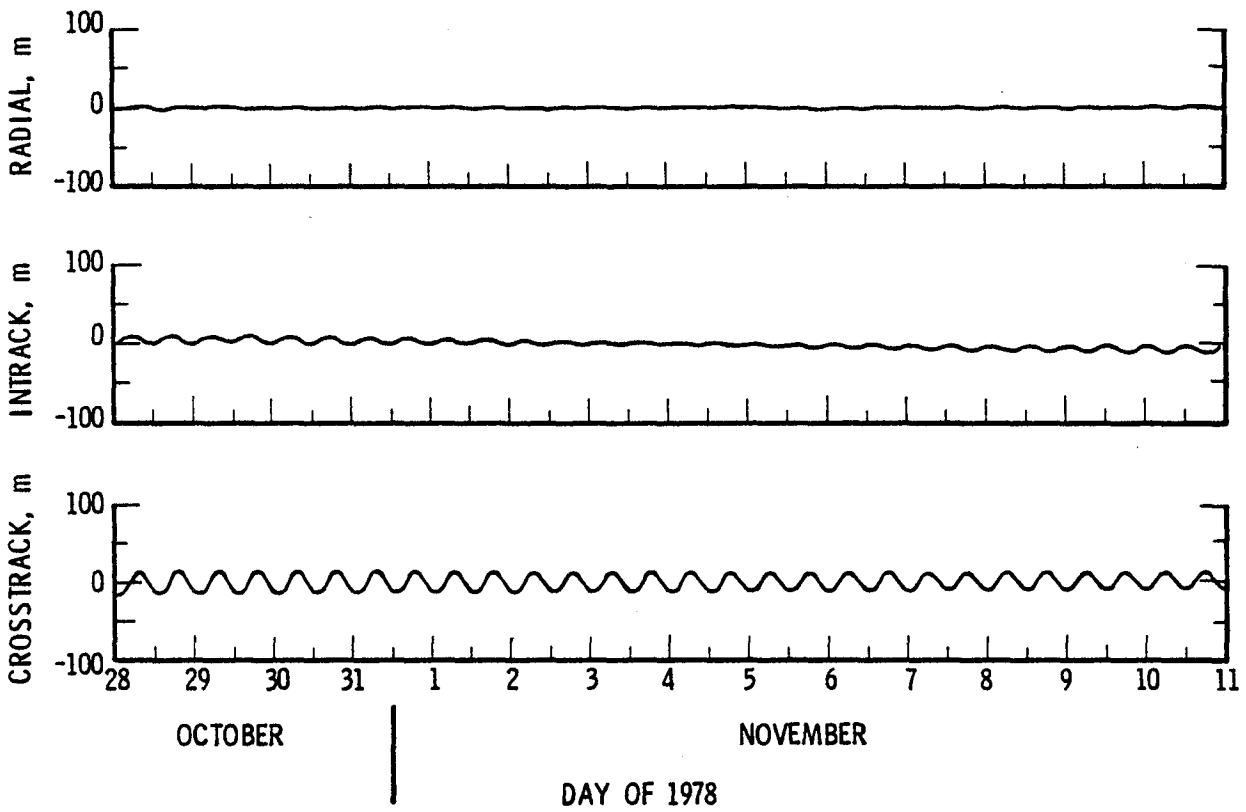
Figure 9.   Best Fit Ephemeris Errors for Simulated
            Navstar 1 Satellite Data

Table III. Special Data Collection Periods

TEST	PERIOD
CS-SEG-1 (1 SV)	15 MAY – 12 JUNE 1978
CS-SEG-1 (2 SV)	15 AUG – 12 SEPT 1978
CS-SEG-1 (3 SV)	13 NOV – 20 DEC 1978
CS-S-1 (4 SV)	29 JAN – 23 FEB 1979
	26 FEB – 25 MAR 1979

4. RESULTS

This section summarizes Phase I Control Segment
performance to date. For more details see Refs 6-9. The
results will address the following issues: ephemeris and
satellite clock prediction accuracy, i.e., data block I (SV
clock) and data block II (ephemeris); almanac accuracy, i.e.,
data block III·

4.1   EPHEMERIS AND SATELLITE CLOCK PREDICTION ACCURACY

4.1.1   Master Control Station System Performance Evaluation

As described in Section 3, this activity is performed
with the MCS software. The results reported in Sections
4.1.1.1 and 4.1.1.2 have been supplied by General Dynamics
Electronics Division. The remainder of Section 4 is based on
analyses performed at The Aerospace Corporation.

4.1.1.1 Measurement Residuals

Satellite positions predicted from the navigation
messages are used by the GPS Master Control Station System
Performance Evaluation software to compute a predicted range
from a given satellite to a Control Segment monitor station
currently tracking that satellite. Corrected smoothed pseudo
range measurements are then converted into a measured range by
subtracting the predicted satellite clock offset and the
current estimate of the monitor station clock offset. The
difference between these measured and predicted ranges provides
a direct indication of the accuracy of the GPS navigation
message.

Fig. 10 summarizes the predicted range residuals to the Vandenberg monitor station for the four GPS satellites. The data presented are the root-mean-square (rms) of the predicted range residuals based on data collected during four satellite testing in February 1979. The daily residuals were shifted along the horizontal axis so the data could be evaluated relative to upload time. Note that the residuals for the four SVs before the daily upload are of the order 3-30 meters. At the upload time, the residuals drop towards zero and then begin to disperse. The residuals are not identically zero at upload time because of the timing involved in computing the evaluation parameter. The navigation message is constructed based upon filter estimates at a particular epoch. These data must be uploaded to the satellites and verified by the Control Segment monitor stations before it is available for evaluation. Hence, the message has aged a minimum of fifteen minutes (the nominal Phase I evaluation interval) before measurement data are available for residual formation.

4.1.1.2 User Range Error

Section 3.1.2 described the URE computation performed by the MCS System Performance Evaluation. The CS-S-1 test · performed from 26 February through 25 March 1979 was a period of stable GPS operation. Daily URE data were accumulated for the four satellites. The root-mean-square (rms) of these URE values are plotted in Fig. 11 as a function of time since the navigation message was uploaded to the satellite. It should be added that the mean value of the URE for each satellite is less than 1.5 meters; hence the rms value can also be interpreted as the standard deviation with no significant error.

As a consequence of the satellite geometries (see Section 2), Navstar 4 is visible to Yuma for less than 2 hours
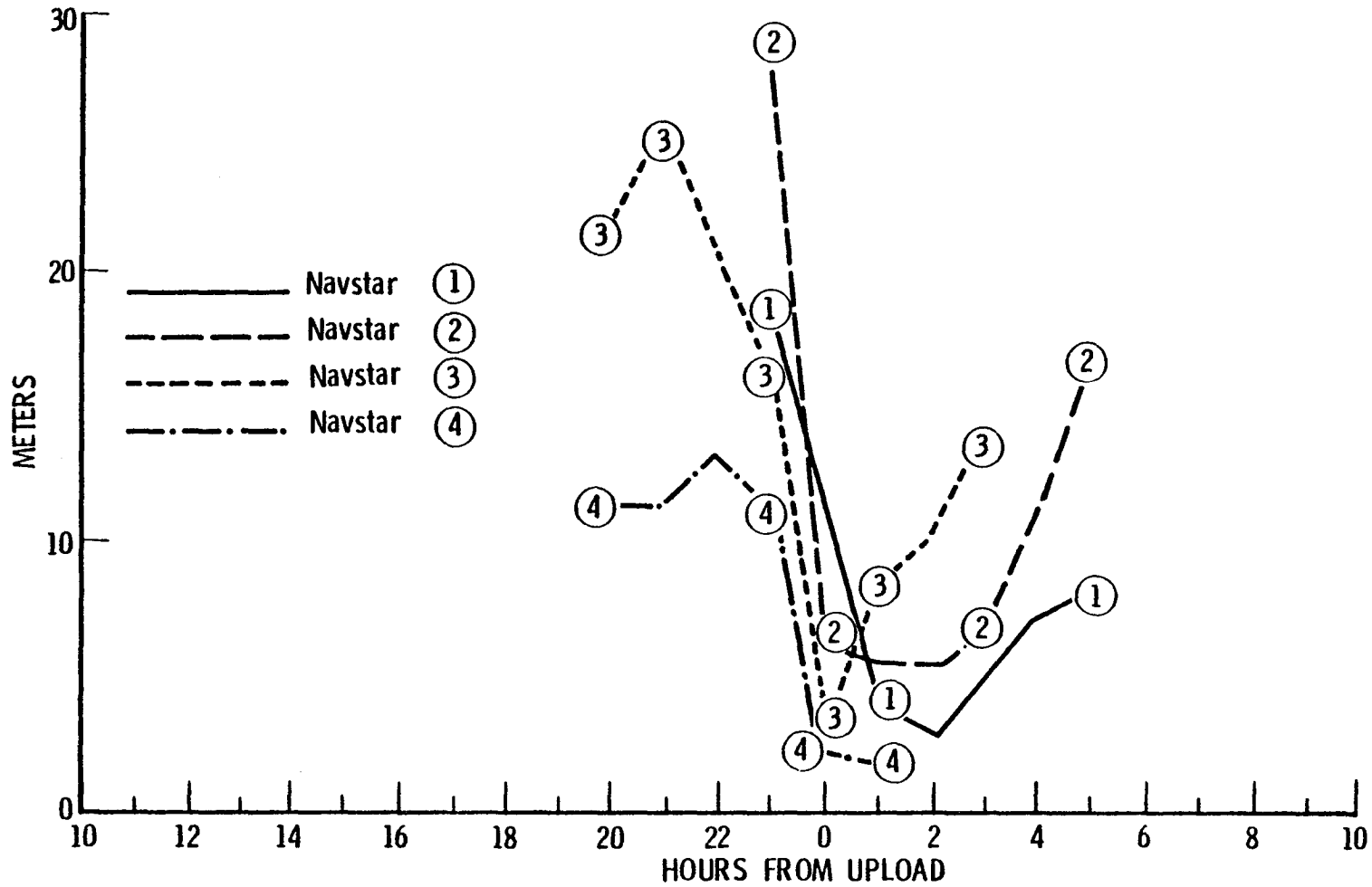
Figure 10. RMS of Predicted Range Residuals at Vandenberg

119
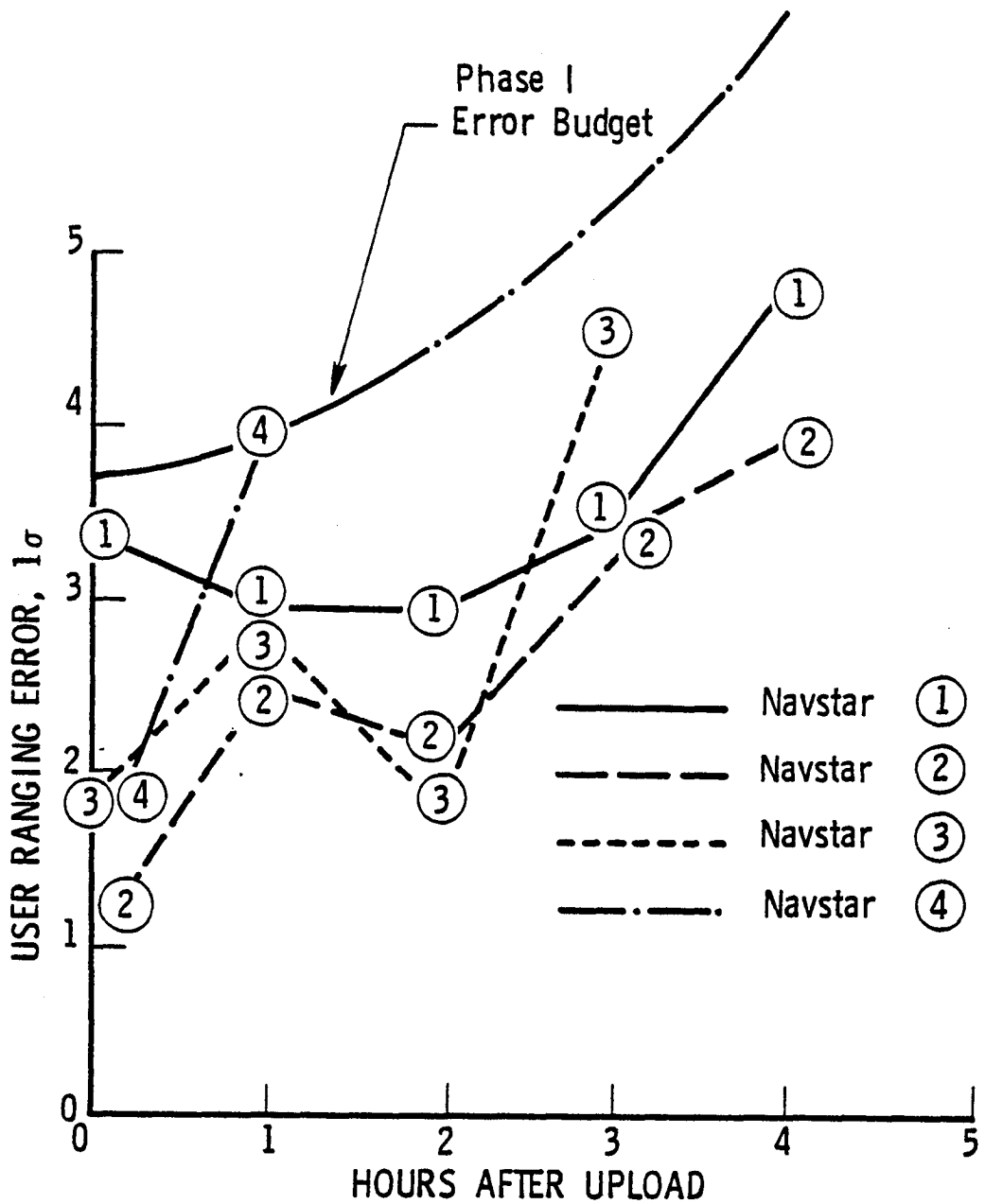
Figure 11.   User Ranging Error Based on MCS System
Performance Evaluation

after the fourth satellite (Navstar 2) rises. During the first two hours after upload Navstars 1, 2, and 3 better the required accuracy by more than one meter. Although Navstar 4 exceeds the one hour error budget by 0.1 meters (4.0 vs 3.9 meters), the difference is quite small. In general, all four satellites better the Phase I accuracy requirements during the entire period they are visible to Yuma after upload.

4.1.2   Independent Validation

The twenty-six navigation messages broadcast by the satellite (one message each hour) predict the position and SV clock offset around the entire orbit, actually extending two hours into the next day. These predictions have been compared against the "truth" solution (BFE/C) prepared by The Aerospace Corporation (see Section 3.2) during the special data collection periods. Figures 12 and 13 present the Navstar 1 and 2 ephemeris and clock errors as determined from the upload messages on 16 Aug 1978 (day 228). The small data loss in the first hour is due to the MCS computation lag between the time the navigation message is prepared and the time it is uploaded, verified, and then broadcast. During this time the satellite is broadcasting the navigation message uploaded previously.

Radial and crosstrack ephemeris errors have a characteristic twelve hour periodicity. Intrack errors, while also of twelve hour periodicity, have a secular error growth in addition. Clock errors, on the other hand, should look more like a random walk. However, the clock errors on 16 August show some periodic characteristics. This appears to be a result of (1) relative paucity of data due to unavailability of Guam tracking station, (2) induced correlations between clock state and ephemeris state estimates due to high altitude (4.2 earth radii) of GPS orbits, and (3) induced correlations due to best fit clock processing.

121
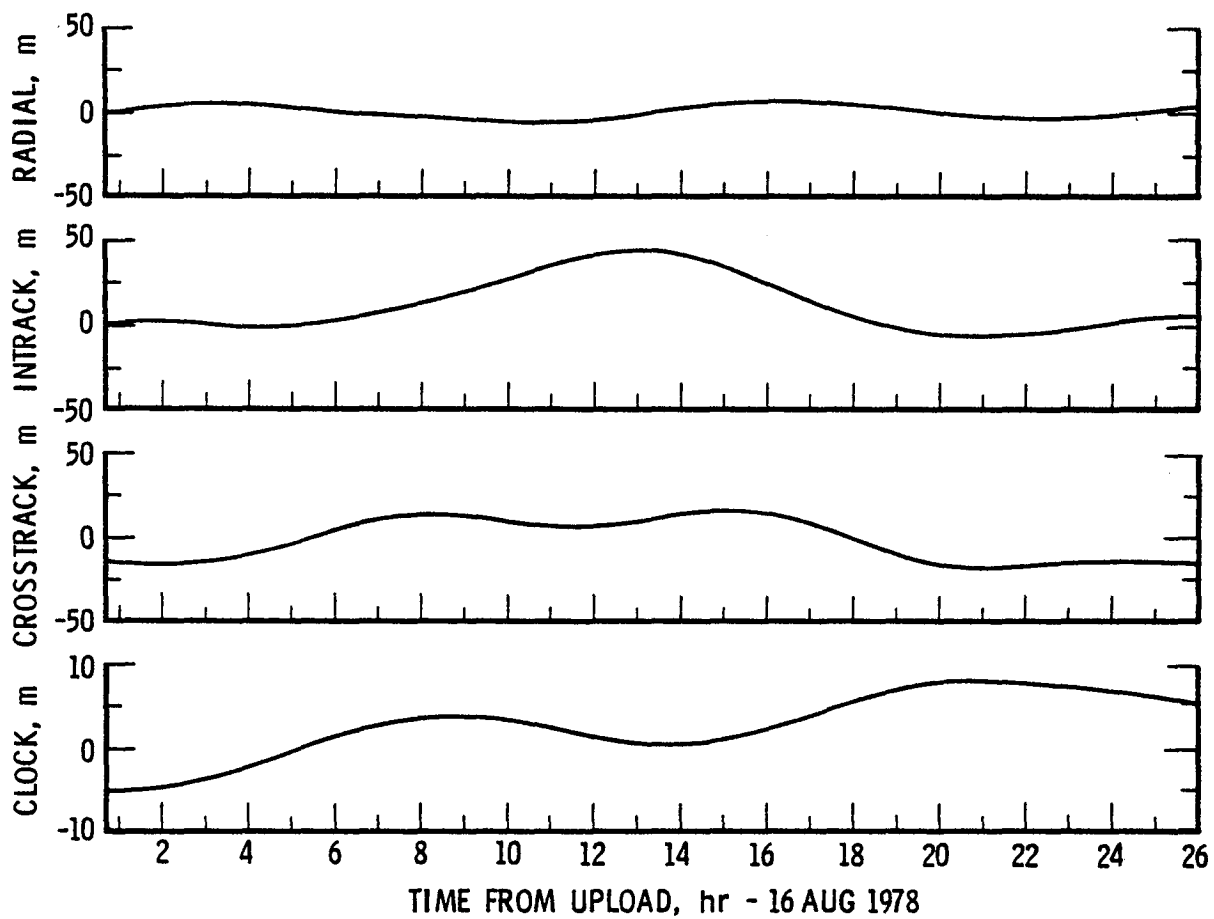
Figure 12.   Navstar 1 Ephemeris and Clock Prediction
Errors for 16 Aug 1978
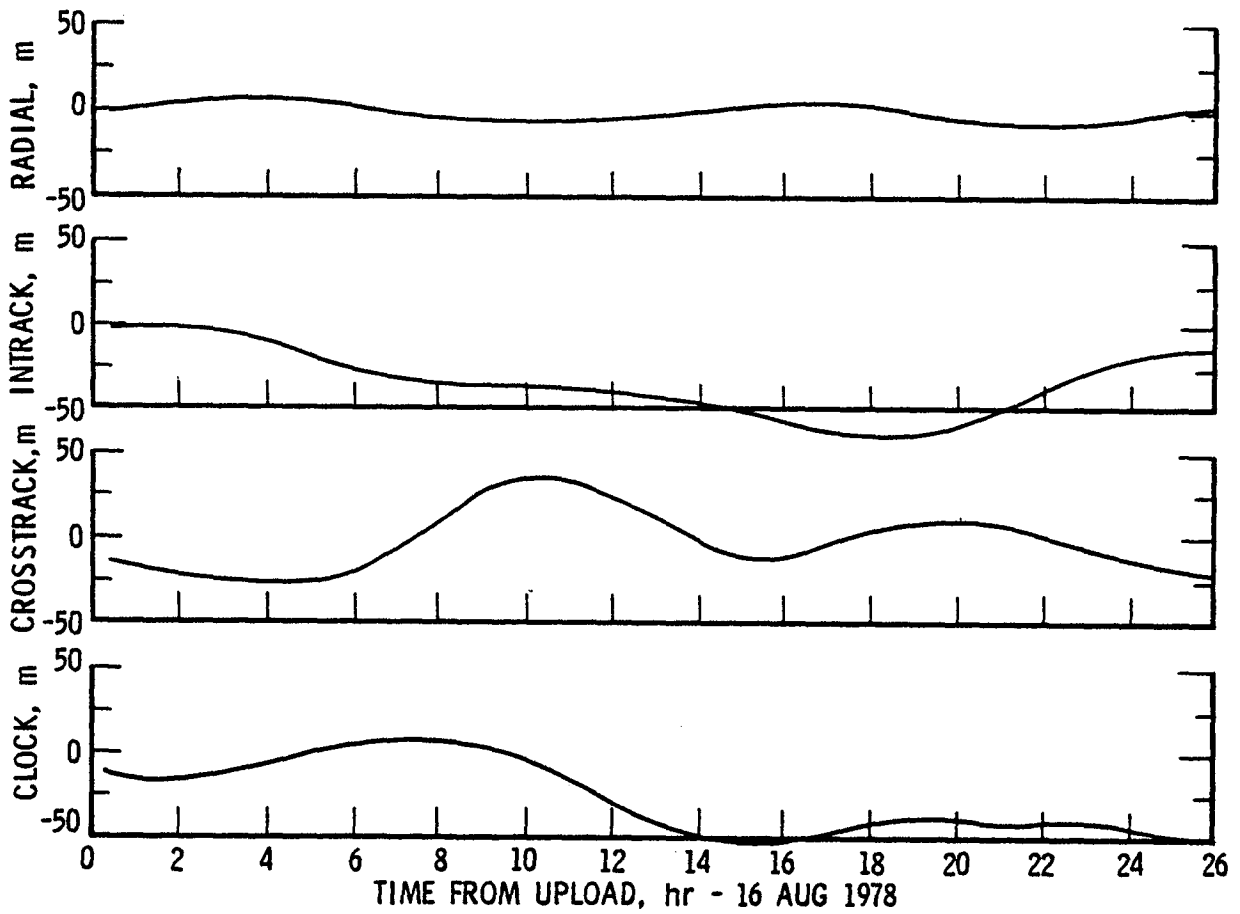
Figure 13. Navstar 2 Ephemeris and Clock Prediction
Errors for 16 Aug 1978

Next, the ephemeris and clock errors are converted to
user ranging errors by mapping the contributions onto the
line-of-sight to (fictional) uniformly distributed users on the
earth's surface. At each time point, the range errors for the
uniformly distributed user population are computed and the
corresponding statistics are tabulated. Fig. 14 presents the
68 percent error curves for Navstars 1 and 2 for 16 Aug 1978.
To interpret this result, remember that 68 percent of all users
who can see the satellite (masking angle is five degrees for
these computations) will incur errors equal to or less than the
value indicated by the curve. On 16 Aug, the maximum global
user range error was 10 meters during the first two hours and
about 22 meters during the twenty four hour period after upload.

4.1.2.1 Two Vehicle Testing

A similar activity was done for each day during which
an upload was generated during the CS-SEG-1 (2 SV) test
period. A total of 10 days between 16 and 31 August had
acceptable uploads (weekends were excluded, and two days had
some difficulties). Cumulative error statistics for the
two-week test period are presented in Fig. 15. Two curves -
one for the first two hour period after the upload message was
generated and the second for the twenty-four hour period after
the upload message was generated - summarize the Control
Segment ephemeris and SV clock prediction performance. To
interpret the figure, given a point on either curve x_1 = URE,
Y1 = probability), one states that for the indicated time span
(i.e., 0-2 hours or 0-24 hours) there is a probability of Y_1,
that a user will incur a URE less than or equal to x_1. Ergo,
there is a 68 percent probability that the user ranging error
is less than 6.5 meters during the first two hours after
upload. While this value is almost two meters beyond the error
budget it is a very positive result when one considers that at
this point in time:
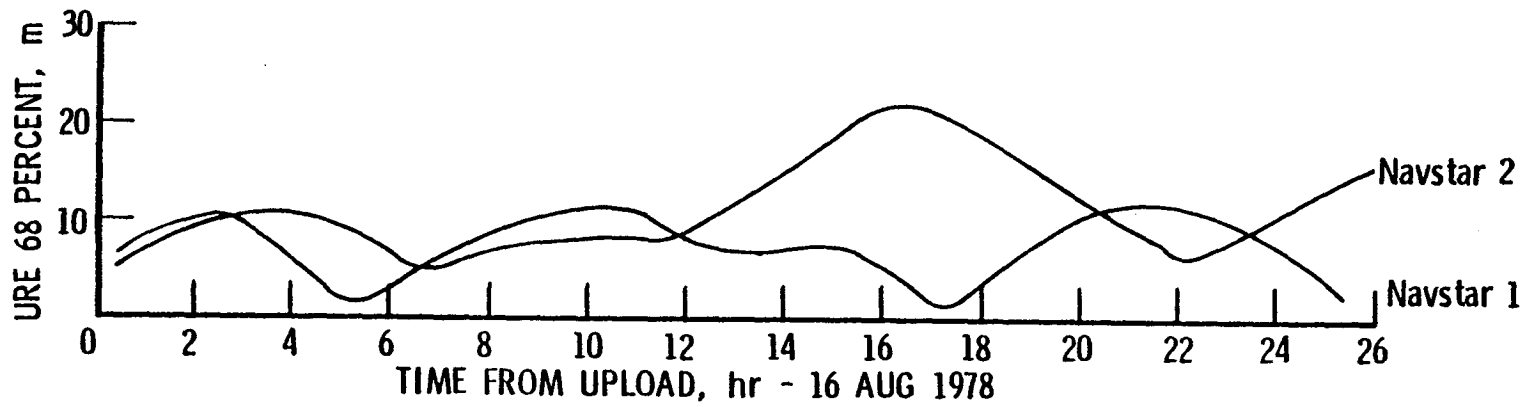
Figure 14. Global User Range Error Statistics
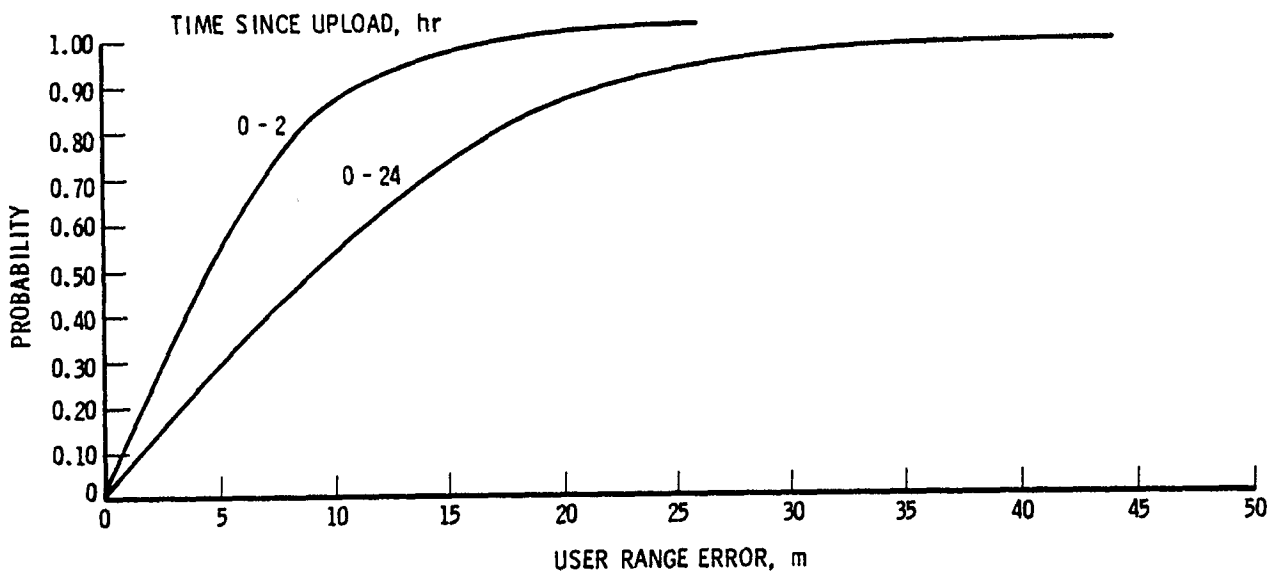
Figure 15. Cumulative Error Distribution From Ephemeris
and SV Clock for All Satellites

126

- Navstar 2 incurred intrack velocity impulses during the attitude control system roll momentum dumping process. This phenomenon was caused by plume impingement during the firing of the 0.1 lb reaction control thrusters. The momentum dump impingement anomaly was identified during the BFE processing - a month or more after the test period.

- The Control Segment software was still in a state of checkout. Several corrections have since been made - primarily in the data base.

The twenty-four hour URE statistics are impressive when one realizes that the SV rubidium clock should contribute nearly 37 meter (1 sigma) to the URE. According to the curve, for the 16-31 Aug. time period, the 68 percent probability yields a URE of 14 meters - which includes ephemeris and clock.

4.1.2.2 Three Vehicle Testing

A similar exercise was performed for the CS-SEG-1 (3 vehicle) test period. Seventeen days in the period 14 November to 8 December had uploads included in the cumulative error statistics shown in Figure 16. Again, two curves are used to summarize the Control Segment ephemeris and SV clock prediction performance; the first depicts performance for the first two hours after an upload while the second is for the twenty four hour period after the upload.

A procedural change strongly affected the character of these results. In an attempt to obtain ephemerides independent of GPS data, the previously referenced tracking data from the Air Force Satellite Control Facility was used as the basis for generating the BFE used in this comparison. This data was not corrected for ionospheric propagation effects at all, and was corrected for tropospheric propagation effects by use of a procedure different from that used at the MCS. While the
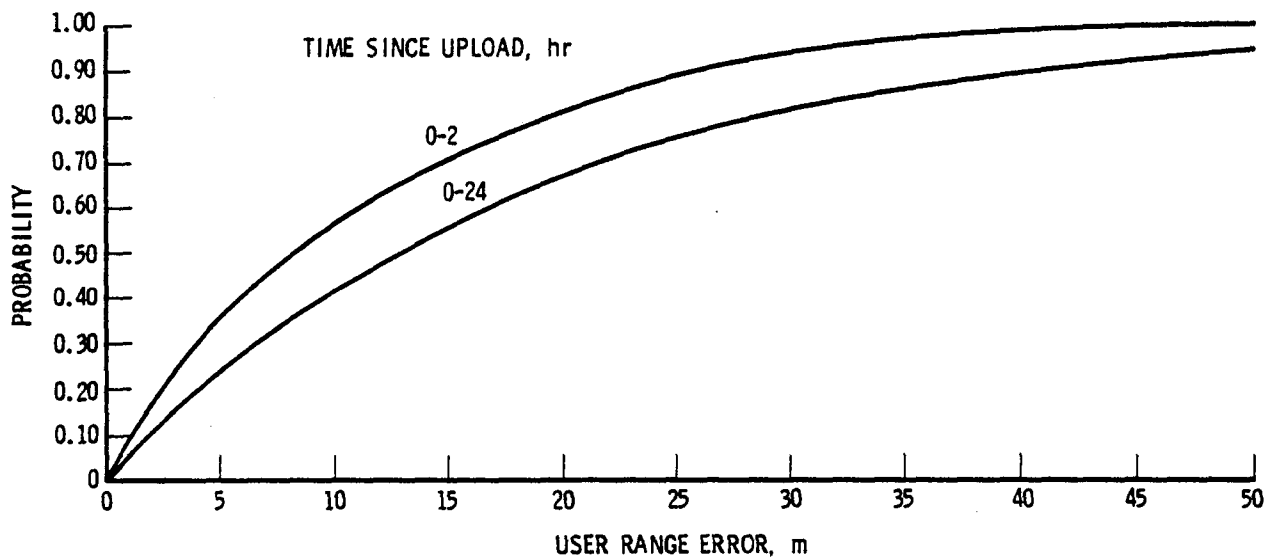
Figure 16.   Cumulative Error Distribution From Ephemeris and
             SV Clock for All Satellites - Three Vehicle Test

long-arc fits to these AFSCF data appeared of acceptable quality, it was subsequently demonstrated that their predict performance was noticeably poorer than those obtained from GPS-obtained data. This poorer predictive capability is sharply evident in these three satellite test results.

Additional problems hampered these analyses;

- A different clock was employed on Navstar 2 during this test than was used on the 2 vehicle test. This clock exhibited a 56 sec-period oscillation throughout this test. Additionally, this clock at that time manifested some as yet unexplained frequency excursions typically of many minutes duration and of several tens of meters' magnitude in pseudo range. These factors have led to worsening of Navstar's prediction performance by a factor of 2 or more.

- Guam monitor station was not operational

- Navstar 2 had a 56 second period anomalous oscillation in the 1575.42 Mhz carrier signal with amplitude 50 times greater than expected

- Navstar 1 had emerged from its eclipse season just prior to the 3 vehicle test span. It has been observed throughout these analyses that orbit and clock prediction are relatively worse in and near eclipse seasons than between eclipse seasons.

- Plume impingement during roll momentum dump firings was again a problem during this test. If anything, the number of momentum dumps was larger in this interval than during the two vehicle test.

4.1.2.3 Four Vehicle Testing

Four vehicle data for the period 29 January - 12 February 1979 was employed to examine the predictive capabilities of that configuration. Ten days of valid uploads are included in this sample. Cumulative error statistics are given in Figure 17, as before, in the four vehicle 2 hour and 24 hour prediction curves.

These data were reduced using a GPS data based BFE Predict Performance characteristics of this configuration and seen to be smaller than the two vehicle data presented earlier. The two hour value of less than 5.5 in with a 68 percent probability is closer to the specification error budget than previously reported values. In this two week interval there were two cases of anomalous clock performance, and the previously noted 56 second oscillation on Navstar 2's clock continued to plague the analysis. However, by the use of the magnetic torque momentum control system the incidence of thrusting to control momentum was eliminated. A change in the MCS data case process noise values resulted in more accurate predictions during this period, as is shown in Figure 17.

Table IV summarizes the 68% values for each of the three described here. It presents data by Navstar vehicle as well as points from the composite curves, Figures 15-17. The specific problems addressed earlier are clearly reflected in the summary.

The four vehicles analyzed here were part of a preliminary examination of four vehicle test results. Both the individual Navstar SV results and the composite are very encouraging as steps toward meeting the specification of 5 meters in 2 hours, 68% of the time. A preliminary look at the
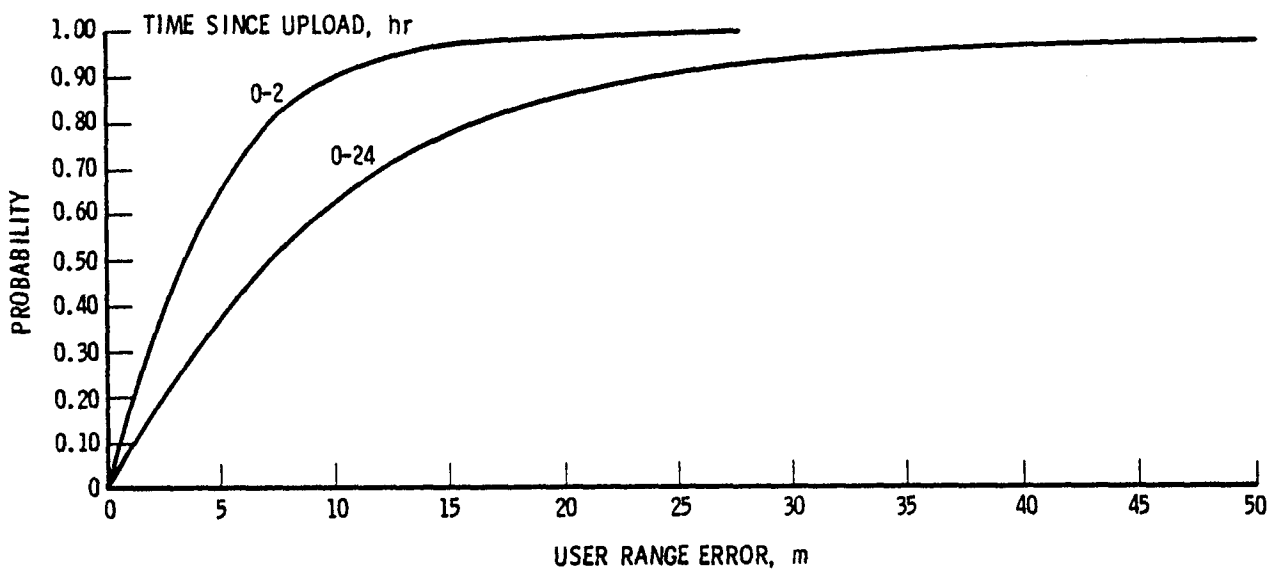
Figure 17.   Cumulative Error Distribution From Ephemeris And
SV Clock for All Satellites - Four Vehicles

Table IV. Test Summaries

Two Vehicle Cumulative Summary

	NAV 1	NAV 2	ALL (B Chart)
68%, 0-2	7.3m	5.5m	6.5m
68%, 0.24	14.1m	12.4m	14 m

Three Vehicle Cumulative Summary

	NAV 1	NAV 2	NAV 3	ALL
68%, 0-2	13.5m	12 m	10 m	13.5m
68%, 0-24	23.5m	29 m	12 m	20.5m

Four Vehicle Cumulative Summary

	NAV 1	NAV 2	NAV 3	NAV 4	ALL
68%, 0-2	5 m	6 m	4 m	7.5m	5.5m
68%, 0-24	11.5m	27 m	12 m	6 m	11.5m

CS-S-1 (see Table III) data indicates it is of higher quality and more nearly free of annoying anomalies. It is anticipated that all vehicles will meet specification value during this period.

Of special interest are the 24 hour predict values, which are much better than had been anticipated from analyses assuming a 1 part in 10^{12} fractional frequency stability clock.

4.2   ALMANAC EVALUATION

The methodology for evaluating the almanac (data block III) message is quite similar to that used for the independent validation of the ephemeris and SV clock messages (see section 4.1.2). Data block III has only one message per satellite per day. Moreover, it is intended to be useful (to much less accuracy) over extended time periods (see Table I). Thus, in evaluating almanac messages, the time scale is in days rather than hours. Here, as in section 4.1.2, the evaluation is based on data collected from 16 to 31 August 1978.

Fig. 18 presents the results of the almanac evaluation for messages generated during the CS-SEG-1 (2 SV) test. These messages spanned the period 16 to 31 August. If the one sigma values of Table I are interpreted as 68 percent probable URE, the almanac accuracies during the 2 SV SEG test appear to satisfy the error budget over the five week evaluation interval.
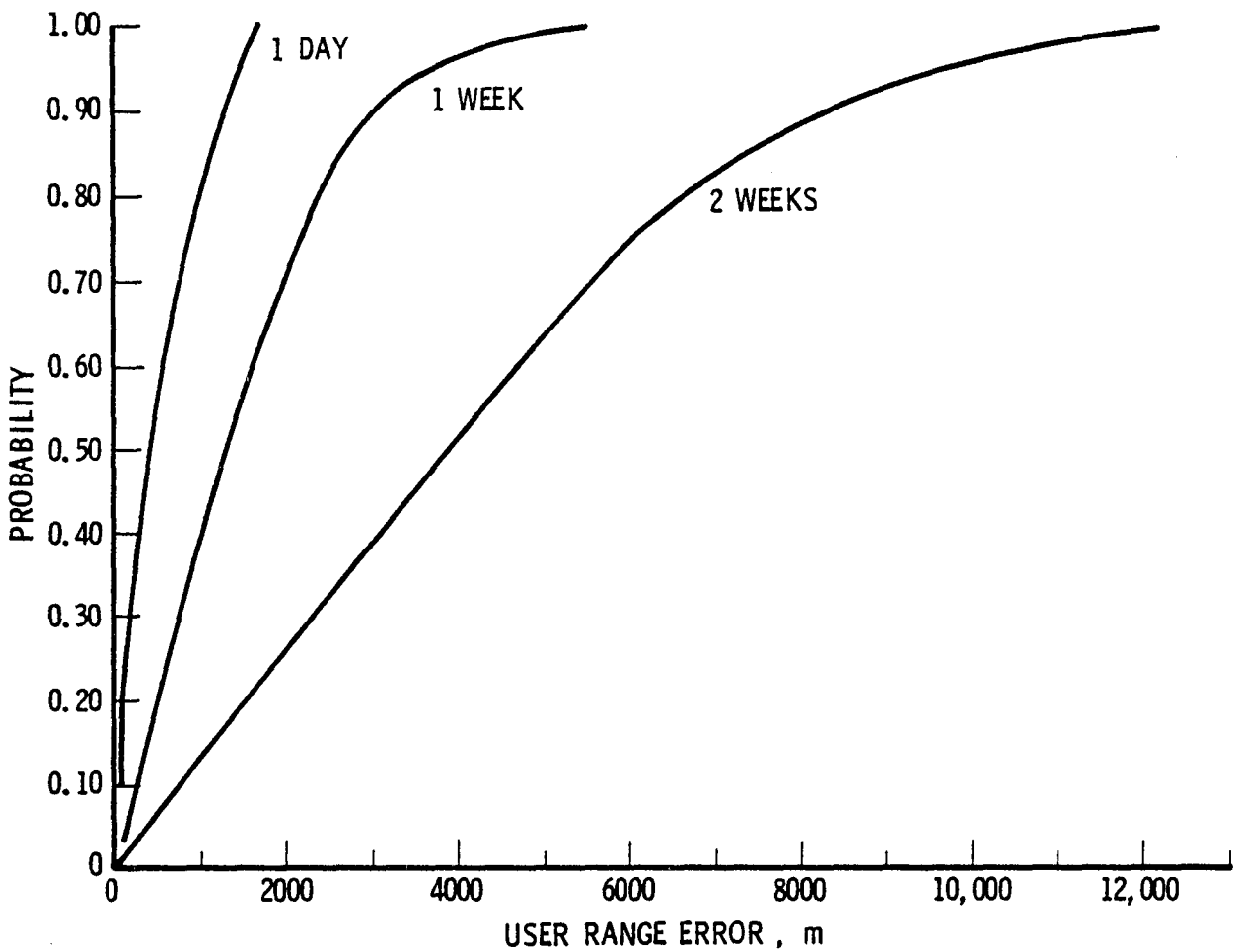
Figure 18. Cumulative Error Distribution for Almanac Message

5. CONCLUSIONS

Control Segment test evaluations have occurred during Spring 1978 (1 SV), Summer 1978 (2 SV), Fall 1978 (3 SV), and Winter 1979 (4 SV). The one SV test period was of little value because of many anomalous conditions. The two SV test period during Summer 1978 had two weeks' usable data. The three SV test period had over three weeks of usable data. Two weeks of 4 vehicle tracking were examined as a preliminary look at the formal four vehicle test data. Analysis on these periods forms the basis of this paper.

GPS system checkouts were still occurring in summer 1978. The evolution of Monitor Stations capability and reliability has increased continually from that period to the present. Plume impingement during momentum wheel unloading, which were causing in-track satellite perturbation approaching 100 meters a day, were identified in the course of these analyses. This problem has been removed through the use of magnetic torque for momentum wheel unloading. The checkout operations included a large number of problems solved, anomalies identified, fixes devised, work-arounds installed, and general systems development. Throughout it all, (perhaps despite it all), the Control Segment continued to perform its functions extremely well. Specifically:

- Control Segment user ranging error contributions were only about 1 meter over the specified values (i.e., 5.5 meters vice 4.6 meters) for the two hour period following upload.

- Twenty-four hour URE values were below what was anticipated from the Phase I rubidium SV clocks.

- Almanac accuracy met the URE budget.

6. REFERENCES

(1) System Specification for The Navstar Global Positioning System, SS-GPS-101B, 15 April 1974.

(2) Space Vehicle Navigation Subsystem and NTS PRN Navigation Assembly/User System Segment and Monitor Station Interface Control Document, MH08-00002-400, Revision F, 13 April 1977.

(3) H. Bernstein, Global Positioning System (GPS) Phase I Accuracy Analysis Concept, Report No. TOR-0076(6474-01)-3, The Aerospace Corporation, El Segundo, California, 25 July 1975.

(4) R. H. Prislin, and D. C. Walker, TRACE 66 Trajectory Analysis and Orbit Determination Program, Report No. TR-0059(9320)-1, Vol. I, The Aerospace Corporation, El Segundo, California, 15 August 1971.

(5) D. A. Conrad, Data Base for GPS Ephemeris End Around Check, TOR-0079(4473-04)-3, 1 April 1979.

(6) Post Launch CS/SV Test, CS-SEG-1 Category II Final Test Report, Revision B, 11 December 1978

(7) Post Launch CS/SV Test, CS-SEG-1 (2 SV), Category II Final Test Report, Revision B, 5 March 1979

(8) Post Launch CS/SV Test, CS-SEG-1 (3 SV) Category II Final Test Report, 30 March 1979 (Draft).

(9) Post Launch CS/SV Test, CS-S-1, Category II Final Test Report, To Be Delivered

AUTONOMOUS SATELLITE ORBIT DETERMINATION DURING THE
DEVELOPMENT PHASES OF THE GLOBAL POSITIONING SYSTEM*

Joan B. Dunham
Computer Sciences Corporation

ABSTRACT

An onboard navigation system was developed to aid the design and evaluation of algorithms used in autonomous satellite navigation with Global Positioning System (GPS) data. The performance of the algorithms designed for a GPS Receiver/Processor Assembly (R/PA) intended for Landsat-D was investigated during the development phases of the GPS (four to six satellites in the constellation). This evaluation emphasized the effects on the orbit determination accuracy of the expected user clock errors, GPS satellite visibility, force model approximations, and state and covariance propagation approximations. Results are presented giving the sensitivity of orbit determination accuracy to these constraints.

INTRODUCTION

The Navstar Global Positioning System (GPS) is a Department of Defense program that will provide navigation information to properly equipped users. A constellation of up to 24 satellites in 12-hour orbits will broadcast coded signals from which the user's position can be determined. The application of GPS to onboard satellite navigation has been previously discussed (References 1, 2). As part of the evaluation of the feasibility of autonomous satellite orbit determination using GPS, an experimental GPS Receiver/Processor Assembly (R/PA) will be placed on Landsat-D, and the resultant orbital solution will be compared to that obtained using more conventional ground-based techniques. This experiment will be conducted during the early phases of GPS, during which there will be four to six GPS satellites available.

The R/PA design proposed for spacecraft applications (Reference 3) consists of a dual-channel receiver and a Digital Equipment Corporation (DEC) LSI-11 processor. The R/PA measures pseudorange and delta pseudorange observations from the GPS signals, estimates the corresponding observations using the GPS navigation message, and uses the observation residuals in a UDU^T formulation of the extended Kalman filter (EKF) to determine the user spacecraft's position, velocity, clock bias and bias rate, and satellite drag coefficient.

Simulation studies are in progress to determine the accuracy attainable with this use of the GPS data, to identify and evaluate the primary sources of error, and to examine the algorithms in the proposed R/PA. As an aid to such studies, an onboard navigation package simulator (ONPAC) was developed on a DEC PDP-11/70 computer, which has computational accuracy similar to that of the LSI-11. The simulator is designed for both premission planning and real-time analysis as well as evaluation of the GPS receiver algorithms.

The simulator is being used in this study to determine the factors affecting the optimum performance of the onboard processor that are mission independent.

Some of these results are presented here. The topics studied include data editing, residual smoothing, fading of the filter memory, clock modeling, state process noise covariance modeling, and GPS selection.

As an aid to the use and evaluation of GPS pseudorange and delta pseudorange observations, the capabilities to simulate and use these observation types were built into the Research and Development Goddard Trajectory Determination System (R&D GTDS). GPS observation can be simulated with R&D GTDS for both ONPAC and R&D GTDS use.

An overview of the steps involved in simulation and use of GPS data are summarized in Figure 1. Both truth model information and simulated data are passed to the ONPAC program. There, the orbit estimation is done, and the estimated trajectory is compared to the truth model.

DATA SIMULATION

The force model used in generating the true user ephemeris can be selected from the options available to the R&D GTDS EPHEM program (Reference 4). These include geopotential harmonic coefficients (up to 21-by-21), drag, solar radiation pressure, and perturbations from the Sun, the Moon, and the other planets.

Data simulation options for parameters affecting the data accuracy are listed in Figure 2. It should be noted that GPS satellites can be scheduled for specific subsets of the total simulation time span. If a GPS satellite is scheduled for observations only during periods when it is not visible, it is "scheduled out" of the data set. The default inclination will also be a modifiable option in the future.

The information passed to ONPAC is summarized in Figure 3. Because all the computations in ONPAC are done in the Earth-centered Earth-fixed (ECEF) coordinate system, this information is in ECEF coordinates.
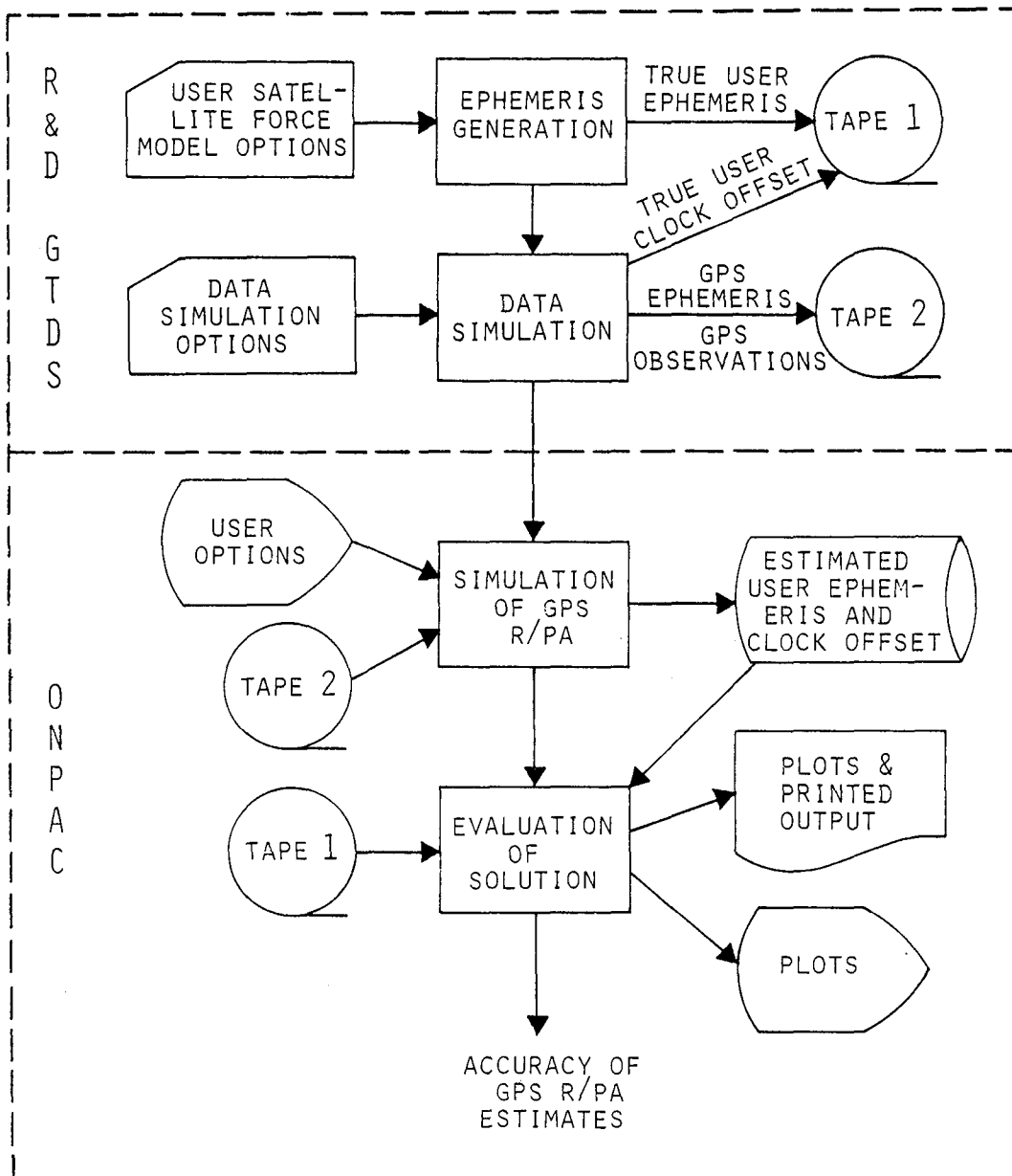
Figure 1. Overview of Analysis Approach

140

- USER CLOCK ERROR MODEL OPTIONS:

  - NO ERROR
  - QUADRATIC
  - RANDOM WALK

- OBSERVATION MEASUREMENT ERRORS

- GPS CLOCK ERROR MODEL OPTIONS:

  - NO ERROR
  - CONSTANT BIAS, UNCORRELATED
  - CONSTANT BIAS, CORRELATED (I.E., ALL GPS
    CLOCKS HAVE THE SAME ERROR)

- GPS CONFIGURATION OPTIONS:

  - 1 TO 24 GPSs (DEFAULTS: 6 IN PHASE I, 12 IN
    PHASE II, 24 IN PHASE III)
  - 3 ORBIT PLANES
  - ALL ORBITS CIRCULAR; INCLINATION = 63 DEGREES;
    12-HOUR PERIODS

- GPS DATA SPACING OPTIONS:

  - Δt_1 (FROM 0 TO $\Delta 0$)
  - Δt_2 (FROM GPS n TO GPS n+1)
  - Δt_3 (FROM LAST GPS IN CONSTELLATION TO GPS #1)

- GPS SELECTION:

  - ALL OBSERVABLE
  - GEOMETRIC DILUTION OF PRECISION (GDOP)
  - EACH GPS MAY BE SCHEDULED FOR SUBSET(S)
    OF THE TOTAL SIMULATION TIME SPAN

- GPS EPHEMERIS ERROR OPTIONS:

  - NONE
  - RANDOM CONSTANTS FOR RADIAL AND CROSS-TRACK
    (H,C); LINEARLY INCREASING ALONG-TRACK (L) TO
    A RANDOMLY SELECTED MAXIMUM:

    -- UNCORRELATED
    -- ORBIT-WISE CORRELATED
    -- TOTALLY CORRELATED

  - SINUSOIDAL:

    -- INPUT IS H,C,L AMPLITUDES, PERIOD (P),
       AND ALONG-TRACK RATE ($\dot{L}$)

    -- DIFFERENT PHASE OFFSET FOR EACH GPS,
       COMPUTATION BASED ON NUMBER OF GPSs
       IN THE CONFIGURATION

Figure 2. R&D GTDS GPS Data Simulation Options

141

FOR EACH OBSERVATION:

t_{OBS} = TIME OF OBSERVATION (INCLUDING USER CLOCK OFFSET)

$T(t_k)$ = USER CLOCK OFFSET = $t_{OBS} - t_k$

$T^D(t_k)$ = USER CLOCK DRIFT AT t_k

ρ_{OBS} = "OBSERVED" OBSERVATION (PSEUDORANGE)

ρ = TRUE OBSERVATION (PSEUDORANGE)

$\Delta\rho_{OBS}$ = "OBSERVED" OBSERVATION (DELTA PSEUDORANGE)

$\Delta\rho$ = TRUE OBSERVATION (DELTA PSEUDORANGE)

$\underline{S}_{GPS}, \underline{\dot{S}}_{GPS}$ = GPS POSITION AND VELOCITY VECTORS IN ECEF
              COORDINATES, INCLUDING THE EFFECT OF GPS
              EPHEMERIS ERRORS

$\underline{r}, \underline{v}$ = TRUE USER POSITION AND VELOCITY VECTORS IN
              ECEF COORDINATES

GPS SATELLITE IDENTIFICATION

TRUTH MODEL INFORMATION PROVIDED DURING DATA GAPS

Figure 3. Simulated Data Produced for ONPAC From R&D GTDS

142

ONPAC ESTIMATION

The ONPAC estimation is done with the UDU^T form of the EKF, as described in the mathematical specifications (Reference 5). The estimation process is briefly described in Figure 4. The a priori state and covariance matrix can be either the values from the last observation processed or the input values. The integration of the satellite equations of motion is done with a modified Euler integrator. The state transition matrix is computed with a Taylor series approximation. Studies have demonstrated that these propagation techniques have sufficient accuracy for nearly circular orbits for the filter as long as the propagation stepsize is held small, i.e., less than 10 seconds.

The ONPAC state vector is given in Figure 5. The clock bias and bias rate are estimated in position and velocity coordinates as the clock offset and drift times the speed of light. The user can select all nine members as the solve-for state, drop the drag and estimate only eight parameters, or drop the drag and clock drift and estimate seven parameters.

Parameters that can be varied in the ONPAC program are listed in Table 1. The force model options for the user satellite are the Earth geopotential up to the 5-by-5 harmonics, rotation terms, and drag. The state transition matrix is computed with a Taylor series approximation and has only a two-body geopotential contribution plus rotation and drag terms. The effect of even further limitations to this force model can be studied, as can the effect of the integrator stepsize. A tunable parameter study can be done with variations of the process noise parameters, the fading memory smoothing factor, maximum values for the memory factor and the residual, and the observation measurement noise.

RESULTS

As part of the autonomous orbit determination evaluation, an experimental R/PA will be placed on Landsat-D. The proposed Landsat-D orbit was used in studies of the orbit determination.
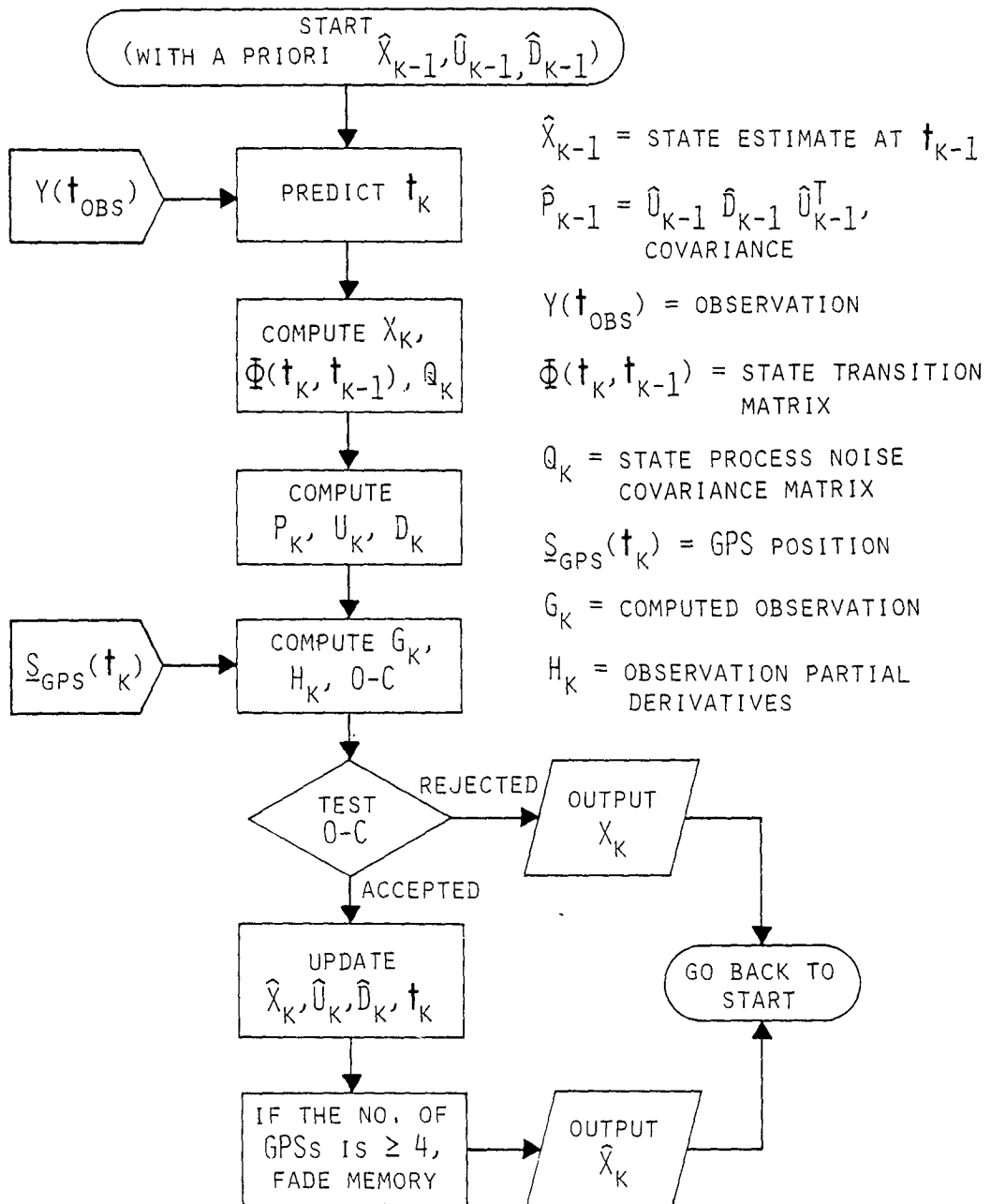
Figure 4. ONPAC Estimation Algorithm

$$
\underline{X} \;=\; \begin{bmatrix} X \\ Y \\ Z \\ B \\ \dot{X} \\ \dot{Y} \\ \dot{Z} \\ \dot{B} \\ D \end{bmatrix}
\begin{array}{l}
\left.\begin{array}{l} \\ \\ \end{array}\right\} \text{CARTESIAN POSITION COMPONENTS IN EARTH-CENTERED, EARTH-FIXED (ECEF) COORDINATES} \\[1em]
\;\; \text{CLOCK BIAS} \\[0.5em]
\left.\begin{array}{l} \\ \\ \end{array}\right\} \text{CARTESIAN VELOCITY COMPONENTS IN ECEF COORDINATES} \\[1em]
\;\; \text{CLOCK BIAS RATE} \\[0.3em]
\;\; \text{DRAG COEFFICIENT}
\end{array}
$$

$$
D \;=\; \frac{C_D \, A_{CX}}{2M}
$$

WHERE A_{CX} = CROSS-SECTIONAL AREA OF THE SATELLITE

M = MASS OF THE SATELLITE

C_D = CONSTANT COEFFICIENT

Figure 5. ONPAC State Vector

145

Table 1. User Options in ONPAC

TYPE	OPTION	ADJUSTABLE PARAMETERS
ACCELERATION MODEL		
GEOPOTENTIAL	–	DEGREE & ORDER, 2-BODY TO 5x5
ATMOSPHERIC DRAG	ON/OFF	TIME CONSTANT, τ_d
EKF ALGORITHM		
RESIDUAL TEST FOR ACCEPTANCE	ON/OFF	p_{MAX}
FADING MEMORY	ON/OFF	β, p_2
PROCESS NOISE	ON/OFF	a^2, q_a, q_b, q_d
SOLVE-FOR PARAMETERS	INCLUDE/EXCLUDE DRAG PARAMETER	–
OBSERVATION MEASUREMENT NOISE	–	σ_ρ^2, $\sigma_{\Delta\rho}^2$
STATE TRANSITION MATRIX	–	ORDER OF APPROXIMATION TO Δt^3
INTEGRATOR	–	STEP SIZE
USER CLOCK	–	TIME CONSTANT, τ_f

Initial conditions for Landsat-D and the GPS satellites are given in Figure 6. The GPS satellites constitute the default Phase I configuration. Since the launch of Landsat-D is expected during the early phases of the GPS, efforts were concentrated on orbit determination using the Phase I and subsets of the Phase I configuration.

Sample results are presented with four different sets of simulated data for October 1, 1980, 0 hours to 6 hours Universal Time (UT). The data simulation options used in common for these data sets are given in Figure 7.

The ONPAC options used for four sample cases used with these data sets are given in Table 2. In addition, all runs were done using a 5-by-5 geopotential, drag in the force model, a state transition matrix approximated to Δt^3, and a 3-second stepsize. The level of process noise used was found from tunable parameter studies to give the best results during periods of poor visibility.

Figure 8 shows the root-sum-square (RSS) position error for the baseline case and the Phase I visibility over the 6 hours of the data span. During periods when the fading memory is used and four or more GPS satellites are in view, the RSS position error is less than 10 meters. The curve has a "flat bottomed" appearance found to be characteristic of the cases when fading memory is used.

The studies discussed here have shown that the best results occur when the fading memory is tuned to the periods of good GPS visibility and the process noise covariance to periods of poor GPS visibility. The fading memory multiplies the covariance matrix and inflates the entire matrix, whereas the process noise is additive to certain terms of the covariance. The fading memory swamps the effect of the process noise when they are used together.

Cases 2 and 3, whose RSS errors are shown in Figure 9, are done with data sets B and C, which include GPS clock bias errors. The GPS satellites are selected with the geometric dilution of precision (GDOP) procedure, which, when six or more GPS satellites are in view, picks for observation only those

LANDSAT-D INITIAL CONDITIONS

Semimajor axis	7086.901 kilometers
Eccentricity	0.001
Inclination	98.181 degrees
Longitude of ascending node	354.878 degrees
Argument of perigee	180.000 degrees
Mean anomaly	0.000 degrees
Period	98.956 minutes

GPS CONFIGURATION AND INITIAL CONDITIONS

PHASE I CONFIGURATION

Inclination	63 degrees
Eccentricity	0.0
Satellites 1, 2, 3:	
- Longitude of ascending node	120 degrees
- Mean anomalies	100, 140, 180 degrees
Satellites 4, 5, 6:	
- Longitude of ascending node	240 degrees
- Mean anomalies	60, 100, 140 degrees
Period	12 hours

Figure 6. Initial Conditions

148

LANDSAT-D FORCE MODEL:

- 8x8 GEOPOTENTIAL
- LUNI-SOLAR PERTURBATIONS
- DRAG
- SOLAR RADIATION PRESSURE

QUADRATIC USER CLOCK ERROR:

- T_1 = 3.3360 x 10^{-5} SECONDS
- T_2 = 3.475 x 10^{-10} SECONDS/SECOND
- T_3 = 5.0 x 10^{-16} SECONDS/SECOND^2

OBSERVATION SPACING:

- Δt_1 = 0.6 SECOND
- Δt_2 = 6 SECONDS
- Δt_3 = 6 SECONDS

OBSERVATION STANDARD DEVIATIONS:

- σ_ρ = 2.0 METERS
- $\sigma_{\Delta\rho}$ = 1.7 CENTIMETERS

OPTIONS VARIED:

- GPS EPHEMERIS ERROR MODEL
- GPS CLOCK BIAS
- GPS CONFIGURATION AND SELECTION

Figure 7. Data Simulation Options Used for Data
Sets A, B, C, and D From R&D GTDS

Table 2. ONPAC and Data Simulation Options Used in Sample Cases

CASE	FADING MEMORY PARAMETERS	σ_ρ	DATA SET	GPS EPHEMERIS ERROR MODEL	GPS CLOCK BIAS	SELECTION
BASELINE CASE						
TEST CASE 1 (3507)	$\beta = 0.2$ $p_2 = 2.0$	8.1 M	A	RANDOMLY SELECTED $(\sigma_H, \sigma_C, \sigma_L) =$ (5M, 5M, 10M)	NONE	PHASE I, ALL
FADING MEMORY/GPS CLOCK BIAS						
TEST CASE 2 (4010)	$\beta = 0.2$ $p_2 = 1.05$	7.5 M	B	SINUSOIDAL $(H,C,L,\dot{L}) = (5M,5M,$ $10M,0.05M/SEC)$ $P = 24$ HOURS	CORRELATED $T_G = 3$ NS	PHASE I, GDOP
TEST CASE 3 (4011)	NOT USED	7.5 M	C	SINUSOIDAL $(H,C,L,\dot{L}) = (5M,5M,$ $10M,0.05M/SEC)$ $P = 12$ HOURS	UNCORRELATED $\sigma_{T_G} = 3$ NS	PHASE I, GDOP
EFFECT OF FOUR IN CONSTELLATION						
TEST CASE 4 (8102)	$\beta = 0.2$ $p_2 = 2.0$	8.1 M	D	SAME AS C ABOVE	NONE	# 2,3,5,6 IN PHASE I

ROOT SUM SQUARE OF POSITION ERROR
FOR BASELINE CASE (DATA SET A)
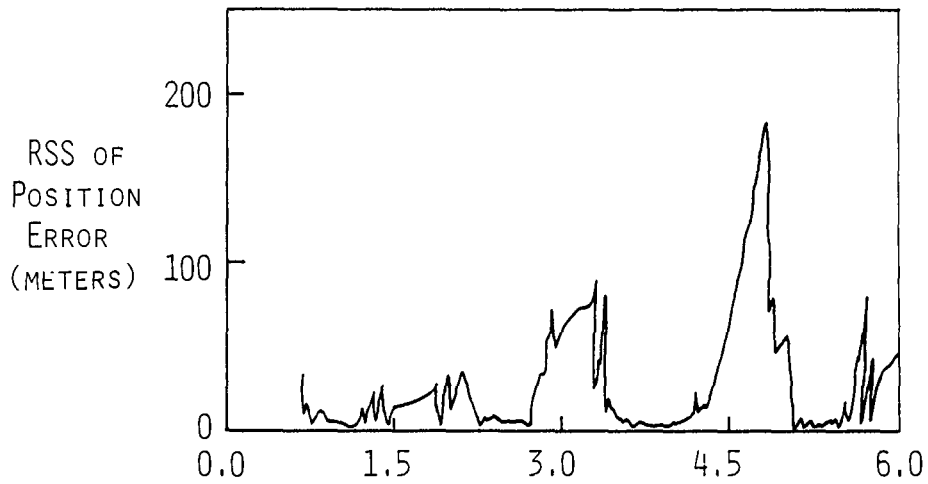
PHASE I - GPS SATELLITE VISIBILITY
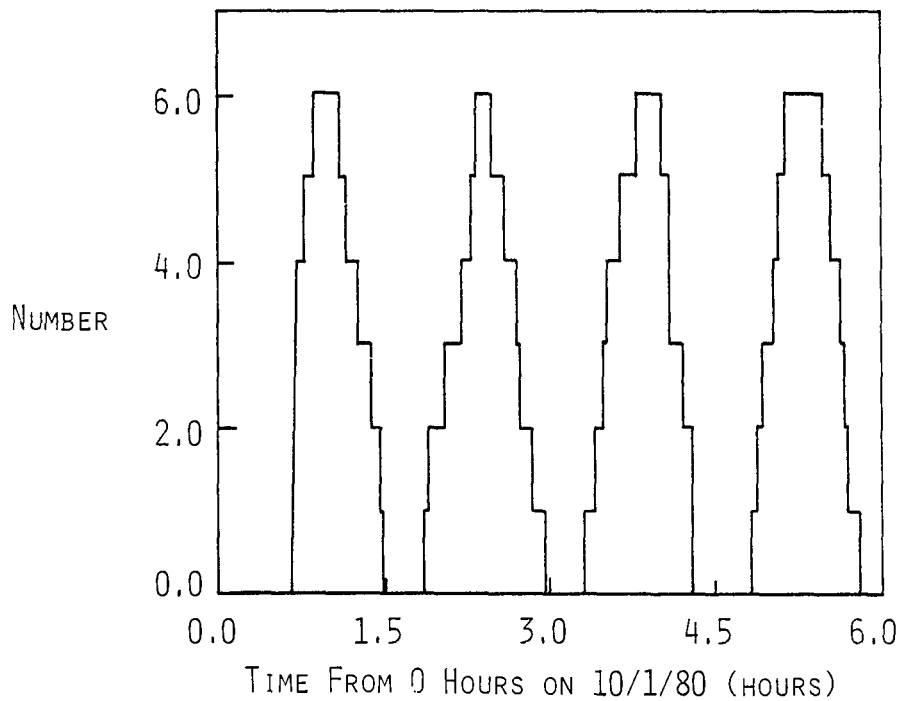
Figure 8. Baseline Case and Visibility

ROOT SUM SQUARE OF POSITION ERROR
FOR TEST CASE 2 (DATA SET B)
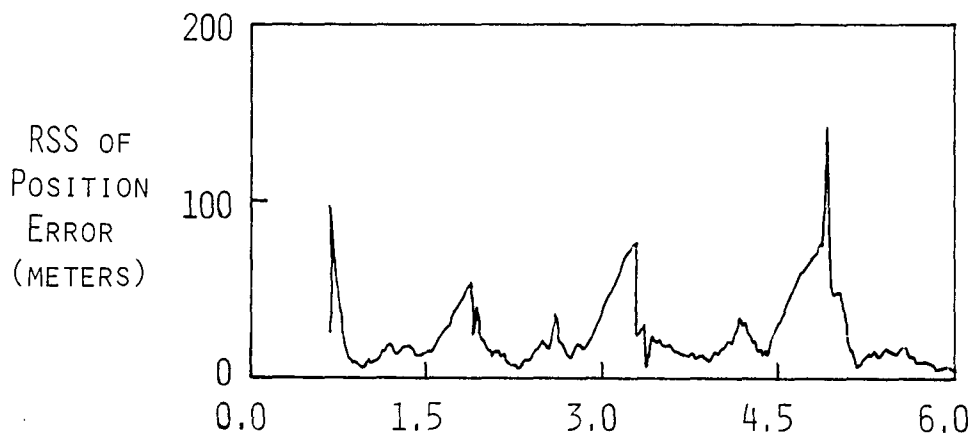
ROOT SUM SQUARE OF POSITION ERROR
FOR TEST CASE 3 (DATA SET C)
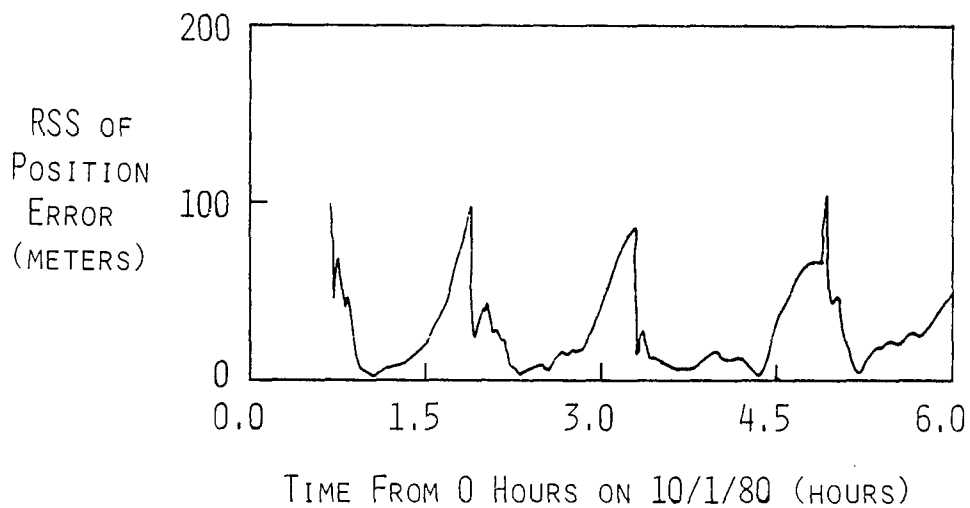
Figure 9. Root-Sum-Square Position Errors of Test Cases 2 and 3

152

four with the best geometric distribution. If four or fewer are visible, those seen are picked for observation.

The effect of the GPS clock bias error is to increase the baseline case RSS position error during periods of good visibility. The fading memory option used in case 2 causes the RSS error to drop to the minimum value more quickly than in case 3 at periods of good visibility and makes the curve plotted flatter than that in case 3. Study of the correlated versus the uncorrelated GPS clock errors shows very little difference in their effects.

Data set D was simulated using only four GPS satellites from Phase I: satellites 2 and 3 in one plane and satellites 4 and 5 in another. Figure 10 shows the visibility and GDOP for this data set. Test case 4, whose RSS error is shown in Figure 11, was run using this data set. The RSS position error grows to more than 300 meters during the data gaps, and the user clock is poorly estimated when fewer than four GPS satellites are visible. Given that the error in the data and the GPS ephemeris is approximately 7 meters, the GDOP from Figure 10 would predict an error in the position determination of 35 meters or more when four GPS satellites are visible. The results in test case 4 are in the 25-through-35-meter range at times of good visibility, within the range predicted by the GDOP.

CONCLUSIONS

The conclusions of the studies are given below.

- The algorithms used are sufficient for accurate orbit determination.

- The errors in orbit estimation are less than those predicted from the GDOP.

- Accurate orbit determination is possible with only four GPS satellites in the constellation.

- The orbit determination accuracy is limited by the GPS ephemeris and clock accuracies.

153

GDOP OF GPSs # 2, 3, 5, 6 FROM
R&D GTDS PHASE I (DATA SET D)
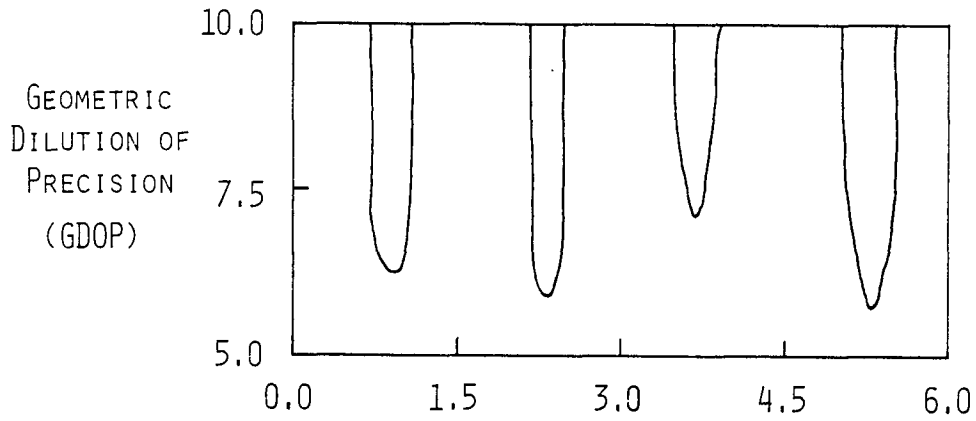
GPS VISIBILITY FOR DATA SET D

TIME FROM 0 HOURS ON 10/1/80 (HOURS)
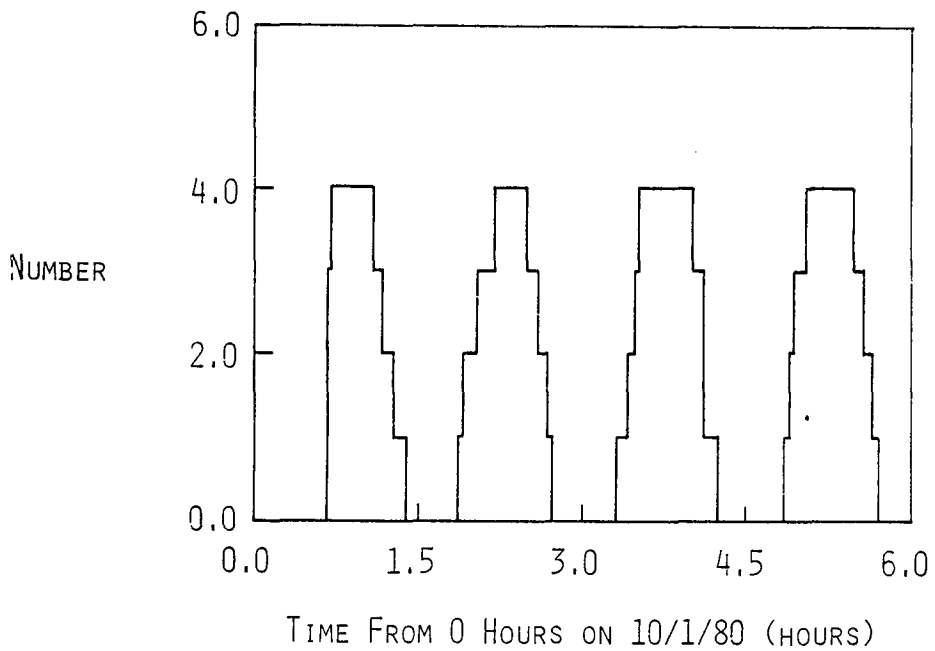
Figure 10. GDOP and Visibility of Data Set D

154

TRUE-ESTIMATED CLOCK BIAS FOR TEST CASE 4 (DATA SET D)
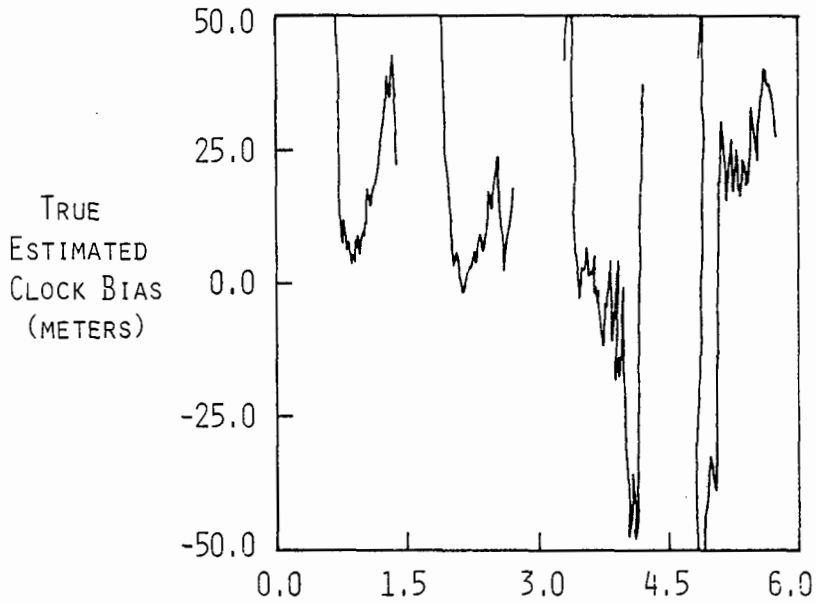
ROOT SUM SQUARE OF POSITION ERROR
FOR TEST CASE 4 (DATA SET D)
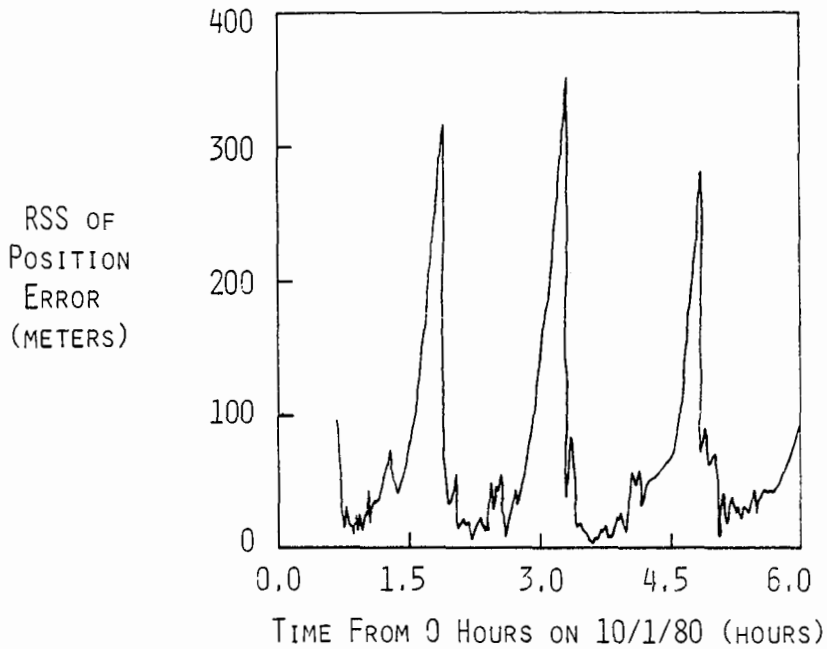
Figure 11.   Clock and Position Errors of Test Case 4

- The fading memory enhances the orbit determination accuracy, especially when the a priori knowledge of the user clock offset is poor.

All computations have been done in double precision; the effect of performing some operations in single precision has not yet been investigated.

The studies discussed here have shown that the filter is not overly sensitive to the tunable parameters. The results presented are typical of the results gathered from a range of parameter values.

ACKNOWLEDGMENTS

REFERENCES

1. A. J. Fuchs, W. H. Wooden, and A. C. Long, Autonomous Satellite Navigation With the Global Positioning System, (paper presented at AAS/ AIAA Astrodynamics Specialist Conference, Jackson Lake Lodge, Wyoming, September 1977)

2. W. H. Wooden and J. B. Dunham, Simulation of Autonomous Satellite Navigation With the Global Positioning System, (paper presented at AIAA/ AAS Astrodynamics Conference, Palo Alto, California, August 1978)

3. Magnavox Advanced Products Division, Technical Proposal for the Receiver/Processor Assembly to be Used in Conjunction With the Global Positioning System Navigation Satellites, June 30, 1976

4. Computer Sciences Corporation, Research and Development Goddard Trajectory Determination System (R&D GTDS) User's Guide (draft), August 1978

5. J. B. Dunham, Mathematical Specifications of the Onboard Navigation Package Simulator (ONPAC), CSC/SD-78/6002, December 1978

A PRECISION RECURSIVE ESTIMATE FOR
EPHEMERIS REFINEMENT (PREFER)

Bruce Gibbs
Business and Technological Systems, Inc.

ABSTRACT

PREFER is a filter/smoother program for orbit determination which is used to refine the ephemerides produced by a batch least squares program (e.g., CELEST). PREFER requires, as input, a file containing the nominal satellite ephemerides and the state transition matrices as generated by CELEST. PREFER interpolates from this file at the times given on the Measurement Data file and processes the measurements in the Kalman filter to estimate the corrections to the nominal trajectory. The filter state also includes other parameters which have an effect upon the orbit determination (e.g., drag, perturbing gravitational accelerations, thrust, measurement biases and refraction parameters, etc.). Because PREFER is estimating the corrections to the nominal values, all partials are evaluated about the nominal trajectory and the filter is linear (not extended).

The measurement data types which PREFER can process include ground range, range difference and Doppler measurements, GPSPAC pseudorange and pseudodelta-range measurements, NAVPAC range difference measurements and altimeter measurements. A GPS Trajectory file supplies the ephemerides of the GPS satellites which are required to process the GPSPAC or NAVPAC measurements. A unique feature of the program is the capability to estimate hundreds of pass-disposable, measurement biases while using storage and computation for only a few biases.

After running the Kalman filter forward to the end of the Measurement Data file, PREFER performs optimal smoothing. A file created by the Kalman filter is read backward in time and the smoothed estimates are obtained by using the recursive formulation of Rauch-Tung-Striebal.

The combination of a Kalman filter and a smoother should result in greatly improved estimates of satellite ephemerides as compared to the batch estimation. Batch estimation is subject to errors because of errors in the dynamic models (e.g., gravitational). A filter/smoother which properly accounts for dynamic (state) noise should weight the data optimally and reduce the estimation errors. Smoothing will produce better estimates (in the middle of the data span) than just a forward filter because past and future data is used to estimate the state at each point in time (a filter uses only past data). Smoothing also tends to average out any dynamic modeling errors which remain.

PREFER's capability for improving orbit determination has been demonstrated on simulated data which contained significant modeling errors. The nominal trajectory had errors as large as 53 meters and the GPS trajectory file had peak errors of 12 meters. However, the PREFER smoother estimate was usually accurate to 3 meters with peak errors of 8 meters. Even during data gaps, the smoothed radial error was always less than 6 meters.

INTRODUCTION

A recursive filter/smoother orbit determination program has been developed to refine the ephemerides produced by a batch orbit determination program (e.g., CELEST, GEODYN). PREFER can handle a variety of ground and satellite-to-satellite tracking types as well as satellite altimetry. It has been tested on simulated data which contained significant modeling errors and the results clearly demonstrate the superiority of the program compared to batch estimation.

Input

The input to the program consists of four files and card input. A file containing the nominal (batch estimate) host satellite ephemerides and the 6 by 6 state transition matrix (from epoch osculating elements to current cartesian elements) is interpolated at the times given on the measurement data file. A GPS trajectory file supplies the ephemerides of the GPS satellites which are required to process the GPSPAC or NAVPAC measurements. A sun/moon file supplies the data which is used in the earth motion model (for ground based measurements). The card input to the program specifies run constants (e.g., time intervals) and *a priori* standard deviations, state noise spectral densities, time constants, etc.

Measurement Types

PREFER can process the following types of measurements.

- Ground Tracking

    Satellite to ground range
    Ground laser range
    Satellite to ground range difference
    Ground Doppler

- Satellite-to-Satellite

    GPS pseudo range and pseudo delta range
    NAVPAC range difference

- Altimetry

    Range to center of earth.

Provisions have been made for handling 50 ground stations and 24 GPS satellites but only 4 ground stations and 15 GPS satellites can be simultaneously observable. This restriction is imposed because of a limitation on the total number of states. Since station position errors, measurement biases, refraction parameters, GPS position errors and timing biases can all be estimated, the state vector could become unwieldly. PREFER has the capability to estimate all these parameters while using storage and computation for only those parameters which are simultaneously observable. This is discussed in later sections. Thus, the limitation is on the number of simultaneously observable stations and GPS satellites. As a practical matter, this limitation is not very restricting since it is unlikely that more than four ground stations

159

would see a low altitude satellite. Furthermore, simulations have shown that for the 24 satellite GPS system, no more than 15 GPS satellites would be observable to a low altitude satellite (without encountering severe refraction problems).

The altimetry measurements are assumed to have been preprocessed with a nominal geoid model so that they are treated as a range to the center of the earth.

Dynamics

A list of the dynamic parameters which PREFER can estimate is given below:

1   Satellite semimajor axis at epoch
2   Satellite eccentricity x sin (argument of perigee) at epoch
3   Satellite eccentricity x cos (argument of perigee) at epoch
4   Satellite inclination at epoch
5   Satellite mean anomaly plus argument of perigee at epoch
6   Satellite right ascension of ascending node at epoch
7   Satellite drag coefficient
8   Perturbing gravitational acceleration (vertical)
9   Perturbing gravitational acceleration (cross-track)
10 Perturbing gravitational acceleration (along-track)
11 Acceleration of 1st thrust segment (vertical)
12 Acceleration of 1st thrust segment (cross-track)
13 Acceleration of 1st thrust segment (along-track)
14 Acceleration of 2nd thrust segment (vertical)
15 Acceleration of 2nd thrust segment (cross-track)
16 Acceleration of 2nd thrust segment (along-track)
17 Host satellite clock timing error
18 Host satellite clock drift rate
19 Altimeter bias.

The first 6 are epoch osculating elements. The drag coefficient, perturbing gravitational accelerations, host clock drift rate and altimetry geoid error (bias) are all assumed to be independent, first order Markov processes. This may not be strictly true but it is a reasonable approximation. The thrust accelerations are assumed to be constant since the thrust durations will be relatively short.

The state transition matrix for the entire system of dynamic parameters and measurement related biases is:

$$\Phi = \begin{bmatrix} \phi_1 & 0 \\ 0 & I \end{bmatrix}$$

where ϕ_1 is:

	OSCULATING ELEM.	C_D	GRAVITY ACCEL.	THRUST ACCEL. (2 SEGMENTS)	CLOCK BIAS & RATE	ALT. GEOID ERROR
OSCULATING ELEM. x, y, z, $\dot{x}$, $\dot{y}$, $\dot{z}$	(full block)	$e^{-\alpha t}$	(full block)	(full block)	0	0
C_D	0	$e^{-\alpha t}$	0	0	0	0
GRAV. ACCEL. A_H, A_C, A_L	0		$\begin{smallmatrix} e^{-\gamma t} & 0 & 0 \\ 0 & e^{-\gamma t} & 0 \\ 0 & 0 & e^{-\gamma t} \end{smallmatrix}$	0	0	0
THRUST T_{H_1}, T_{C_1}, T_{L_1}, T_{H_2}, T_{C_2}, T_{L_2}	0	0	0	$\begin{smallmatrix}1 \\ & 1 \\ & & 1 \\ & & & 1 \\ & & & & 1 \\ & & & & & 1\end{smallmatrix}$	0	0
CLOCK BIAS & RATE Δb, $\Delta \dot{b}$	0	0	0	0	$\begin{smallmatrix}1 & \Delta t \\ 0 & e^{-\gamma t}\end{smallmatrix}$	0
ALT. GEOID ERROR	0	0	0	0	0	$e^{-\gamma t}$

161

The upper left 6 x 6 partition of ϕ_1 is an identity matrix when Φ is being used to perform the time update on the state vector. However, when individual measurements are being processed, the satellite position and velocity in cartesian coordinates at the measurement time must be known. The nominal position and velocity and the transition matrix from epoch osculating to cartesian elements are obtained by interpolation from the host trajectory file. The filter state (which includes the estimated correction to the epoch osculating elements) is multiplied by ϕ_1 to obtain the estimated correction to the nominal cartesian elements.

The upper right partition of ϕ_1 (i.e., the transition from C_d, gravitational accelerations and thrust to cartesian elements) is obtained as an iterated, second order Taylor series. Since the integration time interval will be relatively short (less than 120 seconds) and state noise is included in the formulation, a highly accurate integration method is not required.

The state noise covariance matrix (required by the filter) is obtained by Taylor series integration of the input spectral density matrix.

Kalman Filter

Measurements are processed in a Kalman filter to estimate the corrections to the nominal trajectory. All partial derivatives are evaluated about the nominal trajectory and thus the filter is linear (not extended).

Since the program was intended to process many thousands of measurements, the execution time would have been excessive if the Kalman equations were evaluated for each measurement. Therefore, the measurements are processed in small "mini-batches" (typically 120

seconds), during which time, the dynamics are assumed to be deterministic. Only when proceeding from the epoch of one mini-batch to the next is state noise included in the covariance equations. The term "mini-batch" is intended to indicate the lack of state noise rather than the method of processing since the estimation algorithm is actually the recursive U-D algorithm of Bierman [1].

A unique feature of PREFER is the capability to estimate hundreds of pass-disposable measurement-related biases while using storage and computation for only a few. As measurement data from new stations or GPS satellites is processed, the state vector and covariance matrix are augmented with the *a priori* information for the new measurement parameters. When the station or GPS satellites are no longer visible to the host satellite, the parameters are dropped from the state vector and covariance matrix. These parameters can be deleted from the filter state since they will no longer have an influence on the estimation of "common" parameters (dynamic and other measurement related biases). However, the deletion of parameters from the filter state does complicate smoothing since the lost information must be reconstructed later. This is discussed in another section.

It should be noted that these hundreds of measurement related parameters are probably not observable in a statistical sense, i.e., *a priori* information is required to make the covariance matrix full rank. These parameters are included in the filter state primarily to assure proper weighting of the measurement data.

Figure 1 is a flow chart of the FILTER subroutine. This routine is called once for each mini-batch of data. The flow chart shows the sequence of events required to perform the time update, write information on the disk for smoothing, process data with the U-D algorithm and delete parameters from the filter state.
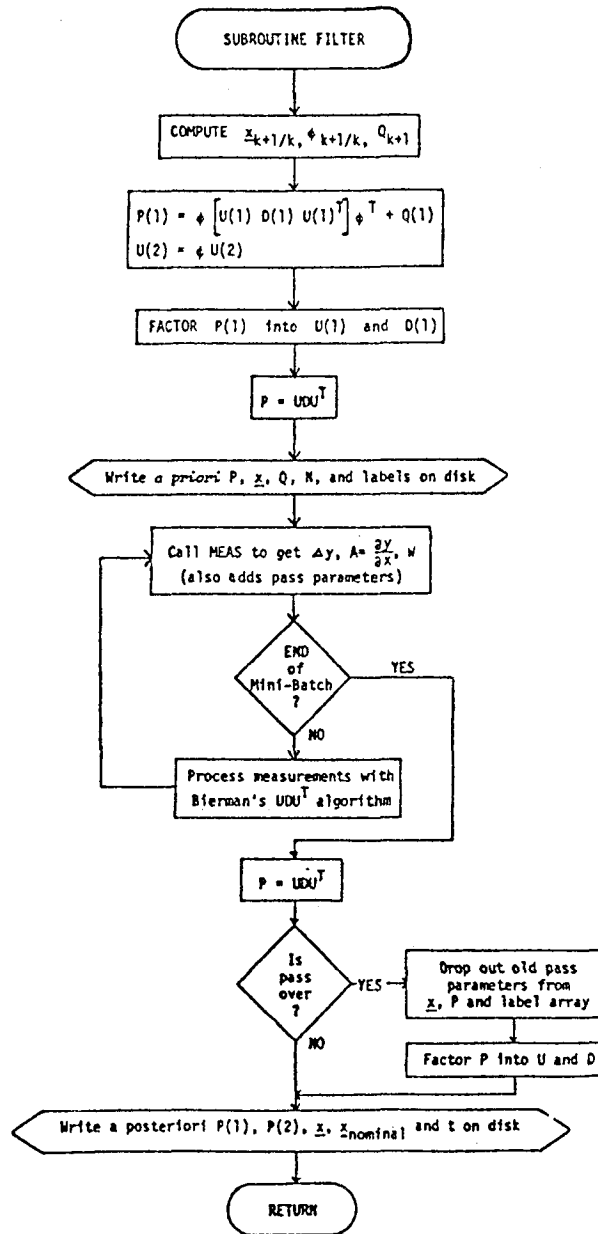
Figure 1 Filter Subroutine

Smoothing

Optimal smoothing is performed using the backward recursion developed by Rauch, Tung and Striebel [4]. The final estimate of the filter is used to initialize the smoother equations. The smoother gain matrix at time t_k is computed as:

$$G_k = \phi_{k+1}^{-1} (I - Q_{k+1} P_{k+1/k}^{-1}) .$$

Then the smoothed state vector and covariance are computed as:

$$\hat{\underline{x}}_{k/m} = \hat{\underline{x}}_{k/k} + G_k (\hat{\underline{x}}_{k+1/m} - \hat{\underline{x}}_{k+1/k})$$

$$P_{k/m} = P_{k/k} + G_k (P_{k+1/m} - P_{k+1/k}) G_k^T$$

where the notation $\hat{\underline{x}}_{i/j}$ means the estimate $\underline{x}$ at time t_i based upon measurements up to time t_j . In other words, $\hat{x}_{k+1/k}$ is the *a priori* estimate at time t_{k+1}, $\hat{\underline{x}}_{k/k}$ is the *a posteriori* estimate at time t_k and $\hat{x}_{k/m}$ is the smoothed estimate at time t_k (t_m is the last data point).

Notice that the gain matrix G_k has the following structure:

$$G_k = \begin{bmatrix} G(1) & G(2) \\ 0 & I \end{bmatrix}$$

where the partitioning indicated separates the dynamic parameters from the biases. Since the number of biases may be several times greater than the number of dynamic parameters, the multiplications by 0 or 1 are avoided in the coding.

Although Kalman filter formulations based upon covariance matrices are more prone to numerical problems than the factored filters, numerical problems are not so severe in the smoother. The smoother equations are only evaluated once per mini-batch rather than for each measurement. Furthermore, the equations for the smoothed $\underline{x}$ and P are uncoupled since the gain matrix only depends upon variables from the filter. Thus, errors in the smoothed P have no effect upon $\underline{x}$.

Disposable Pass Parameters in Smoothing

It is fairly well known that measurement bias parameters need only be included in the filter state during periods when data of the appropriate type is actually being processed. Outside the data interval, the solution for the pass parameters has no effect upon the solution for the common parameters.

We are not aware of any published reference which demonstrates that the "disposable parameter" approach is also valid for smoothing. Therefore, this section shows that the approach is valid and demonstrates how it is implemented for the present problem. The following derivation is basically the same as that given by Tanenbaum.[1]

Fraser and Potter [2] showed that the optimum smoother could also be derived as the linear combination of a forward filter which includes *a priori* information and a backward filter which does not include *a priori*. The results obtained from such a filter will be identical to those obtained by the RTS algorithm.

Consider the case shown in the figure where the forward filter has processed data from pass a but not b while the backward filter has processed data from b but not a .

---

[1]Tanenbaum, M., private communication, NSWC/Dahlgren, December 1977.
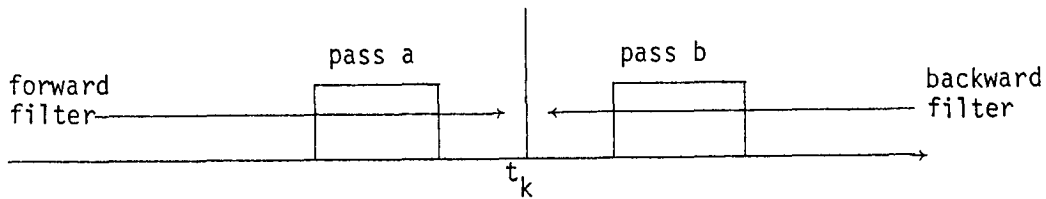
The filter states and covariances at time t are:

Forward   Backward

$$\underline{x}_k = \begin{bmatrix} \underline{x}_c \\ \underline{x}_a \\ 0 \end{bmatrix} \qquad\qquad \underline{x}'_k = \begin{bmatrix} \underline{x}_c \\ 0 \\ \underline{x}'_b \end{bmatrix}$$

$$\begin{bmatrix} P_{cc} & P_{ca} & 0 \\ P_{ac} & P_{aa} & 0 \\ 0 & 0 & \infty \end{bmatrix} \qquad \begin{bmatrix} P'_{cc} & 0 & P'_{cb} \\ 0 & \infty & 0 \\ P'_{bc} & 0 & P'_{bb} \end{bmatrix}$$

where subscript c denotes common parameters. Notice that the *a priori*
information for the pass b parameters of the foward filter is treated
as if it is a measurement which does not actually enter the forward
filter until the pass is begun. It can also be shown (with some dif-
ficulty) that similar results are obtained by allowing it to enter the
filter at the initial time. The smoothed covariance is obtained as a
minimum variance combination of the two estimates. Since the errors in
the two estimates are uncorrelated, the smoothed covariance is simply
the inverse of the sum of the two information matrices*

---

*Operations on matrices containing ∞ must be done with great care.
 The result can, however, be derived more rigorously.

167

$$P_{k/m} = (P_k^{-1} + P_k'^{-1})^{-1}$$

$$= \begin{bmatrix} (P_{cc}^{-1} + P_{cc}'^{-1})^{-1} & P_{cc}'(P_{cc} + P_{cc}')^{-1} P_{ca} & P_{cc}(P_{cc} + P_{cc}')^{-1} P_{cb}' \\ & P_{aa} - P_{ac}(P_{cc} + P_{cc}')^{-1} P_{ca} & P_{ac}(P_{cc} + P_{cc}')^{-1} P_{cb}' \\ & & P_{bb}' - P_{bc}'(P_{cc} + P_{cc}')^{-1} P_{cb}' \end{bmatrix}$$

Notice that the solution for the common parameters does not depend upon the pass parameters. Furthermore, the solution for pass a does not depend upon the pass b parameters (and vice versa). This verifies that it is not necessary to carry the pass parameters outside of the pass. However, we must also verify that the pass parameters can be "reconstructed" in the RTS formulation of the smoother.
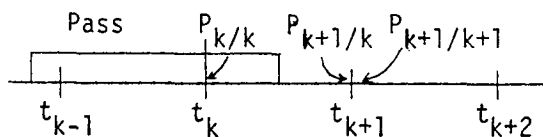
Consider the case shown in the figure. Assume that the smoothed values for t_k are to be computed. $P_{k/k}$ and $P_{k+1/k}$ from the forward filter have the same dimension but $P_{k+1/k+1}$ does <u>not</u> include the pass parameters. Obviously, the smooth covariance, $P_{k+1/m}$, is the same dimension as $P_{k+1/k+1}$. In the RTS equations, the difference $P_{k+1/m} - P_{k+1/k}$ must be computed but these two arrays are of different dimensions. Therefore, we examine whether the missing terms of ΔP can be reconstructed. Using the results from the forward-backward smoother, we find that:

$$P_{k+1/m} - P_{k+1/k} = \begin{bmatrix} \Delta P_{cc} & \mid & \Delta P_{cc}(P_{cc}^{-1}P_{ca}) & \mid & -\Delta P_{cc}(P_{cc}^{-1}P'_{cb}) \\ & \mid & & \mid & \\ & \mid & (P_{ac}P_{cc}^{-1})\Delta P_{cc}(P_{cc}^{-1}P_{ca}) & \mid & -(P_{ac}P_{cc}^{-1})\Delta P_{cc}(P_{cc}^{-1}P'_{cb}) \\ & \mid & & \mid & \\ & \mid & & \mid & -\infty \end{bmatrix}$$

where $\Delta P_{cc} = -P_{cc}(P_{cc}+P'_{cc})^{-1}P_{cc}$ is simply computed as the upper left partition of $P_{k+1/m} - P_{k+1/k}$.

When written in this form, it is obvious that ΔP_{k+1} is singular. This also shows that the "missing" terms of ΔP can be reconstructed by pre- or post-multiplying by the factor $P_{ac}P_{cc}^{-1}$ obtained from $P_{k+1/k}$. The rational for discarding pass parameters _after_ writing the filter _a priori_ to the disk should now be obvious.

By a similar procedure, we can also demonstrate that the pass parameter portion of $\underline{x}_{k+1/m} - \underline{x}_{k+1/k}$ can be reconstructed as

$$\Delta \underline{x}_{k+1} = \begin{bmatrix} \Delta \underline{x}_{cc} \\ (P_{ac}P_{cc}^{-1})\ \Delta \underline{x}_{cc} \end{bmatrix}_{k+1} .$$

The equation for the gain matrix requires that $P_{k+1/k}$ be inverted. It can be easily shown [3] that the same results for the smoothed $\underline{x}$ and P will be obtained whether or not the pass parameters are included in the gain computation. Thus, the final RTS equations used when reconstructing pass parameters are:

$$\underline{x}_{k/m} = \underline{x}_{k/k} + G'\ \Delta\underline{x}_{cc}$$

$$P_{k/m} = P_{k/k} + G'\ \Delta P_{cc}\ G'^{T}$$

where

$$G' = \begin{bmatrix} \phi_{cc}^{-1} \ (I - Q_{cc} P_{cc}^{-1}) \\ \\ P_{ac} P_{cc}^{-1} \end{bmatrix}_k$$

Examples

Two examples using simulated data are given to demonstrate the improved performance of PREFER. The first is relatively trivial in that no modeling errors were included. The test was made simply to evaluate the program response to an initial condition error. Table 1 summarizes the test case and Figure 2 displays the results. The filter position error was initially 20 meters. During the first data pass, the error was reduced to 7 meters but during the subsequent data gap, the error rose to 38 meters. After the first orbit, the filter error remained below 1 meter. However, the smoother position error was less than 1.2 meters for the _entire_ run. The smoother error is largest at epoch because the 1 sigma _a priori_ error is weighted into the solution.

The second example is a more rigorous test of the program. It includes some additional data types and also has significant force modeling errors. Table 2 summarizes the input and Figure 3 displays the results.

The filter estimate has peak errors of 63 meters (mostly cross-track) while the maximum error in the smoother estimate is 11.2 meters (mostly radial) at the epoch. The peak error in the filter estimate occurs at 30 to 40 minutes which corresponds to a minimum error in the nominal trajectory. Apparently the filter had an erroneous estimate of the gravitational accelerations at the time that a data gap occurred.

170

ORBIT   — 350-420 KM ALTITUDE, e = .005, 96.9⁰ INCLINA-
                            TION, 180 MINUTES (2 REVOLUTIONS)

MODEL ERRORS   — NONE (NOMINAL TRAJECTORY IS PERFECT)

TRACKING DATA   — 7 GROUND STATIONS, RANGE DATA ONLY, NO MEASURE-
                            MENT NOISE BUT DATA IS GIVEN A WEIGHT OF 1 METER

ADJUSTED PARAMETERS   — ORBITAL ELEMENTS, MEASUREMENT BIAS AND REFRAC-
                            TION PARAMETERS, STATION POSITION ERRORS

INITIAL CONDITIONS   — FILTER ESTIMATE OF SEMI-MAJOR AXIS AT EPOCH IS
                            PERTURBED BY 20 METERS (1σ)

A PRIORI STANDARD DEVIATIONS

    SEMI-MAJOR AXIS   — 20 M
    e *SIN* ω   — .00001 RADIAN
    e *COS* ω   — .00001 RADIAN
    INCLINATION   — .00001 RADIAN
    ℓ + ω   — .00001 RADIAN
    Ω   — .00001 RADIAN
    STATION BIAS   — 1 M
    STATION REFRACTION   — 0.5 M
    STATION POSITION   — 5 M (EACH COMPONENT)

STATE NOISE SPECTRAL DENSITY

    X, Y, Z   — .03 M/SEC$^{1/2}$

    Ẋ, Ẏ, Ż   — .3x10^{-4} M/SEC$^{3/2}$

Table 1 Summary of Test Case Number 1
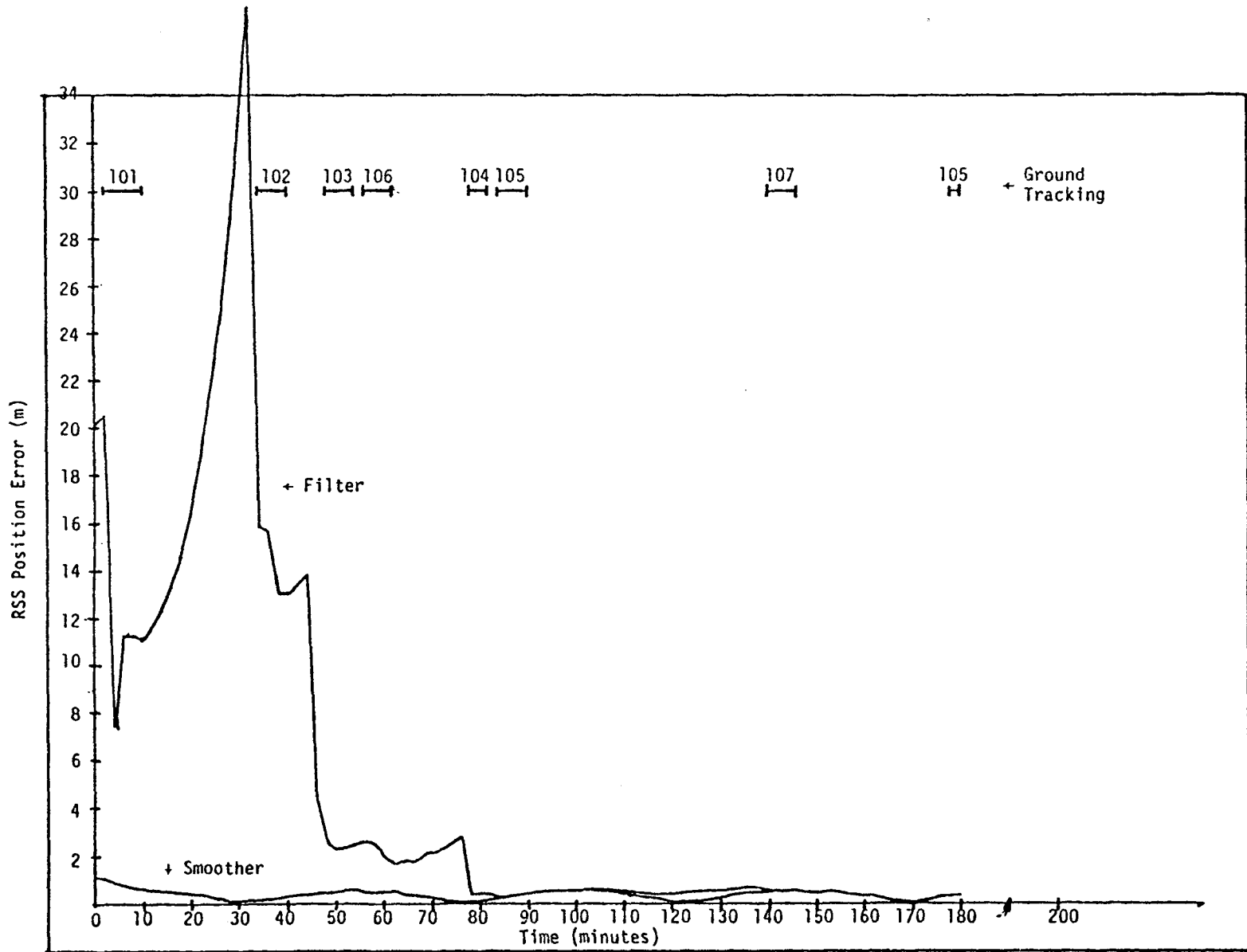
Figure 2 Error in Estimated Position for Example 1

ORBIT   - 165-264 KM ALTITUDE, $e = .0075$, 96.4^O INCLINATION,
                    192 MINUTES (2 REVOLUTIONS)

MODEL ERRORS   - MEASUREMENT DATA GENERATED USING A 25,25 GRAVITY
                    FIELD. NOMINAL TRAJECTORY WAS OBTAINED BY LEAST
                    SQUARES FITTING THE TRUE TRAJECTORY USING A 8,8
                    GRAVITY FIELD. THE RESULTING POSITION ERRORS ARE
                    LESS THAN 53 METERS. ALSO, SINUSOIDAL ERRORS WERE
                    ADDED TO THE POSITIONS ON THE GPS TRAJECTORY FILE.
                    THE STANDARD DEVIATIONS FOR THE PEAK ERRORS WERE:
                    10 METERS ALONG-TRACK, 6 METERS CROSS-TRACK AND
                    2 METERS RADIALLY.

TRACKING DATA   - 16 GROUND STATIONS: ALL HAVE RANGE DATA BUT TWO
                    ·ALSO HAVE RANGE DIFFERENCE AND ANOTHER TWO HAVE
                    DOPPLER DATA. DATA IS NOISELESS BUT IS GIVEN
                    WEIGHTS OF 1 METER (RANGE), 6 CM (RANGE DIFFERENCE)
                    AND 0.2×10^{-10} (DOPPLER). 6 GPS SATELLITES (PSEUDO
                    RANGE AND DELTA-RANGE). DATA HAS MEASUREMENT NOISE
                    OF 1.5 METERS (PSEUDO RANGE) AND 2 CM (PSEUDO DELTA-
                    RANGE). DATA IS WEIGHTED ACCORDINGLY.

ADJUSTED   - C_D, GRAVITATIONAL ACCELERATION, HOST CLOCK ERRORS,
  PARAMETERS   STATION MEASUREMENT BIASES AND REFRACTION, STATION
                    POSITIONS, GPS POSITIONS AND TIMING.

Table 2 Summary of Test Case Number 2

173
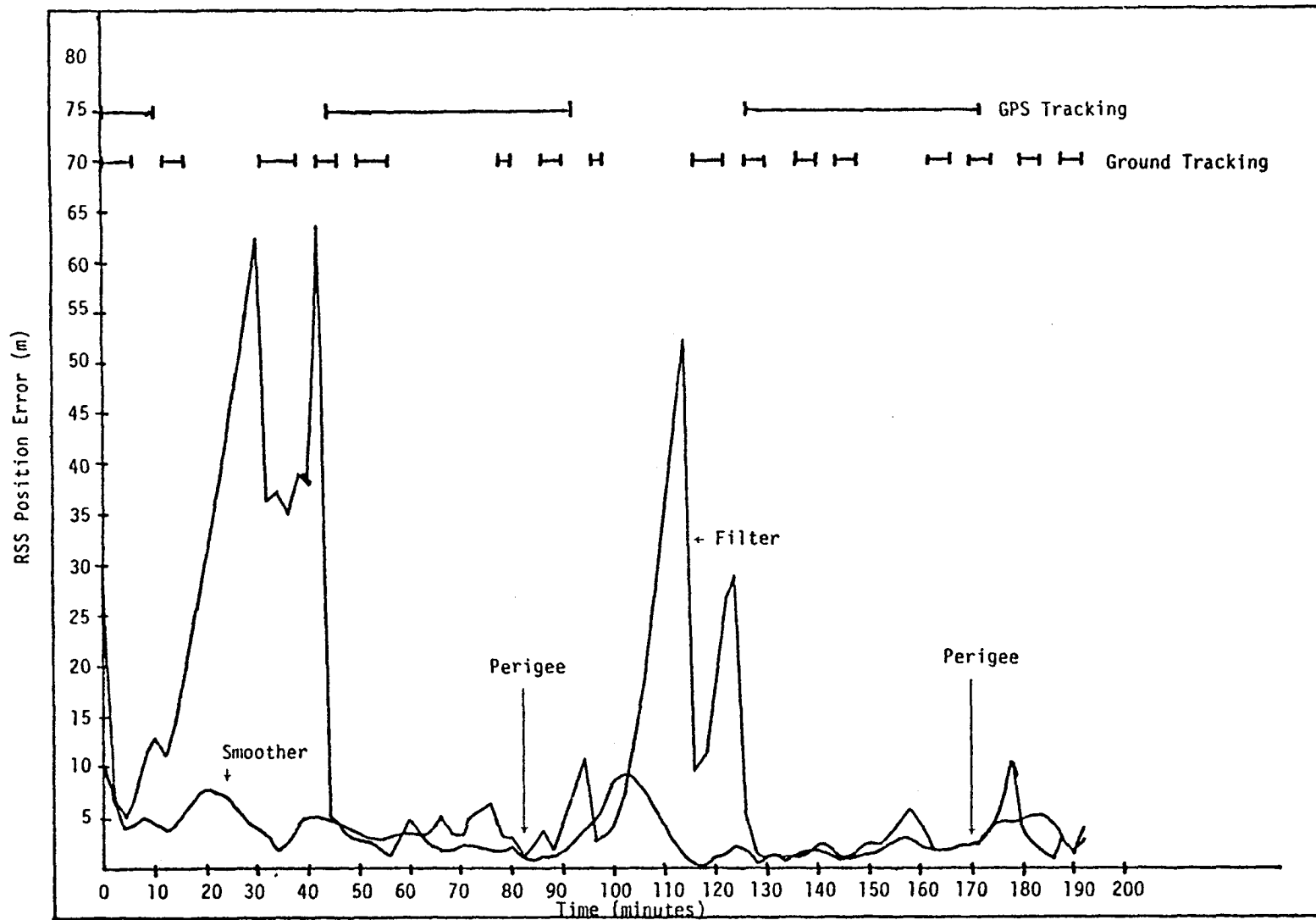
Figure 3 Error in Estimated Position for Example 2

174

Thus, the error quickly increased until more tracking was obtained. However, the filter covariance matrix during the data gaps was also large so that the smoother could correctly weight the filter estimates.

Notice that both the filter and smoother estimates are quite accurate during the periods when GPS tracking is available. During these periods, the smoother estimation error was generally less than three meters and the radial component was accurate to within 1.5 meters. Even during the data gaps, the smoother radial error did not exceed 6 meters (except at the epoch). This large error occurred at 102 minutes from epoch and the nominal trajectory at this time had a 50 meter cross-track error.

It should be noted that no great attempt was made to "fine tune" the input parameters for this example. Presumably the errors could be reduced further by the appropriate choice of state noise variances, time constants, etc.

Summary

The results of the various tests on simulated data demonstrate that PREFER has great potential for improving orbit determination of low altitude satellites.

References

1. Bierman, G. J., _Factorization Methods for Discrete Sequential Estimation_, Academic Press, 1977.

2. Fraser, D. C. and J. E. Potter, "The Optimum Linear Smoother as a Combination of Two Optimum Linear Filters", IEEE Transactions on Automatic Control, August 1969.

3. Gibbs, F. P., "Precision Recursive Estimator for Ephemeris Refinement (PREFER) Mathematical Description", Business and Technological Systems, Inc., TR-78-66, September 1978.

4. Rauch, H. E., F. Tung, and C. T. Striebel, "Maximum Likelihood Estimates of Linear Dynamic Systems", AIAA Journal, Vol. 3, No. 8, August 1965, pp. 1445-1450.

APPLICATION OF OPTIMUM SMOOTHING
FOR IMAGE DISTORTION CORRECTION

Ronald A. Werner
TRW Defense and Space Systems Group

ABSTRACT

Optimum linear smoothing is utilized to estimate certain distortions in Landsat-D images. Measurements that are processed by the smoother consist of designated control point locations within the images. Image distortions that are estimated by the smoother are those induced by Landsat-D satellite navigation errors and slowly-varying attitude and sensor alignment uncertainties. Preliminary results indicate that optimum smoothing produces substantially more accurate distortion estimates than optimum filtering and that optimum smoothing may reduce the number of control points needed to yield a desired image correction accuracy.

INTRODUCTION

Landsat-D is the next of a series of satellites designed to transmit imagery data to the ground to support earth resources management. The primary payload of Landsat D spacecraft is a thematic mapper (TM) and the secondary payload is a multispectral scanner. The mission objective is to produce high quality images of the earth surface for use in agriculture monitoring. The TM has seven spectral bands and 30 meter resolution. It scans the earth 185 km perpendicular to the spacecraft ground track at 7.4 hz rate; spacecraft motion provides the along-track scan. Digitized image data, along with spacecraft attitude measurements, are telemetered real time to the NASA/ Goddard ground station, where the data is processed to produce high precision images: ±5.5 meter (1σ) registration error and ±9.1 meter (1σ) total geometric error.

The raw image data contains distortions due to navigation error, attitude measurement error, and TM misalignment relation to the attitude reference axes. In order to remove these distortions from the image data and thereby achieve the precision images that are required, a Recursive Distortion Estimator (RDE) is designed to estimate the distortions. The measurements used by the RDE are based on locations of control points in the distorted image data, together with their known locations on the ground. The image of each control point is projected onto the ground. Distortion in the image causes the projected position of the control point to differ from its known true position. This difference in position is used by the RDE to estimate the distortion in the image data.

Reference 1 suggests a Kalman filter RDE. This document evaluates an optimum smoother RDE and compares its performance with that of a Kalman filter RDE.

SYSTEM DEFINITION

The system state variables X_i, i = 1 through 6, are defined as follows:

$$
\left.\begin{array}{c} X_1 \\ X_2 \\ X_3 \end{array}\right\} \text{Along-track, cross-track and vertical components of navigated position error}
$$

$$
\left.\begin{array}{c} X_4 \\ X_5 \\ X_6 \end{array}\right\} \text{Roll, Pitch, and yaw attitude measurement error plus instrument misalignment}
$$

$\dot{X}_7$
X_8 } Along-track, cross-track and vertical components of navigated velocity error
X_9

X_{10}
X_{11} } Roll, pitch, and yaw attitude measurement error drift rate plus instrument misalignment rate
X_{12}

The state differential equations are

$$\dot{X}_i = X_{i+6} \quad \text{for } i = 1 \text{ through } 6 \tag{1}$$

$$\dot{X}_i = \sum_{k=1}^{3} \frac{\partial g_{s_{i-6}}}{\partial X_k} X_k + z_i \quad \text{for } i = 7, 8, 9 \tag{2}$$

$$\dot{X}_i = a_i X_{i-6} + b_i X_i + z_i \quad \text{for } i = 10, 11, 12 \tag{3}$$

where g_{s_j} is the jth component of spherical (Keplerian) mass attraction acceleration for $j = 1, 2, 3$ and z_i is Gaussian uncorrelated white noise for $i = 7$ through 12. The coefficients in Equation 3 are $a_i = 0$ and $b_i = -0.00139 \text{ sec}^{-1}$ for $i = 10, 11, 12$. The standard deviation σ_{Zi} of each component of state noise z_i is: $\sigma_{Zi} = 1.52 \times 10^{-5} \text{ m/sec}^{3/2}$ for $i = 7$ and 8, $\sigma_{Z9} = 2.28 \times 10^{-5} \text{ m/sec}^{3/2}$ and $\sigma_{Zi} = 0.0213 \text{ } \mu\text{rad/sec}^{3/2}$ for $i = 10, 11, 12$.

The standard deviations σ_{X_i} of initial uncertainty in each state variable X_i is: $\sigma_{X_1} = 250\text{m}$, $\sigma_{X_2} = 50\text{m}$, $\sigma_{X_3} = 17\text{m}$, $\sigma_{X_i} = 291 \text{ } \mu\text{rad for } i = 4, 5, 6,$

$\sigma_{X_7} = 0.05$ m/sec, $\sigma_{X_i} = 0.02$ m/sec for i = 8, 9, and $\sigma_{X_i} = 0.4$ μrad/sec for i = 10, 11, 12.

The measurements y_1 and y_2 are defined as the along-track and cross-track deviations between the control point image projected onto the ground and true position of the control point. The standard deviation of the noise in each measurement is: $\sigma_{\omega_1} = 3.0$ m and $\sigma_{\omega_2} = 5.0$ m.

In addition to the slowly-varying sensor pointing error (caused by attitude measurement errors and sensor misalignment) that is estimated by the RDE, there is also an uncorrelated (white) pointing error which causes distortion in the image data. The standard deviation of the distortion caused by this random pointing error is 2.55m along-track and 4.73m cross-track.

DESCRIPTION OF SMOOTHING ALGORITHM

The equations for optimum linear smoothing are given in Chapter 6 of Reference 2. The smoothing algorithm utilized for the RDE is called a fixed-interval smoother in Reference 2.

METHOD OF ANALYZING SMOOTHING PERFORMANCE

The RDE performance is evaluated via linear statistical (covariance) analysis. Based on an assumed set of control point locations, the state error covariance matrix is propagated over the smoothing interval by the smoothing equations. The error covariance matrix for along-track and cross-track residual distortions are then computed at each point in the image, based on the state error covariance matrix at that point and the covariances of sensor random pointing errors.

Several cases that were analyzed were repeated assuming that the RDE is a Kalman (optimum) filter. This was done so that Kalman filter performance could be compared with optimum smoothing performance.

SUMMARY OF SMOOTHER PERFORMANCE ANALYSIS RESULTS

The results of this performance analysis show the smoothing algorithm yields substantially more accurate distortion estimation than a Kalman (optimum) filter for the identical case. Furthermore, the smoothing algorithm requires fewer control points to achieve a desired accuracy.

The results also show that the desired distortion compensation accuracy can be achieved with one control point every fourth scene for a series of 40 scenes or by having four control points uniformly distributed over a single scene.

REFERENCES

1. Caron, R. H., Simon, K. W., "Attitude Time-Series Estimator for Rectification of Space-Borne Imagery", Journal of Spacecraft and Rockets (12, 27), January 1975.

2. Meditch, J. S., Stochastic Optimal Linear Estimation and Control, McGraw-Hill Book Co., New York, 1969.

BACKGROUND INFORMATION

- LANDSAT-D SATELLITE TELEMETERS DIGITAL IMAGEY DATA FROM 705 Km ALTITUDE TO NASA/GODDARD GROUND STATION, WHERE IT IS PROCESSED TO PRODUCE PRECISION IMAGES OF THE EARTH SURFACE

- IMAGERY DATA IS PRODUCED BY A THEMATIC MAPER (TM) WHICH SCANS THE SURFACE OF THE EARTH 185 Km AT 7.4 Hz RATE PERPENDICULAR TO THE SATELLITE GROUND TRACK

- THE INSTANTANEOUS FIELD OF VIEW (IFOV) OF THE TM (ONE PICTURE ELEMENT (PIXEL)) IS 30 m x 30 m

- THE RAW IMAGERY DATA CONTAINS SLOWLY-VARYING DISTORTIONS DUE TO NAVIGATION ERROR, ATTITUDE MEASUREMENT ERROR, AND TM MISALIGNMENT, AS WELL AS UNCORRELATED (WHITE) RANDOM POINTING ERRORS

- SLOWLY-VARYING DISTORTIONS ARE ESTIMATED BY THE RECURSIVE DISTORTION ESTIMATOR (RDE) BY COMPARING THE LOCATIONS OF "CONTROL POINTS" IN A SCENE WITH THEIR KNOWN LOCATIONS ON THE GROUND

OBJECTIVES OF RDE

- ESTIMATE AND REMOVE DISTORTIONS FROM IMAGES SO THAT RESIDUAL DISTORTION IS NO GREATER THAN:

    ±5.5 m (1σ) SCENE-TO-SCENE REGISTRATION ERROR

    ±9.1 m (1σ) TOTAL GEOMETRIC CORRECTION ERROR

- MINIMIZE THE NUMBER OF GROUND CONTROL POINTS NEEDED TO ACHIEVE ACCURACY REQUIREMENTS

METHOD OF ANALYSIS

- LINEAR STATISTICAL (COVARIANCE) ANALYSIS

  - STATE ERROR COVARIANCE MATRIX PROPAGATED VIA SMOOTHING ALGORITHM

  - ERROR COVARIANCE MATRIX OF RESIDUAL ALONG-TRACK AND CROSS-TRACK
    DISTORTIONS COMPUTED BASED ON STATE ERROR COVARIANCE MATRIX AND
    STANDARD DEVIATIONS OF UNCORRELATED POINT ERRORS

- KALMAN (OPTIMUM) FILTER PERFORMANCE EVALUATED AS WELL AS OPTIMUM
  SMOOTHING PERFORMANCE

● SUMMARY AND CONCLUSIONS

- OPTIMUM SMOOTHING BY THE RDE PRODUCES SUBSTANTIALLY MORE ACCURATE DISTORTION ESTIMATION THAN OPTIMUM (KALMAN) FILTERING AND REQUIRES FEWER CONTROL POINTS TO ACHIEVE A DESIRED ACCURACY

- ONE CONTROL POINT EVERY FOUR SCENES YIELDS ONLY MODEST DEGRADATION IN ACCURACY RELATIVE TO HAVING ONE CONTROL POINT EVERY SCENE

- DESIRED DISTORTION CORRECTION ACCURACY CAN BE ACHIEVED IN A SINGLE SCENE BY HAVING FOUR CONTROL POINTS UNIFORMLY DISTRIBUTED OVER THE SCENE

185

SYSTEM DEFINITION

- STATE VECTOR DEFINITION:

$\left.\begin{array}{c} X_1 \\ X_2 \\ X_3 \end{array}\right\}$ ALONG-TRACK, CROSS-TRACK AND VERTICAL COMPONENTS OF NAVIGATED POSITION

$\left.\begin{array}{c} X_4 \\ X_5 \\ X_6 \end{array}\right\}$ ROLL, PITCH, AND YAW ATTITUDE MEASUREMENT ERROR PLUS INSTRUMENT MISALIGNMENT

$\left.\begin{array}{c} X_7 \\ X_8 \\ X_9 \end{array}\right\}$ ALONG-TRACK, CROSS-TRACK AND VERTICAL COMPONENTS OF NAVIGATED VELOCITY ERROR

$\left.\begin{array}{c} X_{10} \\ X_{11} \\ X_{12} \end{array}\right\}$ ROLL, PITCH, AND YAW ATTITUDE MEASUREMENT ERROR DRIFT RATE PLUS INSTRUMENT MISALIGNMENT RATE

- STATE DIFFERENTIAL EQUATIONS:

$$\dot{x}_i = x_{i+6} \quad \text{for } i = 1 \text{ through } 6$$

$$\dot{x}_i = \sum_{k=1}^{3} \frac{\partial g_{s_{i-6}}}{\partial x_k} x_k + z_i \quad \text{for } i = 7, 8, 9$$

$$\dot{x}_i = a_i x_{i-6} + b_i x_i + z_i \quad \text{for } i = 10, 11, 12$$

WHERE

$$a_i = 0, \ b_i = -0.00139 \ \text{sec}^{-1}$$

$$\sigma_{z_i} = 1.52 \times 10^{-5} \ \text{m/sec}^{3/2} \quad \text{for } i = 7, 8$$

$$\sigma_{z_9} = 2.28 \times 10^{-5} \ \text{m/sec}^{3/2}$$

$$\sigma_{z_i} = 0.0213 \ \mu\text{rad/sec}^{3/2} \quad \text{for } i = 10, 11, 12$$

- INITIAL STATE UNCERTAINTIES:

$$\alpha_{X_1} = 250 \text{ m}$$

$$\sigma_{X_2} = 50 \text{ m}$$

$$\sigma_{X_3} = 17 \text{ m}$$

$$\sigma_{X_i} = 291 \text{ } \mu\text{rad} \quad \text{for } i = 4, 5, 6$$

$$\sigma_{X_7} = 0.05 \text{ m/sec}$$

$$\sigma_{X_i} = 0.02 \text{ m/sec} \quad \text{for } i = 8, 9$$

$$\sigma_{X_i} = 0.4 \text{ } \mu\text{rad/sec} \quad \text{for } i = 10, 11, 12$$

- MEASUREMENT NOISE (FOR REGISTRATION):

$$\sigma_{\omega_1} = 3.0 \text{ m (ALONG-TRACK)}$$

$$\sigma_{\omega_2} = 5.0 \text{ m (CROSS-TRACK)}$$

- UNCORRELATED RANDOM POINTING ERRORS:

$$\sigma_{R1} = 2.55 \text{ m (ALONG-TRACK)}$$

$$\sigma_{R2} = 4.73 \text{ m (CROSS-TRACK)}$$

COMPARISON OF KALMAN FILTERING WITH OPTIMUM SMOOTHING

- REFERENCE CASE REFLECTS TEMPORAL REGISTRATION ACCURACY WITH THE ERROR MODELS DISCUSSED EARLIER AND ASSUMES ONE CONTROL POINT PER SCENE FOR TEN SCENES

- KALMAN FILTERING, AS WELL AS OPTIMUM SMOOTHING, IS EVALUATED FOR THE REFERENCE CASE

- THE STANDARD DEVIATION (IN METERS) OF RESIDUAL DISTORTION AT THE TIMES WHEN THEY ARE MINIMUM ARE SUMMARIZED AS FOLLOWS:

	KALMAN FILTERING			OPTIMUM SMOOTHING		
	RDE STATE ESTIMATION ERROR (1σ)	UN-CORRELATED POINTING ERROR (1σ)	TOTAL RESIDUAL DISTORTION (1σ)	RDE STATE ESTIMATION ERROR (1σ)	UN-CORRELATED POINTING ERROR (1σ)	TOTAL RESIDUAL DISTORTION (1σ)
ALONG TRACK	1.89	2.55	3.17	1.28	2.55	2.85
CROSS TRACK	2.81	4.73	5.50	1.85	4.73	5.08

- RESULTS PRESENTED SO FAR INDICATE ONLY MODEST IMPROVEMENT BY SMOOTH-
  ING RATHER THAN FILTERING. THIS IS BECAUSE THE STANDARD DEVIATIONS
  OF RDE ERRORS WERE TAKEN AT THE TIMES WHEN THEY ARE MINIMUM

- THE FIGURES BELOW SHOW DRAMATIC IMPROVEMENT IN RDE ACCURACY WHEN
  OPTIMUM SMOOTHING IS USED RATHER THAN KALMAN (OPTIMUM) FILTERING

- THESE PLOTS SHOW THAT FEWER CONTROL POINTS ARE NEEDED TO ACHIEVE THE
  REQUIRED ACCURACY IF THE RDE IS A SMOOTHER RATHER THAN A FILTER

- ALL THE RESULTS THAT FOLLOW ARE BASED ON THE ASSUMPTION THAT OPTIMUM
  SMOOTHING IS UTILIZED IN THE RDE
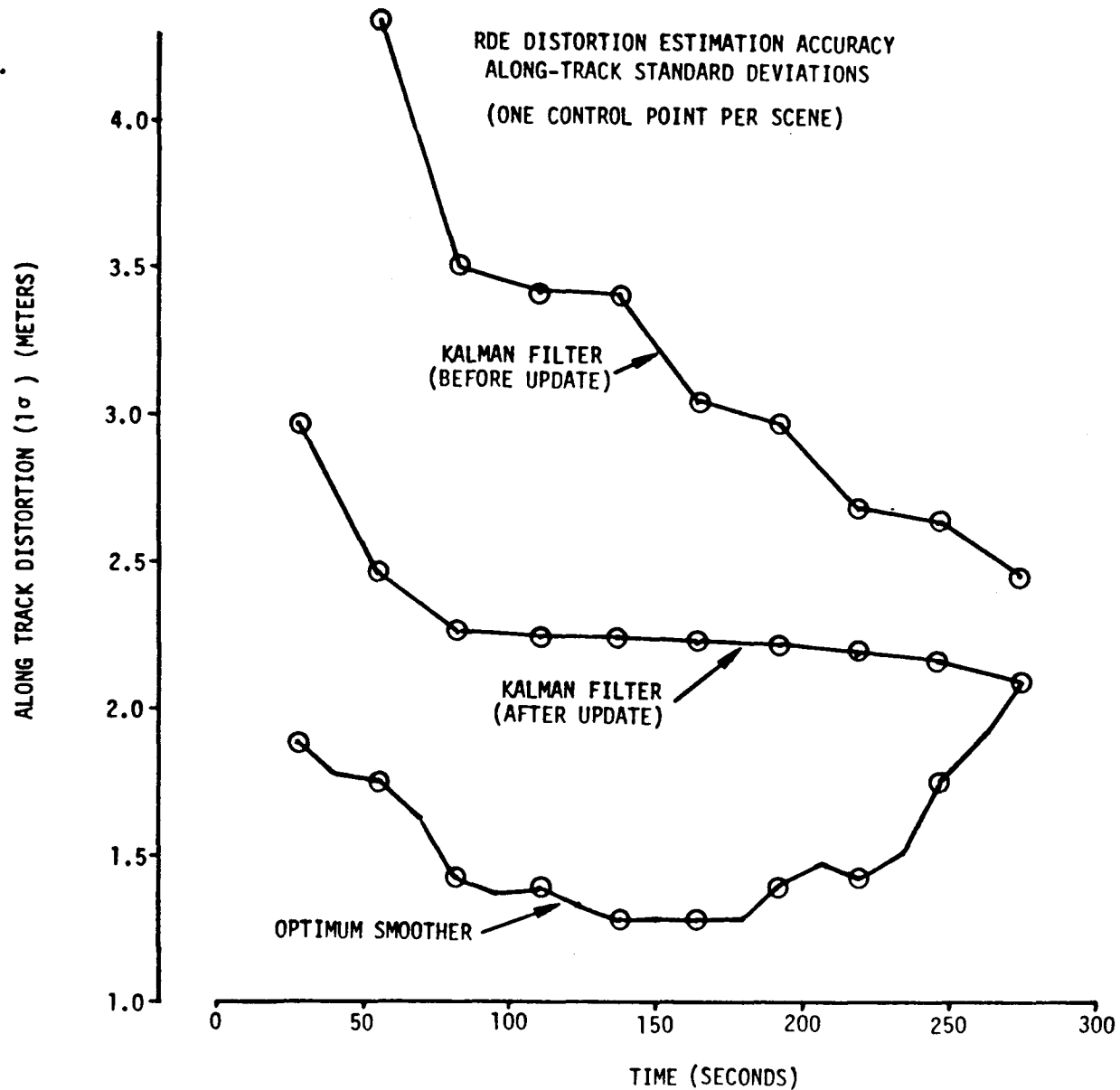
191

COMPARISON OF KALMAN FILTERING WITH OPTIMUM SMOOTHING (Continued)

RDE DISTORTION ESTIMATION ACCURACY
ALONG-TRACK STANDARD DEVIATIONS

(ONE CONTROL POINT PER SCENE)

KALMAN FILTER
(BEFORE UPDATE)

KALMAN FILTER
(AFTER UPDATE)

OPTIMUM SMOOTHER

ALONG TRACK DISTORTION (1σ) (METERS)

TIME (SECONDS)

192

RW-19

RDE DISTORTION ESTIMATION ACCURACY
CROSS-TRACK STANDARD DEVIATIONS

(ONE CONTROL POINT PER SCENE)

KALMAN FILTER
(BEFORE UPDATE)

KALMAN FILTER
(AFTER UPDATE)

OPTIMUM SMOOTHER

CROSS TRACK DISTORTION (1σ) (METERS)

TIME (SECONDS)

193

RW-20

COMPARISON OF KALMAN FILTERING WITH OPTIMUM SMOOTHING (Continued)

RDE DISTORTION ESTIMATION ACCURACY
ALONG-TRACK STANDARD DEVIATIONS
(FOUR CONTROL POINTS OVER ONE SCENE)

KALMAN FILTER
(BEFORE UPDATE)

KALMAN FILTER
(AFTER UPDATE)

OPTIMUM SMOOTHER

ALONG TRACK DISTORTION (1σ) (METERS)

TIME(SECONDS)

194

RW-21
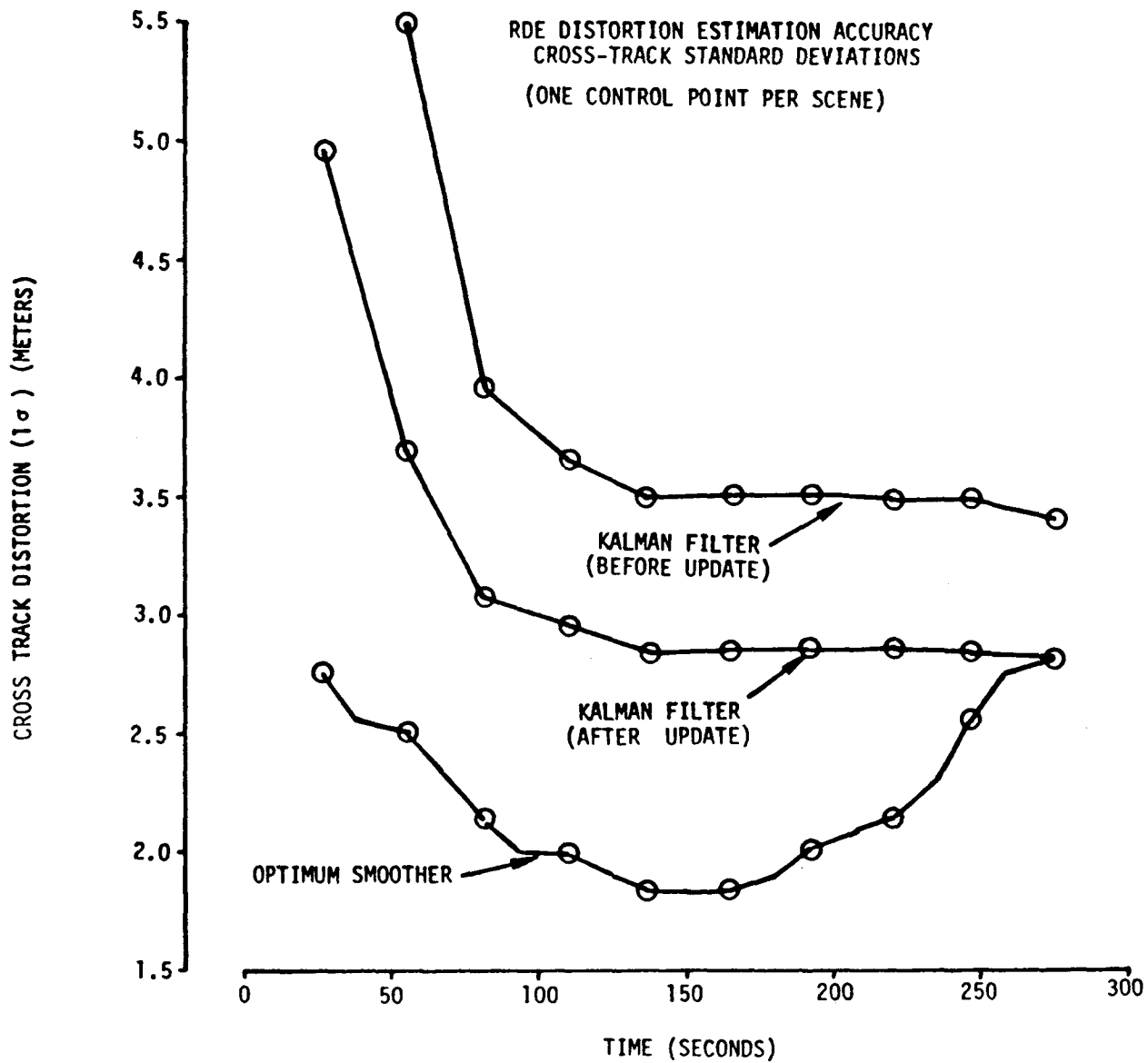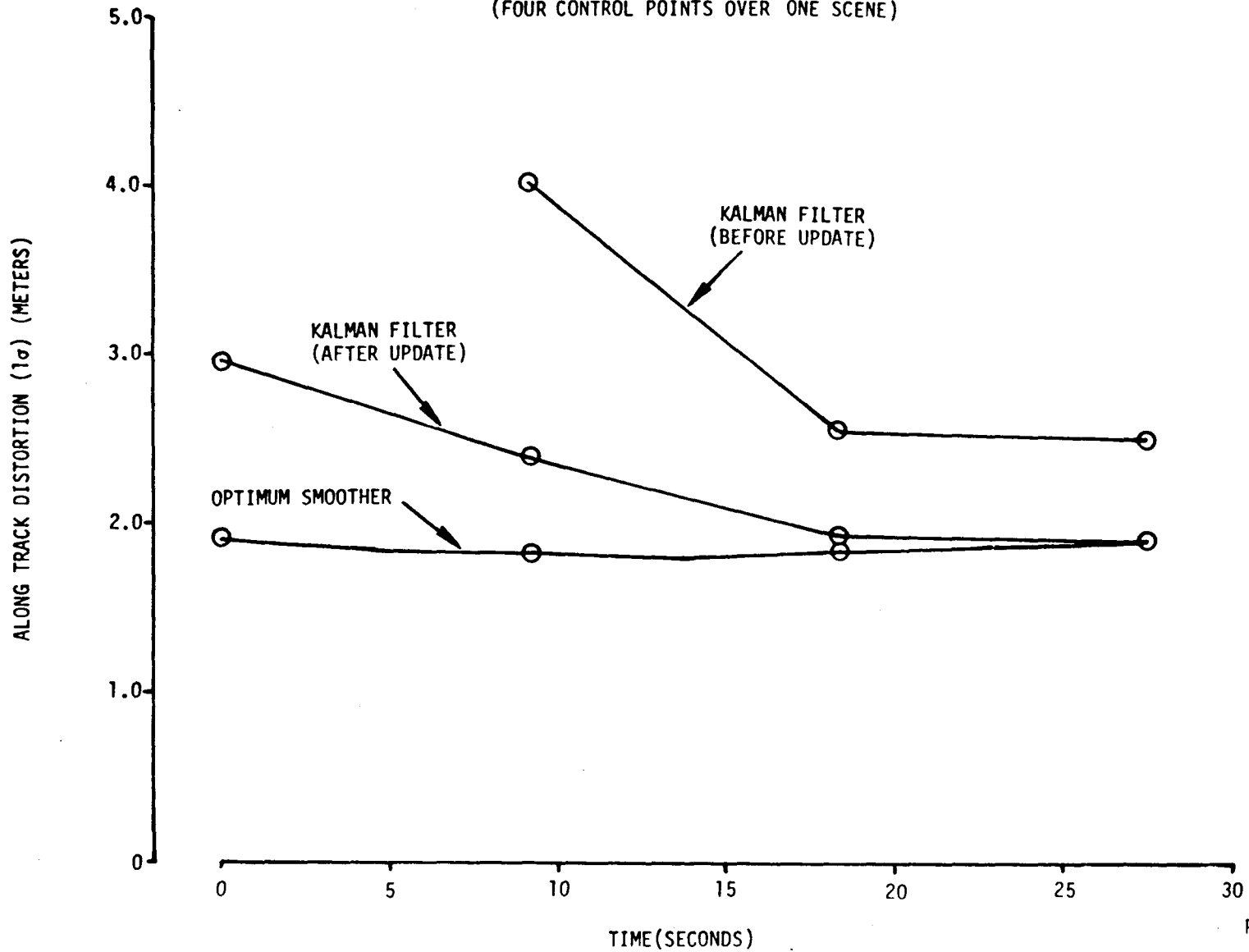
COMPARISON OF KALMAN FILTERING WITH OPTIMUM SMOOTHING (Concluded)

RDE DISTORTION ESTIMATION ACCURACY
CROSS-TRACK STANDARD DEVIATIONS
(FOUR CONTROL POINTS OVER ONE SCENE)

KALMAN FILTER
(BEFORE UPDATE)

KALMAN FILTER
(AFTER UPDATE)

OPTIMUM SMOOTHER

CROSS TRACK DISTORTION (1σ) (METERS)

TIME (SECONDS)

RW-22

195
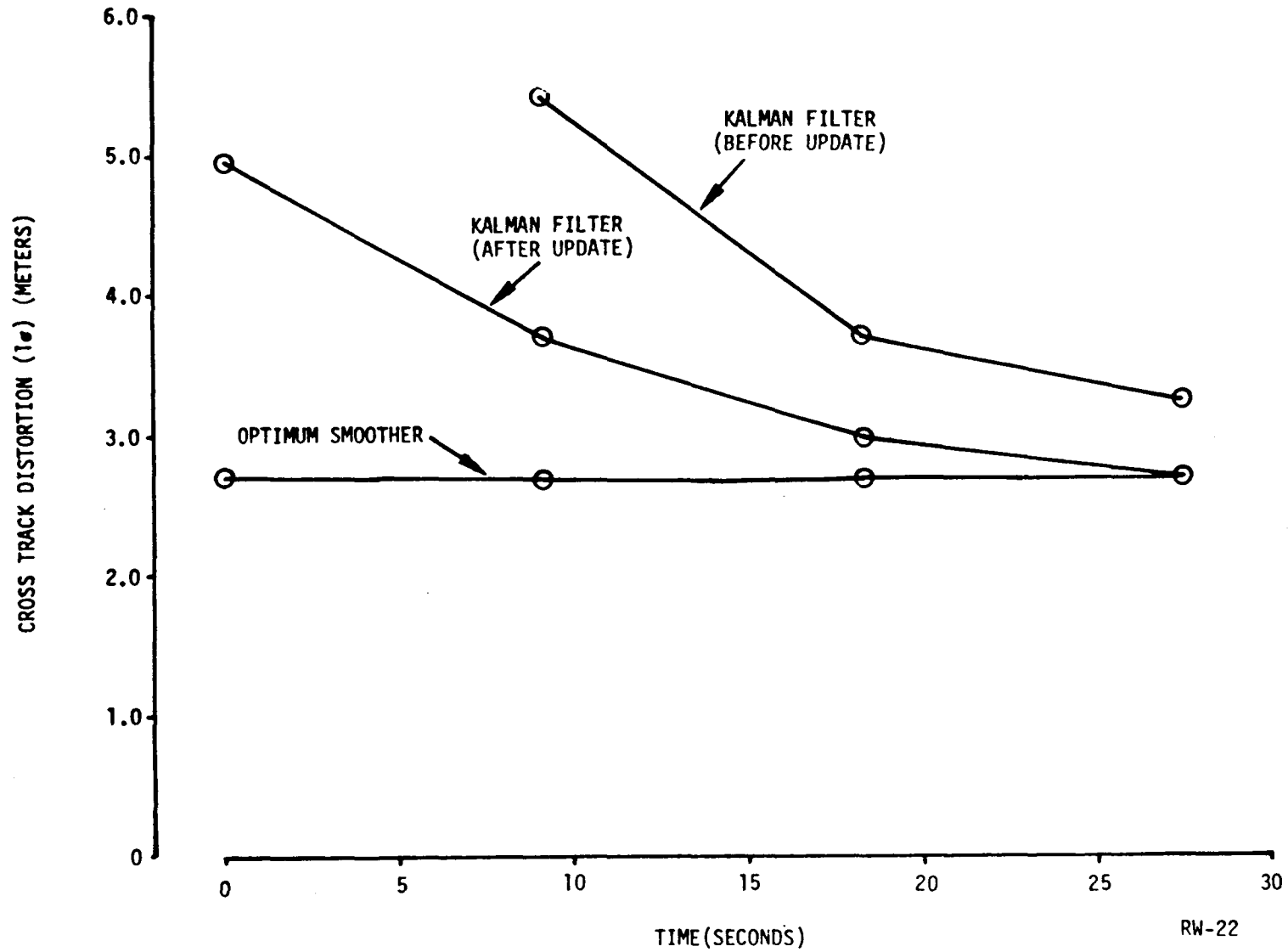
REDUCING THE NUMBER OF CONTROL POINTS PER SCENE

- A TM TEMPORAL REGISTRATION CASE REFLECTING ONE CONTROL POINT EVERY
  FOURTH SCENE WAS ANALYZED

- THE STANDARD DEVIATIONS (IN METERS) OF RESIDUAL DISTORTIONS FOR THIS
  CASE ARE COMPARED WITH THOSE FROM A CASE WITH ONE CP PER SCENE AS FOLLOWS:

	ONE CP PER SCENE			ONE CP EVERY FOUR SCENES		
	RDE STATE ESTIMATION ERROR (1σ)	UNCORRELATED POINTING ERROR (1σ)	TOTAL RESIDUAL DISTORTION (1σ)	RDE STATE ESTIMATION ERROR (1σ)	UNCORRELATED POINTING ERROR (1σ)	TOTAL RESIDUAL DISTORTION (1σ)
ALONG TRACK	1.28	2.55	2.85	1.77	2.55	3.11
CROSS TRACK	1.85	4.73	5.08	2.41	4.73	5.31

- THESE RESULTS SHOWS THAT REDUCING THE NUMBER OF CP's TO ONE EVERY FOURTH
  SCENE DEGRADES TOTAL ACCURACY ONLY SLIGHTLY, AND THE TM TEMPORAL REGISTRATION
  ACCURACY REQUIREMENTS [5.45 M (1σ)] IS STILL SATISFIED

LIMITING THE CONTROL POINT REGION TO ONE SCENE

- SEVERAL TM TEMPORAL REGISTRATION CASES WERE ANALYZED THAT REFLECT UTILIZING VARYING NUMBERS OF CP's UNIFORMLY DISTRIBUTED OVER A SINGLE SCENE IN ORDER TO REMOVE DISTORTIONS FROM THE SCENE

- THE FIGURE BELOW SHOWS HOW THE STANDARD DEVIATIONS OF RESIDUAL DISTORTIONS IN THE SCENE VARY WITH THE TOTAL NUMBER OF CP's UTILIZED TO CORRECT FOR DISTORTIONS

- BASED ON THESE RESULTS, AT LEAST FOUR CP's (DISTRIBUTED OVER THE SCENE) ARE NEEDED TO SATISFY THE TM TEMPORAL REGISTRATION ACCURACY REQUIREMENT

- THESE RESULTS ALSO SHOW THAT FEWER THAN FOUR CP's CAN BE UTILIZED WITH ONLY MODEST DEGRADATION IN REGISTRATION ACCURACY

TM TEMPORAL REGISTRATION ACCURACY VS. NUMBER OF
CP'S UNIFORMLY DISTRIBUTED OVER ONE SCENE

RW-25
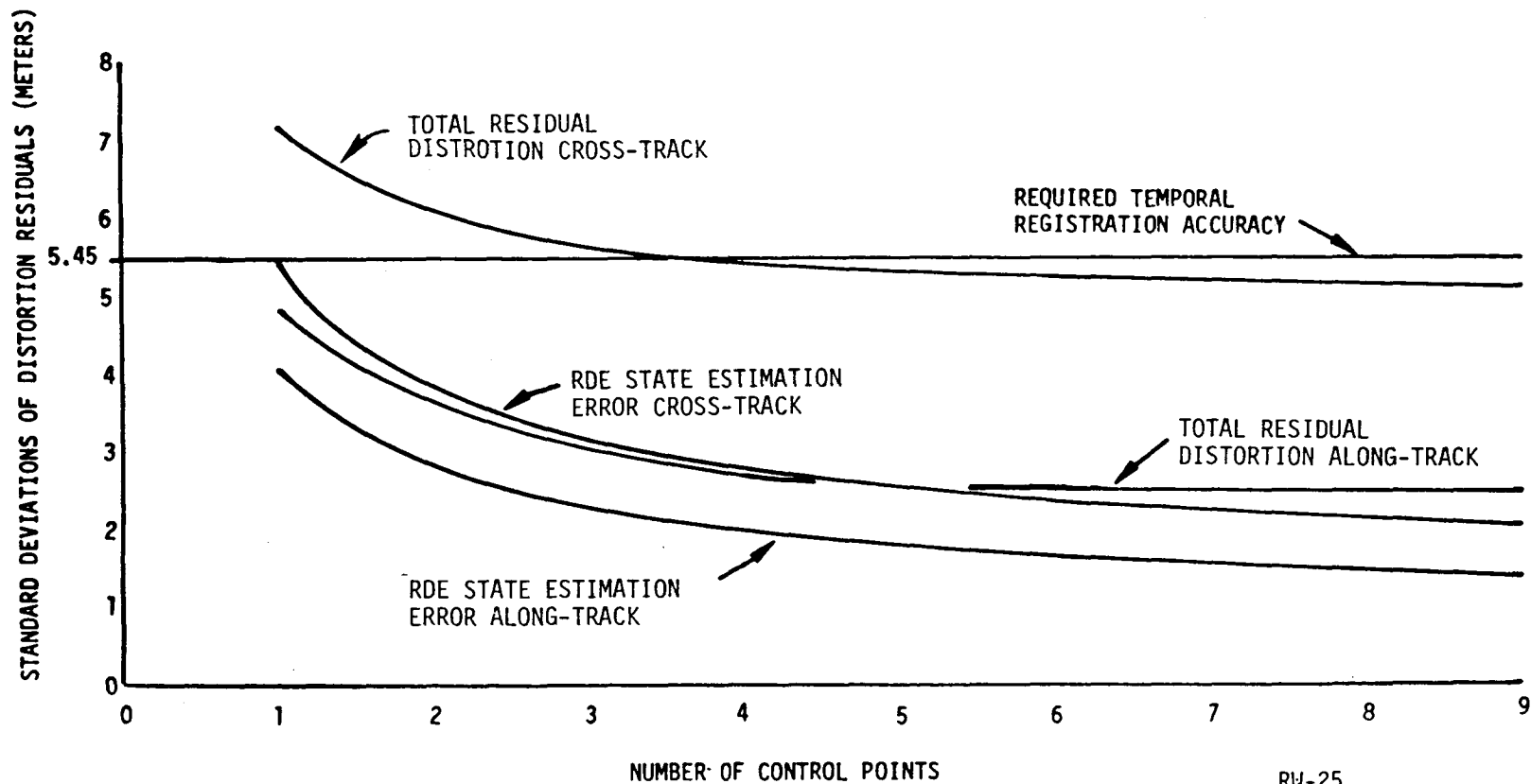
SESSION III

E. J. Lefferts, Chairman

OPTIMAL LARGE ANGLE MANEUVERS
WITH SIMULTANEOUS SHAPE CONTROL/VIBRATION ARREST

James D. Turner and John L. Junkins
Virginia Polytechnic Institute and State University

ABSTRACT

A relaxation method is demonstrated which reliably solves the nonlinear two-point-boundary-value problem which arises when optimal control theory is applied to determination of large angle maneuvers of flexible spacecraft. The basic ideas are summarized and several idealized maneuvers are determined. The emphasis is upon demonstrating the basic ideas and practical aspects of the methodology. References are cited, particularly Turner's dissertation which presents detailed formulations and more general applications.

Discussion of Figures
_____

With reference to Figure 1, we employ the method of assumed modes to obtain a set of ordinary differential equations which govern deflections and rotations. The form of the equations of motion are given in Figure 2. Note the high dimensionality and the variability of the coefficient matrix. Note that solution for the acceleration coordinates is required in order to integrate motion as a function of time, and in order to apply optimal control theory.

Figure 3 displays a partitioned algorithm which efficiently determines the inverse of the high-dimensioned, configuration-variable coefficient matrix. Consistent with this partitioning algorithm, we consider in Figure 4 an algorithm for obtaining partial derivatives of the inverted coefficient matrix with respect to deflection coordinates (required in the optimal control algorithm).

Figure 5 summarizes the state and co-state differential equations which follow from Pontryagin's principle as the necessary conditions satisfied by optimal (minimum quadratic cost) maneuvers. Observe that the initial and final states are generally known, but the initial and final co-states are usually unknown. Thus, as usual, a nonlinear two point boundary value problem (TPBVP) has resulted. Notice the quadratic angular velocity nonlinearity due to "rotational stiffness."

In Figure 6, we summarize an imbedding/relaxation approach which has proven a reliable approach for solving TPBVP's of the above structure. In essence, a one parameter (α) family of problems is constructed that one special member ($\alpha = 0$) has an analytical solution, while another member ($\alpha = 1$) is the true problem of interest. By relaxing α through a sequence of increasing values $0 \leqslant \alpha_i \leqslant 1$, we can extrapolate arbitrarily good initial or final co-state estimates (by adjusting the α-increment) from previous converged solutions, thereby allowing efficient differential corrections to isolate accurate co-states corresponding to each α. Typically, only 4 or 5 α_i values are actually required to reach the desired $\alpha = 1$ solution. This method and related methods are developed and applied to several examples in Reference 3.

Considering now a specific configuration, we refer to Figure 7. The four identical cantilevered appendages are mounted in the same plane to the rigid central hub. We neglect the hub radius in any equation in which it appears divided by the appendage length. Referring to Figure 8, we restrict attention to pure spin rotations and antisymmetric deflections, consistent with spin-up, spin-down, and rest-to-rest maneuvers with the configuration initially and finally undeformed. We consider only the case of torques applied to the hub.

Table 1 describes seven maneuver calculations, corresponding to three sets of maneuver boundary conditions and four different dynamical models. These cases are selected to demonstrate the effects of rotational stiffening and to show that the relaxation method can handle both high dimensionality and nonlinearities.

Figures 9a – c display the angle of rotation, angular rate and torque for the case 1 maneuver (rigid appendages). For comparison, Figures 10a – c display the same variables for cases 2L and 2N of flexible appendages, assuming a 1 mode expansion. It is of interest to note that the flexibility

effects are large indeed. The flexible case torque oscillates anti-symmetrically about the rigid case torque, the desired final angle and angular rate are achieved and the modal amplitude (and its derivative) are simultaneously driven to zero. It is interesting that the linear and nonlinear solutions were identical, to graphical accuracy, due to the small deflections and velocities of this particular maneuver.

Figure 11a – d and 12a – d display angle of rotation, torque history, and amplitudes of the first two modes for cases 3L and 3N, respectively. The maneuver is an extremely rapid spinup from rest to 0.5 rad/sec in 60 sec. The linear (3L) and nonlinear (3N) solutions differ significantly, but the linear solution retains the general shape and amplitudes differ by less than 10% throughout most of the motion.

Figure 13a – g display the angle of rotation, angular rate, torque, and the first four modal amplitudes for case 4L (a rest-to-rest maneuver through a 360° rotation). These results simply show that, indeed, the large rigid rotations and vibration suppression of several degrees of freedom are determined.

We offer the following significant conclusions:

- An Optimal Control Formulation is Presented for General 3 Dimensional Maneuvers of a Class of Flexible Satellites

- A Partitioning Method is Introduced to Invert the Rotational-Vibrational Equations of Motion for Acceleration Coordinates and to Obtain the Adjoint Equations

- An Imbedding/Relaxation Process if Demonstrated for Solution of the Two-Point-Boundary-Value Problem.

- Numerical Studies Indicate that Practical Algorithms Result from these Developments

References

1. Junkins, J.L. and J.D. Turner, "Optimal Continuous Torque Attitude Maneuvers," AIAA preprint #78-1400, presented to the AIAA/AAS Astrodynamics Conference, Palo Alto, CA., August 1978; also, to appear, AIAA Journal of Guidance and Control.

2. Turner, J.D. and J.L. Junkins, "Optimal Large Angle Single Axis Rotational Maneuvers of Flexible Spacecraft," presented to the 2nd AIAA/VPI&SU Symposium on Dynamics and Control of Large Flexible Spacecraft, Blacksburg, VA., June 1979, proceedings in press; also, to appear in AIAA Journal of Guidance and Control.

3. Turner, J.D. "Optimal Large Angle Maneuvers for Large Flexible Space Structures," Ph.D. Dissertation, Virginia Polytechnic Institute and State University, Blacksburg, VA., in press.

THE METHOD OF ASSUMED MODES

The deflection of the jth flexible member is modeled as

$$
\left.
\begin{aligned}
u_j(x,y,z,t) &= \sum_{i=1}^{L_j} \alpha_{ji}(t)\ U_{ji}(x,y,z) = \underline{\alpha}_j^T\ \underline{U}_j \\[6pt]
v_j(x,y,z,t) &= \sum_{i=1}^{M_j} \beta_{ji}(t)\ V_{ji}(x,y,z) = \underline{\beta}_j^T\ \underline{V}_j \\[6pt]
w_j(x,y,z,t) &= \sum_{i=1}^{N_j} \gamma_{ji}(t)\ W_{ji}(x,y,z) = \underline{\gamma}_j^T\ \underline{W}_j
\end{aligned}
\right\} j=1,2,\ldots,n \quad (1)
$$

The sets of spatial "assumed modes"

$$\left\{ U_{11}(x,y,z) \ \ldots\ U_{1i}(x,y,z) \right\} \ldots \left\{ U_{n1}(x,y,z) \ \ldots\ U_{ni}(x,y,z) \right\}$$

$$\left\{ V_{11}(x,y,z) \ \ldots\ V_{1i}(x,y,z) \right\} \ldots \left\{ V_{n1}(x,y,z) \ \ldots\ V_{ni}(x,y,z) \right\}$$

$$\left\{ W_{11}(x,y,z) \ \ldots\ W_{1i}(x,y,z) \right\} \ldots \left\{ W_{n1}(x,y,z) \ \ldots\ W_{ni}(x,y,z) \right\}$$

are <u>prescribed</u>. As minimum requirements, they must

- be linearly independent
- satisfy u, v, w's geometric boundary conditions

The amplitude functions constitute the *configuration vector*
$\underline{n}(t)$

$$\underline{n}(t) = \left\{ \underline{\alpha}_1^T,\ \underline{\beta}_1^T,\ \underline{\gamma}_1;\ \ldots\ \underline{\alpha}_n^T,\ \underline{\beta}_n^T,\ \underline{\gamma}_n^T \right\}^T$$

The amplitude's play the role of discrete generalized coordinates.

Figure 1

ROTATIONAL/DEFLECTIONAL EQNS OF MOTION

DYNAMICS OF FLEXIBLE SATELLITES

$$\{\dot{\theta}\} = [F(\theta)]\{\omega\} \tag{1}$$

$$[J(\eta)]\{\dot{\omega}\} = -[H^T]\{\ddot{\eta}\} + \{f(\theta,\omega,\eta,\dot{\eta},t)\} + \{u\} \tag{2}$$

$$[M]\{\ddot{\eta}\} = -[H]\{\dot{\omega}\} + \{g(\theta,\omega,\eta,\dot{\eta},t)\} \tag{3}$$

Combine (2) & (3)

$$\begin{pmatrix} J(\eta) & \vdots & H^T \\ \cdots & \vdots & \cdots \\ H & \vdots & M \end{pmatrix} \begin{Bmatrix} \underline{\dot{\omega}} \\ \cdots \\ \underline{\ddot{\eta}} \end{Bmatrix} = \begin{Bmatrix} \underline{f} + \underline{u} \\ \cdots \\ \underline{g} \end{Bmatrix} \tag{4}$$

Note

[H] & [M] are constant

$$[J(\eta)] = [J_o] + [J_D(\eta)] \qquad , \quad ||J_D|| << ||J_o|| \text{ (typically)}$$

        Inertia of   Inertia varia-
        undeformed   tions due to
        vehicle   deformations

A problem:

We need eqns of motion in the state space form $\dot{\underline{x}} = \underline{F}(\underline{x},\underline{u},t)$,

but

(i) The coefficient matrix of (4) is variable

(ii) Its dimensions may be several hundred

Figure 2

PARTITIONED/PERTURBATION INVERSION OF THE
COEFFICIENT MATRIX

Name the submatrices:
$$\begin{pmatrix} C_{11} & \vdots & C_{21}^T \\ \cdots & \vdots & \cdots \\ C_{21} & \vdots & C_{22} \end{pmatrix} \equiv \begin{pmatrix} J & \vdots & H^T \\ \cdots & \vdots & \cdots \\ H & \vdots & M \end{pmatrix}^{-1}$$

The C_{ij} can be expressed directly as a function of J, M, H as:

	Form 1	Form 2
C_{11}	$J^{-1} - J^{-1} H^T C_{21}$	$(J - H^T M^{-1} H)^{-1}$
C_{22}	$(M - H J^{-1} H^T)^{-1}$	$M^{-1} - M^{-1} H C_{21}^T$
C_{21}	$-C_{22} H J^{-1}$	$-M^{-1} H C_{11}$

For direct numerical calculations, <u>Form 2</u> is preferred since

(i) $(J - H^T M^{-1} H)$ is a 3 × 3 matrix

(ii) M is generally diagonally dominant (an identity matrix if one first
solves an eigenvalue problem - Note M is positive-definite symmetric)

Figure 3

Rotational/Vibrational Equations of Motion

$$\underbrace{\left(\begin{array}{c:c} \underline{J}(\underline{\eta}) & \underline{H}^T \\ \hdashline \underline{H} & \underline{M} \end{array} \right)}_{\underline{\underline{M}}(\underline{\eta})} \left\{ \begin{array}{c} \dot{\underline{\omega}} \\ \cdots \\ \ddot{\underline{\eta}} \end{array} \right\} = \left\{ \begin{array}{c} \underline{f}(\underline{\theta},\underline{\omega},\underline{\eta},\dot{\underline{\eta}},t) + \underline{u}(t) \\ \\ \underline{g}(\underline{\theta},\underline{\omega},\underline{\eta},\dot{\underline{\eta}},t) \end{array} \right\}$$

or, in inverted form

$$\left\{ \begin{array}{c} \dot{\underline{\omega}} \\ \cdots \\ \ddot{\underline{\eta}} \end{array} \right\} = \left| \underline{\underline{M}}(\underline{\eta}) \right|^{-1} \left\{ \begin{array}{c} \underline{f} + \underline{u} \\ \cdots\cdots\cdots \\ \underline{g} \end{array} \right\}$$

Note

$$\underline{\eta}^T = \{ \eta_1 \quad \eta_2 \quad \cdots \quad \eta_n \}$$

$$\frac{\partial}{\partial \eta_i} \left\{ \begin{array}{c} \dot{\underline{\omega}} \\ \cdots \\ \ddot{\underline{\eta}} \end{array} \right\} = \frac{\partial}{\partial \eta_i} \left[\underline{\underline{M}}^{-1} \right] \left\{ \begin{array}{c} \underline{f} + \underline{u} \\ \cdots\cdots\cdots \\ \underline{g} \end{array} \right\} + \underline{\underline{M}}^{-1} \frac{\partial}{\partial \eta_i} \left\{ \begin{array}{c} \underline{f} + \underline{u} \\ \cdots\cdots\cdots \\ \underline{g} \end{array} \right\}$$

To determine $\dfrac{\partial}{\partial \eta_i} \left| \underline{\underline{M}}^{-1} \right|$, observe

$$\underline{\underline{M}}^{-1}\underline{\underline{M}} = \underline{\underline{I}}$$

from which

$$\frac{\partial}{\partial \eta_i} \left[\underline{\underline{M}}^{-1} \right] \underline{\underline{M}} + \underline{\underline{M}}^{-1} \left[\frac{\partial \underline{\underline{M}}}{\partial \eta_i} \right] = 0$$

or

$$\boxed{\frac{\partial}{\partial \eta_i} \left[\underline{\underline{M}}^{-1} \right] = -\underline{\underline{M}}^{-1} \left[\frac{\partial \underline{\underline{M}}}{\partial \eta_i} \right] \underline{\underline{M}}^{-1}} \quad , \quad i=1,2,\ldots,n$$

where

$$\left[\frac{\partial \underline{\underline{M}}}{\partial \eta_i} \right] = \left[\begin{array}{c:c} \dfrac{\partial \underline{J}(\underline{\eta})}{\partial \eta_i} & 0 \\ \hdashline 0 & 0 \end{array} \right]$$

Figure 4

FORMULATION OF THE OPTIMAL CONTROL PROBLEM

STATE VARIABLES

$$\underline{x}_1 = \{\theta\}, \quad \underline{x}_2 = \{\eta\}, \quad \underline{x}_3 = \{\omega\}, \quad x_4 = \{\dot{\eta}\}$$

STATE DIFFERENTIAL EQUATIONS

$$\dot{\underline{x}}_1 = [F(x_1)]\{\underline{x}_3\} = \underline{F}_1(\underline{x}_1, \ -, \ \underline{x}_3, \ -, \ -, \ -)$$

$$\dot{\underline{x}}_2 = \underline{x}_4 \qquad\qquad = \underline{F}_2(\ -, \ -, \ \ -, \ \underline{x}_4, \ -, \ -)$$

$$\begin{Bmatrix} \dot{\underline{x}}_3 \\ \dot{\underline{x}}_4 \end{Bmatrix} \equiv \begin{Bmatrix} \{\dot{\omega}\} \\ \{\ddot{\eta}\} \end{Bmatrix} = \begin{Bmatrix} \underline{F}_3(\underline{x}_1, \ \underline{x}_2, \ \underline{x}_3, \ \underline{x}_4, \ \underline{u}, \ t) \\ \underline{F}_4(\underline{x}_1, \ \underline{x}_2, \ \underline{x}_3, \ \underline{x}_4, \ \underline{u}, \ t) \end{Bmatrix} = \underline{\underline{M}}^{-1}(\underline{x}_2) \begin{Bmatrix} \underline{f}(\underline{x}_1, t) + \underline{u} \\ \cdots\cdots\cdots \\ \underline{g}(\underline{x}_1, t) \end{Bmatrix}$$

Find $\underline{u}(t)$ generating a trajectory initiating at $\underline{x}_i(t_o)$, terminating at $\underline{x}_i(t_f)$, which minimizes the function

$$J = \frac{1}{2} \int_{t_o}^{t_f} (\underline{u}^T W_{uu} \underline{u} + \sum_{i=2}^{4} \underline{x}_i^T W_{ii} \underline{x}_i) dt$$

HAMILTONIAN

$$H = \frac{1}{2}(\underline{u}^T W_{uu} \underline{u} + \sum_{i=2}^{4} \underline{x}_i^T W_{ii} \underline{x}_i) + \sum_{i=1}^{4} \underline{\lambda}_i^T \underline{F}_i$$

PONTRYAGIN'S NECESSARY CONDITIONS

Co-state Equations

$$\dot{\underline{\lambda}}_i = -\frac{\partial H}{\partial \underline{x}_i} \equiv \underline{G}_i(\underline{x}_1, \ \ldots, \ \underline{x}_4; \ \underline{\lambda}_1, \ \ldots, \ \underline{\lambda}_4; \ \underline{u}, \ t)$$

Optimal Control

Minimize H at each instant with respect to admissible $\underline{u}(t)$, this yields $\underline{u} = \underline{U}(\underline{x}_1, \ \ldots, \ \underline{x}_4; \ \underline{\lambda}_1, \ \ldots, \ \underline{\lambda}_4, \ t)$

Figure 5

IMBEDDING/RELAXATION METHOD FOR SOLVING
TWO-POINT BOUNDARY VALUE PROBLEM

Define merged vector

$$\underline{Z} \equiv \{x^T \quad \underline{\lambda}^T\}^T$$

The coupled state and costate differential equations are then

$$\dot{\underline{Z}} = [A]\underline{Z} + \alpha\{\text{all nonlinear terms}\}$$

- Typically, we know $\underline{x}(t_0)$ and $\underline{x}(t_f)$, but not $\underline{\lambda}(t_0)$, $\underline{\lambda}(t_f)$.

- For $\alpha = 0$, we can solve for $\underline{\lambda}(t_0)$ exactly.

- By taking sufficiently small α-increments, we can use converged $\underline{\lambda}(t_0)$ from neighboring optimal solutions to initiate successive approximations with *arbitrarily good starting estimates* for the unknown $\underline{\lambda}(t_0)$.

- Typically, only 5 to 10 intermediate α-values are required a practical algorithm results.

Figure 6
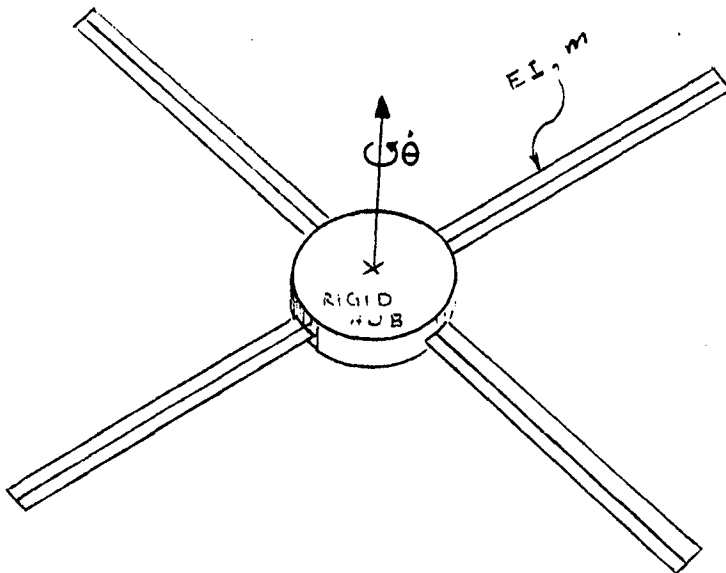
FIGURE 7 UNDEFORMED STRUCTURE
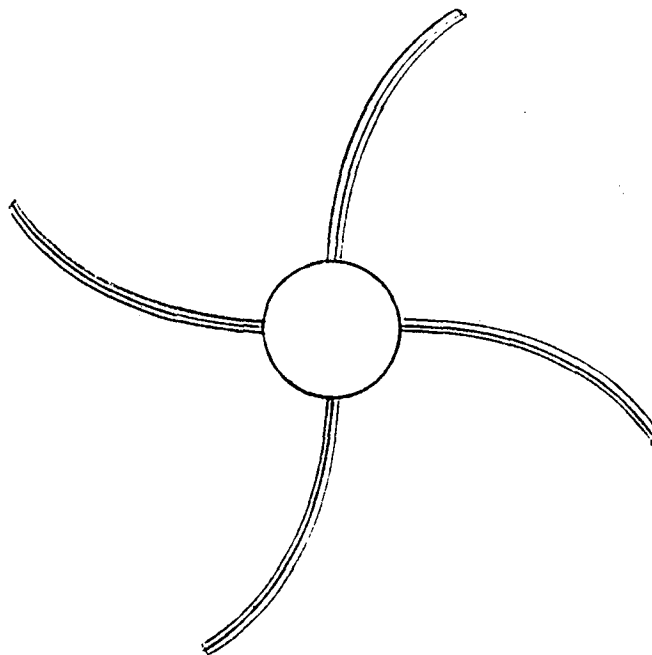
FIGURE 8 ANTISYMMETRIC DEFORMATION

Figure 9a

Figure 9b

Figure 9c

Figure 10a

Figure 10b

Figure 10c
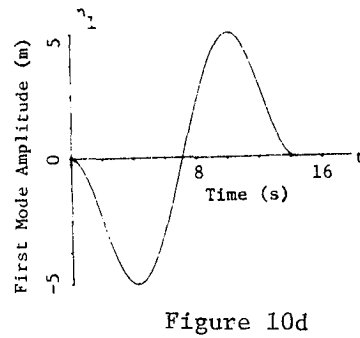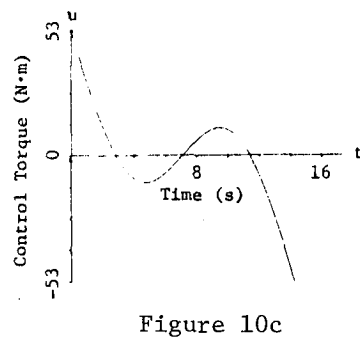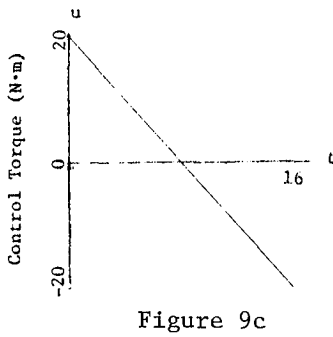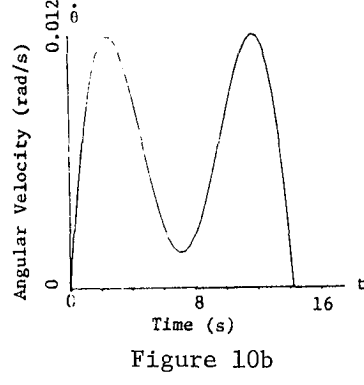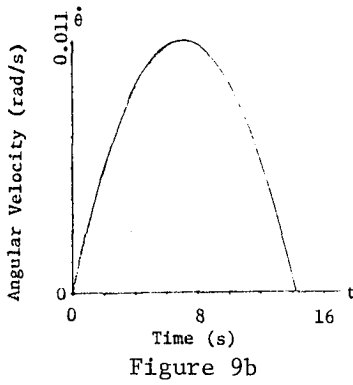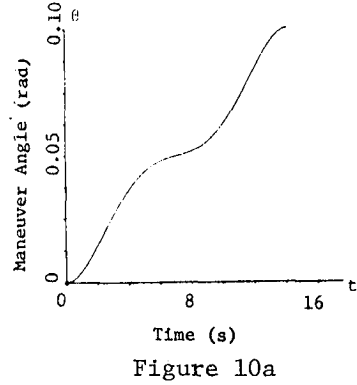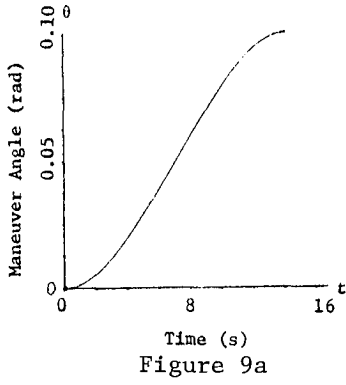
Figure 10d

Figure 9   Case 1 Rigid Body
           Rest-To-Rest
           Maneuver

211

Figure 10   Cases 2L, 2N Flexible
            Appendages Rest-To-
            Rest Maneuver $t_f = 2\pi/\omega_1$
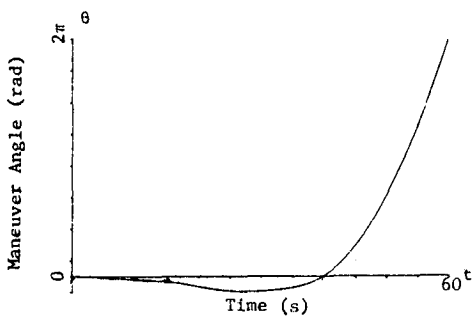
Figure 11a
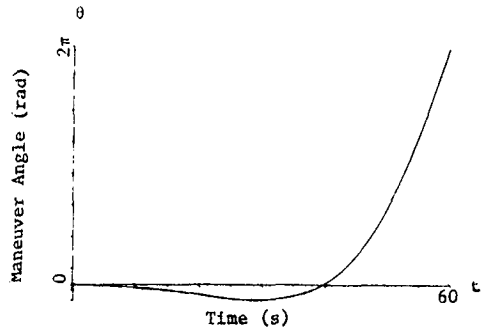
Figure 12a
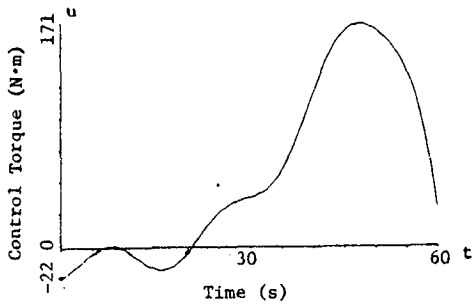
Figure 11b
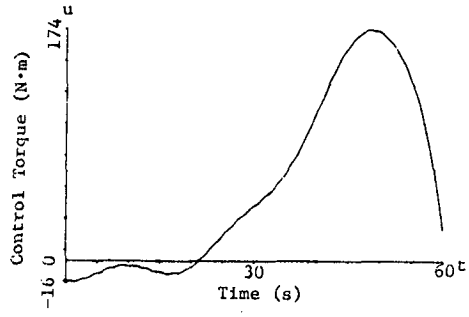
Figure 12b
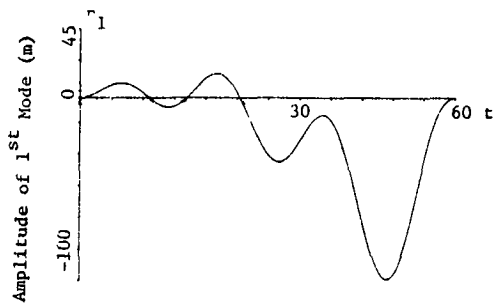
Figure 11c
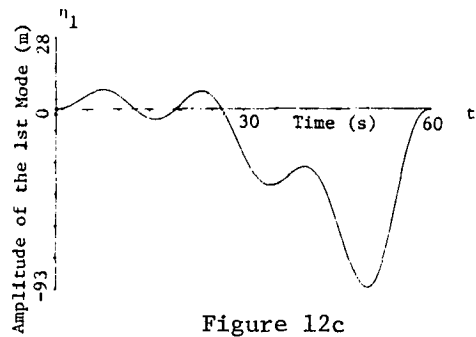
Figure 12c
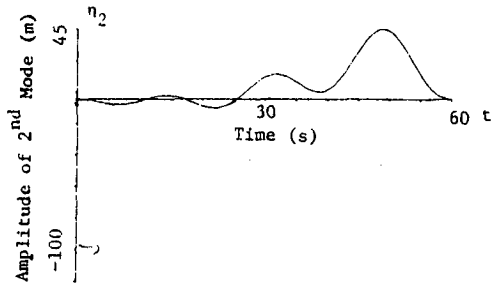
Figure 11d
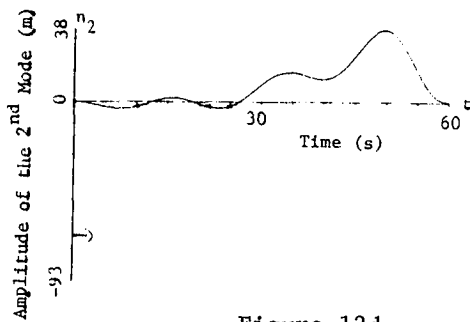
Figure 12d

Figure 11   Case 3L Linear
            Spinup Maneuver

Figure 12   Case 3N Nonlinear
            Spinup Maneuver

212
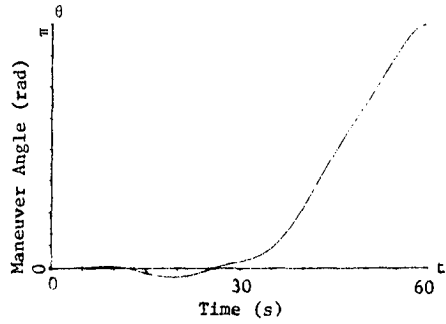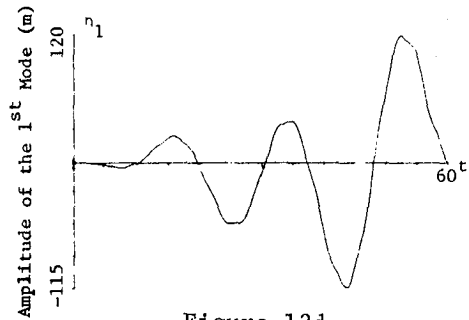
Figure 13a

Figure 13d
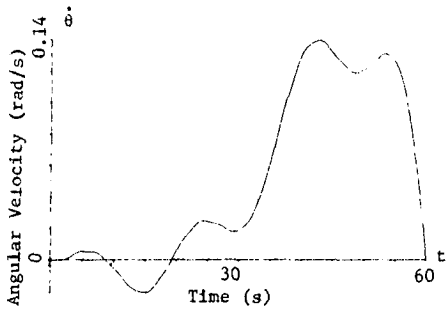
Figure 13b
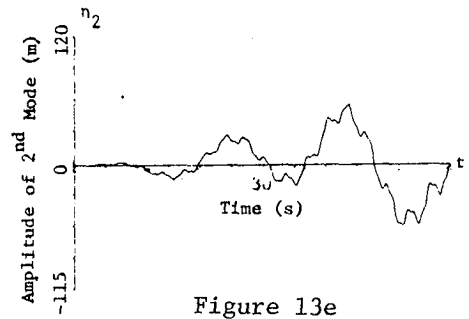
Figure 13e
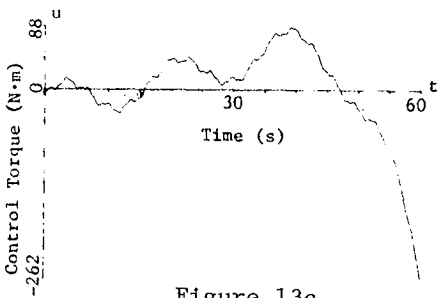
Figure 13c
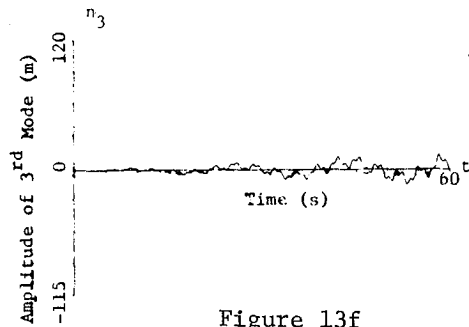
Figure 13f
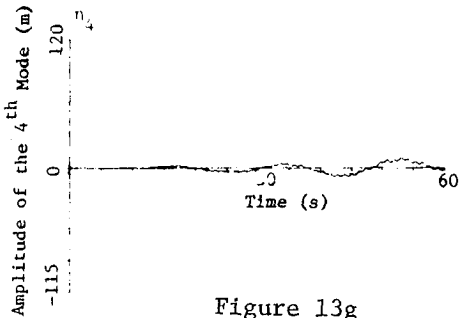
Figure 13g

Figure 13   Case 4L Rest-To-Rest Maneuver
Controlling and Arresting 4 Modes

213

TABLE 1   DESCRIPTION OF TEST CASE MANEUVERS

Case #	Qualitative Description	# of Modes (N)	θ_o (RAD)	$\dot{\theta}_o$ (RAD/SEC)	θ_f (RAD)	$\dot{\theta}_f$ (RAD/SEC)	W_{uu}	W_{ss}
1	Rigid Appendages Rest-to-Rest Maneuver t_f = 14.221 sec.	0	0	0	0.1	0	1.0	[0]
2L	Linear Kinematics Rest-to-Rest Maneuver $t_f = 2\pi/\omega_1$ = 14.221 sec	1	0	0	0.1	0	1.0	[I]
2N	Nonlinear Kinematics Rest-to-Rest Maneuver $t_f = 2\pi/\omega_1$ = 14.221 sec	1	0	0	0.1	0	1.0	[I]
3L	Linear Kinematics Spinup Maneuver t_f = 60 sec	2	0	0	2π	0.5	1.0	[I]
3N	Nonlinear Kinematics Spinup Maneuver t_f = 60 sec	2	0	0	2π	0.5	1.0	[I]
4L	Linear Kinematics Rest-to-Rest Maneuver t_f = 60 sec	4	0	0	π	0	1.0	[I]
4N	Nonlinear Kinematics Rest-to-Rest Maneuver t_f = 60 sec	4	0	0	π	0	1.0	[I]

DESCRIPTION OF THE VISSR IMAGE REGISTRATION
AND GRIDDING SYSTEM

Larry N. Hambrick
National Environmental Satellite Service
National Oceanic and Atmospheric Administration

ABSTRACT

Small scale weather forecasting has created a demand for the accurate earth location of real-time GOES/VISSR data. A year ago an interactive processing system, built by the Space Science and Engineering Center of the University of Wisconsin, was installed at the National Environmental Satellite Service's central facility where it is referred to as VIRGS (VISSR Image Registration and Gridding System). The VIRGS is now operational, delivering a level of accuracy that closely approaches the goal of 1 visible pixel.

The most interesting aspect of the VIRGS implementation has been the development by Dr. Dennis Phillips of a highly efficient accurate software package to compute orbit and attitude on the basis of star and landmarks observations. The package executes in a few seconds on a small computer and allows for human interaction as needed. Recovery of full accuracy following a satellite maneuver requires as little as six hours of observations.

The VIRGS is briefly described in terms of its operations, procedures, product outputs, and accuracy. Potential enhancements of the system include extending the prediction period so as to increase overall efficiency. With the accuracy now available from VIRGS, the routine remapping of VISSR images to remove bothersome dynamic deformations seems feasible as future improvement to the VISSR data service.

ORBIT/ATTITUDE ESTIMATION FOR THE GOES SPACECRAFT USING VAS LANDMARK DATA

H. Sielski, and D. Hall
Computer Sciences Corporation

R. Nankervis, D. Koch
Goddard Space Flight Center

ABSTRACT

A software system is described which provides for batch least-squares estimation of spacecraft orbit, attitude, and camera bias parameters using image data from the Geostationary Operational Environmental Satellites (GOES). The image data are obtained by the Visible and Infrared Spin Scan Radiometer (VISSR) Atmospheric Sounder (VAS). The resulting estimated parameters are used for absolute image registration. Operating on the Digital Equipment Corporation (DEC) PDP-11/70 computer, the FORTRAN system also includes the capabilities of image display and manipulations. An overview of the system is presented as well as some numerical results obtained from observations taken by the SMS-2 satellite over a 3-day interval in August 1975.

SECTION 1 – INTRODUCTION

A variety of spacecraft (S/C) exist which transmit images to the ground to provide meteorological and Earth resource information. Several studies have been concerned with the use of this imaging data for the estimation of the S/C orbit and attitude. Such an estimation procedure can be used for several purposes. The one with which this report is concerned is the use of the estimated S/C orbit and attitude (O/A) parameters for absolute image registration. The estimated O/A parameters are used to predict the geodetic latitude and longitude (ϕ, λ) which correspond to a specified location on an Earth picture. This allows accurate geodetic coordinate determination for temporal phenomena, such as clouds or sea swells.

There are two categories of image data; those from three axis stabilized S/C and those from spin-stablized S/C.

The Landsat and Earth Resource Technology Satellites (ERTS) are examples of three axis stabilized S/C. These produce image data from high inclination (polar) close Earth (900 km altitude) orbits. The use of this data is discussed in Reference 1 which describes a software system for the display and manipulation of image data as well as the use of an extended Kalman filter estimator for the O/A parameter determination.

The geosynchronous Geostationary Operational Environmental satellites (GOES) are examples of spin-stabilized S/C which produce image data. An overview of O/A estimation using this type of data is given in Reference 2, where sample numerical results are presented for the first geostationary Synchronous Meteorological Satellite (SMS-1).

This paper describes a software system developed to provide Bayesian weighted least-squares estimation of spacecraft orbit and attitude parameters using picture data obtained from the VAS (VISSR Atmospheric Sounder) instrument to be flown on the GOES-D. The data consist of ground control points of known geodetic coordinates located on pictures of the Earth taken by the GOES spacecraft. The VAS/NAVPAK (VISSR Atmospheric Sounder Navigation Package) system operates on the Digital Equipment Corporation PDP 11/70 computer.

SECTION 2 - VAS/NAVPAK SOFTWARE OVERVIEW

As shown in Figure 1, the VAS/NAVPAK system can be divided into four functions. First, the Data Base Management (DBM) portion controls file and data manipulation. Second, the picture display and cursor navigation portion controls: (1) picture display on the I^2S, such as image zooming; (2) cursor navigation, including the extraction of picture coordinates (ℓ, e) and the automatic moving of the cursor to the picture coordinates corresponding to a specified longitude and latitude; (3) automatic grey scale correlation between a prestored chip (16 x 16 pixel reference landmark) and a search area about the cursor; (4) the creation of landmark observations. The third VAS/NAVPAK function is the O/A and camera bias estimation. This portion of the system provides for weighted least-squares (DC) estimation of the satellite orbit, attitude, and camera biases. The fourth VAS/NAVPAK function produces the specific navigation parameters which are required over a specified prediction interval (usually 2 days). The navigation parameters are used to annotate the picture data.

2.1 Picture Display and Cursor Navigation

Cursor navigation is the prediction of picture coordinates (ℓ, e) corresponding to a specified geodetic latitude and longitude, given the estimated satellite orbit and attitude and the camera biases for some epoch time.

This is the method by which a prestored video reference area (taken from a VAS picture) is correlated with an area surrounding the cursor on the image displayed by the operator.

2.2 Orbit/Attitude Estimation

The S/C O/A estimation is done with the classical Bayesian weighted least-squares technique. The estimator can use either landmark data, radar tracking data, or both. Only the capability for using landmark data will be

```
                          ┌──────────────┐
                          │  VAS/NAVPAK  │
                          └──────────────┘
```

DBM Data Base Management	Picture Display and Cursor Navigation	O/A Orbit/Attitude Estimator	Navigation Parameter Output

- Manipulation of fun-
damental constants
and flags

- File manipulation

- Display of pictures
IIS

- Manipulation of pic-
tures (zoom)

- Automatic moving of
cursor to specified
goedetic coordinates

- Extraction of picture
coordinates for given
cursor location

- Correlation between
prestored chip (16×16
pixel reference land-
mark) and current
picture search area

- Creation of landmark
observation

- Creation of observa-
tion working files

- Interactive least-
squares (DC) deter-
mination of satellite
orbit/attitude param-
eters and camera
biases

- Predict estimated
state

- Perform the Chebyshev
fitting of position, beta
count, etc.

- Calculate auxiliary
parameters

Figure 1.   VAS/NAVPAK Overview

presented. It is assumed that the working observation files of landmark data have been created before beginning the O/A estimation.

The computational procedure followed for the O/A proceeds in the following steps:

1. An a priori estimate is provided of the solve-for parameters. These parameters will be a subset of:

$$\bar{r}_0, \dot{\bar{r}}_0 \qquad \text{the S/C position and velocity}$$

$$\chi_i, i=1, 5 \qquad \text{S/C attitude model}$$

$$\psi_i, i=1, 5 \qquad \text{coefficients}$$

$$\xi \qquad \text{camera bias}$$

$$\rho \qquad \text{camera bias}$$

$$\Delta \gamma_0 \qquad \text{camera bias}$$

2. For each observation, the S/C position and velocity are found by integrating the equations of motion to the observation time, t_{obs}. For the VAS/NAVPAK system, the integration is performed with a 12th order Cowell method, as described in Reference 3. The force model is selectable by the user and can include a spherical harmonic geopotential expansion terms up to 21 x 21, lunar/solar third body perturbations, and solar radiation pressure.

3. For each observation time, an observation (ℓ, e) pair and partial derviatives are computed corresponding to the geodetic coordinates (ϕ, λ) of the landmark using the S/C position, velocity, attitude, and camera biases.

4. The computed observation pair is used to calculate the observation residuals. The residual is examined to see if it meets the editing criteria. If it does not, it is not used in the solution.

5. After steps 2, 3, and 4 have been performed for all the observations, the new estimate of the epoch S/C state, the attitude, and camera biases, and their covariance matrix, is computed.

6. The new estimate of the solve-for parameters are compared with the previous to see if the least squares process has converged. If the solution is judged to have not converged, the new estimate replaces the a priori in step 1, and the process is repeated.

2.3 Navigation Parameter Output

Spacecraft parameters can be generated for a sequence of overlapping time intervals covering a specified output span. These parameters include spacecraft ephemerides, attitude information, camera biases, eclipse times, and Chebyshev coefficients for position, beta angle, and retransmission correction.

SECTION 3 - THE OBSERVATION MODEL

The observational model in VAS/NAVPAK is a modification of that used in the SMS NAVPAK (Reference 4). The camera bias and attitude representations for the VAS/NAVPAK observational model were reformulated, consulting the VAS working group (Reference 5) and with the assistance of R. Pajerski (GSFC).

The SMS and GOES are geosynchronous spinning spacecraft designed for taking pictures of the Earth in several wavelengths. A camera, or VISSR (Visible and Infrared Spin Scan Radiometer), transmits data to a ground station where a complete picture of the Earth is assembled. The data consist of a grid or matrix of intensity measurements. A line number and an element number specify the location of the intensity measurement within the grid. The line number ℓ, corresponds roughly to longitude. These are shown schematically in Figure 2. For the visible wavelength observations, each picture element (pixel) intensity measurement corresponds nominally to an area on Earth of dimension 1/2 mile by 1/2 mile square. Of course, near the edge of the Earth, foreshortening will enlarge and distort this square. Options exist to handle data whose dimensions are integer multiples of this unit (i.e., 2-mile by 4-mile data). Associated with each line of the picture is a time and angular quantity which relates the starting position of the line to the direction of the Sun in inertial space.

At the ground station preprocessing is performed and full resolution picture segments of 1024 x 1024 pixels are generated. In order to create a landmark observation, the operator first displays a picture or subset of a picture on the I^2S. Then, an identification is made of a particular location on the picture (ℓ, e) pair which corresponds to a known geodetic latitude and longitude on Earth. The geodetic coordinates and the picture coordinates with associated quantities such as time and Sun angle are transferred to an observation file. This constitutes a single landmark observation pair.
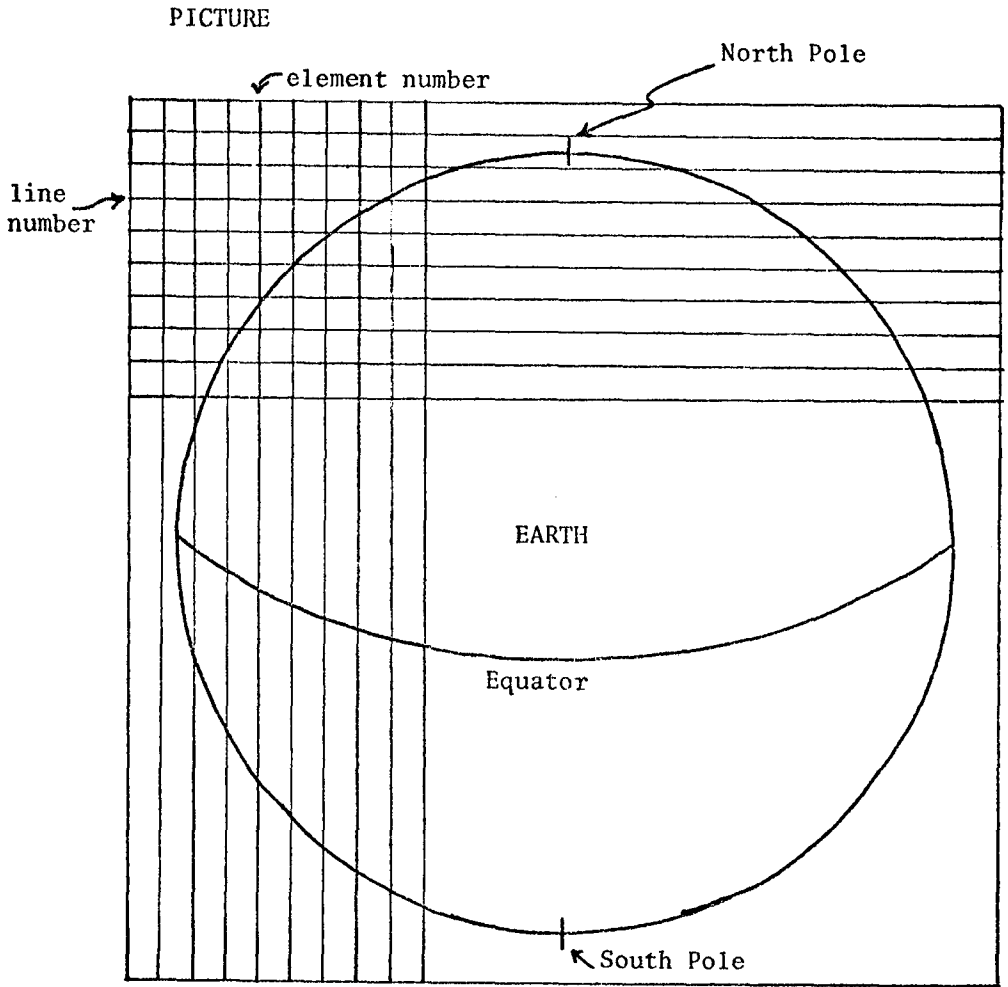
Figure 2. Schematic VAS/GOES Picture

Figure 3 shows the GOES satellite relative to the earth at an instant of time. Except for specific camera constants, the SMS is almost identical to the GOES. Both satellites are cylindrical spinning objects with the longitudinal symmetry axis nearly aligned with the spin axis. The spin axis in turn is nearly aligned with the polar axis of the Earth pointed southward. As the satellite spins, the camera scans across the face of the Earth's disk, from west to east measuring the light intensity for each pixel along a line. The relation between the (ℓ, e) coordinates of each picture and the camera orientation can be shown by comparing the image in Figure 2 with Figure 3. The element, e, is related to the azimuthal camera angle, q. This angle is measured in the satellite spin plane and is the angle between the line of sight (LOS) vector to the landmark and the LOS vector to the left (west) edge of the Earth. The conversion to line element is

$$e = q/RPE \qquad (1)$$

where RPE is the number of radians per line element. The satellite spin plane in Figure 4, perpendicular to the spin axis z', is shown coincident with the spacecraft (S/C) symmetry plane, perpendicular to the S/C longitudinal symmetry axis $z_{S/C}$. In the actual development of the observation equations the general case of a misaligned spin axis is considered.

The line number related to the camera elevation angle, a, as

$$\ell = \frac{a}{RPL} + \ell o \qquad (2)$$

where RPL is the number of radians per line and ℓo is the line number which corresponds to a zero elevation setting of the camera.

The relation of the picture coordinates (ℓ, e) to coordinates of a location on the Earth (φ, λ) depends upon the spacecraft position and attitude, and the camera constants and biases. Several coordinate system transformations are required to express this relation.

NORTH POLE

EARTH COORDINATES

LANDMARK
(ϕ, λ)

GREENWICH
MERIDIAN

ϕ

λ

VAS
SCANNER

VAS SUNSHADE

a

PROJECTION OF LOS
TO LANDMARK ONTO
SPIN PLANE

X

$X_{S/C}$

IMAGE
COORDINATES
(LINE, ELEMENT)

q

LOS TO THE
LEFT (WEST) EDGE
OF THE EARTH.

Z' (SPIN AXIS)

$Z_{S/C}$ (SYMMETRY AXIS)

$-Y'$

$-Y_{S/C}$
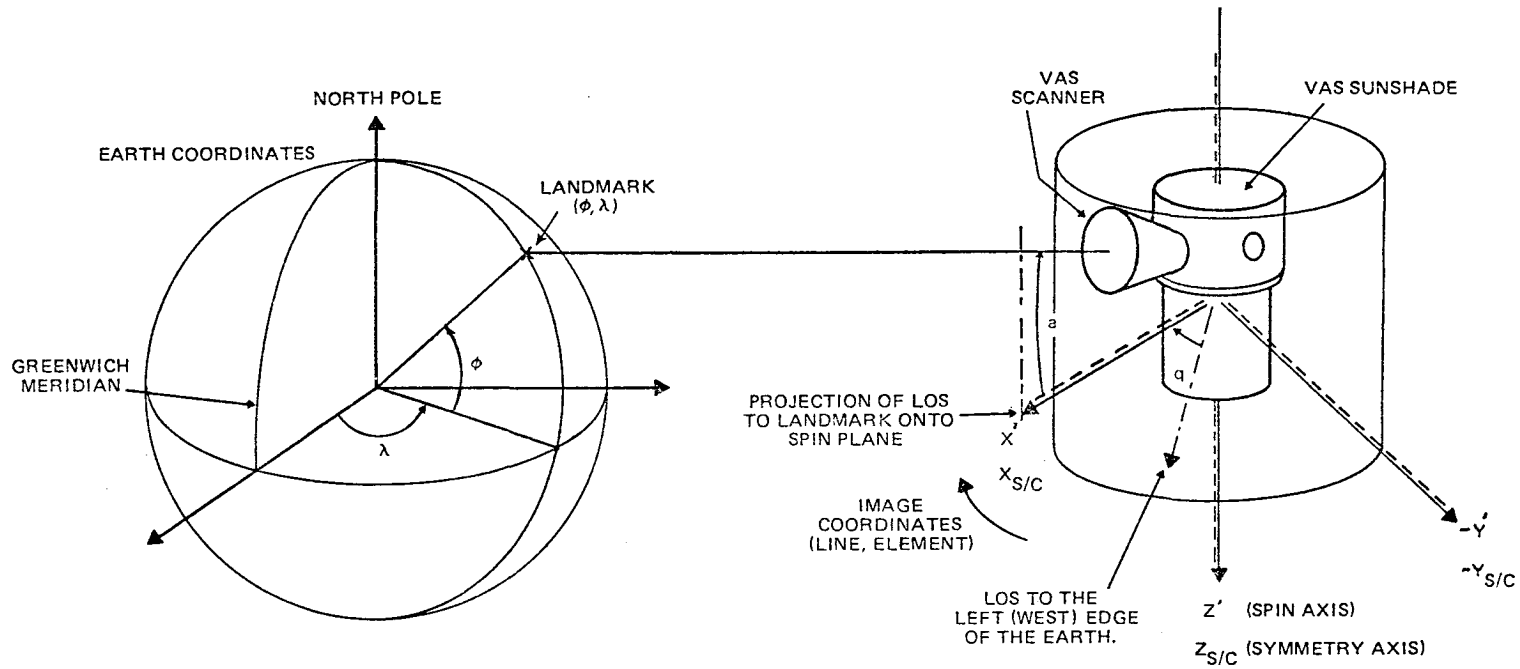
Figure 3.   VAS/GOES Configuration

The satellite spin plane coordinate system, the (x', y', z') system in Figure 3, must be related to the Earth inertial coordinate system in which the satellite position is computed. Figure 4 shows a spacecraft spin plane coordinate system relative to true-of-date coordinates. The x' axis lies in the true-of-date (xz) plane at an angle of χ with respect to the true-of-date (-x) axis. The y' axis forms a right hand orthogonal system.

The transformation matrix S from the (x, y, z) system into the (x', y', z') system is

$$
\begin{bmatrix} x' \\ y' \\ z' \end{bmatrix} = S \cdot \begin{bmatrix} x \\ y \\ z \end{bmatrix} = \begin{bmatrix} -\cos\chi & 0 & \sin\chi \\ \sin\psi\sin\chi & \cos\psi & \cos\chi\sin\psi \\ -\cos\psi\sin\chi & \sin\psi & -\cos\psi\cos\chi \end{bmatrix} \begin{bmatrix} x \\ y \\ z \end{bmatrix} \quad (3)
$$

Since the positive spin axis z' is nearly aligned with the negative z axis of the true-of-date system, the angles χ and ψ will always be relatively small. Also shown on Figure 4 are the right ascension and declination angles (α, δ) which are conventionally used to represent the location of the z' axis. The declination angle is near -90 degrees. The relation of (χ, ψ) to (α, δ) is

$$
\tan\chi = \frac{\cos\alpha}{\tan\delta}
$$
$$
\sin\psi = \sin\alpha\cos\delta. \quad (4)
$$

The location of the z' axis in (α, δ) is expressed as a time varying function as

$$
\delta = \delta_0 + \delta_1 t + \delta_2 \sin(\delta_3 t + \delta_4) \quad (5)
$$

and

$$
\alpha = \alpha_0 + \alpha_1 t + \alpha_2 \sin(\alpha_3 t + \alpha_4) \quad (6)
$$

The model represented by equations (5) and (6) is a symmetric one. Because of the spin stability of the S/C axis, perturbations to (α, δ) or (χ, ψ) are expected to be small.

228
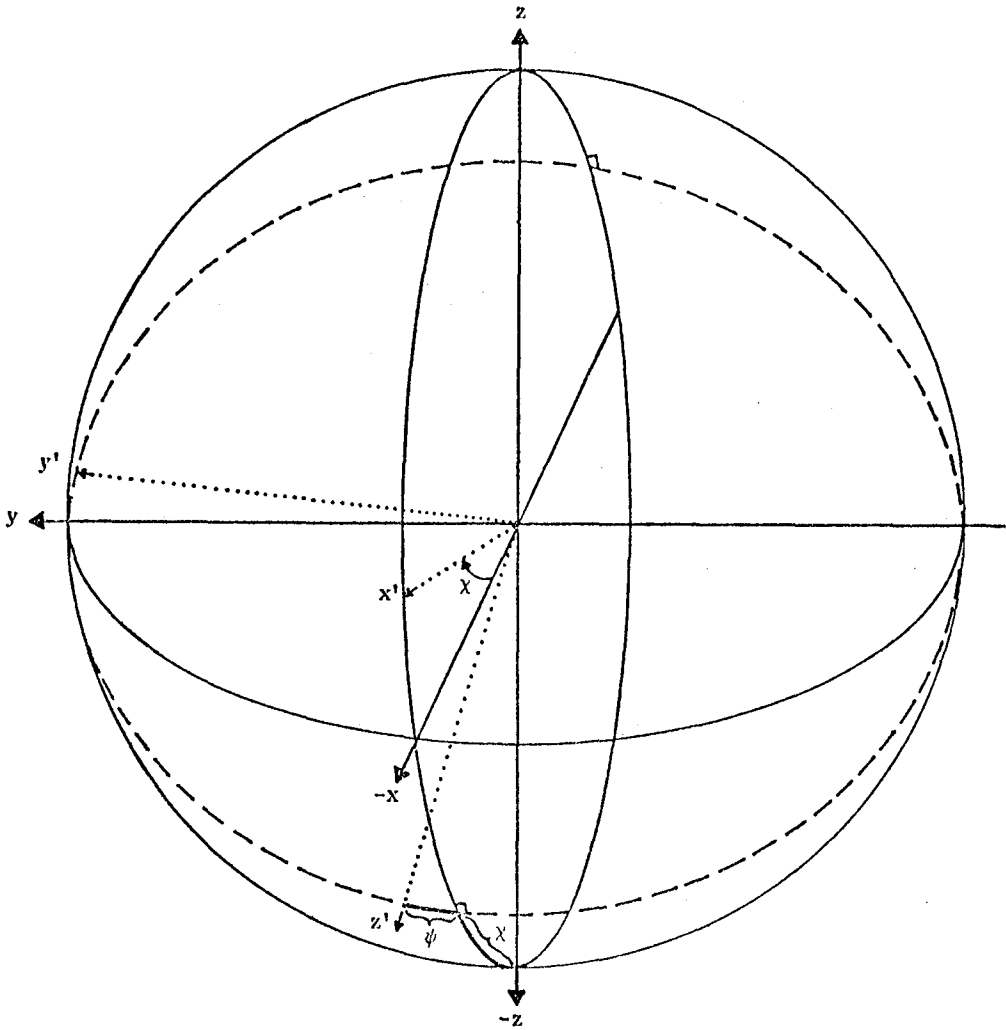
NOTES: (1) (x, y, z) is the true-of-date system. The (xy) plane is the true-of-date Earth's equatorial plane, while z points along the Earth's axis of rotation.

(2) (x', y', z') is the spacecraft spin system. The positive z' axis lies roughly in the direction of the -z true-of-date axis.

(3) The x' axis lies in the xz plane at an angle X above the -x axis. Hence, X is measured in the (x, z) (or, equivalently, (-x, z)) plane from the -x axis to the +x' axis. The angle X is measured positive towards the +z axis.

Figure 4.   True-of-Date and Spin Plane Coordinates

Since the spin axis is nearly aligned with the negative z axis of the true-of-date system, the right ascension angle, α, is sensitive to the precision with which it is computed. For example, if the magnitude of the xy plane projection of z' (line OA in Figure 4) is nearly zero, then a change in sign would cause α to change by 180 degrees. Such a change can occur on successive iterations in the estimation process. The result would be to create divergent oscillations in the attitude correction vector (α, δ). Therefore, it is advantageous to use the (χ, ψ) coordinates for the spin axis location.

The angle ψ is analogous to declination and is the angle between the xz true-of-date plane and the spin axis. It is measured from the xz plane (perpendicular to the xy plane) to the z' axis. The angle χ is analogous to right ascension and is the angle between the z axis and the projection of the spin axis onto the xz plane.

The model for the (χ, ψ) coordinates of the spin axis can be written in a form similar to those of equations (5) and (6)

$$\psi = \psi_0 + \psi_1 t + \psi_2 \sin(\psi_3 t + \psi_4) \tag{7}$$

and

$$\chi = \chi_0 + \chi_1 t + \chi_2 \sin(\chi_3 t + \chi_4). \tag{8}$$

Figure 5 shows the S/C symmetry coordinate system. The $z_{S/C}$ axis is parallel to the S/C longitudinal symmetry axis and $x_{S/C}$ points to the zero elevation angle in the actual VISSR plane. The S/C symmetry plane is perpendicular to the S/C symmetry aixs and is the reference plane from which the true camera elevation is measured. Two VISSR planes are shown; the actual VISSR plane is the plane swept out in elevation as the camera is moved from one spin cycle to another, while the nominal VISSR plane is the plane in which the camera motion is supposed to occur. The angle (measured in the symmetry plane) between the sun sensor plane and the nominal VISSR plane is γ_0.

$Z_{S/C}$ SPACECRAFT LONGITUDINAL
SYMMETRY AXIS

NOMINAL
VISSR PLANE

ACTUAL VISSR
PLANE

$Y_{S/C}$

CAMERA DURING
SPIN n + 1

Δa

γ_0

SUN SENSOR
PLANE

DURING SPIN n

a

$\Delta\gamma_0$

ζ

$X_{S/C\ 0}$

S/C SYMMETRY PLANE

THE NOMINAL ZERO
ELEVATION SETTING
FOR THE CAMERA

$X_{S/C}$
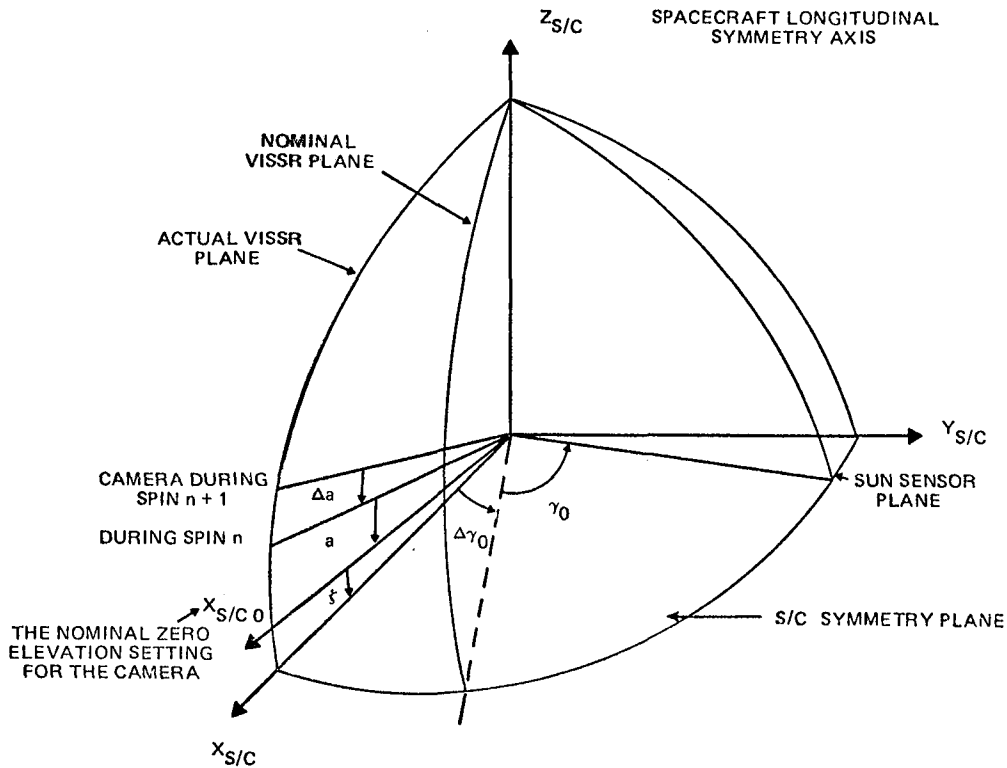
$(X_{S/C},\ Y_{S/C},\ Z_{S/C})$ THE S/C SYMMETRY COORDINATE SYSTEM; $Z_{S/C}$ IS PARALLEL TO
THE S/C LONGITUDINAL SYMMETRY AXIS, $X_{S/C}$ POINTS TO THE ZERO
ELEVATION ANGLE IN THE ACTUAL VISSR PLANE.

γ_0 THE ANGLE IN THE SYMMETRY PLANE BETWEEN THE NOMINAL VISSR
AND THE SUN SENSOR PLANE

$\Delta\gamma_0$ THE ANGLE IN THE SYMMETRY PLANE BETWEEN THE NOMINAL AND
ACTUAL VISSR PLANES

ζ IS THE ELEVATION BIAS ANGLE; THE ANGLE MEASURED IN THE
ACTUAL VISSR PLANE BETWEEN THE CAMERA WHEN IT IS SET AT
A ZERO ELEVATION SETTING AND THE TRUE ZERO ELEVATION

a   THE ELEVATION ANGLE OF THE CAMERA DURING THE nTH SPIN

Δa THE ELEVATION INCREMENT DURING EACH SPIN.

Figure 5.   Spacecraft Symmetry Coordinate System

231

The angle measured in the S/C symmetry plane between the actual and nominal VISSR planes, $\Delta\gamma_0$, is the first camera bias. A second camera bias is ζ, which is an elevation (or line) bias angle. When the camera is set at a zero elevation setting, represented by line $x_{S/C0}$, its true elevation angle is ζ. Angle a is the elevation of a landmark above (or below) the nominal zero elevation point and Δa is the amount by which the elevation is incremented each spin cycle. At the beginning of a picture, a is set to a negative value corresponding to the northern part of the earth and then incremented to positive values towards the southern portion of the earth.

Figure 6 shows the spin plane (or attitude) coordinate system first introduced in Figure 4. Because of the inertial motion of the spin axis (equations (7) and (8)) and the rotation of the earth, the location of a landmark with respect to the spin frame is changing. Moreover, the daily motion of the sun and the spin axis inertial motion causes the solar positions to change with respect to the spin coordinates. However, at the time of a landmark observation, t_S, the azimuth of a landmark, γ_2, and the azimuth of the sun, γ_1, can be determined with respect to the spin system.

Figure 7 shows the spin coordinate system relative to the S/C symmetry frame. The symmetry frame is rotating with respect to the spin frame but Figure 7 depicts the instant that the VISSR plane intersects with x' axis of the spin frame. Notice that the $x_{S/C}$ axis is shown coincident with the x' axis at this instant. This choice is tantamount to forcing the z' axis to lie in the $y_{S/C} z_{S/C}$ plane. This choice as allowable because the bias ζ can absorb the elevation difference (between x' and $x_{S/C}$) which would occur if z' did not lie in the $y_{S/C} z_{S/C}$ plane at this moment.

An angle ρ is defined as the angle, measured in the spin plane, between the nominal VISSR and actual VISSR planes. This represents an azimuthal bias which allows the modeling of error in the azimuthal location of the VISSR plane.

Z' SPIN AXIS

DIRECTION OF A LANDMARK

Y'

a'

γ_2

γ_1

SPIN PLANE

PROJECTION OF THE SUN DIRECTION
ONTO THE SPIN PLANE

$\hat{X}'_{SUN}$

X'
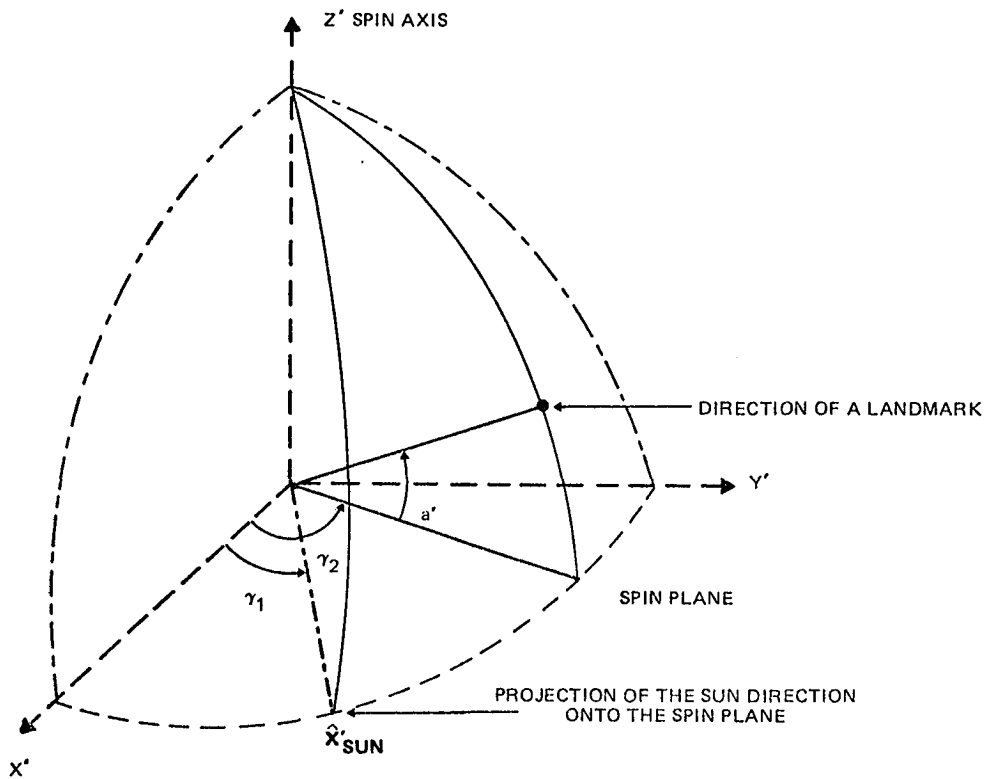
(X', Y', Z')   IS THE SPIN COORDINATE SYSTEM; Z' POINTS ALONG THE SPIN AXIS, Y'
IS DEFINED SO THAT IT IS NORMAL TO THE SPIN AXIS AND LIES IN THE
TRUE-OF-DATE XY PLANE, X' FORMS A RIGHT HANDED SYSTEM WITH
Y' AND Z'.

γ_1 THE AZIMUTH OF THE SUN IN THE SPIN PLANE

γ_2 THE AZIMUTH OF THE LANDMARK IN THE SPIN PLANE.

a'   IS THE ELEVATION ANGLE OF A LANDMARK ABOVE (OR BELOW) THE
SPIN PLANE.

Figure 6.   Spin Plane Coordinate System

233
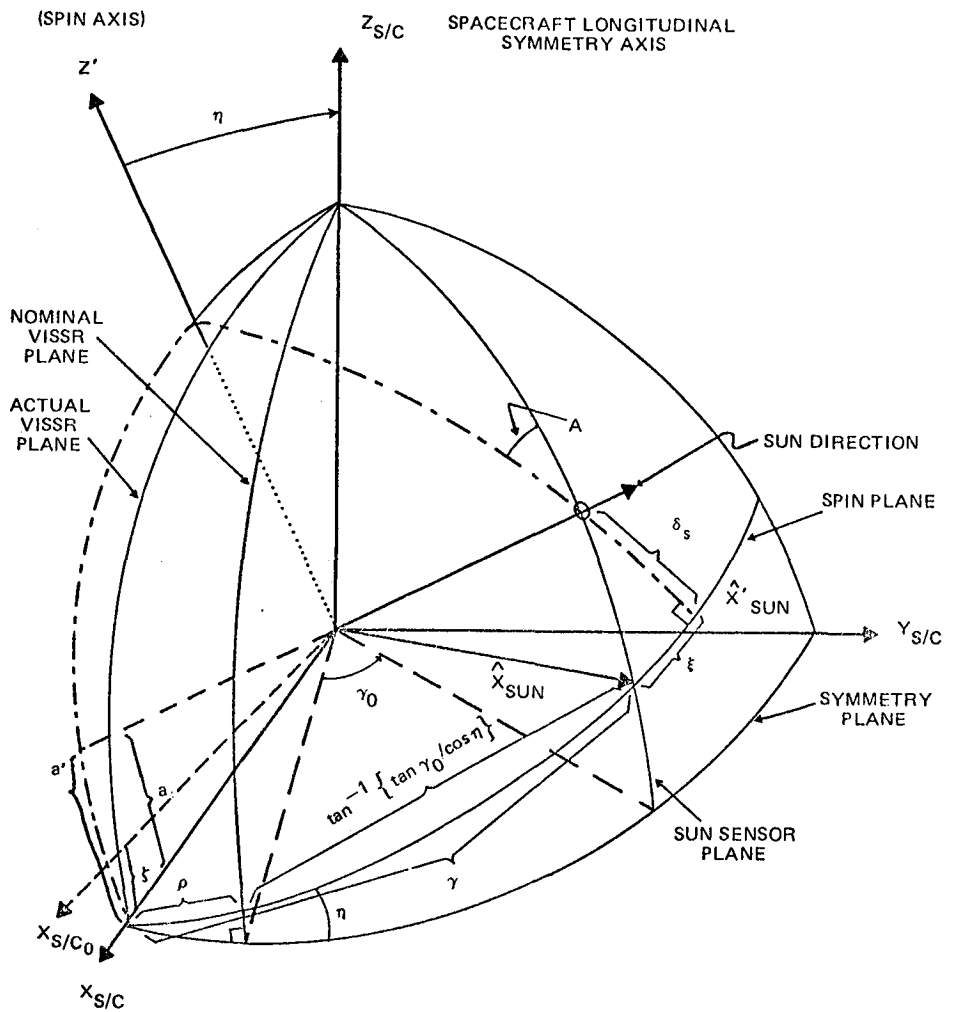
NOTES:

Z′ LIES IN THE $Z_{S/C} Y_{S/C}$ PLANE

a′ IS THE ELEVATION ANGLE OF THE LANDMARK IN THE SPIN SYSTEM

a + ζ IS THE CORRESPONDING ELEVATION OF THE LANDMARK MEASURED IN THE ACTUAL VISSR PLANE

ζ   IS THE CAMERA ELEVATION MISALIGNMENT BIAS.

Figure 7.   Camera and Spin Biases

234

The angle γ is the angle in the spin plane between the actual VISSR plane and the sensor plane, and a is the elevation of the camera at the time a landmark was observed in the S/C symmetry coordinate system.

Since $\hat{X}$'sun, $\hat{X}$sun and the sun direction form a right spherical triangle,

$$\xi = -\tan^{-1}(\tan A \sin \delta_S) \quad . \tag{9}$$

The picture coordinate, ℓ, is the line number or elevation coordinate and is given by,

$$\ell = \frac{a - \zeta}{RPL} + \ell_o \tag{10}$$

where RPL is the radians/line conversion constant and ℓ_o is the line corresponding to a = 0. In practice the elevation angle a' is found in the spin plane and then converted to a.

The second picture coordinate, e, corresponds to an azimuthal angle (measured in the spin plane) between the left (west) edge of the earth and the landmark. The situation is shown in Figure 8 which depicts the spin plane as viewed from the north. The satellite is spinning clockwise. The picture coordinate, e, is thus,

$$e = \frac{\gamma_2 - \gamma_1 - \beta + \gamma - \xi}{RPE} \quad \text{mod } 2\pi \tag{11}$$

where RPE is the number of radians per element and β is the angle through which the satellite has turned from the instant of sun observation by the sun sensor to the observation of the left edge of the earth by the VISSR. The angle γ_1 is the azimuth of the sun and γ_2 the azimuth of the landmark. The angle β is determined by finding, for each line of the picture, the first or leftmost pixel of that line. Each revolution, a body-mounted sun sensor on the satellite detects the sun and produces a sun pulse. For each revolution, a time interval called the β-time (T_β), is computed. This time, which should elapse between the sighting of the sun by the sun sensor and the alignment of the camera with the
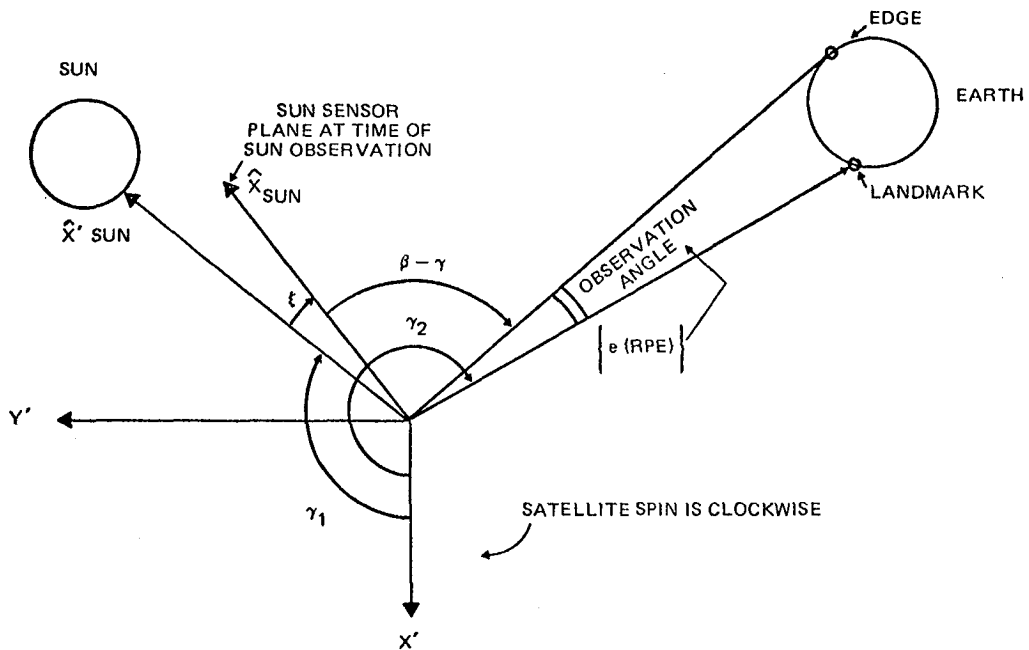
THIS IS A VIEW OF THE SPIN PLANE SEEN FROM THE NORTH. THE (X' Y' Z') SPIN SYSTEM IS RIGHT-HANDED BUT APPEARS LEFT-HANDED IN THIS FIGURE BECAUSE THE SPIN VECTOR Z' IS POSITIVE INTO THE PAGE.

γ_1 IS THE AXIMUTH OF THE SUN (AT TIME t_s)

γ_2 IS THE AZIMUTH OF THE LANDMARK (at t_s)

β IS THE ANGLE THAT THE S/C HAS SPUN BETWEEN THE OBSERVATION OF THE SUN BY THE SUN SENSOR AND THE OBSERVATION OF THE LEFT EDGE OF THE EARTH BY THE USER.

γ IS THE PROJECTION OF THE ANGLE BETWEEN THE VISSR AND SUN SENSOR PLANES.

t_s IS THE OBSERVATION TIME OF THE LANDMARK.

Figure 8.   Spin Plane

236

desired left edge of the earth picture, is used to detect the first element of each line. For each line, the values T_β and t_0 (time of the average sun pulse) are available as recorded data. Since there are 3144960 counts per half spin

$$\beta = \frac{\pi T_\beta}{3144960} \quad \text{(radians)} \tag{12}$$

or

$$\beta = \frac{\pi(T_\beta - 8 \cdot 16^5)}{3144960} + \pi \tag{13}$$

when the sun pulse is 180 degrees out of phase.

SECTION 4 – NUMERICAL RESULTS

The sample results shown below (Figure 9) are for a three day span of SMS-2 data obtained from three images taken twenty-four hours apart. Additional preliminary results taken from NAVPAK runs using a longer data span supplied by NOAA indicates that sub-pixel accuracy is possible by using a suitable set of solve-for parameters and a longer, denser data set. The full results of these and other evaluations of VAS/NAVPAK (e.g., force and attitude model evaluations, propagation/prediction capability evaluation, etc.) will be published in a future paper.

ITERATION REPORT FOR ITERATION   3

CURRENT WEIGHTED RMS   0.727066D+01   PREDICTED WEIGHTED RMS   0.000000D+00
PREVIOUS WEIGHTED RMS   0.727209D+01   SMALLEST WEIGHTED RMS   0.727209D+01
RELATIV CHANGE IN RMS   0.196389D-03   **** DC   CONVRGED   ****
START= 750830 150436.60   END= 750901 150600.09   EPOCH= 750830 150000.00

--- OBSERVATION SUMMARY BY TYPE ---

TYPE	TOTAL NO.	ACCEPTED	WEIGHTED RMS	MEAN RESIDUAL	STANDARD DEV
ELEM	29	24	0.6566D+01	-0.2211D-01	0.3283D+01
LINE	29	24	0.7913D+01	-0.1195D-02	0.3956D+01
RANG	0	0	0.0000D+00	0.0000D+00	0.0000D+00
RDIF	0	0	0.0000D+00	0.0000D+00	0.0000D+00

KEPLERIAN ELEMENTS AND LANDMARK MODEL ATTITUDE PARAMETERS FOR ITER   3

PARAMETER		SOLVE?	CURRENT	PREVIOUS	STA.DEV
SMA	(KM)		42164.9041	42164.9041	
ECC			0.0040	0.0040	
INCL	(DEG)		1.8162	1.8162	
MLON	(DEG)		128.2253	128.2253	
CHI-1	(DEG)	YES	0.4938	0.4938	0.3253D-01
CHI-2	(D/S)		0.0000	0.0000	
PSI-1	(DEG)	YES	-1.8674	-1.8674	0.2964D-01
PSI-2	(D/S)		0.0000	0.0000	

CARTESIAN COORDINATES AND LANDMARK BIASES FOR ITER   3

PARAMETER		SOLVE?	CURRENT	PREVIOUS	STA.DEV
X	(KM)	YES	-26340.0797	-26340.0797	0.2800D+01
Y	(KM)	YES	32882.0857	32882.0857	0.4616D+01
Z	(KM)	YES	-778.1918	-778.1918	0.8142D+01
XDOT	(K/S)	YES	-2.4089	-2.4089	0.1779D-02
YDOT	(K/S)	YES	-1.9121	-1.9121	0.1662D-02
ZDOT	(K/S)	YES	0.0790	0.0790	0.3193D-03
BIAS-1	(DEG)	YES	0.0970	0.0970	0.4514D-01
BIAS-2	(DEG)		0.0000	0.0000	
BIAS-3	(DEG)		0.0000	0.0000	

Figure 9.   Sample Numerical Results

REFERENCES

1.   D. L. Hall and S. R. Waligora, "Orbit/Attitude Estimation with Landsat-1 and -2 Landmark Data" (Paper 79-152, presented at the AAS/AIAA Astro-dynamics Specialist Conference, Provincetown, MA, June 1979).

2.   A. J. Fuchs, C. E. Velez, and C. C. Goad, "Orbit And Attitude State Recoveries from Landmark Data," Journal of Astronautical Sciences, Vol. 23, No. 4, pp. 369-381, October-December 1975.

3.   National Aeronautics and Space Administration, Goddard Space Flight Center, S-582-76-77, Mathematical Theory of the Goddard Trajectory System, edited by J. O. Cappellari, C. E. Velez, and A. J. Fuchs, April 1976.

4.   Computer Sciences Corporation, CSC/SD-76/6094, Navigation Package (NAVPAK) System Description, L. D. McQuinn and R. A. Borenstein, September 1976.

5.   U. S. Government Memorandum, "VAS Orbit/Attitude/Navigation," H. E. Montgomery, October 20, 1977.

ONBOARD IMAGE CORRECTION

D. R. Martin, A. S. Samulon, and A. S. Hamori
TRW Defense and Space Systems Group

ABSTRACT

This paper describes a processor architecture for performing onboard geometric and radiometric correction of LANDSAT imagery. The design uses a general purpose processor to calculate the distortion values at selected points in the image and a special purpose processor to resample (calculate distortion at each image point and interpolate the intensity) the sensor output data. A distinct special purpose processor is used for each spectral band. Because of the sensor's high output data rate, 80 M bit per second, the special purpose processors use a pipeline architecture. Sizing has been done of both the general and special purpose hardware.

I. Introduction

In performing analyses of imagery produced by earth resource observation satellites, it is frequently desirable that two images of the same scene be registered; that is, each physical part of the scene is in the same location on the two images so that the picture elements (pixels) of the two images can be aligned. Such precision is not easy to attain, mainly because of varying distortions and viewing conditions from one image to the next. Registration can be accomplished, however, by estimating these distortions and processing the image data accordingly.

With the advent of LANDSAT D, currently under development, earth resource observation satellites are coming closer to operational, rather than experimental, use.

Key features of LANDSAT D are:

o Ground sample distance of thirty meters

o Geodetic accuracy to 3 meters (RMS) using ground processing

o Visible, near infrared, and thermal infrared spectral bands

o Swath width of 185 kilometers

o Repeated coverage every sixteen days

o Seven spectral bands having eight bit radiometric resolution

While the features of LANDSAT D are all desirable for an operational system, several elements must be added to create a truly operational system. Chief among these is rapid receipt of corrected imagery by the user. Due to the high data rate (10 million picture elements per second), present plans for LANDSAT D involve geometric correction (on the ground) of only ten per cent of the (over land) imagery. Corrected imagery will be produced within two days of transmission with shipment through the mail adding several more days delay between imaging and availability of the data.

LANDSAT D consists of a Multimission Modular Spacecraft (MMS) combined with an instrument module containing the Thematic Mapper (TM). As the spacecraft passes over a region, the TM scans back and forth, as shown in Figure 1. Each scan contains 16 scan lines spaced at approximately 30 meter intervals and provides coverage of seven spectral bands. In each spectral band, the moving image is swept past an array of detectors by the scan mirror action. Each detector combined with mirror scan motion produces one image line in one spectral band. The scan line corrector compensates for spacecraft motion during the scan, thus yielding straight scan lines perpendicular to the spacecraft velocity vector. As the ground footprint of each detector moves 30 meters cross-track, its output is sampled and converted to an 8 bit digital word. These words are then multiplexed to form an 83.268 Mbps data stream.
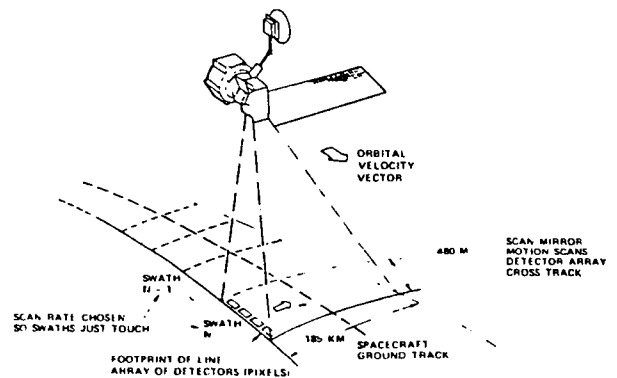
Figure 1. Multispectral Scanning Sensor Geometry

The on-board processing technique described in this paper will provide corrected data in real-time. The registration accuracy, although not as good as that produced by ground processing, will be approximately half the ground sample distance (15 meters). The expected accuracy should be quite sufficient for doing crop yield assessment using multi-date imagery, change detection, and determining progress of environmental disturbances such as crop disease and fire. Further processing on the ground will still be able to provide the extremely high accuracy imagery required relatively infrequently for mapping purposes.

The primary factors that are making on-board image correction viable are: 1) the extremely high accuracy ephemeris information to be available in realtime from the Global Postioning System (GPS), 2) the availability of small, high density, low power memories, and 3) high speed, low power processors.

Even with these technological advances, practical solution of the on-board correction problem requires a subsystem architecture that is a balanced combination of a general purpose computer and special purpose hardware using both parallel and pipeline processing.

More specific details on both the sources of distortion and the geometric correction technique can be found in Reference 1.

II. Registration Problem

Two images of the same region are said to be registered when each physical part of the scene is in the same location in each image. This allows direct comparison of different images of the same region. Unfortunately, unprocessed images do not meet this criterion because of the distortions contributed by the sources discussed in Section III. Ground or on-board processing can be used to correct the imagery. Depending on the amount of on-board correction, the amount of additional ground processing required to complete correction of the imagery will vary. Some of this additional ground processing is very simple and can be done readily by individual users. Therefore, it is important to consider the degree of correction obtainable with different amounts of on-board processing. In this section various levels of registration are defined. To achieve each successive level requires additional on-board capability.

Isodistance Registration

Isodistance registration of different images of the same region requires the scene to have constant interpixel distance and parallel scan lines. Figure 2 illustrates this concept. In the unprocessed images, the distance between pixels is unequal. After isodistance registration has been accomplished, the distance between pixels is
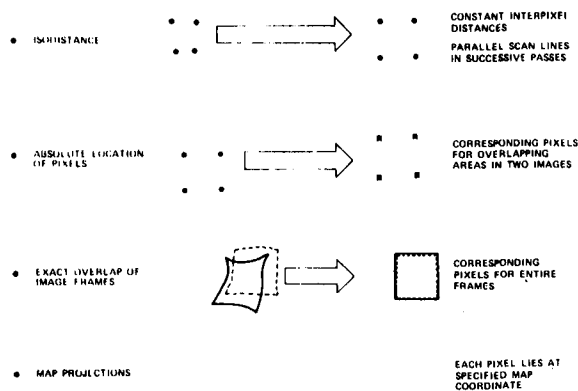
Figure 2. Registration Levels

the same in each image and scan lines are parallel. If the relative alignments of the two isodistance registered images were known, they could be lined up and compared since any two given locations in a scene are separated by the same number of pixels for any two isodistance registered images of the scene. However, knowledge of this misalignment is not required for the on-board isodistance registration. In fact, direct comparison of pixels still will most likely require further interpolation since the relative shift between corresponding pixels is not necessarily an integer number of pixels.

Absolute Location of Pixels

Absolute location of pixels accomplishes everything that isodistance registration accomplishes. In addition, the relative alignment of the two images being compared is always a known number of pixels. This allows direct comparison of the intensity of corresponding pixels without further resampling. This is illustrated in Figure 2 by showing that the square regions can be made to coincide.

In comparison to isodistance registration, the absolute location registration requires a more precise distortion measurement technique. The absolute magnitude of all distortions is important now, not just those which vary during the scene. The corresponding correction technique is comparable for isodistance registration and absolute location registration. Since subsequent resampling on the ground is avoided by absolute location registration, it is clearly advantageous to do it. However, whether or not it can be done depends upon the capability of the on-board distortion measurement technique.

Exact Overlap of Image Frames

The pixels in images which are absolute location registered can be compared by extracting corresponding portions of the two images. Note that the edges of the scene are not required to overlap. Consequently, if subsequent imagery is used to compare with a reference scene, up to four images must be used to reconstruct the same region covered by the original image. This difficulty is overcome by exact overlap registration, which causes the pixels of subsequent images to be in the same position as in the reference images.

This level of registration requires the same distortion measurement capability as absolute location registration. The dichotomy between absolute location registration and exact overlap registration is in the geometric correction technique which must be employed. Relatively little ground processing is saved by this technique compared to absolute location registration. However, if the increase in on-board processing complexity is relatively small, this additional level of registration is worthwhile.

Map Projection Rectification

Map projection rectification requires each pixel in an image to lie at a specified map coordinate; furthermore, the interpixel spacing must correspond to that of the map projection. This requires more than registration, since the repeatability of imagery does not guarantee the image corresponds to any type of map projection.

Production of images which are rectified with
respect to a well-known map projection (e.g., Uni-
versal Transverse Mercator or Space Oblique Mer-
cator) is not attempted in this implementation.
A significant amount of on-board storage is re-
quired to produce map projections such as these.
However, distortion due to earth rotation is
important to eliminate, since this rotation will
affect different images of the same region in a
different way. This requires some sort of map
projection to provide a measure of the effect of
earth rotation. Such a map projection does not
need to be a conventional map projection.

III. Sources of Distortion

Raw data received from the Thematic Mapper
cannot be directly registered with other data scan-
ned on previous passes over the same region because
each unprocessed image is affected by a unique set
of distortions. The four primary causes of dis-
tortion are:

    o Sensor Caused Distortions

    o Attitude Variation

    o Alignment Variation

    o Ephemeris Variation

Image distortion will result in a correspond-
ing registration error if the distortion is not
estimated and removed. After performing this geo-
metric correction, the resulting registration error
is determined by the accuracy with which the dis-
tortion is estimated, not by the actual magnitude
of the distortion. In this section no estimation
or correction is assumed, hence distortion and
registration error are virtually synonymous con-
cepts here.

Sensor Caused Distortion

The scanning motion of the Thematic Mapper
must be precisely the same on successive passes
over a region if no distortion is to be introduced.
Variation in the active scan duration (i.e., scan
velocity) will cause stretching (or compression) of
the pixel spacing within a scan line. Variation in
the scan period will cause the spacing between scan
lines to be different for subsequent images of a
region, causing different images of the same region
to have a different number of scan lines. Figure 3
illustrates these variations.

In addition to variation in scan period and
active scan duration, an additional source of dis-
tortion is scan nonlinearity. That is, the angular
velocity of the scan mirror does not remain pre-
cisely constant during the scan, thus producing
irregularly spaced pixels.

Attitude Variation

In the normal mode of operation, the attitude
of the spacecraft can be commanded to take on any
desired value. Nominally, the attitude is such
that the scans are perpendicular to the orbital
velocity vector with the Thematic Mapper pointing
towards the center of the earth at mid scan. The
attitude of the spacecraft is controlled by the
attitude control system located in the spacecraft.
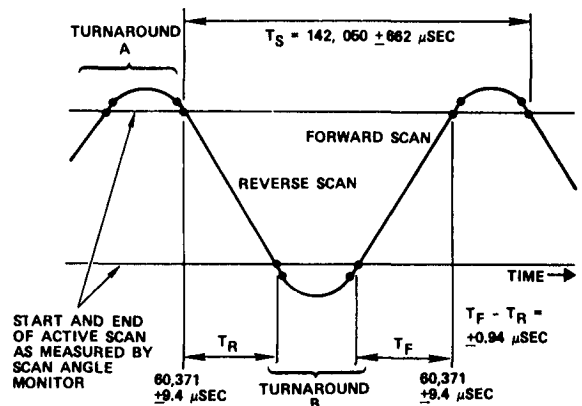
Figure 3. Thematic Mapper Scan Durations

Variation in the absolute attitude of the
spacecraft with respect to a previous pass will
cause an absolute location registration error pro-
portional to this attitude variation. Such vari-
ation is limited by the accuracy of the star
tracker. Isodistance registration requires a
stable attitude reference during the scene, but is
relatively unaffected by the absolute accuracy of
this reference. Consequently, isodistance regis-
tration is primarily determined by the gyro drift
in the stellar-inertial attitude reference system.

Alignment Variation

The attitude of the spacecraft is controlled
by the attitude control system which is located in a
separate structure than the Thematic Mapper. For
the reasons previously cited, the attitude of the
Thematic Mapper must be held constant (with respect
to the earth-pointing frame of reference) to pre-
vent distortion. However, the coordinate axes of
the Thematic Mapper are not the same as those of
the Attitude Control System. The difference be-
tween these sets of axes exhibits both long term
drift and a short term variation due to thermal
effects. Consequently, even if the spacecraft's
attitude were to remain constant, alignment
variation would distort the scanned image.

Ephemeris Variation

The location of the spacecraft with respect to
the ground at a given time of day can vary signi-
ficantly for different passes over a region.
Pixels compared at the same time of day for sub-
sequent passes, with no knowledge of spacecraft
location, can have a significant offset in pixel
location. Absolute location registration requires
that this offset be known and corrected and is es-
sential if different images of the same region are
to be compared.

Variation in the spacecraft altitude for dif-
ferent passes over a region affects pixel spacing
in the cross track direction for both isodistance
and absolute registration. Except for the effect
of variation in the orbital velocity, the differ-
ence in the spacecraft's along track and cross
track position has no impact on isodistance dis-
tortion. The altitude and orbital velocity of the

244

spacecraft changes very little in comparison to the cross track drift for different passes over a region. Consequently, isodistance distortion caused by ephemeris variation is far smaller than the corresponding absolute distortion.

Correcting these variations requires more than a simple shift of the image. Specifically, perspective differences and earth rotation will combine to distort the image data if the spacecraft is not in precisely the same location as on previous passes. Perspective difference arises in part because the Thematic Mapper samples the detectors at equally spaced angular increments. Because of this, the pixel spacing on the ground increases with distance away from the ground track. This variation in pixel spacing prevents simply shifting the image to produce alignment. Earth rotation shifts the scene during the scan, thus producing an image which is significantly skewed with respect to a conventional map projection of the earth's surface. In addition, earth rotation causes skewing of scan lines for different images of the same region.

IV. Distortion Estimation

Registration is accomplished in two steps: estimation or measurement of the various possible factors which affect registration, and compensation for these factors either through data manipulation or spacecraft commands. The first step of this process is the topic of this section; the second step will be addressed in the next section.

The accuracy with which these distortions can be estimated is of particular concern. After the images have been corrected based on the distortion estimate, the remaining registration error is caused primarily by the error in estimating the distortion. The technique usually employed to estimate distortion on the ground uses ground control points which consist of 32 by 32 pixel subimages with known location. The received imagery is correlated with the ground control point to determine the proper position of one pixel. A dynamic model is used for the distortion, with the correlation information serving as observations of the distortion process. By using Kalman filtering, the distortion at each pixel in the image can be estimated and corrected. Variations which occur at a higher frequency than can be measured by ground control points must be measured by some other technique or else simply ignored if they are sufficiently small.

Unfortunately, the use of ground control points requires a significant processing and data storage capability. In order to make on-board processing viable, the distortion measurement technique described here does not use ground control points. The sensor-caused distortions are measured by the scan angle monitor. Alignment is calibrated in a preoperational mode from the ground station by using ground control points. This alignment is transmitted up to the spacecraft and periodically updated. Attitude is determined by using a stellar-inertial attitude reference system which uses an advanced star tracker design. Ephemeris is determined from the Global Positioning System (GPS).

Although this technique is not as accurate as one using ground control points, it is still capable of producing sub-pixel registration. In fact, in the isodistance sense the registration is nearly as good as can be obtained with ground control points. Table 1 summarizes this performance. The pixel spacing for the Thematic Mapper is 30 meters, which means these registration errors are approximately ½ pixel.

Table 1.   One-Sigma Registration Error for On-Board Distortion Measurement Techniques

DISTORTION SOURCE	ALONG-TRACK ERROR (METERS)	CROSS-TRACK ERROR (METERS)
SENSOR	1.6	1.3
MISALIGNMENT	7.3	5.2
ATTITUDE	10.3	10.2
EPHEMERIS	5.0	5.0
RSS	13.7	12.6

Measuring Sensor Distortions

Of all the sources of sensor-caused distortion, by far the largest is variation in scan duration. The Thematic Mapper contains a scan angle monitor which furnishes accurate information both about pixel spacing within a line and pixel spacing between lines. The scan angle monitor (SAM) optically measures when the scan mirror enters the active scan region, when it is at its midpoint, and when it leaves the active scan region. The multiplexer inserts a major frame sync word into the downlink data stream (84 Mbps, interruptible at 8 bit word boundaries) when the SAM indicates the mirror has entered the active scan region. After the end of the scan pulse occurs, the multiplexer inserts an end of scan pattern, line length, calibration and zero restore information.

Scan nonlinearity, if it is significant, will be calibrated for each Thematic Mapper. The extent of this nonlinearity is currently not determined, since Thematic Mapper is not yet operational. A piecewise curve fit can be used to model this nonlinearity, if necessary.

Attitude Determination

The attitude of the spacecraft relative to the true earth-centered inertial frame is determined by 1) approximating the earth-centered inertial frame with an on-board stellar-inertial frame of reference, and 2) commanding the spacecraft to point in a specified direction relative to the stellar-inertial reference.

The three axis attitude reference is derived from integrated gyro data. Attitude and gyro biases are updated periodically from strapdown star tracker measurements which are processed by an on-board algorithm, typically a six-state Kalman filter. If this reference is sufficiently accurate, the attitude distortion is not a matter of concern.

This is possibly the most difficult source of distortion to measure on-board, since the accuracy of the attitude reference system is typically far less accurate than the estimate obtained with ground control points. By using a star tracker of advanced design, a one-sigma attitude reference system accuracy of 3 arc-sec (each axis) is achievable. This is sufficient to attain sub-pixed registration. Even without an advanced star tracker, the isodistance registration will still be excellent.

Alignment Calibration

The attitude of the Thematic Mapper relative to the stellar-inertial frame must be known if the scan is to be of the desired place on the earth. The relative alignment of the Thematic Mapper and the attitude reference system can be determined readily through the use of ground control points. Any other technique for determining this alignment would be extremely difficult. In order to avoid the use of ground control points in an operational mode, this alignment can be performed periodically on the ground and transmitted to the spacecraft. In the absence of significant mechanical stress being placed on the spacecraft, this misalignment should be relatively small. In any event, the effect of this distortion on isodistance registration is minimal because it is slowly varying.

Ephemeris Determination

When operational, the Global Positioning System (GPS) will provide position information accurate to within 15 meters (three-sigma). By using this information to update a Kalman filter model of the spacecraft's orbit, the position, velocity and acceleration of the spacecraft can be accurately estimated. This processing is performed in the GPS receiver, with the results used as inputs to the image processor.

V. Geometric Correction

In order that all images of the same area on the earth be registered with one another, it is necessary to have a reference coordinate system against which to compare each image as it is generated. The goal of the registration procedure, then, is to generate an output image whose pixels correspond to specific locations in the reference coordinate system. The intensity value of each output pixel must be estimated from the data actually scanned by the Thematic Mapper. Thus the generation of each output pixel requires two steps: 1) determination of the location in the actually scanned data corresponding to the specific output pixel, and 2) estimation of the output pixel intensity value from the neighboring scanned values.

Determination of the location in the scanned data corresponding to a specific output pixel requires relating the scanned data to the reference coordinate system. This relation is computed using the GPS ephemeris data, the attitude sensor and control system output, Thematic Mapper scan monitor outputs, and occasional alignment updates. Appropriate selection of the reference coordinate system used is crucial to practical on-board implementation of geometric correction because it affects the amount of data that must be buffered. Because of the complexity of the com-putation relating scanned data to the reference coordinate system, the complete calculation is performed only for a selected subset of points in the coordinate system. The location in the scanned data corresponding to other points in the reference coordinate system is estimated using an interpolation polynomial.

Once the correspondence has been established between locations in the output frame and the scanned data, neighboring scanned values are used to interpolate an estimate of the intensity value of the output pixel. Because some of the neighboring values are produced by different photodetectors, each with its own nonlinear response to the incident illumination, correction of the detector responses precedes the interpolation process.

Correction Calculation

The output point corresponding to a given input pixel can be computed by using the pierce point calculation. The pierce point calculation uses the ephemeris, attitude, and scan information to determine the latitude/longitude of the input pixel on the earth's surface. This is converted into a point in the output space by using an appropriate map projection. The input point corresponding to a given output point can be determined by iteratively estimating the point in the input space based on the resulting pierce point calculation. This has been shown in ground processing to require at most three iterations.

Although the pierce point calculation can be performed for each output pixel, this requires an enormous computational load. The solution to this problem is the creation of an interpolation grid consisting of a subset of the output picture elements. The distortion is calculated only at the grid points with interpolation used to evaluate the distortion at the other output pixels. Note that this interpolation (which is used to evaluate the geometric distortion) has no relation to the interpolator used to calculate the output pixel intensity (cubic convolution interpolator).

The correction calculation must be performed once each scan (0.07 seconds). This calculation must consequently be made as simple as possible to minimize the on-board processing requirements. The reference map projection (coordinate frame) is of particular concern since the latitude/longitude of each pierce point must be converted to this coordinate frame. Properties desired of the map projection include the following:

o Scan lines nearly parallel to the X-axis of the projection (reduce buffering)

o Valid over the entire orbit

o Simple computationally

o Use elipsoidal model for the earth's radius (allow registration)

o X and Y axes nearly perpendicular (two-dimensional resampling)

Although none of the four projection used for ground processing of LANDSAT D data satisfies these properties, a slight variation of the oblique Mercator projection does. Unlike the space oblique Mercator projection, this projection is not swath continuous and must have a different transformed equator for each image frame.

The use of this projection facilitates the four following simplifications in calculating the distortion at the grid points:

o   A simple cross track distance expression to calculate distance relative to known pierce points

o   Linearity of the vertical distortion across the scan line

o   Avoidance of inverse mapping iterations by making a good initial estimate of the distortion at each grid point

o   Distortion calculation at a reduced number of a grid points, with quadratic interpolation used to calculate the distortion at the remaining grid points

By using the first two techniques, only two pierce point calculations are required per scan. The last two techniques significantly reduce the number of evaluations of the cross track distance expression. A computer program was developed which compared the combination of these four simplifications with inverse mapping of pierce points. It showed that at most 0.03 pixel error results.

Using these techniques, the distortion is calculated at grid points spaced once each 64 output pixels. The distortion is assumed to be the same for all sensors in each of the 16 lines, except for fixed delays associated with the time sequence at which the sensors are sampled. The distortion at the remaining pixels is performed using piecewise linear interpolation. The piecewise linear interpolation is extremely simple computationally; consequently, it can be implemented in special purpose hardware along with the resampling of the imaged data. This is extremely important, since the linear interpolation dominates the grid point calculation in terms of number of operations required.

Radiometric Correction

As mentioned previously, the Thematic Mapper produces sixteen image lines in each of seven spectral bands with each mirror scan. (Actually, the thermal infrared band produces only one-fourth as many lines.) Each of the simultaneously scanned lines is produced by a different photodiode. Ideally the response of each photosensor is linear so that its output is proportional to the intensity of the illumination in the specific spectral band. In practice these sensors do not respond linearly. In fact, each sensor has its own unique response curve that can vary gradually over a period of weeks or months.

It is necessary to correct the response to make it linear before performing the resampling operations used to accomplish geometric correction. This is because the resampling process requires interpolating intensity values between scanned lines. The different responses of the sensors cause discontinuities in the scanned image intensity from line to line. The sensor caused discontinuities between lines will produce incorrect interpolated values. Once the interpolated value is produced, compensation for the radiometric distortion is not possible.

Thus an essential part of the geometric correction process is an initial radiometric correction. This radiometric correction is accomplished as follows: The Thematic Mapper has a calibration procedure by which the response curve of individual detectors can be determined when requested from the ground. We propose to approximate these curve by piecewise linear functions. The breakpoints and slopes of the piecewise linear functions will be stored on the spacecraft. As each new sensor output value is produced, the value will be compared with piecewise linear function for that sensor to obtain a corrected intensity value.

Resampling

After the distortion has been estimated, the location of the pixel centerpoints of the Thematic Mapper imagery is known relative to the pixel centerpoints of the reference image. This is illustrated in Figure 4. The regular grid in solid lines represents the set of output pixels to be generated. Intersections in the grids represent the centerpoints of the individual pixels. The task of resampling is to calculate a set of intensity values for the output pixels, based on estimates derived from the intensity values of the input pixels plus calculated distortions. There are different resampling techniques, but all make use of the values of the input pixels in the vicinity of the output pixel to be calculated. This process is called interpolation.
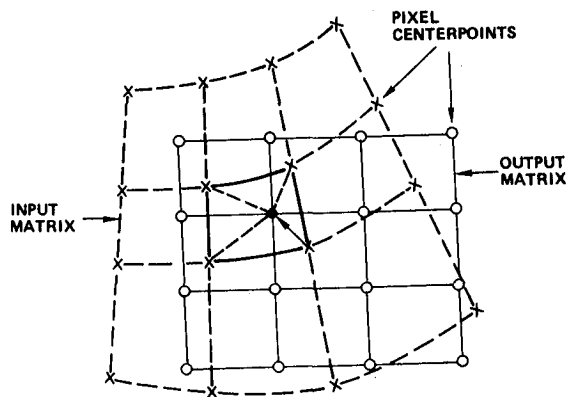
Figure 4.   Resampling with Equally Spaced Output Matrix

Ideally, a two-dimensional bandpass process can be interpolated by passing the imagery through an ideal two-dimensional lowpass filter. The reconstructed image can then be "resampled" at the desired output pixel locations. This is mathematically equivalent to weighting the input pixels according to a two-dimensional (sin x)/x function (the impulse response of an ideal two-dimensional lowpass filter). The (sin x)/x interpolation requires an infinite number of points. However, practical interpolation is accomplished by approximating the (sin x)/x weighting with a relatively small number of input pixels.

Three resampling techniques are in common use today: nearest-neighbor, bilinear interpolation, and cubic convolution. In the nearest-neighbor procedure the value of the nearest input pixel to the desired output pixel is used as the value of that output pixel. Nearest-neighbor resampling is computationally simple, but generally produces distortions in the form of small discontinuities at the edges and borders in an image. It also results in an extremely blocky image.

Bilinear interpolation uses the values of the four pixels surrounding the output pixel to be calculated. The intensity of these pixels are bilinearly averaged to yield the intensity of the output pixels, with the relative weighting depending upon the location of the output pixel. The resulting averaging moves the blockiness of the nearest-neighbor technique but introduces small-scale smearing that results in loss of resolution.

The cubic convolution technique uses the values of the sixteen pixels surrounding the desired output pixel (Figure 4). The weighting function in this case is a two-dimensional cubic spline function which approximates the optimal (sin x)/x interpolator. The one-dimensional cubic spline interpolator (shown in Figure 5) is a piecewise cubic polynominal which is the same as (sin x)/x at the breakpoints and is required to be twice continuously differentiable at the breakpoints. Two-dimensional interpolation is accomplished by performing one-dimensional interpolation within each of the four closet rows to obtain four pixels vertically aligned with the desired output pixel. One-dimensional interpolation in the vertical direction is then performed to obtain the desired output pixel. Interchanging the rows and columns in this procedure yields the same result.

Cubic convolution does not suffer from the blockiness associated with nearest-neighbor interpolation or from the resolution difficulties which plague bilinear interpolution.

$$f'(x) = \begin{cases} 1.0 - 2.25\,|x|^2 + 1.25\,|x|^3 & 0 \le |x| \le 1 \\ 3.0 - 6.0\,|x| + 3.75\,|x|^2 - 0.75\,|x|^3 & 1 \le |x| \le 2 \\ 0 & \text{ELSEWHERE} \end{cases}$$

$$\text{IDEAL } F(X) = \frac{\sin \pi X}{\pi X}$$
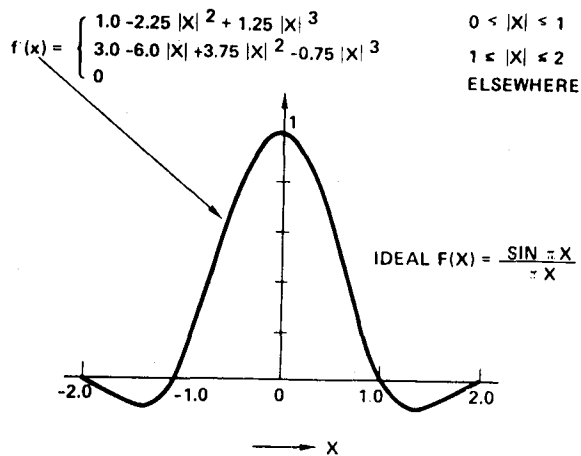
Figure 5. Cubic Spline Interpolation

VI. Implementation

The on-board image processor is functionally divided into two major units: a general purpose programmable processor, and a custom designed resampling processor. A functional block diagram of the entire system is shown in Figure 6. The general purpose processor calculates the recursive distortion coefficients required by the resampling processor and acts as the controller for the resampling processor. The resampling processor performs the along scan and across scan resampling algorithms. In order to perform this resampling, this processor must also perform radiometric correction and skew buffering.
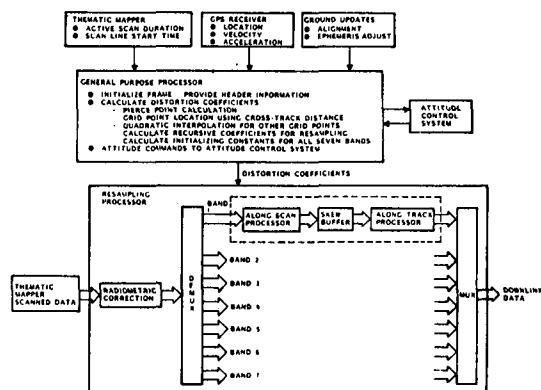
* DOUBLE LINES REPRESENT IMAGE DATA.

Figure 6. On-Board Processing Functional Block Diagram

Computer for Distortion Calculation

During the time required for one scan (0.07 second) the general purpose processor must calculate the distortion coefficients and perform the required control functions for the resampling processor. Table 2 summarizes the number of operations required to perform this calculation. Since virtually all operations require 32 bit accuracy, Table 2 also shows how many single precision (16 bit) operations are required to achieve the required accuracy.

Table 2. Operations Required
for Distortion Calculation

Processing Segment	Number of Operations (Double Precision)				
	Add	Multiply	Divide	Square Root	Trig
Calculate reference points	90	96	10	9	8
Evaluate cross track distance	220	400		20	
Quadratic interpolation	246	336			
Other along scan distortion calculations	202	3			
Cross scan distortion calculation	9	2	1		
Recursive equation initialization	260	140			
TOTAL	1,047	977	11	29	8
Total single precision add/multiply	2,534	4,341			
Total add/multiply per second with factor of two margin	70,952	121,548			

The first processor considered was the NASA Standard Spacecraft Computer - I. Unfortunately, this processor is approximately five times too slow to calculate the distortion coefficients.

The NASA Standard Spacecraft Computer - II was also considered. Its full parallel floating point structure reduces the double precision multiply time to 33.5 microseconds. Consequently, this computer may be capable of performing the distortion calculation, provided the factor of two margin is not required. Its power consumption (110 watts for 8192 words of core memory) is at least twice that required of a processor employing hardware multiplication.

It is estimated that a processor could be developed consuming approximately 30 to 35 watts which has the required capability. For example, a 16-bit version of the 8-bit Payload Signal Processor (PSP) built by TRW and described in Reference 2 would be in this range and would be capable of meeting the performance requirements. The 8-bit version of the PSP is to be space qualified by mid-1979.

This estimate is based on using a 4096 by 40-bit program control memory and a 2048 by 16-bit RAM working memory. Since the processor is not time constrained, extensive use of branching to "subroutines" can be used to keep the program within these limits. Each of these memories requires approximately 10 watts. Combining these memories with the 10 watts required for the CPU yields the 30 watt estimate.

Resampling Processor

The preliminary hardware sizing described in this section employs off the shelf components and is straightforward in design . It does not assume use of yaw control to reduce the number of scan lines stored. This possibility is discussed in the next sub-section. The total number of parts is estimated to be 810, with a total power consumption of 135 watts (20 percent margin is included). The board area is estimated to be 2.2 square feet without redundancy. (Since much of the resampling hardware is identical for each spectral band, reliability considerations will require far less than 100 percent redundancy.) By careful design and use of custom device fabrication, the power consumption might be reduced by a factor of two.

The resampling processor (Figure 7) employs seven separate along scan and cross scan processors, one set for each of the seven spectral bands. A "skew buffer" memory is used to interface the along scan and cross scan processors. It stores 32 scan lines of data (262144 bytes) in each of the six high resolution bands. A single radiometric correction processor precedes the seven along scan processors. There are two microsequencers, one holding the control code for the radiometric and along scan processors and the other holding the control code for the skew buffer and across scan processors. Both microsequencers drive a delay line so the processors for each band receive a delayed version of the same code. The input and output are loaded into high speed First-In-First-Out-Stacks (FIFOS) for the purpose of resynchronizing the data to the processor rate.
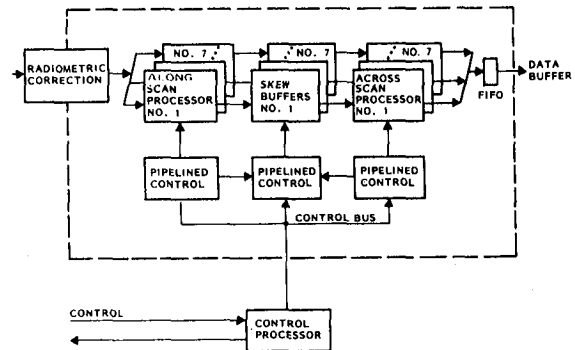
Figure 7. Resampler Block Diagram

249

The radiometric processor operates at 10 mega-samples/second. The along scan and cross scan processors operate at 600 nsec per pixel with sub-cycles of 150 nsec. This is near the limit of their capability with presently available parts. The parts which limit the speed of the processors are the 150 nsec multiplier and the 64k memory chips in the skew buffer. It is anticipated that faster parts will be available in the near term which will increase the speed margin. In addition, a custom-designed multiply/accumulate chip might be employed to decrease the complexity of the processors. The parts and power could also be reduced by using an alternate memory configuration which saves approximately five scan lines of data instead of 32. This would require increased addressing complexity, but results in a factor of six reduction in skew buffer memory. This coupled with the multiply/accumulate chip could potentially reduce power by as much as one-half. The development cost may be greater, however. This discourages their use in a prototype ground version of the resampling processor.

Attitude Control

As described above, ephemeris variation results in scan lines being skewed with respect to the X-axis of the coordinate frame. One technique of compensating for this skew is by using yaw commands. Small, infrequent commands are capable of compensating for ephemeris caused skew. This skew is virtually zero at the equator and increases to as much as six pixels at high latitudes. However, the change in skew is approximately 0.3 pixel during an image frame with the amount of skew being consistent to within a fraction of a pixel at image frame boundaries. This corresponds to a yaw command of 100 μrad given once each 30 seconds, which is well within the capability of the attitude control system. The dynamics of the attitude control system are measured and compensated in the pierce point calculation, so the commands do not adversely affect the registration.

The amount the yaw should be changed is determined by observing the slope of the scan line at some consistent time within each image frame. This can be directly translated into an attitude command and passed to the multimission modular space-craft computer for implementation. This calculation adds virtually no burden to the general purpose distortion calculation computer but can reduce the memory required in the resampler to six lines.

VII. Conclusions

We have shown that on-board correction of LANDSAT D imagery to subpixel accuracy is feasible using currently available technology. Specific methods to accomplish this goal have been described. Estimates of required size and power have been provided for both the special and general purpose hardware used. On-board realtime correction offers the potential of vastly increasing the percentage of images corrected and makes direct readout to users a valuable option.

REFERENCES

[1] "On-Board Image Registration Study", prepared by TRW Defense and Space Systems Group for Goddard Space Flight Center under Contract No. NAS5-23725, January 31, 1979.

[2] S. W. Houston, D. R. Martin, L. R. Stine, "Microprocessor Bit Synchronizer for Shuttle Payload Communications, IEEE Trans. Comm., Vol. COM-26, No. 11, Nov. 1978, pp. 1594-1603.

INCORPORATION OF STAR MEASUREMENTS FOR THE DETERMINATION OF ORBIT AND ATTITUDE PARAMETERS OF A GEOSYNCHRONOUS SATELLITE (AN ITERATIVE APPLICATION OF LINEAR REGRESSION)*

Dennis Phillips
Scientific Programming and
Applied Mathematics, Inc.

ABSTRACT

Currently on NOAA/NESS's VIRGS system at the World Weather Building star images are being ingested on a daily basis. The image coordinates of the star locations are measured and stored. Subsequently, the information is used to determine the attitude, the misalignment angles between the spin axis and the principal axis of the satellite and the precession rate and direction. This is done for both the 'East' and 'West' operational geosynchronous satellites. This orientation information is then combined with image measurements of earth-based landmarks to determine the orbit of each satellite. The method for determining the orbit is simple. For each landmark measurement one determines a nominal position vector for the satellite by extending a ray from the landmark's position towards the satellite and intersecting the ray with a sphere with center coinciding with the earth's center and with radius equal to the nominal height for a geosynchronous satellite. The apparent motion of the satellite around the earth's center is then approximated with a Keplerian model. In turn the variations of the satellite's height, as a function of time found by using this model, are used to redetermine the successive satellite positions by again using the earth-based landmark measurements and intersecting rays from these landmarks with the newly determined spheres. This process is performed iteratively until convergence is achieved. Only three iterations are required.

I.   Introduction

When the first geosynchronous spin stabilized satellites with spin scan cameras were launched, it was hoped that the image of the earth in these satellite generated images would remain stationary so that the dynamics of the world's weather systems could be observed with respect to an earth's reference frame. This hope was not realized.

Eventually (1970-1971) at SSEC of the University of Wisconsin, software packages were developed by Mr. Dennis Phillips and Mr. Eric Smith which generated a satellite attitude from earth based landmark measurements and satellite orbit parameters and which enabled one to transform earth coordinates to image coordinates and vice versa.

Next, Mr. John T. Young, also at SSEC, skillfully adjusted orbit parameters made available from either NASA or NOAA to align pictures with high precision on a regular basis. However, since this approach requires a highly skilled operator and is time consuming, this approach has essentially never been transferred to other installations.

Consequently, when NOAA/NESS convened with SSEC about the transfer of SSEC's navigational capabilities to NOAA/NESS's operations, it was resolved that a proposal of Mr. Dennis Phillips to develop automatic methods to extract attitude parameters and orbit parameters from earth based landmark measurements and earth edge measurements would be founded. As a result, two software packages, COMORB (compute orbit) and UPGORB (upgrade orbit) were developed at SSEC and transferred (June 1978) along with the VIRGS computer system to NOAA/NESS's World Weather Building. In September, 1978 Dr. Dennis Phillips demonstrated the alignment capability of this system and the software started to be used regularly in the operations around May, 1979.

However, in August, 1978, Dr. Ken Chan, Mr. Ron Gird and Mr. Ben Remondi, demonstrated that star images could be detected and measured in the image frame. It was recognized that star measurements would enable a very precise determination of the satellite's attitude and the misalignment between the satellite's spin axis and the satellite's principal axis. Dr. Dennis Phillips of Scientific Programming and Applied Mathematics, Inc. has subsequently modified the SYSNAV software package to accept these star measurements for attitude determination and changed the UPGORB software package to use these attitude and misalignment parameters to generate a Keplerian set of orbit parameters which predictively aligns satellite images 24 hours in the future. This software will be used in the operations very shortly.

II.   Attitude and Misalignment Parameter Determination

Each star measurement (we index the star measurements with the variable i) determines a unit vector (x_i, y_i, z_i) which points parallel to the direction from the satellite to the star. In addition, by using the line number of the position of the star in the image frame, we can determine approximately the angle ϕ_i between satellite's spin axis vector (u, v, w) and the unit vector. We have then, that

$$ux_i + vy_i + wz_i - \cos \phi_i = e_i \text{ for } i=1,\ldots,n$$

where   n is the number of star measurements and e_i is the error incurred at each ith measurement.

The mathematical problem is to minimize

$$S = \sum_{i=1}^{n} (ux_i + vy_i + wz_i - \cos\phi_i)^2$$

subject to the constraint $u^2 + v^2 + w^2 = 1$. We do this by iteration and take advantage of the fact that we know that w is always close to the value -1.

We set $(u_0, v_0, w_0) = (0, 0, -1)$

and iterate

(u_n, v_n) = solution of setting

$$\frac{\partial S(u, v, w_{n-1}) = 0}{\partial u}$$

$$\frac{\partial S(u, v, w_{n-1}) = 0}{\partial v}$$

and normalize by setting

$$w_n = -\sqrt{(1.0 - u_n^2 - v_n^2)}$$

until $(u_n - u_{n-1})^2 + (v_n - v_{n-1})^2 \leq 1.0 \text{ E-12}.$

Convergence is achieved in 2 or 3 iterations.

To realistically model the problem, we have to introduce the possibility of a pitch misalignment angle. Hence, we consider the problem of minimizing

$$S = \sum_{i=1}^{n} (ux_i + vy_i + wz_i - \cos(\phi_i+\phi))^2$$

again subject to the constraint $u^2+v^2+w^2 = 1$. Instead, we consider the equivalent problem

$$S = \sum_{i=1}^{n} (ux_i+vy_i+wz_i+ a\cos\phi_i + b\sin\phi_i)^2$$

subject to the constraints $u^2+v^2+w^2 = 1$

and $a^2+b^2 = 1$.

To solve we set

$(u_0, v_0, w_0, a_0, b_0) = (0,0,-1,0,-1)$

and iterate

$(u_0,v_0,b_0) =$ solution of setting

$$\frac{\partial S}{\partial u}(u,v,w_0,a_0,b) = 0$$

$$\frac{\partial S}{\partial v}(u,v,w_0,a_0,b) = 0$$

$$\frac{\partial S}{\partial b}(u,v,w_0,a_0,b) = 0$$

and normalize by setting

$$w_n = \sqrt{1.0-u_n^2-v_n^2}$$

and $\quad a_n = \sqrt{1.0 - b_n{}^2}$

until $(u_n - u_{n-1})^2 + (v_n - v_{n-1})^2 + (b_n - b_{n-1})^2 \leq 1.0E - 12$

Convergence is still achieved within 2 or 3 iterations.

The roll and yaw misalignment angles are determined by a method which in a mathematical sense is virtually identical to the approach used to find the attitude of the spacecraft.

III.   Orbit Determination

        Once the attitude and misalignment of the spacecraft are determined,
the determination of a set of orbit parameters describing the motion of the space-
craft is relatively straightforward.   By using the attitude and misalignment parameters
along with the line and element numbers of the measurement of image location of
earth-based landmark, one can determine a unit vector in inertial coordinates
which is parallel to the vector from the satellite to earth-based landmark.

        By extending a ray from the landmark towards the satellite and inter-
secting that ray with an earth centered sphere whose height approximately equals
the height of a geosynchronous satellite, one obtains an approximate satellite
position vector $P_i = \begin{pmatrix} x_i \\ y_i \\ z_i \end{pmatrix}$ at time t_i and indexed by i.

INTERSECTION AT
APPROXIMATE
SATELLITE
POSITION

EARTH

RAY EXTENDED TOWARDS
SATELLITE

EARTH-BASED
LANDMARK

SPHERE WITH RADIUS = 42,165 KM CENTERED AT EARTH'S CENTER

257
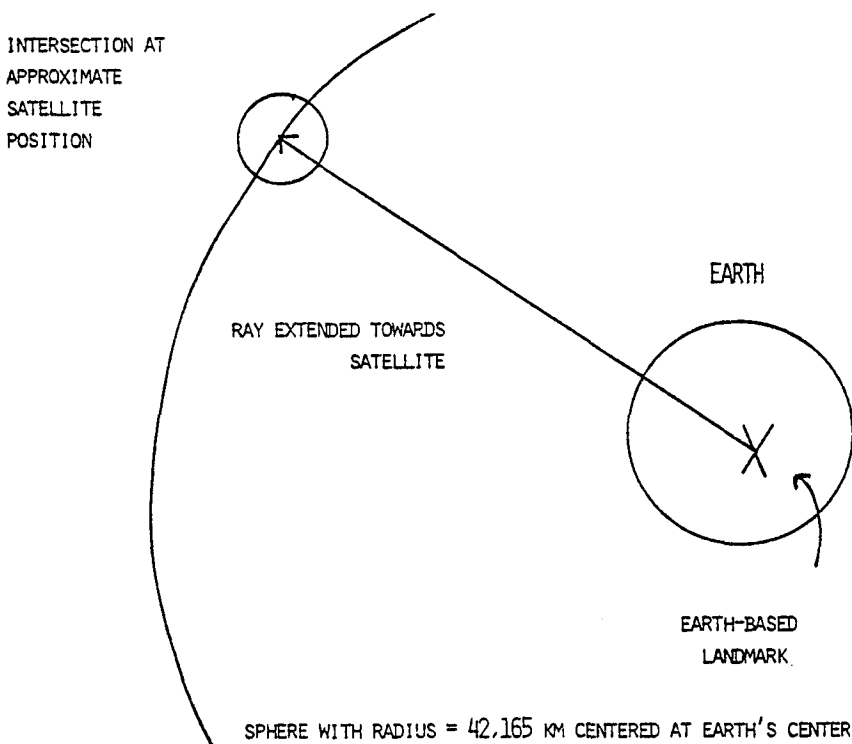
To determine the orbit plane perpendicular we minimize

$$S = \sum_{i=1}^{n} (ux_i + vy_i + wz_i)^2$$

subject to the constraint $u^2 + v^2 + w^2 = 1$

where here (u,v,w) is the orbit plane perpendicular and n is the number of approximate satellite positions.

The quantities

$$ux_i + vy_i + wz_i$$

should be close to zero by the definition of a perpendicular. The sum S is minimized by using exactly the same method used to find the spin axis vector.

All that is left to be determined is the motion of the satellite within its orbital plane. We model this motion with equation $t_i = c_1 + c_2 \alpha_i + c_3 \sin\alpha_i + c_4 \cos\alpha_i$ where the t_i's are the times the approximate satellite position vectors are determined, the α_i's are the angular positions of the approximate satellite position vectors around center of the earth with respect to some arbitrary reference axis and the c_i's are to be determined. This model is exactly Keplerian within .03 km for eccentricities less than .01.

The c_i's are determined by using linear regression to minimize

$$S = \sum_{i=1}^{n} (c_1 + c_2\alpha_i + c_3 \sin\alpha_i + c_4 \cos\alpha_i - t_i)^2.$$

A time span of 18 hours is necessary to determine c_2 and the other c_i's can be determined within a time span of 10 hours.

Estimates of the satellite's orbital variation of height as a function of time are obtained from the C_i's and used to recalculate the satellite approximate position vectors from the earth-based landmark measurements. This is done iteratively until a convergence criteria is satisfied. This requires 5 to 6 iterations. Finally, the orbit plane perpendicular and the constants C_i's are converted to standard Keplerian constants.

IV.   Evaluation Criteria for Attitude and Orbit Generating Software

1.   The amount of training and background required for each
     system operator

2.   The relative convenience and ease of use of the system

3.   The total man and computer resources necessary to operate the
     system

4.   Current operation status

5.   Accuracy

6.   Time required to recover operational accuracy after maneuvers

7.   Future development prospects

V.   Future Developments

       A.   Sun pulse documentation information will be used to detect and measure the effects of nutation and these effects will be removed

       B.   Attitude precession will be determined automatically

       C.   The orbit model will be improved to increase accurate propagation periods; eventual goal is to propagate accurately up to 7 to 10 days.

1. Report No. NASA CP-2123	2. Government Accession No.	3. Recipient's Catalog No.
4. Title and Subtitle FLIGHT MECHANICS/ESTIMATION THEORY SYMPOSIUM		5. Report Date August 1980
		6. Performing Organization Code 582
7. Author(s) Arthur J. Fuchs, Editor		8. Performing Organization Report No.
9. Performing Organization Name and Address Goddard Space Flight Center Greenbelt, Maryland 20771		10. Work Unit No.
		11. Contract or Grant No.
		13. Type of Report and Period Covered
12. Sponsoring Agency Name and Address National Aeronautics and Space Administration Washington, D.C. 20546		Conference Publication
		14. Sponsoring Agency Code

15. Supplementary Notes

16. Abstract

This document is a compilation of papers presented at the Flight Mechanics/
Estimation Theory Symposium held October 17-18, 1979, at the Goddard Space
Flight Center.

17. Key Words (Selected by Author(s)) Astrodynamics	18. Distribution Statement STAR Category 13 Unclassified — Unlimited

19. Security Classif. (of this report) Unclassified	20. Security Classif. (of this page) Unclassified	21. No. of Pages 268	22. Price* A12

National Aeronautics and
Space Administration

Washington, D.C.
20546

Official Business
Penalty for Private Use, $300

SPECIAL FOURTH CLASS MAIL
BOOK

U.S.MAIL

NASA

POSTMASTER: If Undeliverable (Section 158
Postal Manual) Do Not Return